SCALE INVARIANT DYNAMICS OF INTERFACES AND SHEARED SOLIDS

by

Joel Thomas Clemmer

A dissertation submitted to Johns Hopkins University in conformity with the requirements for the degree of Doctor of Philosophy.

Baltimore, Maryland

August, 2019

Abstract

In this thesis we study three types of non-equilibrium processes: the depinning of elastic interfaces, the yielding of sheared disordered solids, and the fracture and granular flow of brittle solids. All three display scale-invariant behavior. The first two systems evolve in discrete bursts of motion or avalanches whose magnitudes follow a power law distribution, while breakup of brittle solids produces a power law distribution of grain sizes.

The motion of elastic interfaces is studied using simulations of the random field Ising model. The interface is driven by gradually increasing an external magnetic field, leading to a series of avalanches whose maximum size diverges at a critical field. Growth is anisotropic, with the height of an avalanche growing as its width to a power $\chi = 0.85 \pm 0.01$. Scaling relations and finite-size scaling techniques are used to relate χ to other critical exponents. The roughness exponent of the growing interface is predicted to equal χ but is substantially smaller at accessible system sizes.

ABSTRACT

Molecular dynamics simulations are used to study critical behavior in slowly sheared disordered solids. The average flow stress rises as a power β of the strain rate. Finite-size scaling is used to determine β and the exponent describing the divergence of the correlation length with distance to the critical point. The temporal correlations in the average kinetic energy of the system are used to measure the dynamical exponent relating the duration of an avalanche to its spatial size.

Lastly, a discrete element model of brittle systems is developed. The model parameters can be calibrated to match specific material properties including elastic constants and fracture toughness. The model is used to study the impact of defect density and strain rate on the fracture of sheared brittle solids. A measure of damage is related to the initial yield and fragmentation. Subsequent granular flow produces a power-law distribution of grain sizes that suggests critical behavior at quasistatic strain rates and large strains. The maximum grain size decreases with increasing strain rate.

Primary Reader: Mark O. Robbins, Professor of Physics

Secondary Reader: Robert L. Leheny, Professor of Physics

Acknowledgments

I would like to especially thank my advisor Mark Robbins for the guidance, discussions, and Fortran code that made this work possible. He demonstrated not only the importance of physical insight and comprehensive analysis but also how to be an effective mentor. I also greatly appreciate the assistance and advice provided by many other professors at the university. In particular, I want to thank Lori Graham-Brady, Michael Falk, Ryan Hurley, Brian Camley, and Bob Leheny.

My colleagues in office 329 throughout the years, Mike, Tristan, Lin, Thomas, Joe, Marco, Vicente, and Kurmanbek, were instrumental in helping me complete this work. This includes brainstorming how to solve programming bugs and what word might fit in a crossword puzzle. I am thankful for both their help and their friendship.

Finally I want to thank my friends and family for their continued support. My parents for always encouraging my studies and my wife Taisha for all the love and patience.

Dedication

Dedicated to my family, my wife Taisha, and my cat Tikaboo.

Contents

List of Tables

List of Figures

Chapter 1

Introduction

1.1 Scale Invariance

A physical system exhibits scale invariance when its statistical properties appear the same under rescalings of length or time.[1] For instance, a fractal image looks the same when the viewer zooms in or out on the image. This is equivalent to rescaling all spatial coordinates by some factor, $x \to bx$. Functions can also exhibit anisotropic scale invariance. For instance, a self-affine function is one in which a rescaling of the argument is equivalent to a rescaling of the global function: $f(bx) = b^{\zeta} f(x)$ where ζ is known as the Hurst exponent. Self-affine scaling is observed in stock market prices as well as the height of the earth's surface.[2,3]

In some cases, it is easy to identify the origin of scale invariance and the exact value of the self-affine exponent ζ. For instance, in a one dimensional random walk one can

consider the position of the walker as a function of time $x(t)$. The root mean squared (rms) displacement of the walker grows as the square root of the time. Therefore, one can deduce that a statistically similar walk (assuming one cannot resolve the size of a step) is produced by rescaling time by a factor of b while rescaling the position by $b^{1/2}$: $x(bt) \sim b^{\zeta} x(t)$ where $\zeta = 1/2$. Note that there is not a strict equality as the rescaled function is only statistically similar to the original. In this case, the scale invariance simply arises from the addition of random numbers. In other cases, it is not as simple.

One particular class of scale invariance emerges from the dynamics of driven disordered systems. Similar scaling behavior occurs in many seemingly disparate systems. Gutenberg and Richter discovered that the energy E released by earthquakes is power-law distributed,[4] $P(E) \sim E^{-\tau}$, with an exponent τ.[5] This implies that earthquakes are scale invariant and there is no characteristic size up to the upper cutoff of the power-law due to the finite size of a fault.[6] Such power-law distributions have also been seen in the magnetization of a ferromagnetic material. As domain walls rearrange and align with the field, they produce bursts of noise called Barkhausen noise. The magnitude of this noise is also power-law distributed.[7,8] Earthquakes and Barkhausen noise also produce temporally scale invariant time signals with a non trivial exponent known as a pink noise exponent.[9,10]

Scale invariant distributions have also been identified in many other dynamical processes, including fracture and fragmentation. The propagation of a crack front displays jerky dynamics similar to earthquakes.[11] The resulting crack surface also displays self-affine roughness.[12] The volumes of rock fragments generated from ballistic impact, crushing, erosion, etc have often been found to be power-law distributed and many different exponents

have been measured.[13,14] Lastly, the size distribution of ice floes in the ocean produced by melting, freezing, and collisions also follows a power law.[15,16]

1.2 Dynamical Criticality

Models of scale invariance often draw on the concepts of equilibrium critical phenomena.[17] Critical points occur at second order phase transitions, such as the water vapor critical point or the Curie point for ferromagnetic materials. Away from the critical point there is a correlation length ξ that characterizes the maximum range of correlations. This correlation length diverges as the system approaches the critical point. At the critical point fluctuations occur on all scales and correlations decay as a power of distance. Critical points can be characterized by a set of scaling exponents that describe the decay of correlations and the divergence of ξ near the critical point. Renormalization group theory calculates these exponents from the scaling of thermodynamic functions with increasing length scale. A powerful result is that systems that share the same underlying symmetries and dimension fall into universality classes and are described by the same set of critical exponents.[18] For example fluid phase separation and Ising ferromagnets are in the same universality class. This implies that a simple, reduced model that contains the correct fundamental symmetries and interactions can be used to study the critical behavior of a real system.

An analytical connection between avalanches and criticality was first formulated in 1983 when Fisher proposed a mean field theory describing the presence of a critical point at the onset of sliding of charge density waves.[19] This is known as a depinning transition

as it separates a pinned, static phase from a moving phase. The critical behavior at the transition could be described by renormalization of a dynamical equation of motion rather than thermodynamic functions like the free energy.[20,21]

Depinning transitions are found in a large class of d dimensional driven interfaces.[22,23] In $d = 2$, examples include the dynamics of a crack front,[11,24] fluid contact lines,[25,26] and forest fire fronts.[27] In $d = 3$, depinning transitions have been studied in fluid invasion in porous rock,[28] the motion of magnetic domain walls discussed above,[29,30] and cell migration.[31] In all these cases, interfaces propagate through a medium containing quenched disorder. Quenched disorder consists of hetereogeneities that are frozen into the system and do not vary in time. This is in contrast to annealed disorder where the noise fluctuates in time. At small driving forces an interface is pinned by the quenched disorder and will not advance. As the driving force is increased, the interface advances in a series of bursts or avalanches. The size of the largest avalanche grows as the driving force approaches a critical value F_c. At F_c, the size of avalanches follows a power-law distribution. As the force is increased above F_c, the noise is no longer capable of pinning the interface and it propagates with some finite velocity that grows as a power of the distance above the critical force.

Critical behavior has also been observed when yield stress materials are sheared. Yield stress materials such as granular packings,[32,33] colloids,[34] bubble rafts,[35] and foams[36] will not flow unless a critical stress is exceeded. The yielding transition is therefore a transition between a jammed phase and a flowing phase, much like the onset of motion in depinning. It has been argued that interface depinning and the yielding transition are in the same universality class and can be described using the same mean field theory exponents.[37] Other

work suggests the exponents are different[38,39] due to different symmetries in the elastic interactions coupling different regions.[40] It has also been demonstrated that the addition of inertia in yielding changes the critical exponents of avalanches.[38,39] Inertia is important in many physical systems such as earthquakes.

1.3 Self-Organized Criticality

An interesting question still remains, why do so many dynamical systems in nature demonstrate critical behavior? To reach an equilibrium critical point a control parameter must be finely tuned to a critical value of the temperature, density, or some other state variable. A theory was proposed in 1988 by Bak, Tang, and Weisenfeld that systems with many interacting degrees of freedom may contain a critical attractor, some minimally stable state that systems evolve to.[41] This was termed self-organized criticality. This idea was exemplified by the evolution of a growing sand pile. As sand is slowly and randomly dropped onto a pile, the pile grows until it reaches a critical slope at which point depositing additional grains triggers avalanches on all length scales, a critical steady state.

Although later work demonstrated real sand piles do not actually produce true critical behavior,[42,43] the theory of self-organized criticality provided a motivation for the origin for the emergence of critical dynamical behavior. As Fisher had also pointed out, if the critical point is at zero rate, one does not need to tune a parameter but merely drive the system slowly.[22] More recent work has converged on this view as the most common origin for non-equilibrium critical phenomena such as the depinning and yielding transitions.[44]

It has been suggested that the process of fragmentation at finite rates[45,46] and the subsequent breakup of grains in flow,[14] known as comminution, represent instances of self-organized criticality. If these processes do represent critical behavior, the nature of such a critical point is not well understood. For instance, it is not clear what dynamical equation could be studied under renormalization or what would be the equivalent to a steady state in comminution, since grains may continue to fracture at large strains. We show below that increasing rate lowers the maximum size of grains and thus criticality in flow can only occur at zero rates.

1.4 Outline of Thesis

Each of the three following chapters focuses on a different example of non-equilibrium scale invariance emerging in a disordered system. Since the systems are very different, each chapter contains a detailed introduction with background material on past work, a description of the methods used, a discussion of the results, and a summary. In each case, we use computer simulations to identify fundamental behavior and determine critical exponents corresponding to each critical point. We study simple, idealized models, but the measured exponents are expected to apply to a wide range of physical systems in the same universality class. As in equilibrium systems, the universality class should only depend on symmetries and not on the specific form of atomic interactions, crystal lattice, or other details.

In the second chapter we explore the dynamics of interfaces driven through a d di-

mensional random medium. Most studies of interface depinning have assumed that the interface can be reduced to a single valued function of the $d-1$ dimensions perpendicular to the direction of motion. This assumption simplifies the analysis but artificially breaks the isotropy of the underlying Hamiltonian. Real interfaces are fully d dimensional manifolds and can be multivalued. To address this limitation, our simulations model fully $d=3$ dimensional domain wall motion in the random field Ising model. Avalanches grown in the model are anisotropic with the height normal to the interface $\ell_\perp$ scaling as a power of the lateral extent $\ell_\parallel$: $\ell_\perp \sim \ell_\parallel^\chi$ where χ is distinct from previous studies of depinning. A scaling theory that incorporates anisotropy is derived and tested by studying many properties of the system using finite-size scaling techniques.

The third chapter examines the related problem of the yielding transition. We use molecular dynamics simulations in two and three dimensions and finite-size scaling techniques to accurately identify the critical exponents governing the scaling with strain rate for the first time. Scaling relations are obtained and tested for the behavior of a range of system properties near the critical point including the average flow stress, fluctuations in the flow stress, temporal correlations, and diffusion.

In the fourth chapter we study the fracture and granular flow of brittle, isotropic solids. This chapter describes how the model is constructed to capture key material properties such as the elastic moduli and fracture toughnesses. Then we present results highlighting the impact of defect density and strain rate on the initial fracture of two and three dimensional solids. In particular we track the growth of cracks and the evolution of a damage parameter and relate this to the stress in the system. Next, we look at comminution in the granular

flow regime. Our model produces a power-law distribution of grain sizes in both two and three dimensions in the quasistatic limit. At a finite rate, there exists a maximum grain size that decreases with increasing rate. Finally, we discuss how material properties affect the statistics of grains and the internal friction.

The final chapter discusses general conclusions from the work. Results from the three prior chapters are condensed and relations to other work are discussed. Future directions of research are proposed.

Chapter 2

Anisotropic Avalanches in Depinning

2.1 Introduction to Depinning

As mentioned in the introduction, an important class of non-equilbrium critical behavior is that of the motion of an elastic interface through a medium with quenched disorder.[19] This is a very diverse class of systems and includes problems such as magnetic domain wall motion,[29,30] fluid invasion in porous media,[28] contact line motion,[25,26] and the propagation of crack fronts.[11,24] The onset of athermal motion of a driven interface is called a depinning transition and occurs at a critical driving force F_c. As F increases towards F_c the interface advances between stable states in a sequence of bursts of motion termed avalanches. Avalanches in depinning exhibit scale-free behavior and have a power-law size distribution.

The maximum size of an avalanche grows as F approaches F_c and can be related to a diverging correlation length. For $F > F_c$ the interface is never stable, and avalanches are associated with fluctuations in the rate of growth. As F increases, these fluctuations become smaller. The value of F_c is determined by a competition between the disorder and the elastic cost of deforming the interface. Different universality classes have been identified, depending on whether disorder is large or small[8,30,47–49] and whether elastic interactions are local or have a long, power-law tail.[50,51]

A magnetic domain wall or fluid interface can have any orientation in a d dimensional system and the driving force always favors advance perpendicular to the local orientation. At high disorder, the growing interface becomes self-similar with a fractal dimension related to percolation.[52] At low disorder, elastic interactions are able to spontaneously break symmetry and enforce an average interface orientation.[28,30,53,54] The interface becomes self-affine, and fluctuations in height along the average surface normal rise as ℓ^ζ where $\zeta < 1$ is the roughness exponent and ℓ is the displacement in the $d-1$ dimensions along the interface.

Most models of interface motion focus on the self-affine regime and begin with the assumption that the height is a single-valued function.[20,21,55–60] While this simplifies the application of analytical methods, it explicitly breaks the spatial symmetry of the physical system and may thus change the universality class. The above models also use an approximation for the elastic energy that is only valid when derivatives of the height are much less than unity. These assumptions may not be self-consistent because the regions of extreme disorder which are important to pinning[61] also create large forces and therefore

large surface slope and curvature.[62] Moreover, motion can be stopped at any field by a single unflippable spin or uninvadable pore. Such extreme regions need not stop a fully $d-$dimensional interface. A multi-valued interface can have overhangs that advance around regions of strong disorder and merge to create enclosed bubbles that are left behind the advancing interface. This process is clearly observed in advancing fluid interfaces.[63]

In this chapter we examine the critical depinning transition in a model that does not impose an interface orientation, the $d = 3$ random field Ising model (RFIM).[48] Simulations with more than 10^{12} spins are analyzed using finite-size scaling, and scaling relations between exponents are derived and tested. While the domain wall between up and down spins is not single valued, growth is strongly anisotropic. The correlation lengths along and perpendicular to the interface diverge near the critical point with different exponents $\nu_{\|}$ and $\nu_{\perp}$, respectively. Individual avalanches show the same growing anisotropy, with the height scaling as width to the power $\chi = \nu_{\perp}/\nu_{\|} = 0.85 \pm 0.01$. The anisotropy is also consistent with scaling relations for the distribution of avalanche volumes and lengths and the maximum volume and lengths. The scaling of the total rms interface roughness is consistent with $\zeta = \chi$, and the power law describing changes in roughness with separation along the interface appears to approach χ as L increases near the critical point.

These results are quite different from earlier work on the RFIM. Calculated exponents were consistent with scaling relations that assumed $\chi = 1$[53] but used systems with linear dimensions more than 40 times smaller[30] for which we show finite-size effects are significant. Later work used systems up to four times larger and found $\chi = 0.9 \pm 0.1$ was still consistent with unity.[64] All earlier work concluded that the roughness exponent ζ was consistent with

the mean field value of 2/3 and less than χ.

The results are compared to studies of the quenched Edwards-Wilkinson (QEW) equation, a single-valued interface model that is often used for domain wall motion.[57,59,60,65] Some exponents, such as the power law describing the distribution of avalanche volumes are nearly the same in both models.[30,59] However the anisotropy is quite different.

In Sec. 2.2 we describe the implementation of the RFIM model and different growth protocols used. Results are presented in Secs. 2.3 to 2.6. In Sec. 2.3, the critical field and correlation length exponent are first identified using the fraction of avalanches which span the system. Next the divergence of avalanches as the system approaches the critical field and the distribution of avalanches at the critical field are calculated. Finally we propose a scaling of the total volume invaded in the system as a function of distance to the critical point. In Sec. 2.4 we look at the morphology of avalanches including the average dependence of the height on the width and the distributions of widths and heights. Next we consider the scaling of avalanches that span the system. In Sec. 2.5 we study the scaling of the interface morphology. We look at the total width of the interface, self-affine scaling, and the statistics of overhangs. Finally in Sec. 2.6 we look briefly at behavior for different strengths of disorder. In Sec. 2.7 we summarize our results and compare to past work.

2.2 Methods

We simulate athermal motion of a domain wall in the RFIM on a cubic lattice in $d = 3$. The Hamiltonian of the system is given by:

$$\mathcal{H} = \sum_{<i,j>} s_i s_j - \sum_i (\eta_i + H) s_i \tag{2.1}$$

where $s_i = \pm 1$ is the state of the i^{th} spin, H is the external magnetic field, and η_i is the local random field. Interactions extend only to nearest neighbors and the coupling strength is defined as the unit of energy. The random local field is taken to be Gaussian distributed with a mean of zero and a standard deviation of Δ.

Previous work has determined that there exists a critical value of the noise $\Delta_c \sim 2.5$ separating two universality classes.[54] In the limit of $\Delta > \Delta_c$, fluctuations in noise dominate the Hamiltonian such that interactions become irrelevant. Therefore, the local orientation of the interface does not significantly favor a direction of growth and the problem reduces to invasion percolation.[30,66] The invaded volume has a self-similar hull described by percolation theory.[52] In the limit of small noise, $\Delta < \Delta_c$, interactions lead to more compact, cooperative growth producing a self-affine interface. In Sec. 2.6 we briefly study systems at a range of Δ and verify the transition from isotropic growth above Δ_c to anisotropic growth below Δ_c. Exponents for several Δ below Δ_c are consistent and we focus on results for $\Delta = 1.7$ in all other sections.

Interfaces are grown with fixed boundary conditions along the direction of growth and periodic boundary conditions perpendicular to growth. The upper and lower boundaries

consist of layers of down and up states respectively, necessitating the presence of a domain wall within the bulk. In the periodic directions, the system has a width of $L_x = L_y = L$ while the height of the box along the direction of growth is typically set to $L_z = 2L$. A larger vertical dimension helps ensure the upper boundary condition does not interfere with growth for most simulation runs.

Systems are initialized with all spins in the down state except for the bottom layer, creating an initially flat domain wall. Spins are only allowed to flip up if they lie on the interface, i.e. if one of their neighbors is up. This requirement is motivated by models with a conservation law such as fluid invasion where fluid must flow along a connected path to new regions.[48] This rule ensures that there is a single domain wall separating the unflipped region at large z from flipped spins and is the usual assumption in scaling theories of interface motion through a disordered medium. In contrast, studies of Barkhausen noise in hysteresis loops of the RFIM allow disconnected spins to flip and this changes things like the critical disorder Δ_c.[8,49,67]

The RFIM considered here only has cubic symmetry, but past studies show that scaling of interface growth is isotropic in both the self-affine and self-similar regimes.[55,68,69] Planar growth along facets of the lattice only occurs for a bounded distribution of random fields at very weak disorder.[69,70] This is in sharp contrast to models that explicitly break symmetry by assuming the interface is a single-valued function of height.[55,57,59,60,65,68] Some 2+1 dimensional models even have direction-dependent critical fields and other anisotropic properties.[55,68] Given the established isotropy of growth in our model we consider the simplest case where the sides of the box are aligned with the nearest-neighbor directions and

the initial interface has a (001) orientation.

Growth occurs athermally through single spin-flip dynamics. The external magnetic field is initialized to the lowest value that will excite a single spin on the interface to flip up. The stability of neighboring down spins is checked and they are flipped up if this lowers the global energy. This procedure can lead to a chain reaction and is repeated until all spins are stable along the interface. The "no-passing rule"[71,72] guarantees that the resulting interface is independent of the algorithmic order in which spins are flipped. The magnetic field is then increased to flip the least stable remaining spin and the process is repeated until either the interface reaches the upper boundary or the field is well above the critical point. Less than 2% of systems of size $L = 1600$ hit the boundary at a height of 3200 before reaching the critical field. This process produces invaded volumes such as the examples in Fig. 2.1 rendered using the Open Visualization Tool (OVITO).[73]

Each time the external field is incremented, the resulting cluster of flipped spins is recorded and grouped as a single avalanche. The volume and linear dimensions of each avalanche are calculated. Because the interactions are short range, all spins in a cluster are connected. Some avalanches can have a length of L or larger in the direction perpendicular to growth due to the periodic boundary conditions. If these avalanches percolate, colliding with a periodic image of themselves, specifying their lateral size is ambiguous. We will refer to these avalanches as spanning avalanches and two examples are seen in Figs. 2.1a-b. We exclude spanning avalanches from most analysis unless otherwise mentioned. Avalanches which are truncated by reaching the upper boundary are always excluded.

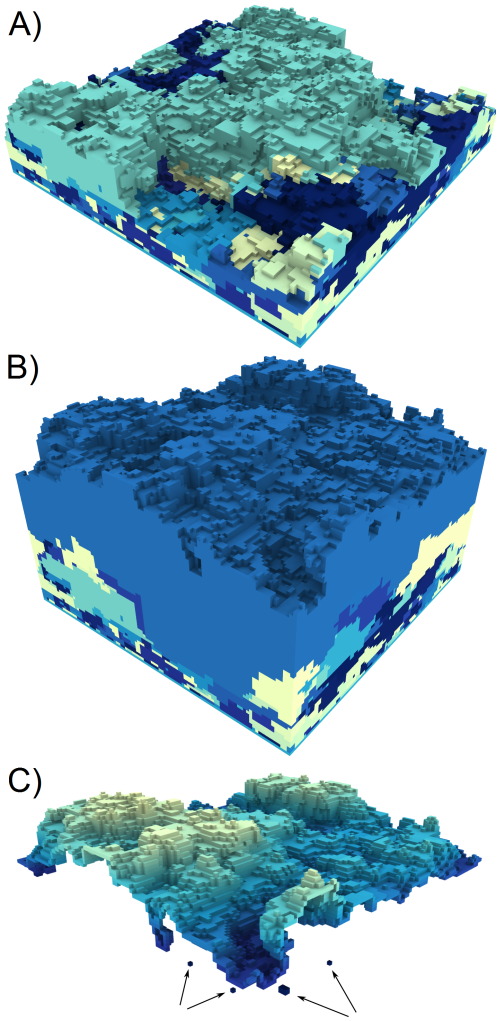

Figure 2.1: Flipped spins in a sample simulation of size $L = 100$ are shown for different stages of growth corresponding to (a) $H \approx 1.44579$ and (b) $H \approx 1.45853$. Contiguous spins are grouped by their associated avalanche and colored accordingly. Along the cross-section one can see more examples of small avalanches at low heights which grew at smaller values of the external field H. At larger heights, growth occurred at a higher value of H and larger avalanches are visible. The final avalanche (teal) in (a) is an example of a semi-spanning avalanche that wraps across a periodic boundary condition and percolates. The final avalanche (blue) in (b) is an example of a fully-spanning avalanche that has a footprint of L^2 and advances the entire interface. The set of spins which could potentially flip in response to an increase in H in (b) are rendered in (c). These unflipped spins can either be on the external interface or contained inside a bubble. Four bubbles consisting of either six unflipped spins or a single unflipped spin are indicated by arrows. The remaining visible region constitutes the external interface. Note that it is not a single-valued function of height and large overhanging regions are visible at the bottom cross-section. Particles are colored by height for improved visibility.

We further divide spanning avalanches into two classes: semi-spanning and fully-spanning avalanches. We define the footprint of an avalanche as the total area of all flipped spins projected into the $x - y$ plane. The footprint of any avalanche is contained in the interval $[1, L^2]$ by definition. We define semi-spanning avalanches as percolating events that have a footprint less than L^2. A specific example is shown in Fig. 2.1a. Fully-spanning avalanches are percolating events that have a footprint equal to L^2 such as the final avalanche seen in Fig. 2.1b. The differences between these two classes of spanning avalanches are discussed in Subsec. 2.4.3.

Any unflipped down spin with a neighbor in the flipped up state is a potential site for an avalanche. However, as seen in Fig. 2.1c, these spins can be sorted into two topologically distinct regions: the external interface and bubbles. The external interface consists of spins that are connected to the upper boundary of the cell by an unbroken chain of unflipped spins. This interface delimits the extent of propagation. Alternatively, certain spins with a strong pinning force may become surrounded by the domain wall and enclosed in a bubble. While avalanches could still grow in bubbles, they would be heavily constrained by the geometry of the bubble and would not contribute to the structure of the external interface. Therefore they are excluded from all analysis in this chapter. This rule is analogous to the problem of incompressible fluid invasion where growth within bubbles is not allowed. The average fraction of volume behind the external interface that is in bubbles is quite small and nearly independent of H and L. For $\Delta = 2.1$, bubbles make up less than 0.02% of the volume and for $\Delta = 1.7$ this fraction decreases below 0.001% as seen in Fig. 2.2.

In addition to the growth protocol described above, a second protocol was also imple-

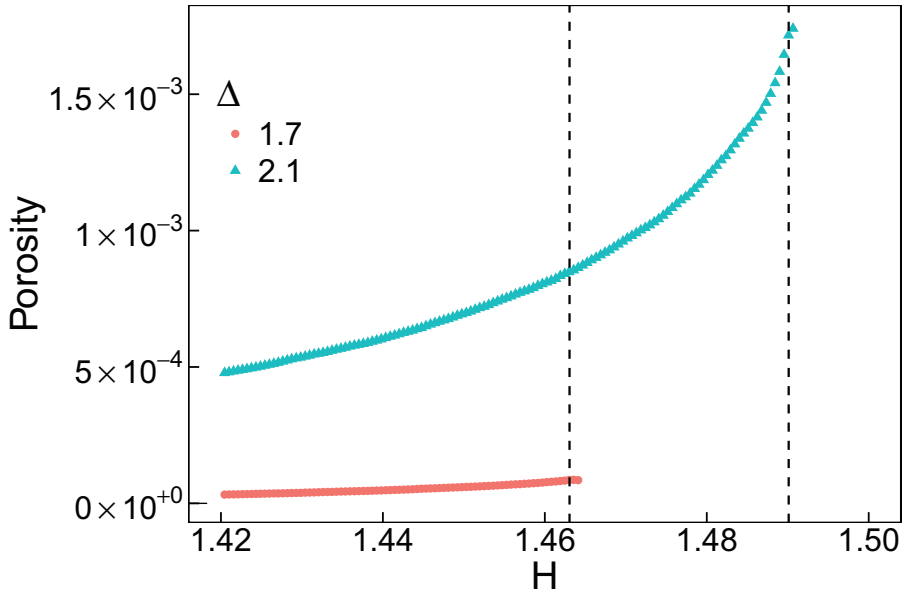

Figure 2.2: Porosity or the percent of volume in bubbles versus the distance to the critical field $\Delta H = H_c - H$ for systems with $\Delta = 2.1$ (blue) and 1.7 (red). Here $H_c = 1.490115$ and 1.46305 for $\Delta = 2.1$ and 1.7 respectively.

mented. In this method, the external field is set at a fixed value and unstable spins are continually flipped until the interface is stable. In this protocol, we do not resolve individual avalanches. This allows for efficient parallelization of the code allowing simulation of larger system sizes. As referenced before, the "no-passing rule"[71,72] guarantees the resulting interface does not depend on the parallelization scheme. Using the primary protocol and tracking individual avalanche growth, we simulate systems up to a size of $L = 3200$ and with the alternate protocol we reached system sizes of $L = 25600$, flipping more than 10^{12} spins. At all system sizes, many simulations were run with different realizations of disorder and results were averaged.

2.3 Avalanche Volume

In this section we look at the statistics of the magnitude or volume of an avalanche. First we determine the critical field by studying the fraction of volume invaded that consists of spanning avalanches in Subsec. 2.3.1. Next we look at the divergence of the average avalanche volume to identify the critical exponent associated with their size in Subsec. 2.3.2. This exponent is then related to theoretical distributions of avalanche magnitudes and predictions are verified in Subsec. 2.3.3. Finally, we use these results to propose a theory describing the scaling of the total volume invaded in Subsec. 2.3.4.

2.3.1 Fraction of Volume from Spanning Events

As the external field is increased, the domain wall advances through a sequence of avalanches. The size of the largest avalanche increases with external field, indicating a growing correlation length. The critical field H_c is defined as the field where the correlation length diverges and interfaces in an infinite system will depin and advance indefinitely. In a finite-size system the depinning transition is broadened. There is a range of H where the correlation length is comparable to the system size L. In this range, interfaces in some systems will remain pinned while others will advance to the top. In this subsection we will use finite-size scaling methods to determine H_c and the scaling of the in-plane correlation length $\xi_{\|}$ from simulations with different L.

For a self-affine system, correlations may be different for motion along and perpendicular to the interface. We define a correlation length along the interface as $\xi_{\|}$ and a correlation length in the direction of growth as $\xi_{\perp}$. Both are expected to diverge at the critical field in

an infinite system with exponents $\nu_\parallel$ and $\nu_\perp$, respectively:

$$\begin{aligned} \xi_\parallel &\sim |H_c - H|^{-\nu_\parallel} \\ \xi_\perp &\sim |H_c - H|^{-\nu_\perp}. \end{aligned} \tag{2.2}$$

We define $\chi = \nu_\perp/\nu_\parallel$ such that $\xi_\perp \sim \xi_\parallel^\chi$.

The total volume invaded over an interval of external field is defined as the number of spins that become unstable and flip. For a finite system, a fraction F_s of these flipped spins will be part of system-spanning avalanches, while the rest are in smaller avalanches. At very low fields where $\xi_\parallel \ll L$, no avalanches will span the system and $F_s = 0$. At very large fields, $H > H_c$, $F_s \to 1$ as the system becomes depinned at all system sizes and the largest, spanning avalanches dominate the increase in volume.

Fig. 2.3 shows the change in F_s with H for different system sizes. For each L, the size of increments in H was chosen to be small enough to resolve the transition but large enough to reduce noise. After calculating F_s for each interval, the curves were further smoothed by applying a rolling average across all sets of three adjacent intervals. At fields above H_c, many systems have already reached the top of the box and stopped evolving. We therefore discarded poorly sampled data points at large values of $H > H_c$. The transition from growth by finite avalanches to spanning avalanches sharpens as L increases. Using a simulation cell of height $2L$ ensured that F_s was not significantly affected by finite system height.

In finite-size scaling theory one assumes that the only important length scales in the

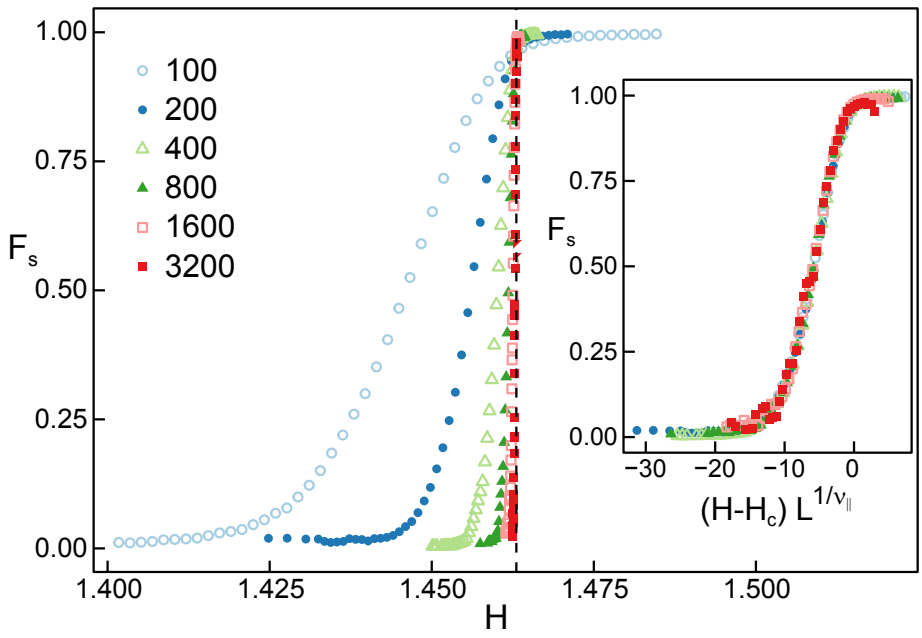

Figure 2.3: The fraction of volume invaded due to system spanning avalanches over a small interval of H is calculated for the values of L indicated in the legend. A dashed vertical line indicates $H_c = 1.46305$. The inset shows the collapsed data using the finite-size scaling procedure described in Eq. (2.3) with a value of $H_c = 1.46305$ and $\nu_{\|} = 0.79$.

system are the correlation lengths, $\xi_\parallel$ and $\xi_\perp$, and the system size, L. Finite-size effects are expected when the largest correlation length approaches L. The simulation cell is taller than it is wide and we find $\xi_\perp < \xi_\parallel$, so $\xi_\parallel$ dominates the finite-size effects. Functions like F_s then depend on the dimensionless scaling variable $L/\xi_\parallel$. Using Eq. 2.2, F_s can be expressed in terms of the field as:

$$F_s \sim f\left((H - H_c)L^{1/\nu_\parallel}\right) \tag{2.3}$$

where the scaling function f should be independent of L. Given the limiting behavior of F_s, $f(x)$ must approach zero for $x \ll -1$ and one for $x \gg 1$. Note that Eq. 2.3 gives $F_s = f(0)$ for all L at $H = H_c$. Therefore the critical field must correspond to the location where all curves cross in Fig. 2.3. This intersection occurs at a value of $H_c \sim 1.46304 \pm 0.00003$. Here and below, the error bars do not represent a standard deviation, but indicate the maximum range over which data collapse within statistical fluctuations. Koiller and Robbins had previously found H_c for various values of Δ in this system.[54] Although the value of H_c was not explicitly determined for $\Delta = 1.7$, our result is consistent with interpolations of their data from nearby values of Δ.

Eq. 2.3 also implies that all curves should collapse when plotted against $(H - H_c)L^{\nu_\parallel}$ for the correct value of $\nu_\parallel$. For all scaling collapses in the following plots, we choose to use a common value of $H_c = 1.46305$ based on consideration of the above estimate of H_c and the scaling of other system properties discussed later in the manuscript. The inset of Fig. 2.3 shows a successful collapse of F_s with a value of $\nu_\parallel = 0.79$. Based on the sensitivity of the collapse to changes in $\nu_\parallel$, the data is consistent with $\nu_\parallel = 0.79 \pm 0.02$. This value is close to prior estimates of $\nu_\parallel = 0.75 \pm 0.02$[54] and 0.75 ± 0.05[30] in the RFIM. Ref. 30 and 54

used scaling approaches that assume $\chi = 1$, which may have impacted the reported value. The RFIM with a uniform instead of Gaussian distribution of random fields is expected to be in the same universality class and past simulations found $\nu_{\|} = 0.77(4)$.[70] For the QEW model of interface growth, the mean field value of ν is found to be 3/4.[21] Arguments in Ref. 20 suggest 3/4 is a lower bound on the actual exponent. Epsilon expansions give 0.67 and 0.77 to first and second order, which suggests that ν could be slightly above the mean-field value.[57]

The maximum distance a depinning avalanche can advance the interface is set by the box height. One might wonder whether this artificial threshold could affect the scaling of F_s. As an alternative measure, we considered the footprint of an avalanche, the projected area in the $x - y$ plane of all spins flipped by an avalanche. This measure is independent of how far an avalanche propagates in the $\hat{z}$ direction. Over an interval of H, avalanches will cumulatively advance the interface over a region equal to the sum of their footprints. Note that some avalanches may overlap such that certain regions may advance more than once. In analogy to F_s, one can then define the fraction of the area advanced by spanning avalanches, F_a. We find F_a scales in the same manner as F_s with consistent estimates of H_c and $\nu_{\|}$. This verifies that the results of F_s are not affected by alternative scaling behavior of spanning avalanches.

Another useful measure is F_{ss}, the fraction of growth in semi-spanning avalanches. Fig. 2.4 shows that F_{ss} obeys a scaling relation like (2.3) with the same H_c and $\nu_{\|}$ but a different scaling function $f_{ss}(x)$. For each L, F_{ss} rises from zero at small H to a maximum below H_c and then drops as fully-spanning avalanches begin to dominate growth. From Figs. 2.3 and

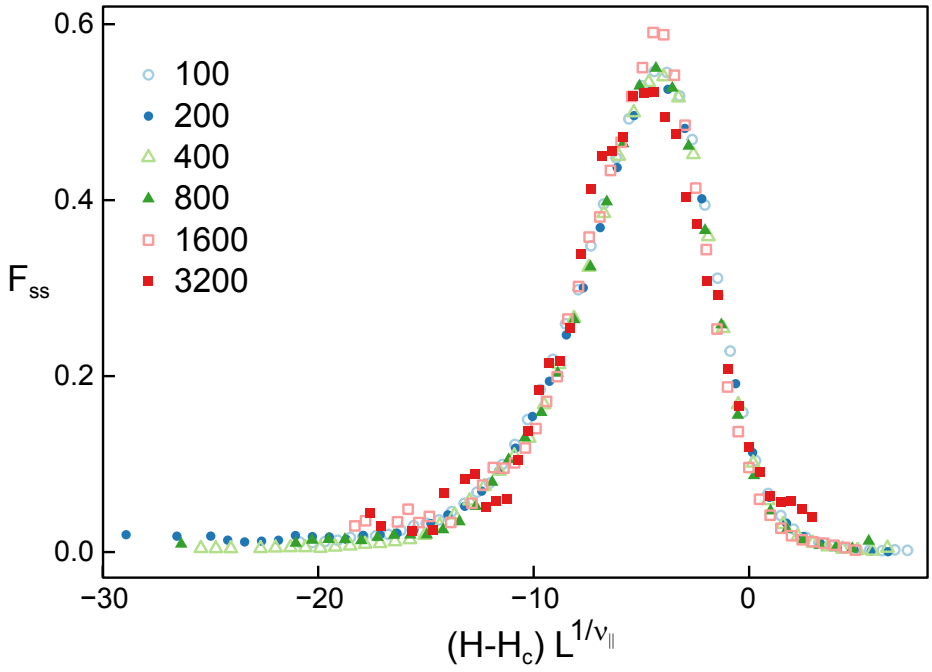

Figure 2.4: The fraction of volume invaded due to semi-spanning avalanches over a small interval of H is calculated for the values of L indicated in the legend and scaled according to a finite-size scaling procedure similar to Eq. (2.3). The collapse uses values of $H_c = 1.46305$ and $\nu_{\|} = 0.79$.

2.4, we see that semi-spanning and fully-spanning avalanches begin to be important when $H_c - H$ is smaller than about $10L^{1/\nu_{\|}}$ and $5L^{1/\nu_{\|}}$, respectively. This is useful in estimating the region where $L > \xi_{\|}$.

Note that $f(0)$ has a value of about 0.97 that is very close to unity. This implies that almost all the incremental growth near H_c is due to spanning avalanches. Spanning avalanches also make up roughly 75% of the cumulative invaded volume from the initial flat interface to H_c. The importance of large avalanches is related to the power-law distribution of avalanche sizes that we discuss in the next two subsections.

2.3.2 Divergence of Avalanche Volumes near H_c

As noted above, spanning avalanches are more related to depinning above H_c than the approach to H_c from below. In addition, their height is bounded only by the arbitrary height of the simulation box. In contrast, the vertical growth of non-spanning avalanches is naturally correlated to their lateral extent. Thus we focus here on non-spanning avalanches, providing a discussion of spanning avalanches in Subsec 2.4.3. Non-spanning avalanches that grow close to H_c, after the appearance of spanning avalanches, are included as they exhibit the same scaling as avalanches grown prior to the first spanning avalanche.

We define a normalized probability distribution of non-spanning avalanche volumes S, $P(S, H, L)$, which depends on both the current value of the field H and the size of the system L. At the critical point, the distribution of avalanches is expected to decay as a power law with an exponent τ, $P(S, H_c, \infty) \sim S^{-\tau}$. Away from the critical point the power law will extend to a maximum volume, $S_{\max}$, that reflects the influence of a limiting length scale ℓ. In general this will be the smaller of the system size L and the correlation length $\xi_{\|}$. The maximum volume will scale as power of this length, ℓ^{α}, where α is another critical exponent.

Having defined the behavior of the distribution, we can determine how statistical moments of avalanches depend on $S_{\max}$. The m^{th} moment of the avalanche volume is calculated

by integrating the distribution up to the maximum avalanche cutoff $S_{\max}$:

$$\langle S^m \rangle = \int P(S,H,L) S^m dS \tag{2.4}$$

$$\langle S^m \rangle \sim \int^{S_{\max}} S^{m-\tau} dS \tag{2.5}$$

For values of $m > \tau - 1$, this integral is dominated by the largest avalanches and scales as:

$$\langle S^m \rangle \sim S_{\max}^{m-\tau+1}. \tag{2.6}$$

Alternatively, if $m < \tau - 1$, the integral is dominated by the smallest avalanches and will not diverge as a power of $S_{\max}$ but instead saturate. As shown next, the integral diverges for $m = 1$, but not for $m = 0$. This implies that $1 < \tau < 2$ and that $P(S,H,L)$ is independent of H and L for small S.

We will focus on the average size $\langle S \rangle$ ($m = 1$) as the lowest moment that gives information about $S_{\max}$. We define the variable $\Delta H \equiv H_c - H$ as the distance to the critical field from below. To study the variation of $\langle S \rangle$ with ΔH, S is averaged over all nonspannning avalanches that nucleated in an interval of field. The width of the interval decreases as the logarithm of ΔH for $\xi_\parallel < L$ to minimize changes in $S_{\max}$ over the interval. A fixed width is used for $\Delta H L^{1/\nu_\parallel} < 2$, where $\xi_\parallel \gg L$.

Fig. 2.5a shows the increase in $\langle S \rangle$ with decreasing ΔH at different L. For each L, $\langle S \rangle$ shows a power law divergence, $\langle S \rangle \sim \Delta H^{-\phi}$, and then saturates at a value of ΔH that shrinks with increasing L. In the power law regime where $L > \xi_\parallel$, we can use Eq. 2.6 and

$S_{\max} \sim \xi_{\|}^{\alpha}$ to determine a scaling relation:

$$\phi = \nu_{\|}\alpha(2-\tau). \tag{2.7}$$

In the saturated region, $\xi_{\|} > L$, $S_{\max} \sim L^{\alpha}$ and $\langle S \rangle \sim L^{\phi/\nu_{\|}}$.

Given the above scaling behavior we can construct a finite-size scaling ansatz similar to Eq. (2.3):

$$\langle S \rangle \sim L^{\phi/\nu_{\|}} g\left(L^{1/\nu_{\|}}\Delta H\right) \tag{2.8}$$

where $g(x)$ is a new scaling function. In the asymptotic limit of $x \gg 1$, $g(x)$ will scale as $x^{-\phi}$ to reproduce the power law in Eq. (2.6). Alternatively, when $x \ll 1$, $g(x)$ must approach a constant such that $\langle S \rangle \sim L^{\phi/\nu_{\|}}$.

Finite-size scaling only holds near the critical point. Close examination of Fig. 2.5a shows that the slopes of curves for all L change for $\Delta H > 10^{-2}$. This is consistent with later results in the text that show critical behavior only for $\Delta H < 10^{-2}$. Thus we only include fields in this range in finite-size scaling collapses. Note that $\langle S \rangle$ has saturated at $\Delta H > 10^{-2}$ for $L = 100$. Results for $L = 25$ and 50 saturated even farther from the critical regime and we do not include results for these small systems in this chapter.

Fig. 2.5b shows a scaling collapse of curves for different L using $\nu_{\|} = 0.79$ and $\phi = 1.64$. Testing the sensitivity of the collapse to these parameters, we estimate uncertainties of $\nu_{\|} = 0.79 \pm 0.02$, consistent with our above estimate, and $\phi = 1.64 \pm 0.04$. A direct measure of ϕ from Fig. 2.5a yields 1.64 ± 0.04. Within errorbars, this is consistent with the result

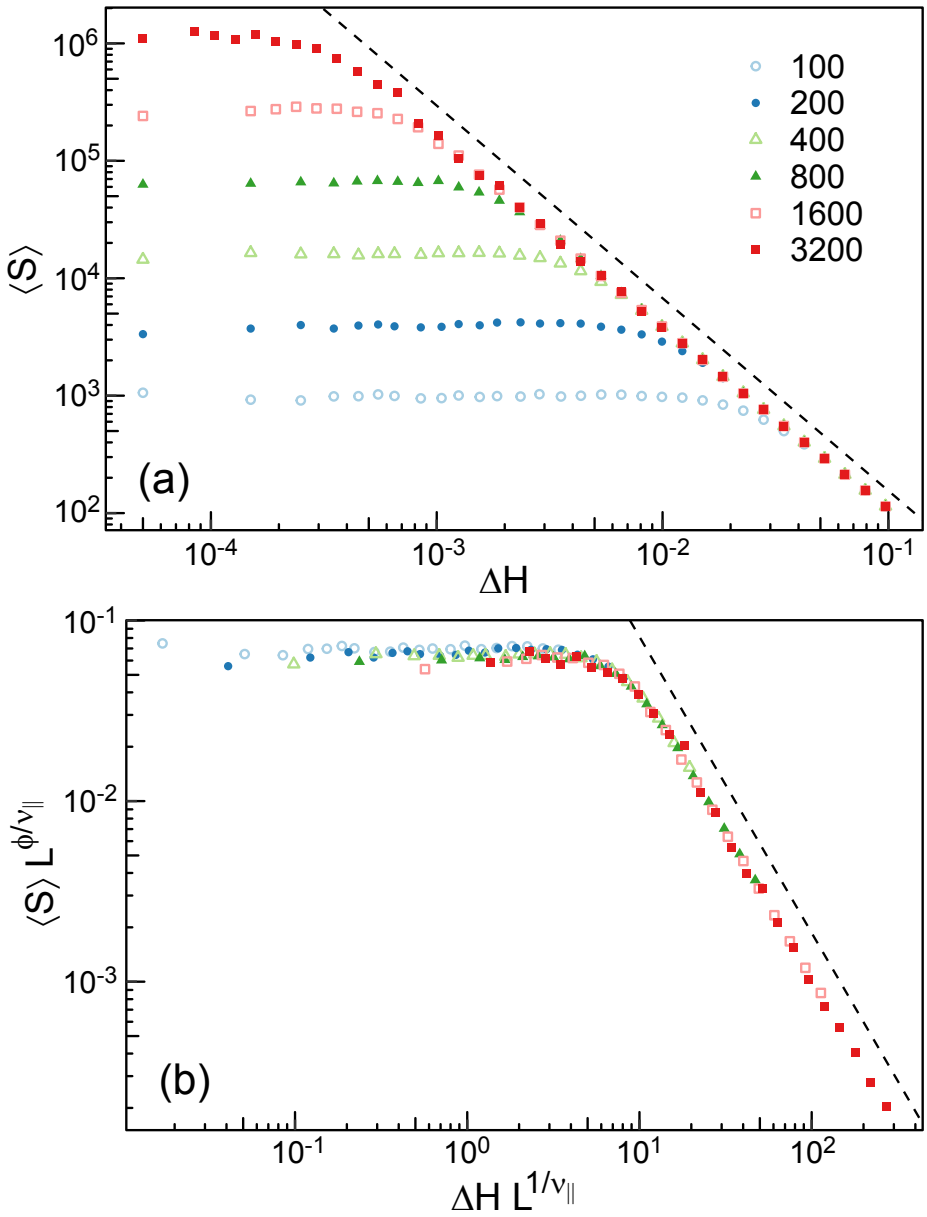

Figure 2.5: (a) The average volume of an avalanche $\langle S \rangle$ calculated at different values of ΔH for systems with size L indicated in the legend. Note that the slope characterizing changes in $\langle S \rangle$ drops slightly for $\Delta H > 10^{-2}$. (b) Scaling collapse for Eq. (2.8) with values of $\phi = 1.64$ and $\nu_{\|} = 0.79$. Only data near the critical point $\Delta H < 10^{-2}$ are included. Dashed lines in both panels indicate power-law scaling with $\phi = 1.64$.

from Ref. 30, $\phi = 1.71 \pm 0.11$.

A similar scaling procedure could also be performed on larger moments. However, the higher moments do not depend on any additional exponents and they have increased sensitivity to the largest events which are the hardest to sample.

2.3.3 Avalanche Distribution

Having seen how the maximum avalanche volume $S_{\max}$ depends on H and L, we next focus on the regime near H_c, where $\xi_\parallel > L$, and calculate the distribution of S in order to isolate the exponents τ and α. In this limit, $S_{\max}$ will no longer be limited by $\xi_\parallel$ but rather by L. We select avalanches that nucleated sufficiently close to the critical point such that $\xi_\parallel > L$ and designate the distribution as $P(S, L)$, dropping the dependence on field. Based on the length of the plateau in Fig. 2.5b, we consider all non-spanning avalanches in the range $0 < \Delta H < 10L^{-1/\nu_\parallel}$. This is consistent with the range where spanning avalanches dominate growth in Figs. 2.3 and 2.4. Consistent scaling results were obtained for half and one tenth of this range.

To calculate $P(S, L)$, avalanches are logarithmically binned by size and the number of events in each bin is divided by the size of the bin before normalizing the distribution. The resulting distributions, seen in Fig. 2.6a, have a clear power-law regime followed by a cutoff at a value of $S_{\max}$ that grows with increasing system size. As noted above, the fact that $P(S, L)$ is constant at low L implies $\tau > 1$. This is consistent with a direct evaluation of the slope which gives $\tau = 1.28 \pm 0.01$. More accurate values are obtained by finite-size scaling.

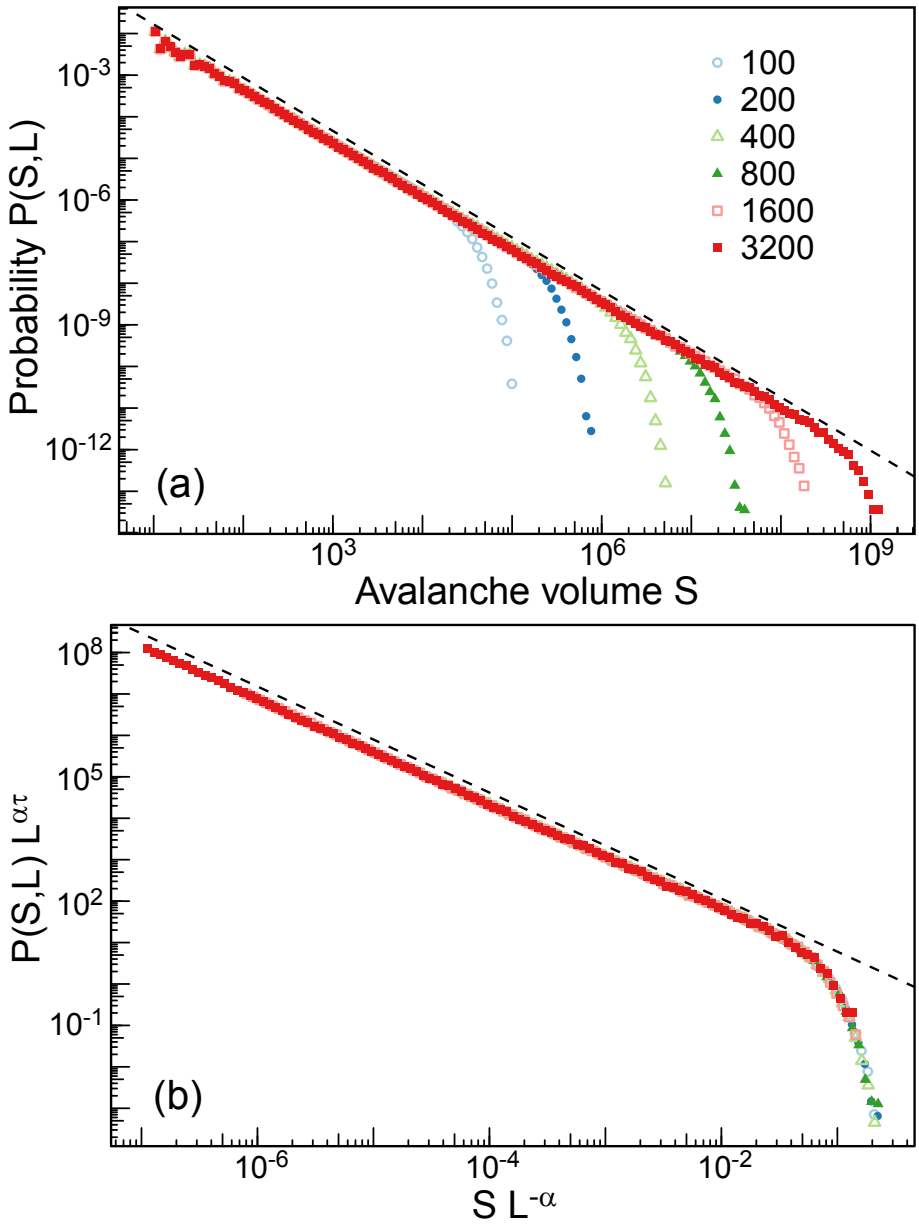

Figure 2.6: (a) The probability distribution of the volume of avalanches is calculated for the system sizes indicated in the legend at ΔH sufficiently close to the critical point such that $\xi_{\|} > L$, corresponding to $\Delta H < 10L^{-1/\nu_x}$. The dashed line represents a power law with $\tau = 1.28$. (b) The same data is collapsed by scaling with system size according to Eq. (2.9) with exponents $\tau = 1.28$ and $\alpha = 2.84$. Avalanches of $S < 10^3$ are excluded from the scaling.

The cutoff seen in Fig. 2.5b will depend only on the ratio of S to $S_{\max}$ allowing us to write an expression for the distribution as:

$$P(S, L) \sim L^{-\alpha\tau} f_p(S/L^{\alpha}) \tag{2.9}$$

where $f_p(x)$ is another universal scaling function. For $x \gg 1$, f_p goes to zero while for $x \ll 1$ one must have $f_p(x) \sim x^{-\tau}$ in order to recover the power-law scaling with S. This scaling should only apply for sufficiently large S and L. In the previous subsection we found changes in behavior for $\Delta H < 10^{-2}$. Here we see evidence of deviations from scaling in avalanches with $S < 10^3$. In Subsec. 2.4.1 we see the discreteness of the lattice is important for these small avalanches and thus they are excluded from finite-size scaling collapses. Including them does not significantly affect our best fit estimates for exponents but affects the quality of the collapse.

Fig. 2.6b shows a finite-size scaling collapse based on Eq. (2.9). Based on the quality of the fit we estimate the values and uncertainties of the exponents as $\tau = 1.280 \pm 0.005$ and $\alpha = 2.84 \pm 0.02$. As noted above, this value of τ is between 1 and 2 and is consistent with direct evaluation of the slope in Fig. 2.6a and the value found for the RFIM in Ref. 30, $\tau = 1.28 \pm 0.05$. From Eq. (2.7), our values of τ and α predict $\phi = 1.62 \pm 0.05$ which is in agreement with the directly measured value.

2.3.4 Volume Invaded

In Subsec. 2.3.2 the scaling of the average volume of an avalanche $\langle S \rangle$ was determined. Here the analysis is extended to develop a scaling relation for the divergence of the total integrated volume. Over a small increase in external field from H to $H + dH$, the interface will advance a volume dV:

$$dV \sim \langle S \rangle_A A(H, L) R(H, L) dH, \tag{2.10}$$

where A is the number of spins on the external interface and the nucleation rate R is the number of avalanches nucleated per spin per change in field. Here, $\langle S \rangle_A$ indicates an average over all avalanches including spanning avalanches. Since the largest avalanches dominate $\langle S \rangle_A$ for $\tau < 2$, spanning avalanches contribute most to dV. This explains why F_s is near unity close to H_c (Fig. 2.3). We begin by studying how A and R evolve with increasing H and L.

The area A is defined as the number of flipped spins that are on the external interface and adjacent to unflipped spins. One could also count the number of unflipped spins adjacent to these flipped spins or the number of bonds between flipped and unflipped spins. These measures differ by less than 0.1% for all H and L and thus give the same scaling behavior.

The area of the interface is initially equal to L^2. As the interface advances and roughens, A increases. Even a single-valued rough interface defined on the cubic lattice will have $A > L^2$ because of discrete steps in height on the lattice. If the interface steps up by

n sites, there will be n spins on the interface at the same x, y. Overhangs produce a further increase in A because there may be multiple horizontal interfaces at each x, y. The contribution of overhangs to A is discussed in Subsec. 2.5.3.

To remove the trivial dependence of area on L^2, we define the relative area $A_R(H, L) \equiv A(H, L)/L^2$. Figure 2.7 shows how A_R grows as H approaches H_c. For each L, the value of A_R saturates as ΔH decreases. The onset of saturation occurs at the same ΔH as other quantities discussed in this chapter, and is associated with $\xi_\parallel$ reaching L. In contrast to other quantities, the limiting value of A_R remains finite. Since Figure 2.7 is a linear-log plot, one can see that A_R grows less than logarithmically with increasing L. The inset of Fig. 2.7 shows that the data is consistent with convergence to a finite limiting value $A_{R,\mathrm{Lim}} = 2.05$ as $L \sim \infty$. Data for all L and $\Delta H < 10^{-2}$ are collapsed by assuming a power law approach to $A_{R,\mathrm{Lim}}$ with an exponent ψ:

$$A_{R,\mathrm{Lim}} - A_R(H, L) \sim L^{-\psi/\nu_\parallel} f_A\left(\Delta H L^{1/\nu_\parallel}\right) \tag{2.11}$$

where $f_A(x)$ is a new scaling function that saturates for $x \ll 1$ and scales as $f_A(x) \sim x^\psi$ for $x \gg 1$. The quality of the collapse is consistent with $\psi = 0.23 \pm 0.05$ and $A_{R,\mathrm{Lim}} = 2.05 \pm 0.05$. Due to the dependence on many parameters, it is difficult to get more accurate estimates of these values.

The value of $A_{R,\mathrm{Lim}}$ increases with the strength of the noise Δ. For $\Delta = 2.1$, we find $A_{R,\mathrm{Lim}} = 3.52 \pm 0.05$ with the same value of ψ within our errorbars. In the self-similar regime ($\Delta > \Delta_c$), the surface area of the invaded volume will scale at least as rapidly as

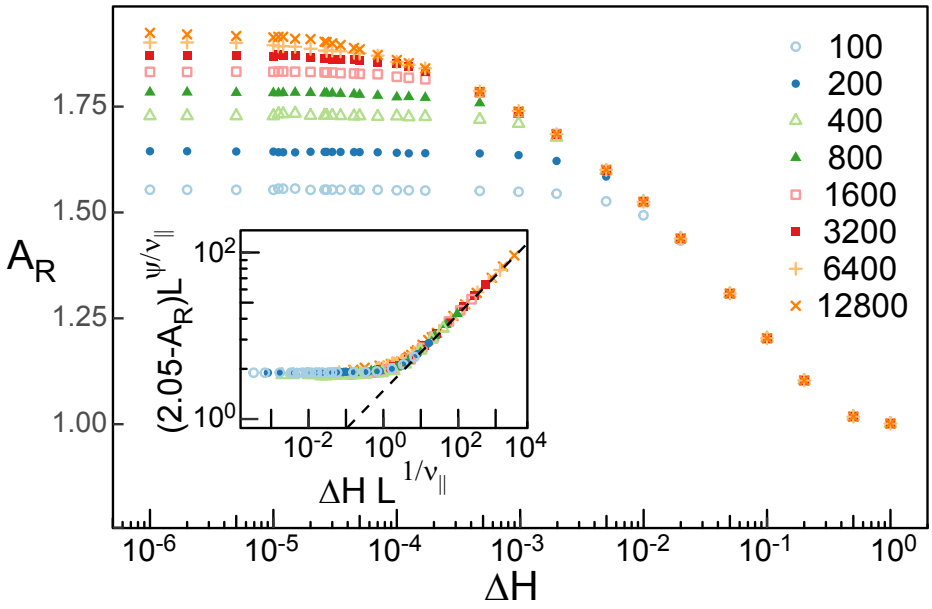

Figure 2.7: The surface area of the external interface normalized by L^2 is shown as a function of external field for L given in the legend. Inset: Collapse of data in main panel for $\Delta H < 10^{-2}$ using Eq. 2.11 for $A_{R,\mathrm{Lim}} = 2.05$, $\psi = 0.23$ and $\nu_{\parallel} = 0.79$. Data was generated using the alternative growth protocol where spins are flipped until a stable interface is reached at a fixed value of the external field.

L^{D_f}, where $D_f > 2$ is the fractal dimension. Therefore, we expect $A_{R,\mathrm{Lim}}$ to diverge as Δ approaches Δ_c, but do not study this transition here.

We now turn our focus to the rate $R(H, L)$ at which avalanches nucleate per spin per increment of external field. The rate R is calculated by tallying the number of avalanches, both spanning and non-spanning, nucleated over an interval of field and then dividing the total by the duration of the interval and the surface area. Intervals are evenly spaced on an axis of $\log \Delta H$. As seen in Fig. 2.8, R does not depend on L and becomes independent of ΔH for $\Delta H < 10^{-2}$. This is part of the evidence used to determine that the critical region is limited to $\Delta H < 10^{-2}$. Fig. 2.8 confirms that sufficiently close to the critical point the nucleation rate is independent of ΔH and extensive with the surface area. This is expected

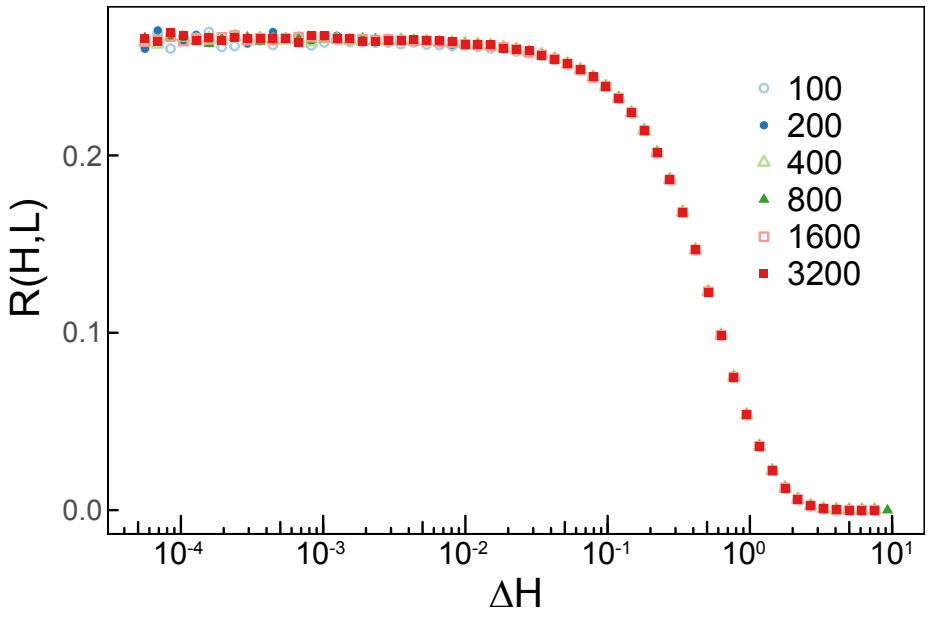

Figure 2.8: The rate of avalanche nucleation $R(H, L)$ over logarithmically spaced intervals of H for values of L indicated in the legend.

for interface motion since the interface moves into new regions of space and the no-passing rule is obeyed[20,53] and was verified for the case of fluid invasion.[53] Note that very different behavior has been observed for critical behavior in sheared systems where the entire system is perturbed by internal avalanches and they produce stresses that are not positive definite. In these systems the rate of avalanches rises less rapidly than the system size.[38,39,74,75]

Equipped with these results, we now derive an expression for the total volume invaded at fields below the onset of finite-size effects or spanning avalanches. If no avalanches span the system, then $\langle S \rangle_A = \langle S \rangle$. From Eq. (2.6), $\langle S \rangle \sim \Delta H^{-\phi}$ diverges as H approaches H_c. For small enough ΔH, A_R and R are approximately constant. In this limit, the total

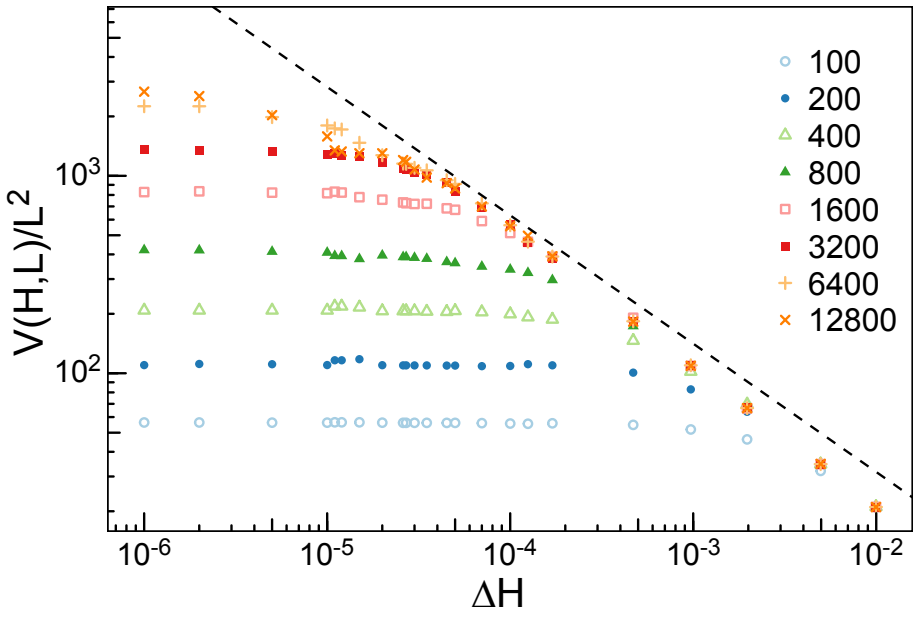

Figure 2.9: The total volume invaded normalized by L^2 is calculated as a function of H for values of L indicated in the legend. A power law with exponent $1 - \phi = -0.64$ is overlaid for comparison and follows the data for about a decade.

volume invaded per unit area scales as:

$$\langle V \rangle / L^2 \sim \int \langle S \rangle dH \sim \int \Delta H^{-\phi} dH \sim \Delta H^{-\phi+1}. \tag{2.12}$$

Figure 2.9 shows V/L^2 as a function of H and L. A dashed line indicates the expected power law divergence using the value of $\phi = 1.64$ from Subsec. 2.3.2. The data appears to follow the expected scaling for about a decade from 5×10^{-5} to 5×10^{-4}. Finite-size effects set in at smaller ΔH. As shown above, the variation in A_R remains significant down to $\Delta H \sim 5 \times 10^{-4}$.

2.4 Avalanche Morphology

The measurement of the exponent α in Fig. 2.6 allows us to estimate the anisotropy of correlations in the system. In d dimensions, the largest avalanches will span an area $\sim \xi_{\parallel}^{d-1}$ and reach a height $\sim \xi_{\perp}$. From Eq. (2.2) and the definition of χ, this implies $\alpha = d - 1 + \chi$. Previous scaling relations assumed that $\chi = 1$[28,30] or the roughness exponent ζ.[20] Our result for α implies $\chi = 0.84 \pm 0.03$ in three dimensions, which is midway between unity and previous measurements of $\zeta \sim 2/3$.[30,54] This would imply that χ is a distinct exponent and there is a novel anisotropy in the RFIM not previously seen in other depinning systems. To test this, we consider the morphology of avalanches in this section. In Subsec. 2.4.1, we calculate the moments of individual avalanches to determine how the width and the height of avalanches vary. Next in Subsec. 2.4.2 we calculate the distributions of the width and height. Finally in Subsec. 2.4.3 we look at how the scaling of spanning avalanches differs from non-spanning avalanches.

2.4.1 Avalanche Height Versus Width

In order to define the width $\ell_{\parallel}$ and height $\ell_{\perp}$ of an avalanche, we define a second moment tensor with components $l_{\alpha\beta}$, where α and β represent the directions x, y, or z. Given an avalanche with a center of mass located at $(x_{\rm cm}, y_{\rm cm}, z_{\rm cm})$, we define the tensor components as:

$$l_{\alpha\beta} = \frac{1}{S} \sum_{i=1}^{S} (\alpha_i - \alpha_{\rm cm}) (\beta_i - \beta_{\rm cm}) \tag{2.13}$$

where the summation over i corresponds to a sum over all S spins flipped by the avalanche. For avalanches that cross a periodic cell boundary, the positions of spins are unwrapped across the boundaries such that their position is measured relative to the original nucleation site.

Since periodic boundary conditions force the global motion to proceed in the $\hat{z}$ direction, avalanches will align with this orientation on average. However, an individual avalanche may nucleate and grow along a locally sloped region of the surface. In these instances, the avalanche's normal vector may not correspond to $\hat{z}$. To avoid biasing the results by assuming a local growth direction, we considered the eigenvalues of the second moment tensor, a method used in Ref. 64. We associate $\ell_\perp^2$ with the smallest eigenvalue and $\ell_\parallel^2$ with the geometric average of the largest two eigenvalues.[1] This decision is based on both the fact that $\xi_\perp < \xi_\parallel$ and the fact that growth is promoted along the local interfacial orientation due to the destabilizing effect of flipped neighbors. This definition will minimize the ratio $\ell_\perp/\ell_\parallel$ and therefore will also minimize estimates of χ.

The corresponding eigenvectors of the second moment tensor indicate the direction of growth. At small scales, the orientation of the interface is arbitrary and the direction of the eigenvector $\hat{v}_{\min}$ associated with the smallest eigenvalue also varies. For self-affine surfaces the orientation is more sharply defined at large scales. We find $\hat{v}_{\min}$ becomes more aligned with $\hat{z}$ as the size of the avalanche, S, increases relative to the size of the system. We quantify this alignment by the polar angle θ defined as $\cos\theta = \hat{v}_{\min} \cdot \hat{z}$. For $L = 3200$, avalanches with $S \sim 10^8$ have a root mean square (rms) deviation in angle from $\hat{z}$ of $\sim 6^\circ$.

[1] Using the arithmetic mean gives equivalent results.

In contrast, the rms angular deviation grows to $\sim 39^\circ$ for small avalanches consisting of 10^3 spins.

Values of $\ell_\parallel$ and $\ell_\perp$ were calculated for avalanches which nucleated sufficiently close to the critical point such that the largest avalanches were limited by system size rather than the correlation length. As in the previous subsection, the range was set to $0 < \Delta H < 10L^{-1/\nu_\parallel}$. In Fig. 2.10a, $\ell_\perp$ is plotted as a function of $\ell_\parallel$ for a representative set of avalanches grown in a system of $L = 3200$. There is a broad spread among individual avalanches but $\ell_\perp$ clearly grows sublinearly with $\ell_\parallel$, implying $\chi < 1$ and thus that avalanches become proportionately flatter as they grow in size. The power law rise is also clearly larger than previously measured values of the roughness exponent, $\zeta = 0.67$, and consistent with our estimate of $\chi = 0.84$ at the start of this section.

To accurately measure χ, we binned avalanches by $\ell_\parallel$ and calculated the average value of $\ell_\perp$ for systems of a given L. Fig. 2.10b shows that the mean height of an avalanche grows as a power of the width before being cut off due to finite-size effects. Note that the apparent power law changes for very small avalanches. The height can only vary in discrete steps of unity and this will affect the scaling of avalanches with small $\ell_\perp$. Based on the change in slope in Fig. 2.10b and the lack of scaling for $L < 100$, we only include avalanches with $\ell_\perp > 2$ in scaling collapses. This corresponds to $\ell_\parallel \sim 5$ and $S \sim 10^3$, which is consistent with the cutoff used in scaling $P(S, L)$.

In the critical region, results for $\ell_\parallel$ and $\ell_\perp$ should collapse when each is scaled by an appropriate power of the system size L. The maximum width of an avalanche is limited

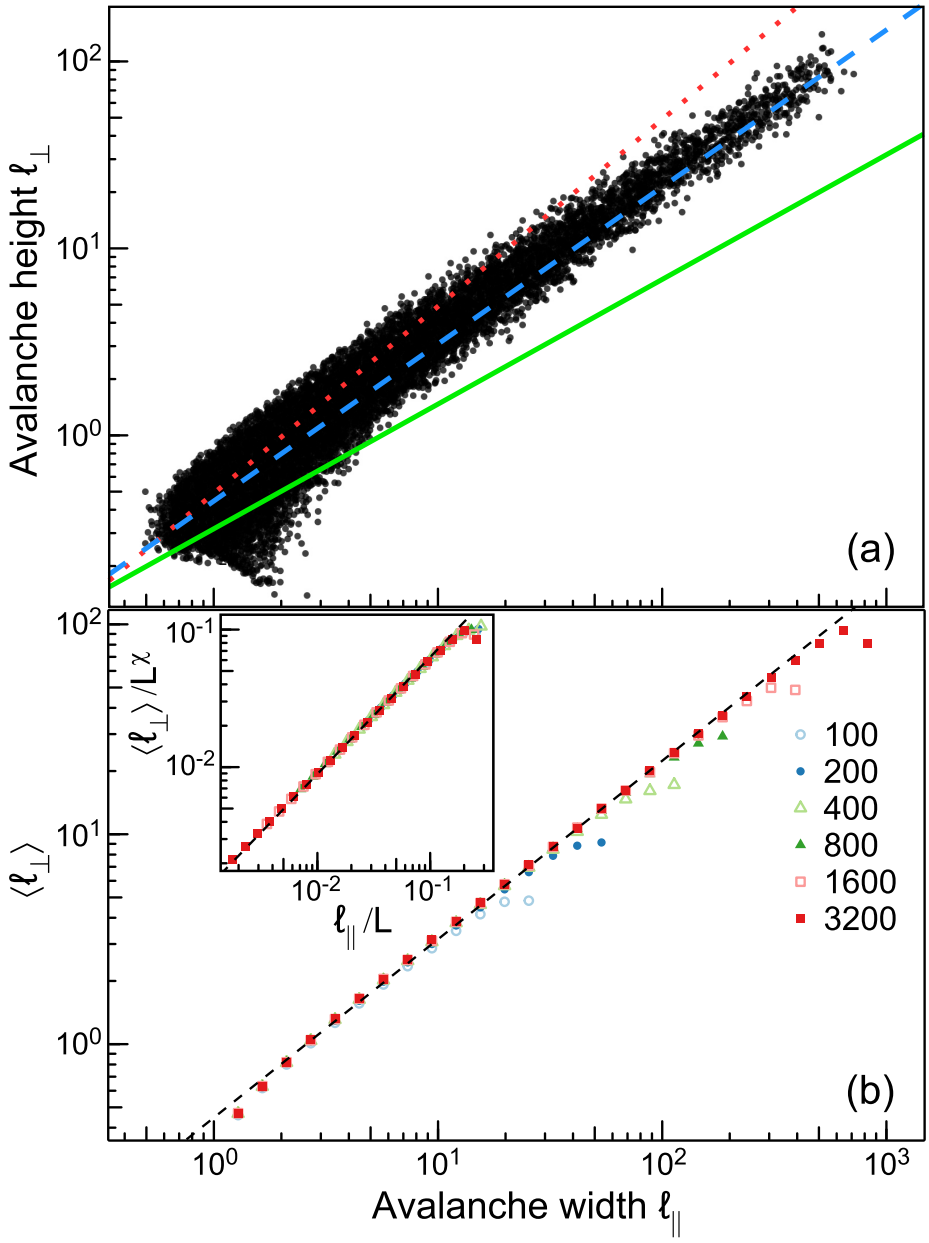

Figure 2.10: (a) Sizes of individual avalanches along and perpendicular to the interface in systems of $L = 3200$ near H_c. Lines indicate power laws corresponding to $\chi = 1$ (dotted, red), 0.84 (dashed, blue), and 2/3 (solid, green). (b) Mean avalanche heights as a function of width for the system sizes indicated in the legend for $\Delta H < 10L^{-1/\nu_\parallel}$. Avalanches are binned by their width and the average height is calculated for the system sizes indicated in the legend. The dashed line has a slope of $\chi = 0.85$. In the inset, data for different L with $\ell_\parallel > 5$ are collapsed by scaling the avalanche width by L and the height by L^χ for $\chi = 0.85$.

by L due to the finite box size and the restriction that an avalanche is non-spanning. The corresponding maximum height an avalanche can attain must scale as L^{χ}. The inset in Fig. 2.10b shows that curves for different L collapse when each length is scaled by its maximum value. Varying χ, we find a collapse is achieved for the range of $\chi = 0.85 \pm 0.02$. Alternatively, one could bin by $\ell_{\perp}$ and average $\ell_{\parallel}$. This process produces similar values of χ.

We also studied the quantities $\ell'_{\parallel} \equiv \sqrt{l_{zz}}$ and $\ell'_{\perp} \equiv (l_{xx} l_{yy})^{1/4}$, which measure anisotropy relative to the periodic boundaries. As seen in Fig. 2.11, the scaling behavior is similar to using moments but not as good. There appears to be a slight upwards shift in the height $\ell'_{\perp}$ of avalanches with increasing system size, particularly for smaller avalanches. As described in Sec. 2.5, a larger system will ultimately reach a rougher final interface. This will increase the apparent $\ell'_{\perp}$ by mixing in $\ell'_{\parallel}$. We therefore focus on the principal component definition in the next subsection as it produced cleaner results.

2.4.2 Distributions of Width and Height

As for the distribution of avalanche volumes in Subsec. 2.3.3, one can also define the probability for a given linear dimension at a given H and L, $P(\ell, H, L)$ where ℓ is either $\ell_{\parallel}$ or $\ell_{\perp}$. These distributions are expected to decay as a power law with an exponent $\tau_{\parallel}$ or $\tau_{\perp}$. This power law will only persist up to a maximum cutoff set by either the correlation length or the system size. As in Fig. 2.6a, we focus on the critical distribution $P(\ell, L)$ at H close enough to the critical point that avalanches are limited by the finite system size rather than the correlation length. Figs. 2.12a-b show $P(\ell_{\parallel}, L)$ and $P(\ell_{\perp}, L)$, respectively. The

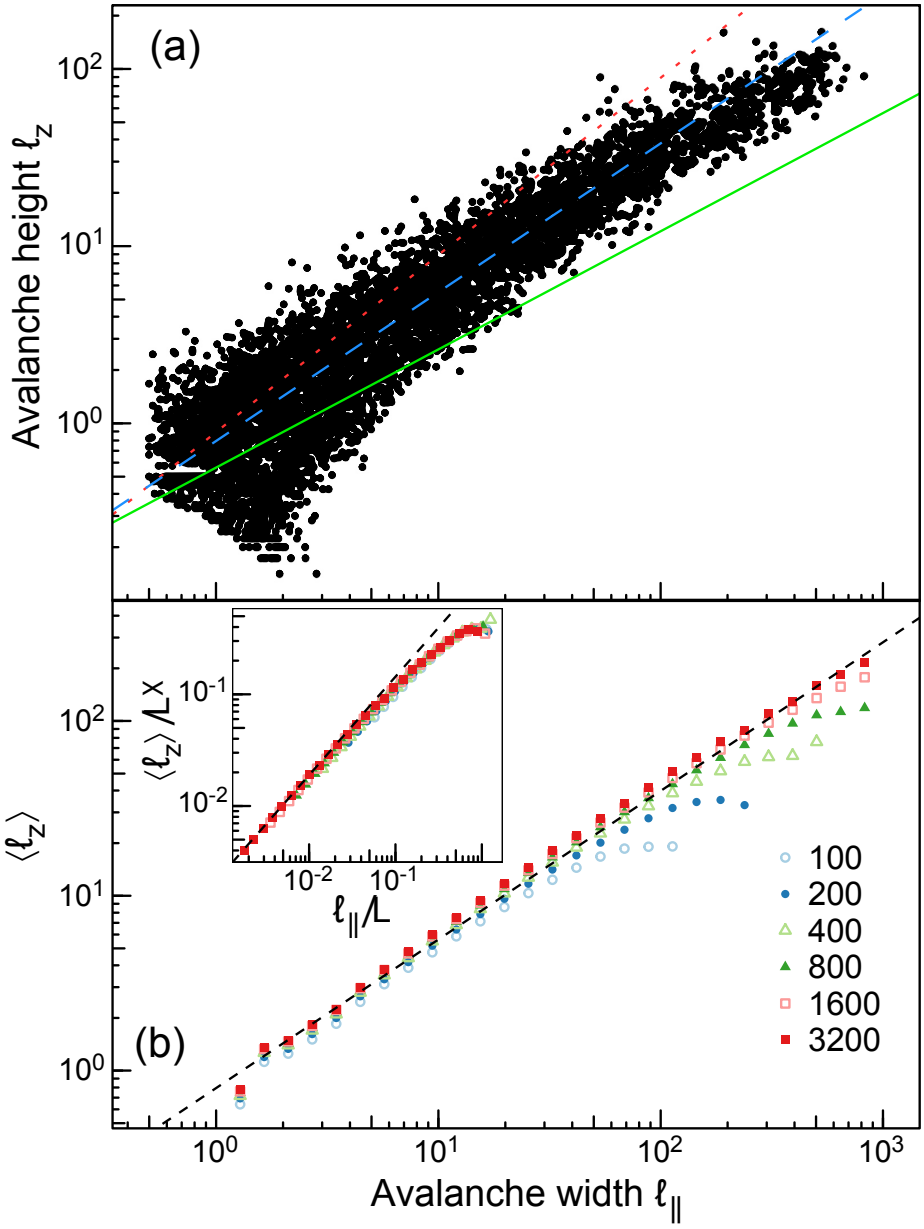

Figure 2.11: (a) The height and width of the avalanches shown in Fig. 2.10 but measured along the $\hat{z}$ direction and in the $x-y$ plane rather than from the moments of the avalanche. (b) The average height of avalanches along $\hat{z}$ is binned and averaged for different widths in the $x-y$ plane for the indicated L. The dashed line has a slope of χ. Curves are collapsed in the inset for $\ell_\parallel > 5$ by scaling the avalanche width by the system size L and the height by L^χ with $\chi = 0.85$.

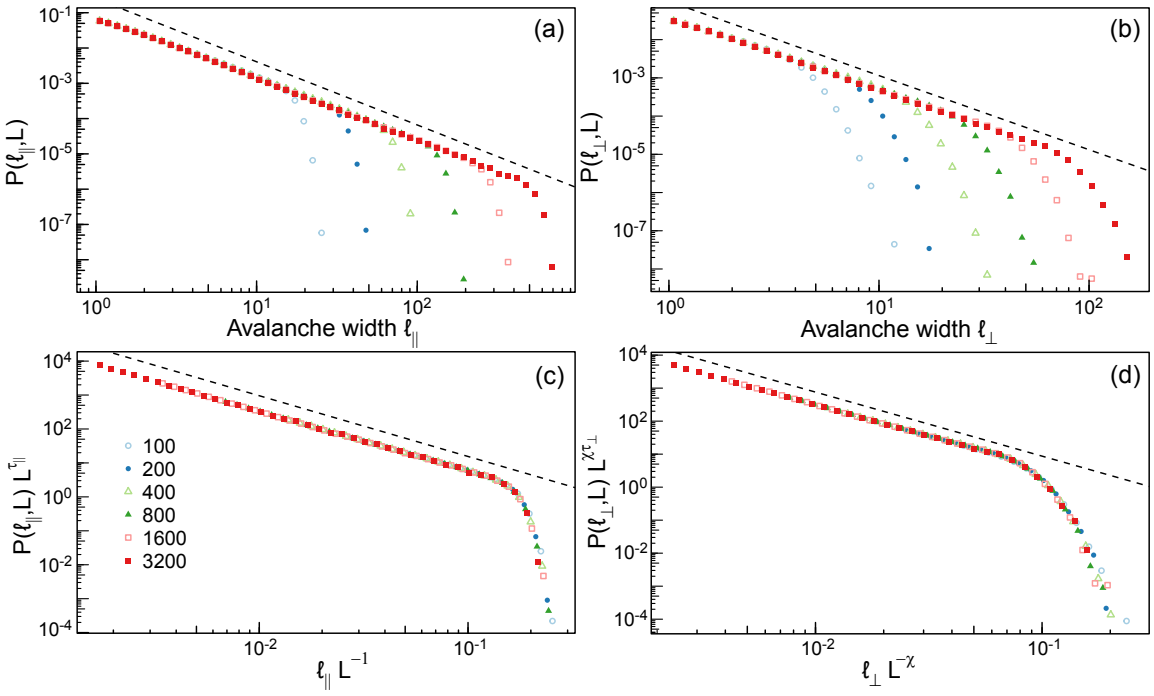

Figure 2.12: The probability distributions of the (a) width and (b) height of avalanches for values of L indicated in the legend of (c) that grew at fields near the critical regime $0 < \Delta H < 10L^{-1/\nu_\parallel}$. The distributions in (a) and (b) are collapsed by scaling with system size using exponents $\chi = 0.85$, $\tau_\parallel = 1.79$, and $\tau_\perp = 1.94$ in (c) and (d), respectively. Data for $\ell_| < 5$ or $\ell_\perp < 2$ are excluded from scaling. Dashed lines in each panel indicate the power law determined from finite-size scaling.

distributions are seen to decay with different exponents before being cut off at a threshold that grows with L.

Following Eq. (2.9), one can construct finite-size scaling equations for the distributions of the heights and widths of avalanches. As demonstrated in Fig. 2.10b, the maximum width of an avalanche will scale in proportion to L and the maximum height will scale in proportion to L^χ. Thus α in Eq. (2.9) is replaced by 1 or χ for $\ell_\parallel$ and $\ell_\perp$, respectively. Figs. 2.12c-d show finite-size scaling collapses for both quantities. By varying the choice of exponents we determined the data is consistent with $\tau_\parallel = 1.79 \pm 0.01$, $\tau_\perp = 1.94 \pm 0.02$,

and $\chi = 0.85 \pm 0.01$. In both collapses, we exclude avalanches with length scales $\ell_\parallel < 5$ or $\ell_\perp < 2$ since they do not follow the power-law scaling in Fig. 2.10a.

The τ exponents are not independent and can be related to each other as derived in Ref. 64. In Fig. 2.10a, one can see that, on average, individual avalanches exhibit the same anisotropy as the correlation lengths, typically $\ell_\perp \sim \ell_\parallel^\chi$. Thus we assume this scaling will hold when considering the statistics of many avalanches. For length scales $\ell_\parallel < \xi_\parallel$ and $\ell_\perp < \xi_\perp$ we can equate the probability that avalanches are in a range with corresponding values of $\ell_\parallel$ and $\ell_\perp$: $P(\ell_\parallel)d\ell_\parallel \sim P(\ell_\perp)d\ell_\perp$. Using this expression, one can derive a scaling relation relating the τ exponents to χ:

$$\chi = \frac{\nu_\perp}{\nu_\parallel} = \frac{1-\tau_\parallel}{1-\tau_\perp} \tag{2.14}$$

Using our estimates of $\tau_\parallel$ and $\tau_\perp$, this yields an estimate of $\chi = 0.84 \pm 0.02$, again consistent with our findings. Similarly, one can relate the rate of avalanches over a small interval of volumes, dS, to the rate of avalanches over a small interval of widths, $d\ell_\parallel$, and derive a relation between τ for the volume distribution and $\tau_\parallel$:[64]

$$\tau = \frac{d-2+\chi+\tau_\parallel}{d-1+\chi}. \tag{2.15}$$

Plugging in our values for $\tau_\parallel$ and χ we find a prediction of $\tau = 1.28 \pm 0.01$ in strong agreement with the value directly measured in Fig. 2.6.

One other scaling relation is implied by our results. As noted in the previous subsection

and Subsec. 2.3.4, the ratio $\langle V \rangle / L^2 \propto \Delta H^{-(\phi-1)}$ near H_c. This is proportional to the average height of the external interface because the volume left behind in bubbles is a small constant fraction of the total volume. The average height of the interface should be at least as big as the height of the largest avalanches. Since $\ell_\perp \propto \Delta H^{-\nu_\perp}$, this implies $\phi - 1 \geq \nu_\perp$. Within our errorbars, our directly measured values of $\phi - 1 = 0.64 \pm 0.04$ and $\nu_\perp = 0.67 \pm 0.02$ are consistent with this relation and suggest that:

$$\phi = 1 + \nu_\perp. \tag{2.16}$$

The numerical results in Refs. 28 and 30 were consistent with $\chi = 1$ and they tested a scaling relation $\phi = 1 + \nu$ that is equivalent to Eq. 2.16 in that limit.

Overall, in these past two subsections we proposed and tested a theory of avalanches that accounts for the anisotropy in correlation lengths. From these results, we identified several measures of χ confirming it is distinct from both 1 and the previously measured roughness exponent. Next we explore how this scaling changes for spanning avalanches.

2.4.3 Spanning Avalanches

Defining the morphology of a spanning avalanche is complicated. Having percolated, each flipped spin has different paths connecting it to a nucleation site in any periodic images. There is no longer a well defined reference point to define the lateral position (x, y) of a flipped spin. Therefore, neither the second moment tensor $l_{\alpha\beta}$ nor its eigenvalues are uniquely defined. However, the height of an avalanche can still be estimated using the

metric $\ell'_\perp = \sqrt{l_{zz}}$ as the calculation of l_{zz} is not affected by the periodicity of the lateral boundary conditions. As discussed above, this is not an ideal measure of the height for small avalanches. However, spanning avalanches are large and sample the global slope of the interface. Therefore spanning avalanches are expected to closely align with $\hat{z}$ such that $\ell'_\perp$ is a reasonable measure of their height.

From the definition of χ and Eq. (2.2), the height of the typical non-spanning avalanche is expected to grow as a power of S with exponent $\chi/\alpha \approx 0.3$. As spanning avalanches detect the finite boundaries there is no guarantee that they will obey the same scaling.

To test for deviations from scaling, we calculate $\ell'_\perp$ and S for all avalanches nucleated close to the critical point for $L = 3200$. As above, we considered fields in the range $0 < \Delta H < 10L^{-1/\nu_\parallel}$ such that $\xi_\parallel > L$. In Fig. 2.13, $\ell'_\perp$ is plotted as a function of S for a sample of avalanches of size $S > 10^6$. Data is separated by the degree of spanning for each avalanche. Although there is a large amount of scatter for $S < 5 \times 10^9$, $\ell'_\perp$ is seen to grow as a power of S. This data is consistent with the predicted exponent of $\chi/\alpha = 0.3$. Above this scale, the height starts to grow proportionally to S. This threshold approximately corresponds to the division between semi and fully-spanning avalanches.

The distinct scaling of fully-spanning avalanches seen in Fig. 2.13 can be understood in the context of their definition. Once an avalanche grows to have a footprint of L^2, the width of the avalanche is fixed at the box size. Growth in the total volume must then be proportional to an increase in height. As seen in Fig. 2.1, a fully spanning avalanche can have a much larger aspect ratio of height to width than a semi-spanning avalanche. One

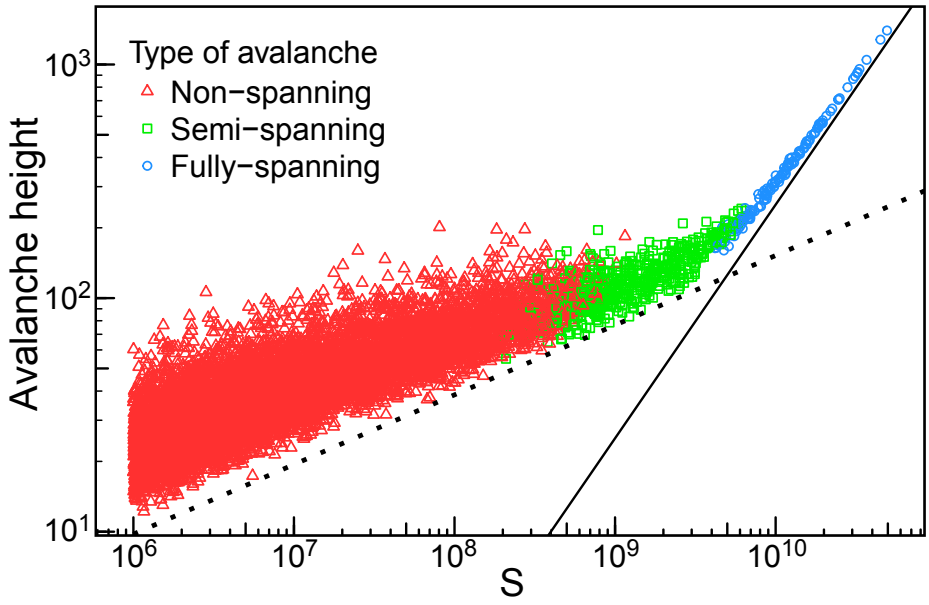

Figure 2.13: Height of an avalanche in the $\hat{z}$ direction as a function of volume. As indicated in the legend, non-spanning avalanches are red triangles, semi-spanning avalanches are green squares, and fully-spanning avalanches are blue circles. Straight lines have a slope of $\chi/\alpha \approx 0.3$ (dotted) and 1.0 (solid).

might also anticipate this change in scaling due to similarities of fully-spanning avalanches to depinning. Once an avalanche grows to have a footprint L^2, flipped spins cover the entire cross-section. Although it is still possible for some parts of the multivalued interface to be pinned, they are usually left behind in bubbles and the external interface is totally renewed. Thus, fully-spanning avalanches are more representative of motion above the depinning transition and their scaling is not relevant to the behavior at $H < H_c$ of interest in this chapter.

To verify this interpretation, we also analyzed the probability distribution of S including semi-spanning avalanches, $P_{SS}(S, L)$, as well as all avalanches, $P_A(S, L)$. These distributions are calculated using the same method used in Fig. 2.6a. In Fig. 2.14, (a) $P_{SS}(S, L)$ and

(b) $P_A(S, L)$ are scaled using the scaling ansatz in Eq. (2.9). These collapsed curves both resemble those of $P(S, L)$ in Fig. 2.6b for $S/L^\alpha \lesssim 10^{-2}$. Above this scale, the distributions deviate due to the inclusion of spanning avalanches.

In Fig. 2.14a, we see the upper cut off $P_{SS}(S, L)$ collapses. Therefore, the maximum volume of semi-spanning avalanches grows as L^α. This is in agreement with the behavior seen in Fig. 2.13 where semi-spanning avalanches scale in the same manner as non-spanning avalanches. However, the maximum volume of fully-spanning avalanches no longer scales as L^α. As seen in Fig. 2.14b, $P_A(S, L)$ has two drops at large S. The first scales as L^α and reflects the limiting size of semi-spanning avalanches. The second drop occurs at a threshold scaling as L^3 and is due to fully-spanning avalanches. As a fully-spanning avalanche has a width of L, this scaling implies the maximum height scales proportional to L. In our protocol, avalanches are censored if their growth is interrupted by hitting the top of the box. This produces an artificial maximum height L. Therefore, this phenomenon is consistent with our above argument: fully-spanning avalanches depin and advance the interface by an amount that scales with L.

2.5 Interface Morphology

Having identified a distinct anisotropy in avalanches, we now explore how this impacts the morphology of the advancing interface. One can study the statistical properties of stable interfaces without resolving all preceding avalanches. Therefore, we were able to use our alternative growth protocol where we simply flip spins until a stable interface is reached at

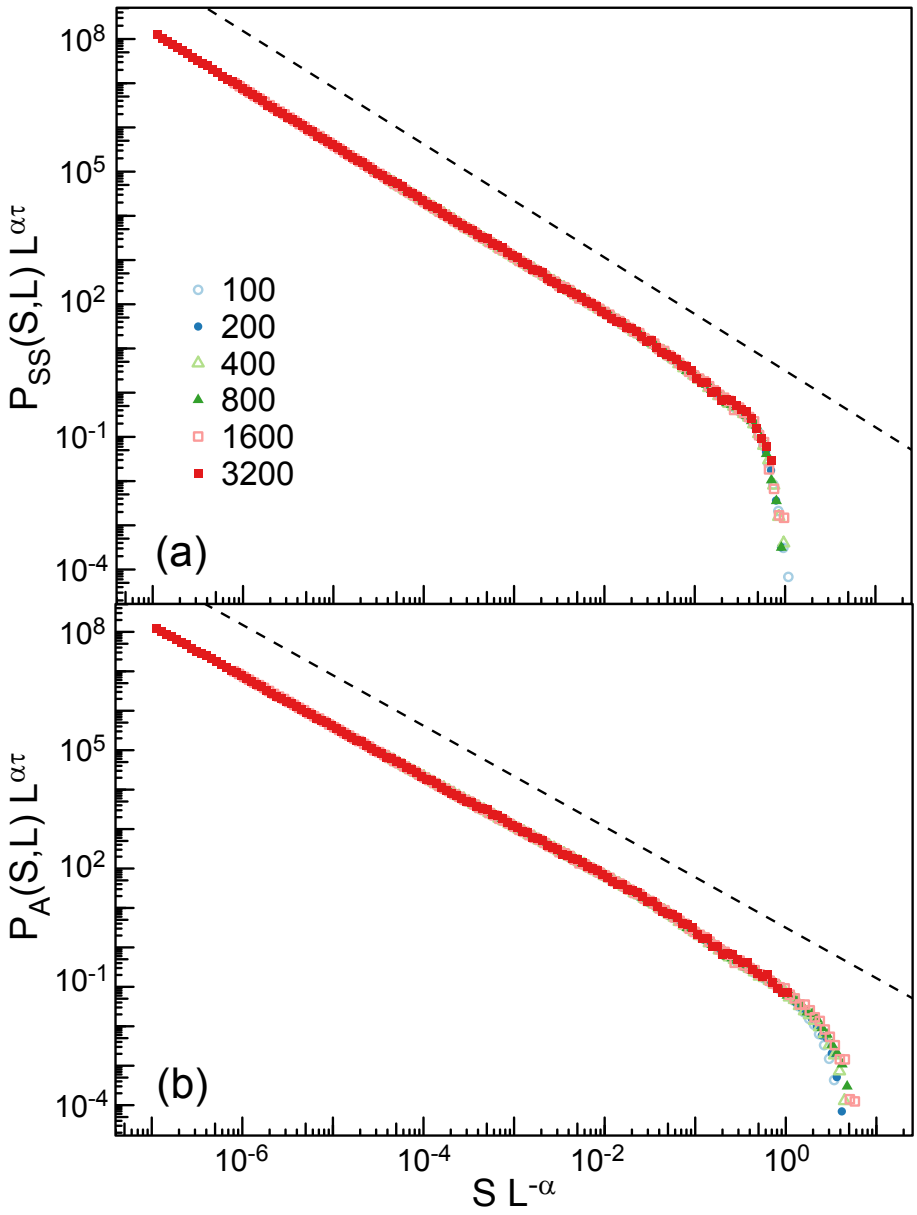

Figure 2.14: The probability distribution of avalanche volumes is calculated including (a) non-spanning and semi-spanning avalanches and (b) all avalanches for values of L given in the legend. Data are rescaled using the scaling relation in Eq. (9) with exponents $\tau = 1.28$ and $\alpha = 2.84$. In (a) the data collapse on to a common curve. In (b) data collapse below a drop in the curves that occurs at $SL^{-\alpha} \lesssim 0.1$. Then curves for larger L extend to larger $SL^{-\alpha}$. This portion of the curves collapses if α is increased to 3, indicating that the height of spanning avalanches scales with L instead of L^{χ}. The dashed lines show a power law decay with $\tau = 1.28$.

a fixed field. The no-passing rule guarantees that this stable interface is independent of the growth rules, and efficient parallelization of the code allows us to study system sizes up to $L = 12800$. In the following we identify the interface position with the set of flipped spins on the external interface that are adjacent to unflipped spins. Using the unflipped spins gives nearly identical results, particularly at large scales. In Subsec. 2.5.1 we first look at the scaling of the total interface roughness then look at the roughness on smaller length scales in Subsec. 2.5.2 to test self-affine scaling. Finally, in Subsec. 2.5.3 we look at the properties of overhangs on the surface.

2.5.1 Total Interface Roughness

We first explore the total interface roughness, $W_T(L, \Delta H)$, defined as the root mean squared (rms) variation in the height $h(x, y)$ of all interfacial spins on the external interface. Note that the height is multivalued and all spins at a given x and y are included in calculating W_T. Fig. 2.15a shows how W_T grows as H approaches H_c for different L. The interface starts as a flat plane with $W_T = 0$ at large ΔH. As ΔH decreases, the interface advances and roughens. For each L, W_T grows as an inverse power of ΔH and then saturates. Saturation occurs at a larger roughness and smaller ΔH as L increases.

W_T is expected to grow at least as rapidly with decreasing ΔH as the height of the largest avalanches, i.e. $\xi_\perp$. Smaller or larger variations could be observed if successive events were anticorrelated or correlated on scales of order $\xi_\parallel$ to spread or concentrate growth. Assuming there are no such correlations, we predict $W_T \sim \Delta H^{-\nu_\perp}$ from Eq. (2.2). Fitting the power-law region in Fig. 2.15a gives $\nu_\perp = 0.67 \pm 0.02$. Given our measured value of $\nu_\parallel$

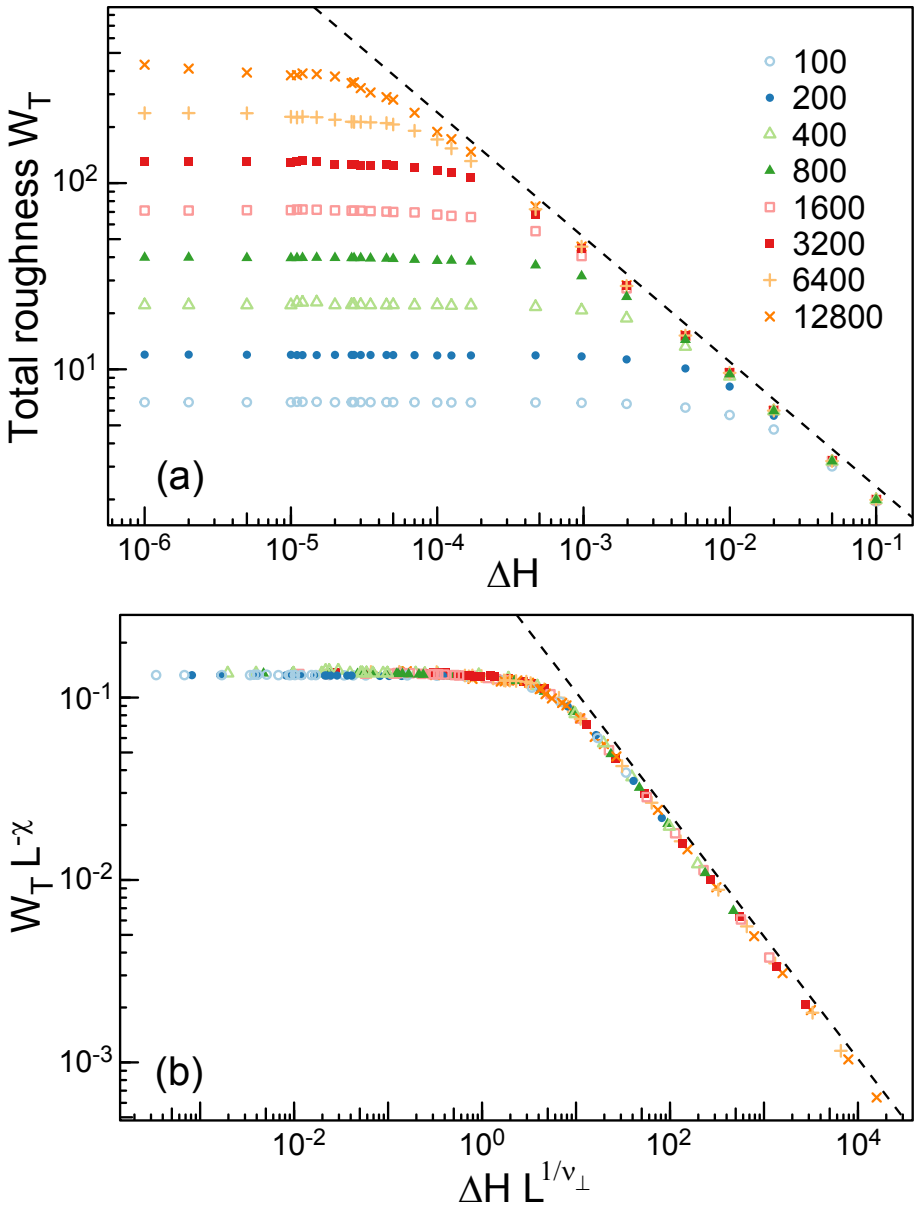

Figure 2.15: (a) The rms height variation of the external interface W_T as a function of external field is shown for the values of L indicated in the legend. A dashed line of slope $\delta = 0.65$ is shown. (b) The same data is shown after scaling the axes with powers of system size using $\chi = 0.85$ and $\nu_\parallel = 0.79$.

this implies $\chi = 0.85 \pm 0.04$ in close agreement with our other results for χ.

The finite-size saturation of W_T in Fig. 2.15a can be understood in terms of the scaling of the maximum height of an avalanche with L. The maximum height of a non-spanning avalanche is seen in Fig. 2.12 to grow in proportion to L^{χ}. This would suggest W_T will saturate at a value proportional to L^{χ}. Close to H_c, fully-spanning avalanches will also contribute to the structure of the interface. As discussed above, fully-spanning avalanches have a height that scales as L. However, as seen in Fig. 2.1, the height of a fully-spanning avalanche is not necessarily correlated with the interface width. If the entire interface is advanced a fixed distance it does not change the width of the interface. Only the external topology of a fully-spanning avalanche is relevant. Assuming fully-spanning avalanches do not alter the scaling with L, we propose the following scaling ansatz for W_T:

$$W_T \sim \xi_{\perp} f_W \left(L/\xi_{\parallel} \right) . \tag{2.17}$$

where $f_W(x)$ is a new scaling function. To satisfy the limiting scaling behavior, $f_W(x)$ goes to a constant for $x \ll 1$ and scales as x^{χ} for $x \gg 1$.

Fig. 2.15b shows a finite-size scaling collapse of the data in Fig. 2.15a. As before, we restrict data to $\Delta H < 10^{-2}$ as the lower fields do not represent critical behavior. Good scaling collapses are obtained for $\chi = 0.85 \pm 0.01$ and $\nu_{\parallel} = 0.79 \pm 0.02$. These values are consistent with those found above. It is worth noting that W_T saturates at $\Delta H \approx 10 L^{1/\nu_{\parallel}}$ for different L. This onset of finite-size saturation in W_T occurs at about the same field as the onset of finite-size effects in $\langle S \rangle$ shown in Fig. 2.5b. This is evidence that fully-spanning

avalanches do not alter the scaling of the total interfacial width as assumed by the ansatz in Eq. (2.17).

2.5.2 Test of Self-Affine Scaling

The anisotropy in avalanches and the fact that W_T grows sublinearly with L are consistent with self-affine scaling. For a self-affine surface, the rms variation in height W over an ℓ by ℓ square in the $x-y$ plane scales as:

$$W(\ell, H, L) \sim \ell^{\zeta} \tag{2.18}$$

where ζ is the roughness or Hurst exponent.[76] For a finite system, one expects the total roughness to scale as L^{ζ}, implying $\zeta = \chi$ from the results above. This is inconsistent with past values of ζ and we now test this scaling.

One complication is that the surface height $h(x, y)$ is not a single-valued function, as usually assumed for self-affine surfaces. In order to circumvent regions of strong pinning, the system is capable of lateral growth that produces overhangs in the external interface. Previous studies have shown that these overhangs have a characteristic size that diverges as $\Delta \to \Delta_c$.[54] We focus on $\Delta = 1.7$ to reduce their size, but found similar behavior for $\Delta = 2.1$, 2.0, 1.5, and 1.0.

To calculate W, the periodic $x-y$ plane was divided into square cells of edge ℓ. For each cell, all interfacial sites contained in the projected area were used to calculate the rms variation in height over the cell. Taking an average over N_ℓ cells of size $\ell \times \ell$ gives the scale

dependent roughness:

$$W(\ell, \Delta H, L) = \frac{1}{N_\ell} \sum_i \sqrt{\langle (z - \langle z \rangle)^2 \rangle} \tag{2.19}$$

where the summation is across all N_ℓ cells and the angular brackets represent averages within each cell.[2]

Figure 2.16a shows how $W(\ell, \Delta H, L)$ evolves during growth for $L = 12800$. The curves rise more slowly with ℓ below a lower scale $\ell_{\min}$. This is associated with the size of the overhangs mentioned above, which lead to a finite width even for $\ell = 1$. For both single and multivalued interfaces we find different scaling with ℓ below $\ell_{\min} \sim 25$. For larger ℓ, W appears to rise as a power law before saturating at a roughness that grows as H approaches H_c. This asymptotic value corresponds to $W_T(L, \Delta H)$.

Closer inspection shows that the power law rise in W with ℓ is of limited range and has a power-law exponent that depends on ℓ and ΔH. To reveal this, W is multiplied by $\ell^{2/3}$ and replotted in Fig. 2.16b. This would produce horizontal lines if ζ had the mean field value of 2/3.[77] For small ΔH ($L^{1/\nu} \Delta H < 10$), there may be a factor of 30 over which the curves are straight and thus follow a power law. However, there is a steady rise in the slope with ΔH. Fig. 2.16c shows similar scaled plots of W at the critical field for different L. Once again there is a power law region that grows with L, but no clear saturation in slope that would indicate an approach to the limiting ζ. For $\Delta H = 10^{-6}$ and $L = 12800$, the slope has risen to about 0.75, which is substantially above the mean-field exponent but well below χ (straight dashed line).

The results in Fig. 2.16 imply either that growing interfaces are still affected by fi-

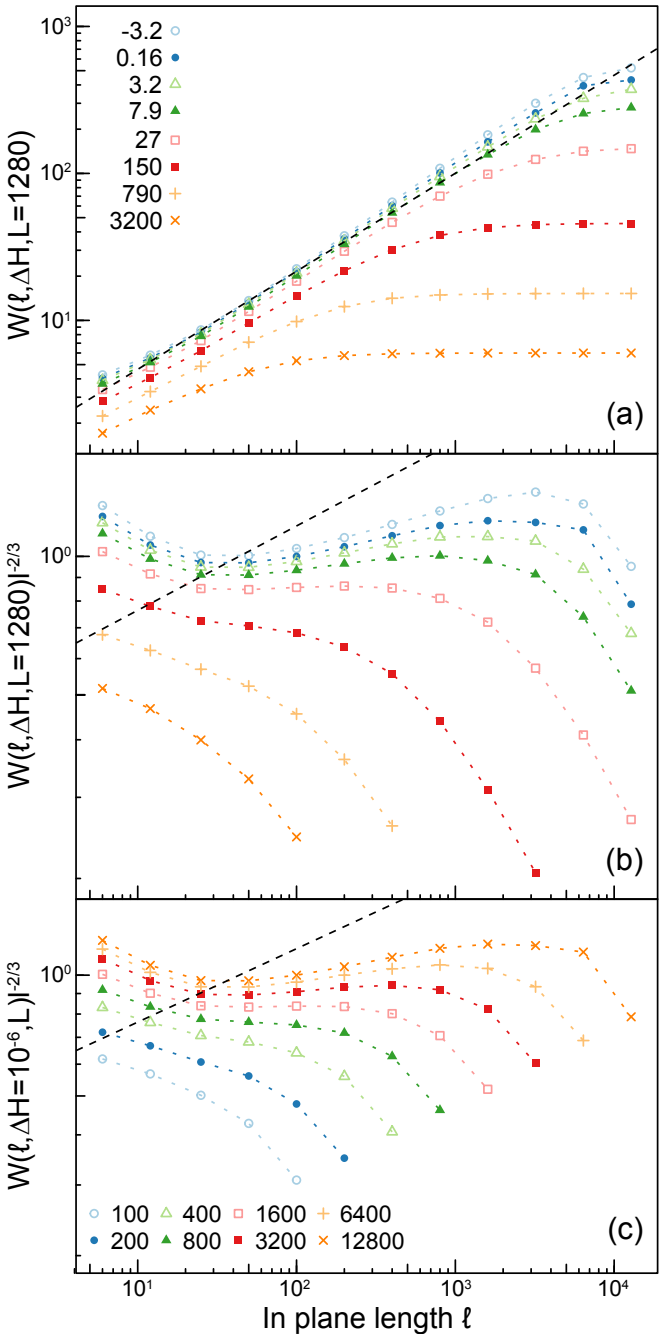

Figure 2.16: (a) The rms fluctuation in height $W(\ell, \Delta H, L)$ is calculated for a system of size $L = 12800$. Values of $\Delta H L^{1/\nu_\parallel}$, rounded to two significant digits, are indicated in the legend. A dashed line is drawn with a slope of 2/3. (b) The same values of W are divided by the mean-field power law $\ell^{2/3}$. A line is included that would correspond to 0.85. (c) The variation of W with ℓ at $\Delta H = 10^{-6}$ for the indicated values of L. Once again W is divided by the mean-field behavior and the line corresponds to $\zeta = 0.85$.

nite system size or that the interfaces are not simply self-affine. Some growth processes produce multi-affine surfaces where different moments of the height variation produce different scaling exponents. To test this we studied the scaling of the mean absolute value of height changes and the fourth root of the fourth power of height variations. The same scaling behavior was observed as for the rms height change. We also examined the scaling of single-valued interfaces corresponding to the highest spin at a given x, y or the average spin height at each x, y. In Fig. 2.17a, the single valued roughness, W_s, is plotted as a function of ℓ and in Fig. 2.17b W_s is divided by $\ell^{2/3}$. Similar to past results,[54,78,79] we see the roughness differs slightly at small ℓ. However, the single-valued interfaces show the same shift in power law with ΔH and L, with similar exponents.

Another possibility is that depinning avalanches erase memory of the initial interface orientation and that subsequent growth is self-affine relative to the new local orientation. To test this we used a technique like that used in finding the normal component of avalanches. For each interface section of size $\ell \times \ell$ normal to the global growth direction the moment tensor was calculated and the smallest eigenvalue was taken as the height variation. This approach maximizes the apparent ζ because it reduces the roughness at small ℓ and has little effect at large ℓ. In Fig. 2.17c the smallest eigenvalue W_e is plotted as a function of ℓ and in Fig. 2.17d it is divided by $\ell^{2/3}$. The range of power-law scaling is smaller using this metric and the exponent showed a similar increase with decreasing ΔH and increasing L. The largest value of the apparent slope increased only to 0.79 which is still smaller than χ.

The origin of the change in apparent exponent seems to be the variation in roughness at small ℓ with increasing L and decreasing ΔH. Growing interfaces often follow the Family-

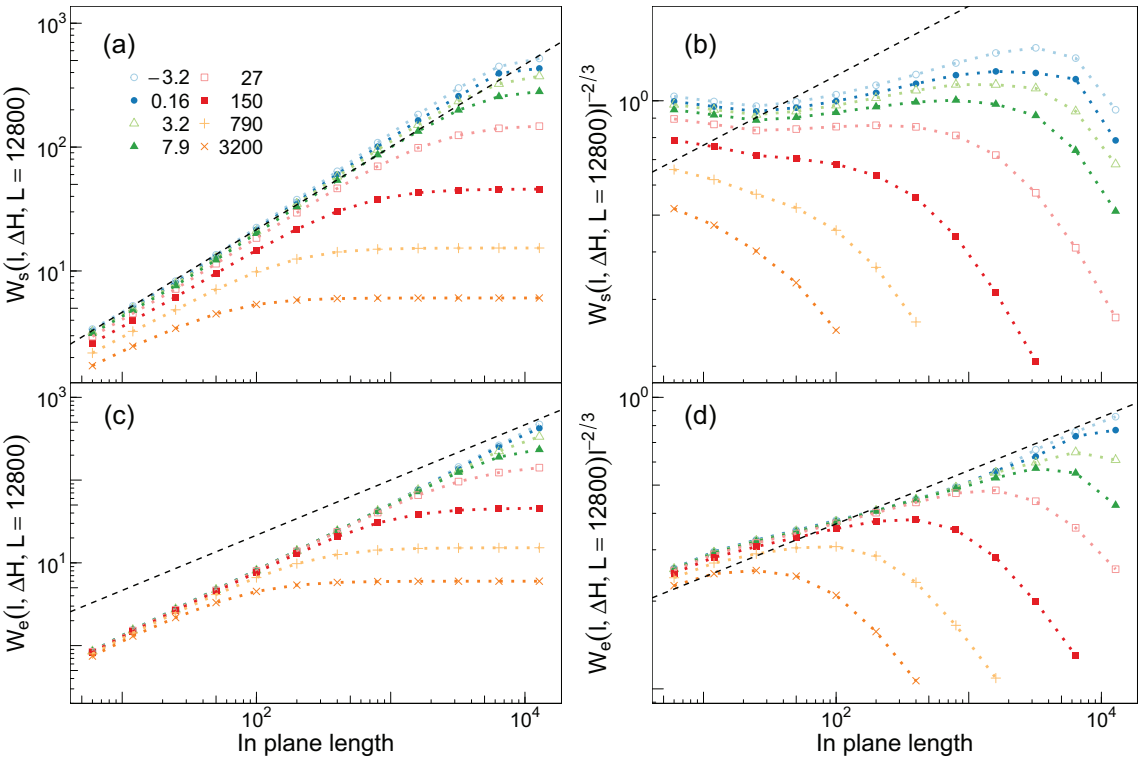

Figure 2.17: (a) The rms fluctuation in height $W_s(\ell, \Delta H, L)$ for a single valued interface is calculated for a system of size $L = 12800$. Values of $\Delta H L^{1/\nu_\parallel}$, rounded to two significant digits, are indicated in the legend. A dashed line is drawn with a slope of 2/3. (b) The same values of W_s are divided by the mean-field power law $\ell^{2/3}$. A line is included that would correspond to 0.85. In (c) and (d), similar curves to (a) and (b) are shown except the roughness is calculated using the smallest eigenvalue of the multivalued interface W_e.

Vicsek relation.[80] At each position the roughness grows as ℓ^{ζ} and then saturates. The value of ℓ where saturation occurs grows as the interface advances, as does the total roughness. Fig. 2.16 shows similar behavior with decreasing ΔH with one important difference. The value of W at points before saturation rises steadily as the interface advances, while Family-Vicsek scaling assumes that the small ℓ roughness is unchanged.

Fig. 2.18 shows how the roughness at a fixed ℓ varies with L close to the critical point ($\Delta H = 10^{-6}$). The previous subsection showed that $W_T = W(\ell = L, \Delta H = 0, L) \propto L^{\chi}$. If $W(\ell, \Delta H = 0, L) \propto \ell^{\chi}$ with no dependence on L, then one would have $W(L, 0, L)/W(\ell, 0, L) \propto (L/\ell)^{\chi}$ and the plots in Fig. 2.16 would be power laws with the same slope. However, $W(\ell, 0, L)$ grows with L and this decreases the ratio $W(L, 0, L)/W(\ell, 0, L)$ and thus the apparent exponent. If W rose as a power of L, there would be a persistent difference between ζ and χ. However the linear-log plot in Fig. 2.18 shows that the growth in W is slower than logarithmic. This supports the conclusion that ζ converges to χ in the thermodynamic limit and the variation with L in W at small ℓ is large enough to explain the apparent difference of ~ 0.1 for our system sizes.

Finally, we look at how the roughness at a fixed ℓ and L saturates as $\Delta H \to 0$. In Fig. 2.19a, $W(\ell = 25, \Delta H, L)$ is plotted as a function of ΔH for different system sizes indicated in the legend. As ΔH decreases, W is seen to rise before saturating at a distance to the critical point that decreases with increasing L. At $\Delta H = 0$, it appears that the roughness approaches an asymptotic limit, defined as $W_{\rm lim}(\ell)$, as $L \to \infty$. In Fig. 2.19b, the difference $\Delta W = W_{\rm lim}(25) - W$ is plotted as a function of ΔH for $W_{\rm lim}(25) = 9.85$. At values of $\Delta H > 10^{-2}$, ΔW appears to decay as a power of decreasing ΔH with an exponent of

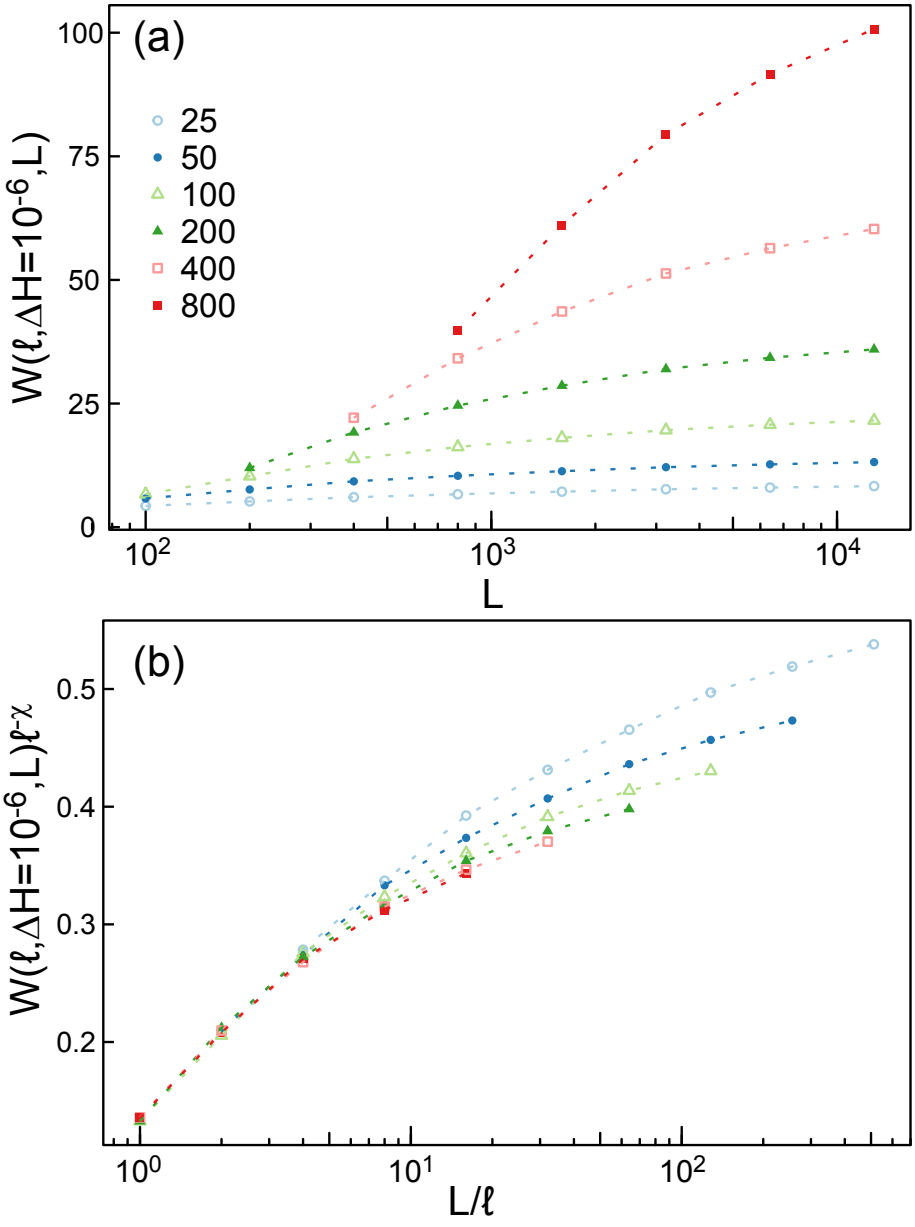

Figure 2.18: (a) The roughness at ℓ equal to the values indicated in the legend is calculated as a function of L at a field of $\Delta H = 10^{-6}$. (b) The values of W and L in (a) are normalized by ℓ^{χ} and ℓ respectively.

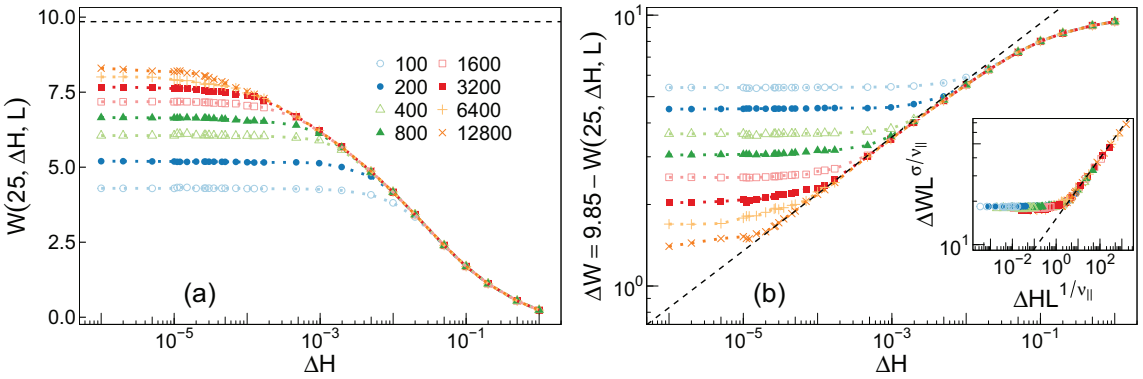

Figure 2.19: (a) $W(\ell = 25, \Delta H, L)$ as a function ΔH for L indicated in the legend. A horizontal dashed line indicates a value of $W = 9.85$. (b) Curves of $\Delta W = 9.85 - W(25, \Delta H, L)$ versus ΔH. A dashed line is drawn with slope 0.21. Inset includes data scaled according to Eq. 2.20 using $\nu_{\|} = 0.79$ and $\sigma = 0.21$. Only data for $\Delta H < 10^{-2}$ is included in the scaling collapse.

$\sigma = 0.21 \pm 0.07$. As L increases, this power law is cut off closer to H_c. Accurately measuring the value of σ is difficult as any identifiable power law depends on the choice of $W_{\rm lim}(25)$. Here $W_{\rm lim}(25)$ was chosen such that the power-law extends the closest to the critical field for $L = 12800$. As before, we can use finite-size scaling theory to construct a scaling ansatz:

$$\Delta W \sim L^{-\sigma/\nu_{\|}} f_{\Delta W}(\Delta H L^{-1/\nu_{\|}}) \tag{2.20}$$

where $f_{\Delta W}(x)$ is a new universal scaling function. To match the observed behavior, we predict $f_{\Delta W}(x)$ approaches a constant for $x \ll 1$ and $f_{\Delta W}(x) \sim x^{-\sigma}$ for $x \gg 1$. This scaling equation is used to collapse the data in the inset of 2.19b. This analysis suggests one may be able to extract the roughness in the limit of infinite system size on a length scale ℓ and may help identify ζ.

In Fig. 2.20a, Eq. 2.20 is used to scale curves of ΔW for $\ell = 12 - 400$. Here the value of σ

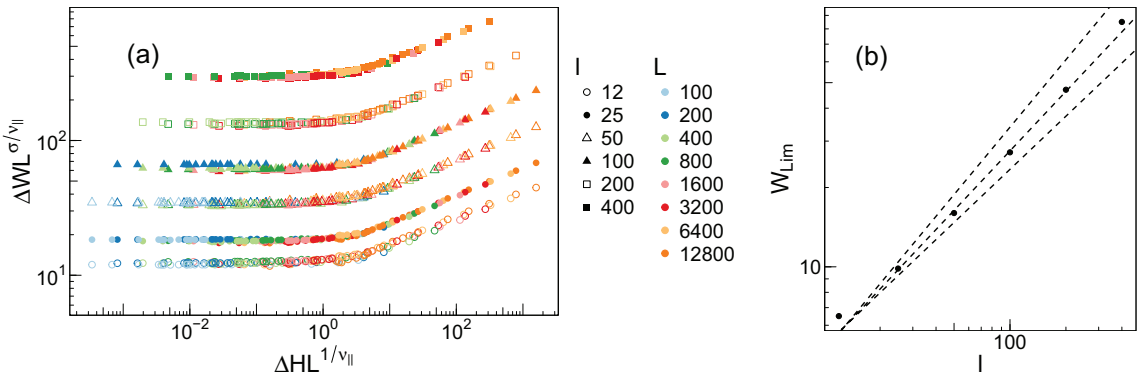

Figure 2.20: (a) Scaled data such as that seen in the inset of Fig. 2.19 for values of ℓ indicated by shape and L indicated by color in the legend. Scaling collapses are based on Eq. 2.20 using values $\nu_{||} = 0.79$ and $\sigma = 0.21$. Only data for $\Delta H < 10^{-2}$ and $\ell < L$ is included in the scaling collapse. In (b), values of $W_{\rm lim}(\ell)$ used for the collapse in (a) are plotted as a function of ℓ. Dashed lines are drawn with slopes 0.67, 0.79, and 0.85.

is assumed to be fixed to 0.21, while different values of $W_{\rm lim}$ were used for each collapse. No systematic method was employed to fit the value of $W_{\rm lim}$ so one anticipates significant error. Data from larger systems sizes would greatly improve estimates. The values of $W_{\rm lim}$ used are plotted as a function of ℓ in Fig. 2.20b. These values represent a theoretical roughness at the critical point for an infinitely large system, $W(\ell, \Delta H = 0, L = \infty)$. From the data in Fig. 2.20b, one cannot determine whether there is an obvious power law $W_{\rm lim} \sim \ell^{\zeta}$ but estimates are consistent with $\zeta \gtrsim 0.79$. The larger values of ℓ are the most important but also have the most error.

It is interesting to compare our results to previous studies. Past simulations for the RFIM[30,54] were consistent with $\zeta = 0.67 \pm 0.3$, but used $L \leq 768$ and only saw scaling to about $\ell = 300$. Our results for comparable L give similar apparent slopes, but data for larger L reveal that this slope is not the limiting value. Studies of models with explicitly broken symmetry and single valued interfaces have found $\zeta = 0.753 \pm 0.002$ using systems

with $L \leq 400$.[58] It is possible that breaking symmetry leads to a reduction in ζ, but it would be interesting to verify this with larger simulations. Indeed epsilon expansion calculations for single-valued models yielded $\zeta = 0.67$ and 0.86 at first and second order, and estimated a converged value of 0.82 ± 0.1.[57] It is interesting that the last prediction is close to the value of χ found here.

2.5.3 Overhangs

In the previous subsection, we found that the interface continues to roughen on length scales $\ell < \xi_{\|}$ as H increases, complicating measurement of the roughness exponent. This subsection quantifies the contribution of overhangs to the roughness as systems approach the critical point and shows that they become irrelevant as $L \to \infty$.

To identify multivalued locations on the interface, we first find the minimum and maximum height of the interface at each (x, y), $h_{\min}(x, y)$ and $h_{\max}(x, y)$, respectively. The interface is multivalued wherever the difference $dh(x, y) \equiv h_{\max}(x, y) - h_{\min}(x, y)$ is nonzero.

Looking at Fig. 2.1 one sees that $dh(x, y)$ can be nonzero where there is a vertical cliff or a true overhang with unflipped spins below. If $N(x, y)$ is the number of interface spins at (x, y), then there will be a cliff with no overhangs where $N(x, y) = dh(x, y) + 1$. The total number of unflipped spins that are part of one or more overhangs at (x, y) is $\Delta z(x, y) = dh(x, y) - N(x, y) + 1$. The fraction of the projected interface that contains an overhang, F_{O}, is just the fraction of (x, y) where Δz is nonzero.

Figure 2.21 shows how F_O evolves with ΔH and L. Initially, the interface is flat and

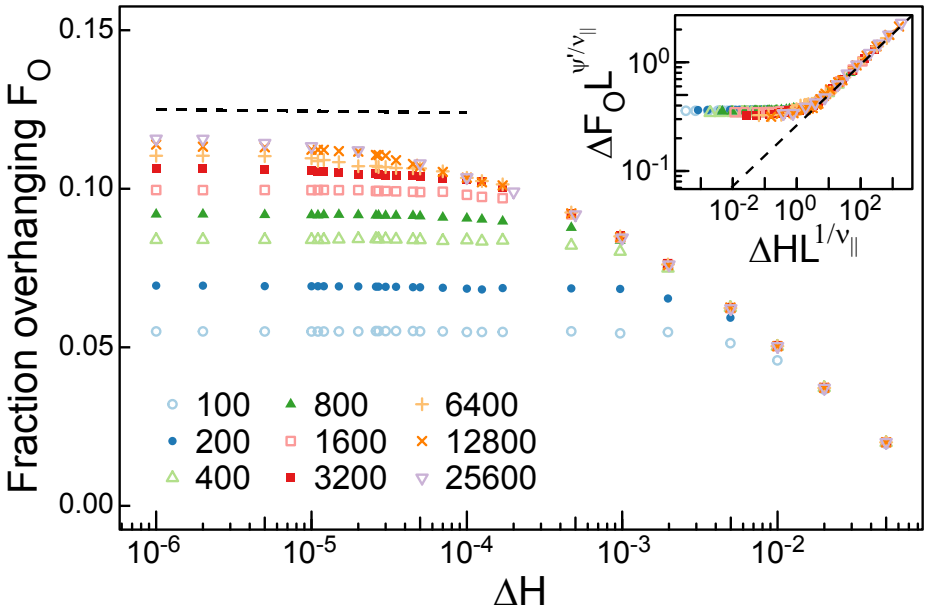

Figure 2.21: The percentage of the projected area for which there are overhangs on the interface is calculated as a function of distance from the critical field at the L indicated in the legend. A horizontal dashed line indicates 0.124. Inset: the data in the main panel is collapsed using a similar finite-size scaling ansatz to Eq. (2.11) where $\Delta F_O = 0.124 - F_O$ and $\psi = 0.3$. A dashed line with slope 0.3 is overlaid on the data.

F_O is zero for all L. As the system approaches the critical point, F_O grows for all L before saturating at a field ΔH that decreases with increasing L. The saturating percentage rises more slowly than logarithmically with L and appears to approach an asymptotic limit between 12 and 13% as $L \to \infty$. Assuming that the difference ΔF_O from the asymptotic value decays as $\Delta H^{-\psi'}$ one can derive a scaling relation analogous to Eq. (2.11). As shown in the inset of Fig. 2.21, the data can be collapsed fairly well with $\psi' = 0.3 \pm 0.05$ and a limiting fraction of 0.124 ± 0.005. Note that the fraction of the surface where cliffs occur is roughly twice F_O, and that both fractions increase as Δ rises towards Δ_c.

The above analysis shows a significant portion of the interface consists of overhangs and suggests that they could impact the scaling of interface roughness. However, the average

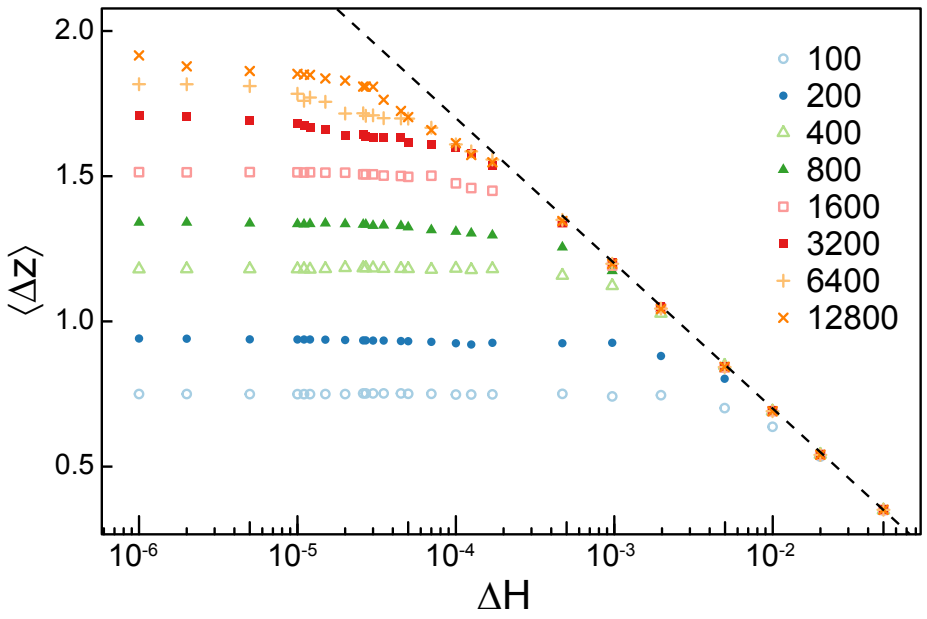

Figure 2.22: The average overhang height is calculated at different values of the external fields for the indicated L. A line of logarithmic growth is included for comparison.

of the total height in overhangs at a given position, $\langle \Delta z \rangle$ grows slowly. As seen in Fig. 2.22, $\langle \Delta z \rangle$ appears to diverge logarithmically as $H \to H_c$ before saturating at a value that increases roughly logarithmically with L. Ref. 54 found a similar slow growth in dh, which is always greater than Δz. Because of the slow growth, the ratios $\langle \Delta z \rangle / L^{\chi}$ and $\langle dh \rangle / L^{\chi}$ go to zero as $L \to \infty$ and $H \to H_c$ when $\Delta < \Delta_c$.

Next we consider the probability distribution of individual values of Δz, $P(\Delta z)$. In Fig. 2.23, $P(\Delta z)$ is plotted as a function of Δz for the indicated values of $\Delta H L^{1/\nu_\parallel}$ and $L = 12800$. As $H \to H_c$, the distribution decays more slowly and larger overhangs are identified. It is possible that one may be able to extract a length scale λ describing this rate of decay although it is not obvious there is a domain of pure exponential decay. Using a least mean squares regression over the range of $P(\Delta Z) = 10^{-4}$ to 10^{-5}, we extracted the

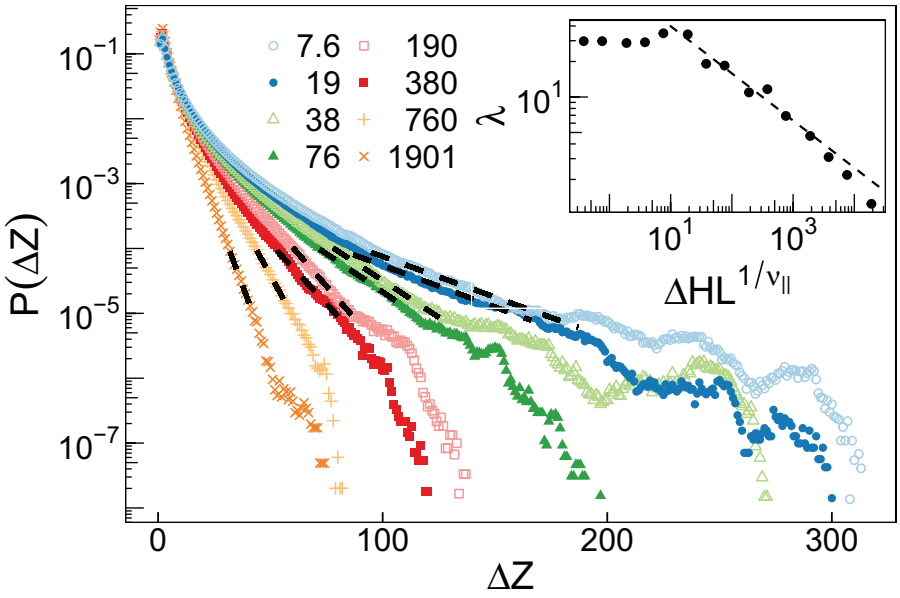

Figure 2.23: The distribution $P(\Delta z)$ as a function of Δz for the indicated $\Delta H L^{1/\nu_\parallel}$ for $L = 12800$. The data is sampled at $\Delta H = 10^{-6}$. $W_T(L)$ is approximated as $0.13L^\chi$ for $\chi = 0.85$. Dashed lines indicate decay lengths of $1/\lambda$. Inset shows values of λ versus $\Delta H L^{1/\nu_\parallel}$ with a dashed line representing a power law with exponent -0.4.

values of λ plotted in the inset of Fig. 2.23 as a function of $\Delta H L^{1/\nu_\parallel}$. We find λ possibly grows as a power law with exponent 0.4 with decreasing $\Delta H L^{1/\nu_\parallel}$ before saturating at the onset of finite-size effects. This is an interesting exercise but it is unclear whether this accurately represents the divergence of a length scale governing the height of overhangs. It would be useful to further study this result with larger systems.

Alternatively, we also find the distribution is well approximated by a stretched exponential with an exponent near 0.5 as shown in Fig. 2.24. Log-linear plots of $P(\Delta z)$ versus $\Delta z^{1/2}$ in Fig. 2.24 at $\Delta H = 10^{-6}$ follow straight lines until the statistical errors become too large. To reveal the scaling of overhangs with L, $\Delta z^{1/2}$ is normalized by a fit to $W_T(L)$ from Fig. 2.15, $W_T(L) \approx 0.13L^\chi$ with $\chi = 0.85$. Because successive lines in Fig. 2.24 shift

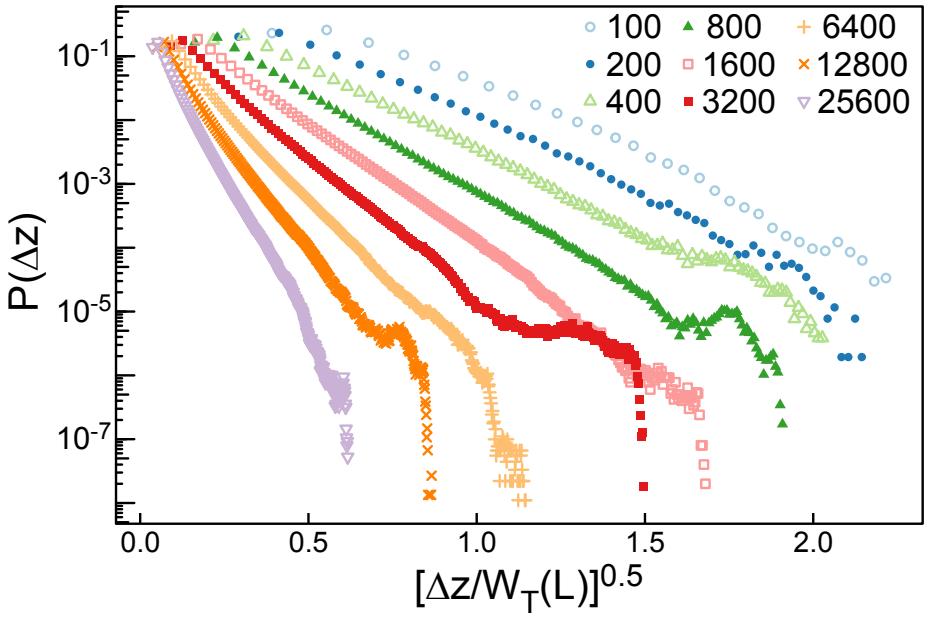

Figure 2.24: The distribution $P(\Delta z)$ as a function of $(\Delta z/W_T(L))^{0.5}$ for the indicated L. The data is sampled at $\Delta H = 10^{-6}$. $W_T(L)$ is approximated as $0.13L^{\chi}$ for $\chi = 0.85$.

to the left with increasing L, overhangs shrink relative to the total rms interface roughness $W_T(L)$ as L increases. The distribution of fluctuations in the width of the interface from the mean is roughly Gaussian, suggesting the largest overhangs are comparable to the maximum local fluctuations in the height for small L. In comparison, at large L the largest overhangs are only a fraction of the rms roughness and much less than the maximum fluctuations in height. We therefore conclude that overhangs can lead to significant finite-size effects in small systems but are an irrelevant contribution to the surface morphology in the thermodynamic limit.

Overhangs are not isolated features and one expects there to be lateral correlations. To account for lateral structure, we clustered adjacent (x, y) locations where $\Delta z > 0$ into aggregated overhangs and calculated the total volume V of each aggregated overhang. The

volume is simply defined as the sum of all the clustered values of Δz. The probability distribution of V decays as a power of V with an exponent consistent with $\tau_O \sim 1.87 \pm 0.05$ as seen in Fig. 2.25. This power law extends to an upper cutoff $V_{\max}$ that increases as $H \to H_c$. Assuming $V_{\max} \sim \Delta H^{-\eta}$ with η a new exponent, we propose the following scaling ansatz

$$P(V) \sim \Delta H^{\eta \tau_O} g_O(V \Delta H^{\eta}) \tag{2.21}$$

where $g_O(x)$ is a universal scaling function which scales as $x^{-\tau_O}$ for $x \ll 1$ and rapidly decays to zero for $x \gg 1$. This relation will only hold before the onset of finite-size effects at $\Delta H L^{1/\nu_\parallel} \approx 10$. Using this relation, the data in Fig. 2.25 is collapsed in the inset. Based on the sensitivity of the collapse, we estimate $\eta \sim 1.3 \pm 0.1$ and $\tau_O \sim 1.87 \pm 0.05$. The relation of these exponents to others is currently unknown.

As the exponent $\tau_O < 2$, the arguments used in Subsec. 2.3.2 imply that the volume of the largest overhangs will dominate the average volume. Fig. 2.25 implies that the maximum volume diverges as $H \to H_c$, so the characteristic volume of an aggregated overhang will also diverge. However, this divergence is considerably slower than the divergence of the volume of the largest avalanche which scales as $\Delta H^{-\nu_\parallel \alpha} \sim \Delta H^{-2.25}$. Thus as with other results in this subsection, the nontrivial scaling of overhangs may lead to interesting finite-size effects but becomes irrelevant at the critical field in infinite systems.

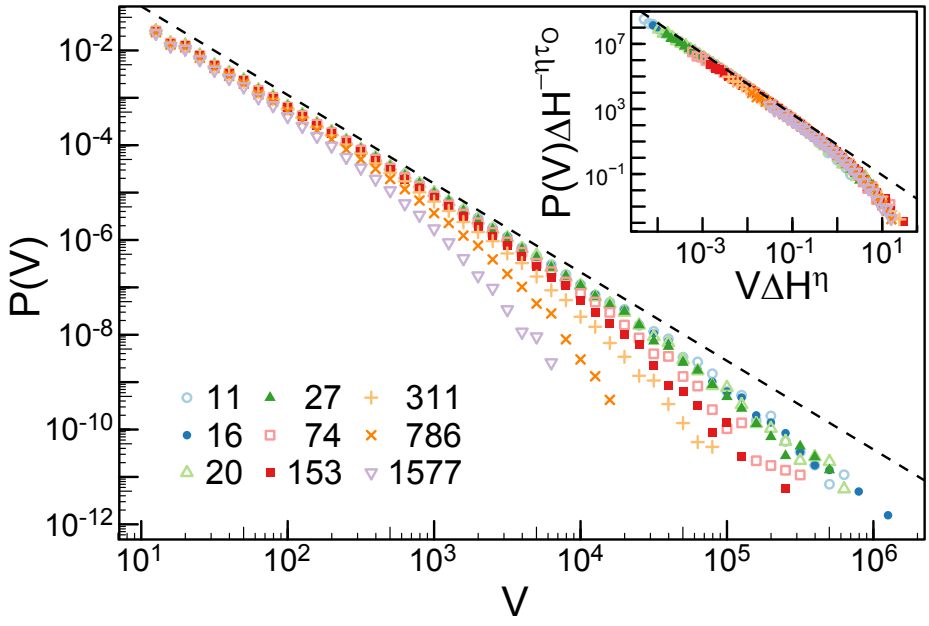

Figure 2.25: The probability distribution of the volume V of aggregated overhangs is calculated at values of $\Delta H L^{1/\nu_\parallel}$ indicated in the legend for $L = 12800$. Note that $\Delta H < 0.01$ for all curves. A dashed line indicates a power law of exponent 1.87. Inset: the data in the primary panel is collapsed using eq. (2.21) and values of $\eta = 1.3$ and $\tau_O = 1.87$.

2.6 Varying the Strength of the Disorder

In this final section, we briefly look at varying the strength of the disorder Δ. As noted above, previous work has identified a critical value of the disorder $\Delta_c \approx 2.5$.[54] This multicritical point separates a self-similar regime ($\Delta > \Delta_c$) from the self-affine regime studied here ($\Delta < \Delta_c$).

In the self-similar regime one expects isotropic growth. As interactions are relatively less important than the random field, growth does not depend heavily on local orientation but rather percolates through random regions where the noise promotes growth. Therefore, avalanches are expected to be isotropic. To confirm this theory, avalanches were grown in systems of $\Delta = 3.5$ for a variety of system sizes. A critical field of $H_c \approx 1.3637$ was roughly

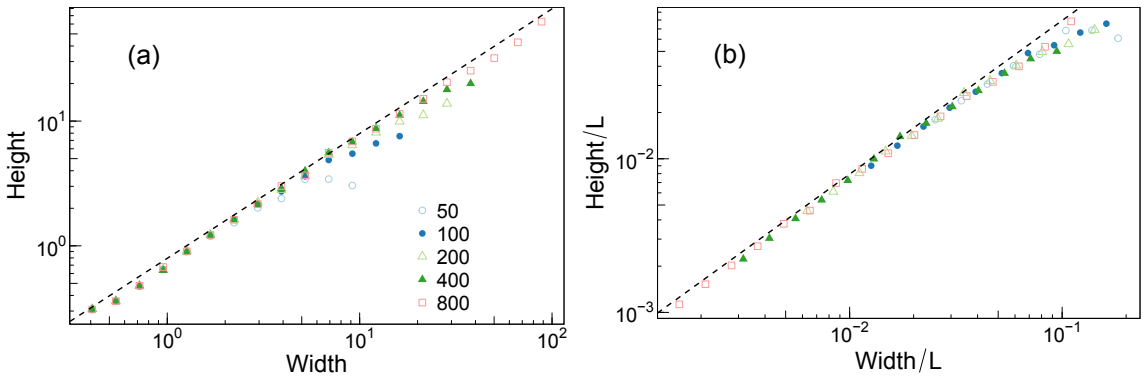

Figure 2.26: (a) Mean values of $\ell_\perp$ as a function of $\ell_\parallel$ for $\Delta = 3.5 > \Delta_c$ and for the system sizes indicated in the legend. The dashed line has a slope of unity. (b) Data for different L with $\ell_\parallel > 1$ are collapsed by scaling both axes by L.

identified by studying the divergence in the total volume invaded. Using a value of $\nu = 0.88$ from Koiller and Robbins,[54] non-percolating avalanches that nucleated close to the critical point, $(H_c - H) < 20L^{-1/\nu}$, were identified. As in Sec. 2.4, the eigenvalues of the second moment tensor were used to define $\ell_\parallel$ and $\ell_\perp$. One can no longer necessarily associate these metrics with a width and height of an avalanche as there is no reason to assume avalanches will have a particular orientation. Instead, these metrics are best understood as the smallest and largest dimensions of an avalanche.

In Fig. 2.26a the average value of $\ell_\perp$ is calculated for logarithmically spaced bins of $\ell_\parallel$ for systems of a given L. Similar to Fig. 2.10a, the average value of $\ell_\perp$ scales as a power of $\ell_\parallel$ for $\ell_\parallel > 1$ before saturating due to finite-size effects. Direct measurement of the power law is consistent with an exponent of unity, implying avalanches scale isotropically. Scaling both $\ell_\perp$ and $\ell_\parallel$ by L for $\ell_\parallel > 1$, one finds the curves collapse as seen in Fig. 2.26b. This confirms expectations that avalanches are isotropic in the self-similar regime.

Next, we test whether the scaling of the total interfacial width, W_T, depends on Δ.

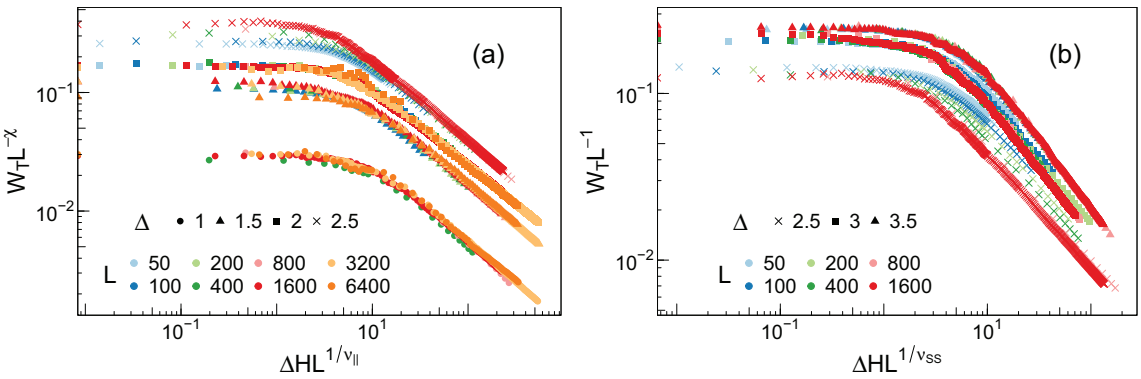

Figure 2.27: Plots of the total interface roughness as a function of ΔH for different Δ are collapsed according to the finite-size scaling relation in Eq. (2.17). (a) Results for $\Delta < \Delta_c$ collapse with $\chi = 0.85$ and $\nu_\parallel = 0.79$. (b) Results for the self-similar regime, $\Delta > \Delta_c$, collapse with $\chi = 1$ and $\nu = 0.84$. Results for the critical point, $\Delta = 2.5$, do not collapse in either panel.

Data was run for values of $\Delta = 1.0$, 1.5, 2, 2.5, 3, and 3.5 and values of $H_c = 1.4066$, 1.4517, 1.4831, 1.5101, 1.4773, and 1.3637 were used, respectively. As above, these values of H_c were approximately identified by observing at what field the volume invaded diverges as a function of L. In Fig. 2.27a, curves of W_T as a function of $\Delta H = H_c - H$ for the indicated values of $\Delta \leq \Delta_c$ and L are scaled according to Eq. (2.17) using values of $\chi = 0.85$ and $\nu_\parallel = 0.79$. For $\Delta < \Delta_c$, all curves are seen to collapse indicating $\chi = 0.85$. In contrast, data for $\Delta = 2.5$ does not collapse.

In contrast, equivalent curves for $\Delta \geq \Delta_c$ are collapsed in Fig. 2.27b using $\chi = 1$ and $\nu = 0.84$. Again, curves for $\Delta = 2.5$ do not collapse suggesting this data is very close to the multicritical point. This is further evidence that correlations are isotropic in the self-similar regime.

	Values	Prior RFIM	QEW	Predictions
$\nu_\parallel$	0.79(2)	0.75(5)[30]	0.80(5)[81]	0.77[57]
		0.77(4)[70]		
		0.75(2)[54]		
$\nu_\perp$	0.67(2)			
α	2.84(2)			
τ	1.280(5)	1.28(5)[30]	1.30(2)[59]	
			1.25(2)[60]	
$\tau_\parallel$	1.79(1)			
$\tau_\perp$	1.94(2)			
ϕ	1.64(4)	1.71(11)[30]		
ζ	≥ 0.75	0.67(2)[30]	0.75(2)[81]	0.86[57]
		2/3[54]	0.753(2)[58]	
χ	0.85(1)			0.86[57]

Table 2.1: Summary of critical exponents found here for the RFIM and prior results for the RFIM and QEW equation with corresponding references. Prior studies of the RFIM were consistent with $\nu_\perp = \nu_\parallel$ and $\chi = 1$. Predicted exponents are from two-loop renormalization group calculations. Numbers in parentheses give uncertainties in the last significant digit. Scaling relations involving these exponents are found in equations (2.7), (2.14), (2.15), (2.16).

2.7 Summary of Depinning

Finite-size scaling studies of systems with linear dimensions from 100 to 12800 spins were used to determine critical behavior at the onset of domain wall motion in the 3D RFIM. Most interface growth models force the interface to be a single-valued function and fix the mean direction of growth. In contrast, an interface in the RFIM can move in any direction and the driving force is always perpendicular to the local surface. Nonetheless, the interface breaks symmetry and locks in to a specific growth direction when the rms random field is small enough, $\Delta < \Delta_c \approx 2.5$. Results are presented for $\Delta = 1.7$, but similar scaling was observed for $\Delta = 1.0$, 1.5, 2, and 2.1. Critical exponents are summarized in Table 2.1.

At the critical driving field in an infinite system there is a transition from motion through unstable jumps between stable states to steady motion at a nonzero velocity. In a finite system the transition occurs over a finite range of fields. Near H_c there is a growing probability that avalanches may span the system and even advance the entire system (fully spanning avalanches). Finite-size scaling of the fraction of volume invaded by spanning and fully spanning avalanches was used to determine H_c and the in-plane correlation length exponent $\nu_{\|}$ (Fig. 2.3). Past studies used either the fraction of sites invaded in a cubic system[30] or the probability of spanning a cubic system.[54] This overestimates H_c because growth is anisotropic and the typical height of the interface at H_c is only of order L^{χ}. The correlation length exponent is also affected.

As H approaches H_c from below, the mean volume of avalanches grows as $\langle S \rangle \sim \Delta H^{-\phi}$ until it saturates due to the finite system size. The value of ϕ and an independent measure of $\nu_{\|}$ are obtained by scaling results for different L (Fig. 2.5 and Eq. (2.5)). At H_c the probability distribution of S decreases as $S^{-\tau}$ up to a maximum size that scales as L^{α} (Fig. 2.6). The values of α and τ were determined by scaling the distributions for different L. Independently determined exponents agreed with the scaling relation given in Eq. (2.7).

The mean height and width of avalanches and their distributions must obey analogous scaling relations. Finite-size scaling collapses in Subsec. 2.4.1 test these relations and reveal a clear anisotropy in growth (Fig. 2.10). The height of avalanches $\ell_{\perp}$ diverges with a different exponent $\nu_{\perp}$ near H_c and the height and width of individual avalanches are related by $\ell_{\perp} \sim \ell_{\|}^{\chi}$ with $\chi = \nu_{\perp}/\nu_{\|}$ (Fig. 2.12). The divergence of the mean height of the interface is consistent with the growth in the size of the largest avalanche: $\nu_{\perp} = 1 - \phi$ (Eq. (2.16)).

Table 2.1 contrasts results obtained here with past studies of the RFIM and related models. Refs. 30 and 54 assumed $\chi = 1$. This leads to a reduced set of scaling relations that were consistent with their exponents. Note that their values of $\nu_{\|}$, τ, and ϕ are consistent with our results but have much larger error bars because of the smaller system sizes available. Slightly larger systems in Ref. 64 gave an indication that χ was less than unity, but could not rule out $\chi = 1$.

The largest difference from past work on the RFIM is the value of ζ. These references considered the scaling of roughness with ℓ at a given L and found results were consistent with the mean field value of $2/3$.[30,54] As seen in Subsec. 2.5.2, this measure is strongly affected by system size. The slope on log-log plots rises continuously as H goes to H_c and L increases. Results for $L \sim 1000$ are consistent with $\zeta \approx 2/3$, but values up to 0.75 are observed for $L = 12800$ (Fig. 2.16). These changes appear to be related to overhangs that lead to growing roughness at small scales as L increases. The results in Subsec. 2.5.3 support the conclusion that these changes become irrelevant at the critical point. We find that the total rms roughness is not significantly affected by overhangs and scales as L^{χ} with $\chi = 0.85 \pm 0.02$ for all $L \geq 100$ (Fig. 2.15).

Table 2.1 also includes results for the evolution of single valued interfaces governed by the QEW Equation. Estimates of the avalanche distribution exponent τ are consistent with the value measured in Subsec. 2.3.3 for the RFIM.[59,60] The roughness exponent ζ found in the QEW equation is consistent with our lower bound for ζ although it is distinct from χ.[58] Interestingly, results from two-loop functional renormalization group analysis indicate $\zeta = 0.86$.[57] This prediction of ζ is even closer to the exponent χ identified in this chapter.

Finally, scaling relation results from simulations[81] of $\nu_{\|} = 0.80 \pm 0.05$ and the two-loop renormalization group result[57] of $\nu_{\|} = 0.77$ cannot be distinguished from our measurement of $\nu_{\|}$ for the RFIM.

Comparing numerically measured exponents for the RFIM and QEW equation, one cannot conclusively determine whether they are distinct. However, our measure of ζ is a lower bound which we anticipate will approach $\chi = 0.85$ with increasing L, while simulations of the QEW give the smaller value of $\zeta = 0.75$.[81] This difference suggests the RFIM resides in a different universality class than the QEW equation. Furthermore, although the morphology of overhangs becomes irrelevant in the thermodynamic limit, the ability of a fully d dimensional interface to grow laterally is still important and fundamentally changes the system's response to extreme pinning sites. We find over 10% of the projected area consists of overhangs indicating lateral growth is an important mechanism in the propagation of RFIM domain walls.

The anisotropy of individual avalanches has not yet been measured in the $d = 2{+}1$ QEW equation, however Rosso et al.[59] measured the maximum size of avalanches in $d = 1 + 1$ and found it scales as $\xi^{1+\zeta}$. The anisotropy of avalanches has also been directly studied in single-valued models of directed percolation depinning (DPD) in $d = 2 + 1$, producing results consistent with $\chi = \nu_{\perp}/\nu_{\|} = \zeta$ where $\zeta = 0.58 \pm 0.03$.[82] It is interesting that $\chi = \zeta$ in DPD although it is important to note that DPD resides in a distinct universality class described by the quenched Kardar-Parisi-Zhang equation.[55,56]

The studies presented here show that finite-size effects remain important until very

large system sizes and small ΔH. Given recent conclusions about the importance of rare events in the QEW model,[61] it would be interesting to extend past QEW studies to the much larger sizes studied here. Further studies on the RFIM and QEW models are also needed to clarify the relation between χ and ζ. This work clearly identifies an anisotropy exponent $\chi = 0.85$ in several independent measures that have not been applied to the QEW. While the roughness exponent measured for individual interfaces approaches χ, it remains significantly below χ even for $L = 12600$. An important topic for future work will be to confirm that ζ approaches χ as predicted by current scaling theories or show that ζ remains distinct from χ and new theories are needed.

Chapter 3

Yielding

3.1 Introduction to Yielding

Yield stress materials, or Bingham plastics, are materials that do not flow unless a critical yield stress σ_c is exceeded. This type of behavior has been identified in a wide variety of disordered solids including foams, emulsions, colloids, granular media, and bulk metallic glasses.[83] The transition from a jammed state to an unjammed state at σ_c is known as the yielding transition[40] and is a particular type of jamming transition.[84]

The behavior of yield stress materials at this critical point is remarkably similar to that of the depinning interfaces discussed in the previous chapter. As σ is quasistatically increased towards σ_c, the system experiences local plastic rearrangements or avalanches. The maximum size of an avalanche diverges as $\sigma \to \sigma_c$. This divergence in avalanche size corresponds to a diverging correlation length that represents the maximum length scale of

cooperative motion in avalanches, $\xi \sim (\sigma - \sigma_c)^{-\nu}$ where ν is a critical exponent. Above σ_c, the system will flow with an average strain rate $\dot{\epsilon}$ that scales as $\dot{\epsilon} \sim (\sigma - \sigma_c)^{\beta}$ where β is a critical exponent commonly known as the Herschel-Bulkley exponent.[85] Close to σ_c, there are large fluctuations in flow caused by localized avalanches. As σ continues to increase, these fluctuations decrease.

In the thermodynamic limit, the yielding transition corresponds to an infinitely small strain rate. In a finite system, which is typically studied due to experimental or computational constraints, the transition from jamming below σ_c to flowing above σ_c is broadened over a range of stresses. Therefore, the yielding transition is often studied using constant strain rate as opposed to constant values of the stress. Experiments on bulk metallic glasses[86,87] as well as molecular dynamic simulations[38,39] at quasistatic strain rates have identified a power-law distribution of the magnitude of avalanches. The size of the largest avalanche has been found to diverge with increasing system size.[38,39] The measured exponents are inconsistent with those found in depinning, implying that yielding is in a different universality class. Coarse grained mesoscopic models have also seen similar scaling of avalanches[75,88–90] although it is not clear whether these models accurately represent the universality class of a continuous system.

Some researchers have argued that yielding is in the same universality class as depinning, but simulations have shown the critical exponents are different.[38–40] The biggest discrepancy is in the rate of avalanche nucleation, which scales extensively for depinning and subextensively for yielding.[38,39] Lin and Wyart have argued that the yielding transition is distinct from the depinning transition due to the nature of interactions between regions

of the systems.[40] In depinning, interactions always have the same sign. If one region of the interface advances it pulls all nearby regions with it. In contrast, in a sheared solid, the activation of a shear transformation zone, the fundamental unit of rearrangement in a disordered solid,[91] produces a multipolar stress field.[92] This implies that as one region of the solid relaxes it may stabilize or destabilize neighboring regions depending on their relative position.

In this work we study the limit of finite strain rates (FSR) using molecular dynamics simulations of 2D and 3D disordered solids containing up to 7×10^6 particles. We use finite-size scaling techniques to accurately measure several critical exponents for the first time in 2D and 3D including ν and β as well as the dynamical exponent z which relates the duration of an avalanche to its size. We also propose new scaling relations that provide bounds on β/ν using measures of quiescence in the system. Finally we describe and test a theory for the scaling of temporal correlations with strain rate.

In Sec. 3.2 we describe the simulation methods and initial system preparation. Typical behavior in steady state flow at a constant strain rate is then presented in Sec. 3.3. In Sec. 3.4 the average flow stress is collapsed using a finite-size scaling ansatz providing accurate measurements of σ_c, ν, and β. The fluctuations in stress are then addressed in Sec. 3.5, followed by a discussion of the emergence of quiescence and the implied bound on β/ν in Sec. 3.6. We next identify the scaling of temporal correlations in avalanches by analyzing the power spectra of the kinetic energy versus time in Sec. 3.7 and finite-size effects in Sec. 3.8. In Sec. 3.9 we look at particle transport, identifying a novel dependence on system geometry in 2D. A further brief look at the impact of deformation geometry is given in Sec.

3.10. Finally, in Sec. 3.11, we provide a summary of results in this chapter, compare to results in other works, and propose open questions for future research.

3.2 Methods

We simulate pure shear of two and three dimensional disordered packings using molecular dynamics. The systems are bi-disperse and are similar to models used in other work studying the yielding transition.[38,39,93–95] The two types of disks or spheres are labeled A and B and have the same mass m. Particles of type i and j interact through an attractive Lennard-Jones (LJ) potential: $U_{ij}(r) = 4u_{ij}\left((a_{ij}/r)^{12} - (a_{ij}/r)^{6}\right)$, where a_{ij} and u_{ij} are the diameter and interaction strength, respectively. To limit the range of interactions, the potential is smoothly interpolated to zero at $r_c = 1.5a_{ij}$. This is accomplished using a fourth order polynomial function that starts at a distance of $1.2a_{ij}$.

Particles of type A and B have radii $0.5a$ and $0.3a$, respectively, where a is taken as the unit of length. The radii are additive, so the effective diameters are $a_{AA} = a$, $a_{AB} = 0.8a$ and $a_{BB} = 0.6a$. The self-interaction strengths are $u_{AA} = u_{BB} = u$, where u is taken as the fundamental unit of energy. We have considered two values of the cross interaction, $u_{AB} = u$ and $2u$. Increasing the strength of the cross interaction encourages the system to mix so we refer to the two choices as the neutral and mixing models, respectively. The values of a_{ij} are chosen to help ensure that the system remains disordered as it is sheared by adding geometrical frustration.[93,96] While bidispersity increases the energy barrier to nucleate and grow crystalline domains,[97] the ground state of the neutral model is still a phase separated,

crystalline state and segregation was observed in 2D simulations. In contrast, the ground state of the mixing model is expected to be a mixed configuration due to energetically favorable cross interactions. No evidence of segregation or crystallization was observed in our simulations and, unless noted, results presented below are for the mixing model.

A unit of time can be defined as $t_0 = \sqrt{a^2 m/u}$. All quantities in the following text are presented in units of a, u, t_0 or appropriate combinations. For example strain rates are in units of t_0^{-1} and stress is in units of u/a^d, where d is the spatial dimension.

Simulations were run in LAMMPS using the velocity-Verlet algorithm with a timestep of $\Delta t = 0.005$.[98] The focus here is on critical behavior of athermal, overdamped systems. Thus a Langevin damping force was applied to all particles: $\vec{F}_{\text{damp}} = -\Gamma m \vec{v}_{na}$, where $\vec{v}_{na}$ is the non-affine component of the velocity that reflects deviations from the local environment. No Langevin noise term is added since the effective temperature is zero. Unless noted, $\Gamma = 2$, which is well within the overdamped regime.[38,39]

Initial particle configurations were prepared in a manner similar to that used in prior papers.[93,94] Particles were randomly placed in a square or cubic box of side length L with periodic boundary conditions and initial density ρ_i. The number of particles of type N_A and N_B had a fixed ratio of $N_A/N_B = (1+\sqrt{5})/4$. A cosine potential was then applied between particles to separate overlapping particles for a time of about 25. This potential was then replaced with the LJ potential and the system was expanded to the desired final density ρ over another time interval of 25. Simulations in 3D used $\rho_i = 1.8$ and $\rho = 1.7$ and the final cubic box length ranged from $L = 20$ to 162. Simulations in 2D used $\rho_i = 1.6$ and

$\rho = 1.4$, and the final square box had $L = 55$ to 1753.

Systems were deformed under pure shear by applying an affine transformation to particle positions at a constant uniaxial strain rate $\dot{\epsilon}$. The components of the stress tensor $\sigma_{\alpha\beta}$ were calculated from the virial and kinetic energy.[99]

Initial simulations used conventional periodic cells with fixed orientation. The x dimension of the periodic cell, L_x, was expanded at strain rate $\dot{\epsilon} \equiv \frac{1}{L_x}\frac{dL_x}{dt}$, while the remaining dimensions were contracted to preserve area or volume. In 2d, y was contracted at $\dot{\epsilon}$, while for 3D, y and z were contracted at $\dot{\epsilon}/2$. This contraction limits the maximum strain that can be applied because L_y eventually becomes comparable to the range of interactions.

To access larger strains we imposed the same pure strain deformation using Kraynik-Reinelt (KR) boundary conditions in 2D[100] and generalized KR boundary conditions in 3D.[101] These methods deform the box shape and change the choice of periodic lattice vectors in a sequence of steps that prevents any cell dimension from becoming too small. Our implementation of these boundary conditions was heavily based on the source code of Nicholson and Rutledge.[102] Modifications were made to apply the strain through an affine shift in particle positions as opposed to using the SLLOD equations of motion.[103]

Fig. 3.1 illustrates the evolution of shear stress $\sigma \equiv (2\sigma_{xx} - \sigma_{yy} - \sigma_{zz})/4$ and pressure $p \equiv -(\sigma_{xx} + \sigma_{yy} + \sigma_{zz})/3$ with strain for the neutral and mixing potential. This data is for 3D systems with $L = 80$ and $\dot{\epsilon} = 2 \times 10^{-4}$, but similar results are seen for other systems and in prior work.[38,39] For both potentials, there is a peak in σ at about 7% that indicates yield. This initial yield stress is known to depend on the preparation of the initial state.[104–106]

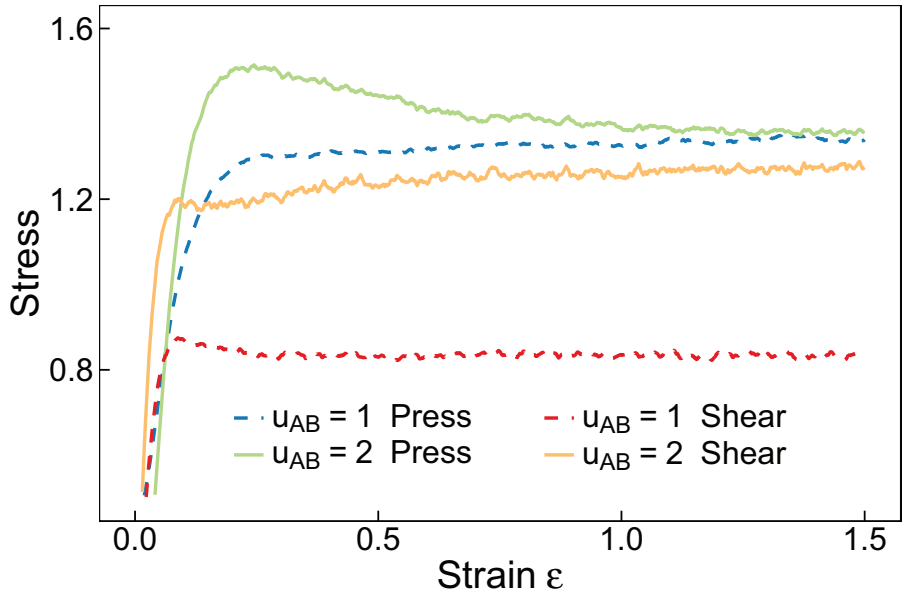

Figure 3.1: The shear stress (red/yellow lines) and the pressure (blue/green lines) are plotted as a function of strain for the models indicated in the legend. Dashed lines indicate the neutral potential while solid lines indicate the mixing potential. Data is collected from a system of size $L = 80$ at a rate of $\dot{\epsilon} = 2 \times 10^{-4}$.

From Fig. 3.1 we see that the shear stress shows a clear evolution with strain up to $\epsilon \sim 0.25$ to 0.5, while the pressure continues to evolve until strains of 1 or more. Studies of the radial distribution functions show that the structure evolves during this initial period. The number of AB neighbors increases for mixing interactions and decreases for the neutral potential, leading to segregated regions in 2D.

Our goal is to study critical behavior after the system has reached steady state so the data below uses the KR approach. To ensure data are only collected after all memory of the initial preparation has been erased, systems were first sheared over a strain of 20 at a high rate, $\dot{\epsilon} = 10^{-3}$ and 2×10^{-3} in 2D and 3D, respectively. The strain rate was then slowly incremented downward, straining at each lower rate until a new steady state was reached.

The strain to reach steady state after each change in rate decreased with decreasing rate, and saturated when finite-size effects were evident. We checked that simulations starting from lower rates and higher rates gave the same results.

The applied strain rate $\dot{\epsilon}$ varied between 10^{-3} and 10^{-7} in 2D and 2×10^{-3} and 2×10^{-7} in 3D. During deformation we evaluated the shear stress, pressure, kinetic energy per particle K, and diffusive motion of particles relative to the affine deformation, $\langle|\Delta\vec{r}|^2\rangle$. Energy introduced through shear is dissipated by the Langevin damping described above.

3.3 Time Dependence of Stress and Kinetic Energy

Figure 3.2(a) shows the variation of shear stress with strain in steady-state shear at the indicated strain rates. The system is 3D with $L = 40$, but similar trends are seen for all systems. We first discuss behavior in the quasistatic (QS) limit, illustrated by the results for $\dot{\epsilon} = 2\times10^{-7}$. The stress rises linearly as elastic energy is stored in the system and then drops when the system becomes mechanically unstable, causing an avalanche of plastic rearrangement. During each avalanche, stored elastic energy is converted into kinetic energy as shown in Fig. 3.2(b). Since we are in the overdamped limit, K follows the rate of energy dissipation through plastic deformation. In between avalanches there is a small background level that grows with rate. During each avalanche, K rises as plastic deformation spreads and then decays as the rate of plasticity drops back towards zero. In the QS limit, K reaches the background level before the next instability is triggered. The integral of K over the duration of an avalanche corresponds to the energy per particle dissipated and is

proportional to the drop in stress $\Delta\sigma$. In general there is a correspondence between K and $d\sigma/dt$ that is verified in Sec. 3.7.

The QS curves in Fig. 3.2 show a broad distribution in the magnitude of the stress drop $\Delta\sigma$ and kinetic energy released. Many avalanches produce drops in stress, $\Delta\sigma$, that are hard to see because the percentage change is small. The plot of K shows an expanded view of the first 10% of the strain in Fig. 3.2(a). The peak energy varies by more than 6 orders of magnitude for the avalanches shown and the integrated energy dissipated varies even more. Past studies of this system examined the critical scaling in the limit of low rates.[38,39] Since σ is intensive, the total released energy scales as $S \equiv L^d \Delta\sigma$ where d is the spatial dimension. There is a power-law distribution of S, $P(S) \propto S^{-\tau}$, in the thermodynamic limit. In a finite system the maximum avalanche size $S_{\max} \sim L^{\alpha}$ where $\alpha = 0.9 \pm 0.05$ and 1.1 ± 0.1 in 2D and 3D, respectively.[38,39] As $L \to \infty$ the QS stress approaches a critical value σ_c and the fluctuations in stress vanish as discussed in the next subsection.

3.4 Scaling of Steady State Flow Stress

In the limit of infinite system size, the system will be jammed ($\dot{\epsilon} = 0$) if a constant stress less than σ_c is applied. At $\sigma > \sigma_c$, the system will flow at a finite rate that grows with the distance to the critical stress:

$$\dot{\epsilon} \sim (\sigma - \sigma_c)^{\beta} \quad , \tag{3.1}$$

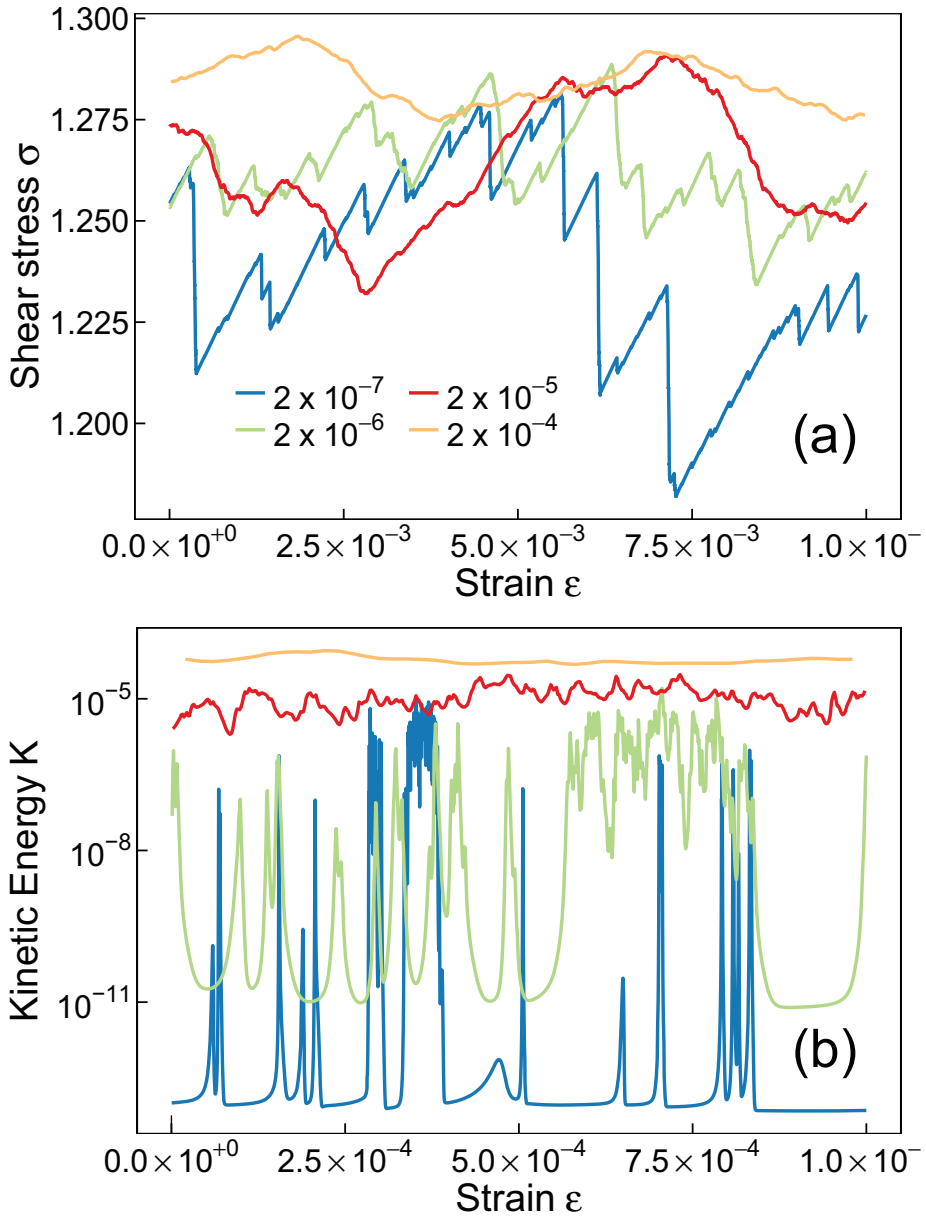

Figure 3.2: Example traces of shear stress (a) and average kinetic energy (b) as a function of strain for a 3D system of size $L = 40$ in steady state. The system was strained at the rates indicated in the legend of (a). Note that the range of strains in (b) is smaller to reveal all avalanches. Small avalanches produce stress drops smaller than the line width in (a).

where β is a critical exponent. This relation is commonly known as the Herschel-Bulkley law[85] and at stresses sufficiently close to σ_c one expects to see critical behavior and a unique value of β for a wide class of materials that all reside in the same universality class.

Our simulations are at constant strain rate, but Eq. 3.1 still applies in the thermodynamic limit. As expected, Figure 3.2 shows an increase in the mean stress with increasing shear rate. There is also an important change in the form of the curves. Both the stress and kinetic energy become smoother with increasing rate. Each avalanche takes time to evolve. As the strain rate increases, new mechanical instabilities are nucleated before large avalanches finish. In Fig. 3.2, increasing $\dot{\epsilon}$ from 2×10^{-7} to 2×10^{-6} reduces the maximum size of stress drops and K does not decrease much between some stress drops. By $\dot{\epsilon} = 2 \times 10^{-5}$, the stress shows undulations rather than sharp drops and one can no longer distinguish individual avalanches or quiescent periods between avalanches in the kinetic energy.

The changes in Fig. 3.2 can be related to a characteristic correlation length ξ that diverges as σ approaches the critical stress:

$$\xi \sim |\sigma - \sigma_c|^{-\nu} \quad , \tag{3.2}$$

where ν is a second critical exponent. Combining this expression with Eq. 3.1 yields:

$$\xi \sim \dot{\epsilon}^{-\nu/\beta} \quad . \tag{3.3}$$

This length scale represents the maximum spatial range over which particles cooperatively rearrange during an avalanche. A finite system will be in the QS limit when $\xi > L$, so that avalanche size is only limited by the finite system dimensions. The system will move to the finite strain rate (FSR) limit when the rate is large enough that $\xi < L$, and rate limits avalanche size. In Fig. 3.2, this transition occurs somewhere between $\dot{\epsilon} = 2 \times 10^{-6}$ and 2×10^{-5}. From Eq. (3.3) the transition rate should scale as $L^{-\beta/\nu}$ and scaling results for different L will allow β/ν to be determined.

Fig. 3.3 shows the variation of shear stress with rate for the indicated system sizes in 2D and 3D. Each point represents an average over ensembles as well as a strain interval in steady-state. Data are only presented up to $\dot{\epsilon} = 10^{-3}$ in 2D and 2×10^{-3} in 3D because higher rates showed large deviations from critical scaling as discussed in Sec. 3.7. Systems with $L > \xi$ are expected to exhibit the same stress. At high rates, the correlation length is small and results for all but the smallest L in 3D have converged onto a common curve by $\dot{\epsilon} = 10^{-3}$. As the strain rate decreases, the correlation length grows until it reaches the size of the next largest system, $L = 40$. This system then transitions to the QS regime, and finite-size effects cause a deviation from the critical stress curve. The inset of Fig. 3.3(b) shows how results for each L deviate from those for larger L as $\dot{\epsilon}$ decreases. Note that for each L there is a limiting yield stress, $\sigma(0, L)$, as $\dot{\epsilon} \to 0$. As L increases, $\sigma(0, L)$ increases towards the critical yield stress σ_c.

The Herschel-Bulkley law in Eq. 3.1 applies to infinite systems. Therefore, we first focus on data taken from systems that have not yet developed finite-size effects because $\xi < L$. For this subset of the data, $\langle\sigma\rangle$ does not depend on L and thus is representative of

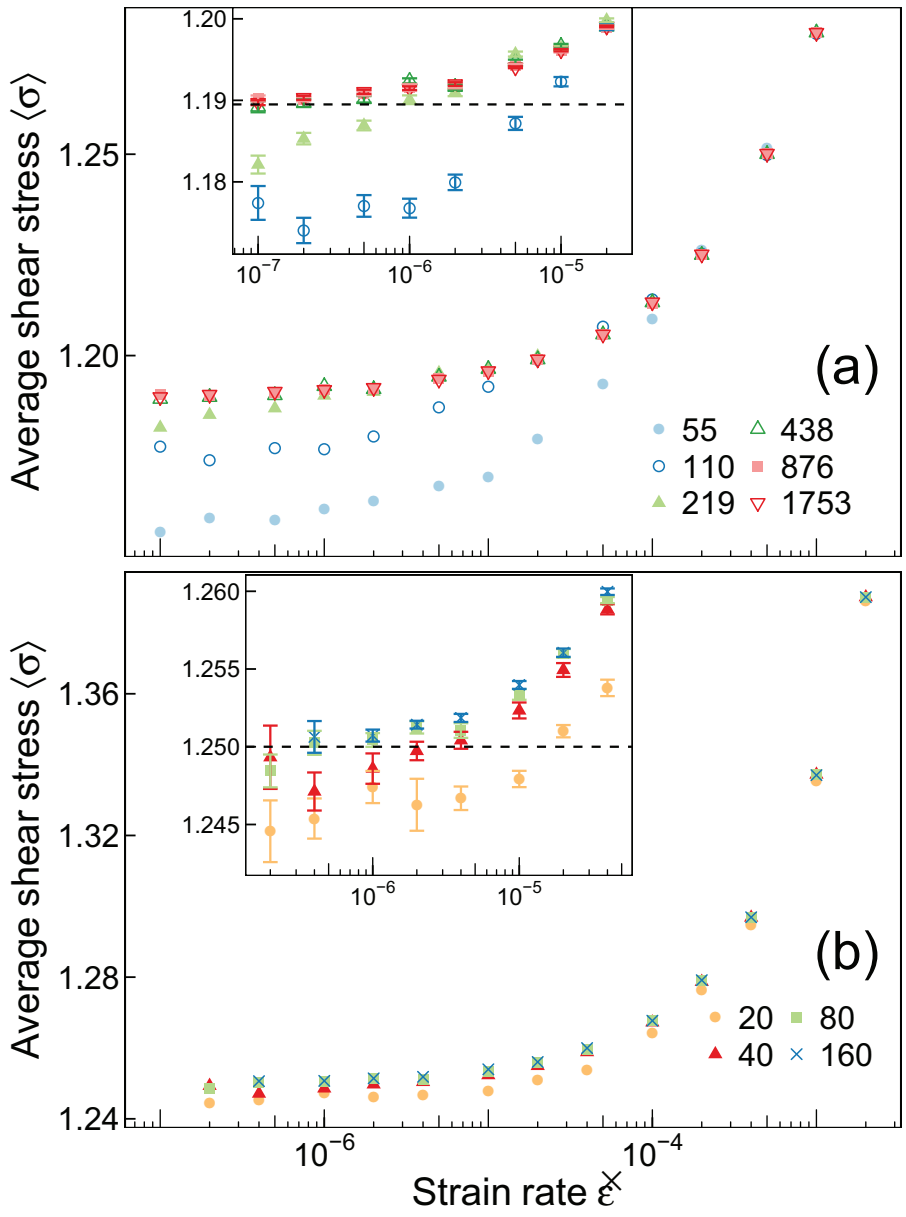

Figure 3.3: The average shear stress as a function of strain rate for systems of size L indicated in the legends for (a) 2D and (b) 3D. The insets in each panel show a zoomed view of low rate data. The horizontal dashed lines indicate $\sigma_c = 1.1895$ in 2D and 1.2500 in 3D.

an infinite system. To reveal the power-law scaling, we plot σ against $\dot{\epsilon}^{1/\beta}$ for the value of β that produces the best straight line. As shown in Fig. 3.4, the best fit gives $\beta = 1.76 \pm 0.05$ in 2D and 1.50 ± 0.05 in 3D. The errorbars represent an estimate of the range where the available data is consistent with power-law scaling. Using a least mean squares linear regression, we can then identify an intercept of $\sigma_c = 1.1899 \pm 0.0005$ and 1.2498 ± 0.0005 for 2D and 3D, respectively. These error bars are roughly estimated by accounting for the standard error of the fitted parameter, uncertainty in β, and uncertainty in what data is included in the fit. This estimate of σ_c is refined in later plots yielding best estimates of 1.1895 in 2D and 1.2500 in 3D.

The emergence of finite-size effects in Fig. 3.3 provides information on the rate dependence of ξ that can be extracted using finite-size scaling techniques. As is typical in finite-size scaling theory, we assume that the only relevant length scales in the system are L and ξ. Then the shear stress will only depend on the dimensionless scaling variable $L/\xi \propto L\dot{\epsilon}^{\nu/\beta}$ and L. The resulting scaling ansatz can be written as:

$$\langle\sigma\rangle - \sigma_c \sim L^{-1/\nu} g(\dot{\epsilon} L^{\beta/\nu}) \tag{3.4}$$

where $g(x)$ is a universal scaling function. For large $\dot{\epsilon}L^{\beta/\nu}$ finite-size effects are unimportant and the critical scaling is recovered if $g(x) \sim x^{1/\beta}$ for $x \gg 1$. For small x, g must approach a constant that represents the shift of $\sigma(0, L)$ from σ_c.

Equation 3.4 implies that results for all L should collapse if $(\langle\sigma\rangle - \sigma_c)L^{1/\nu}$ is plotted against $\dot{\epsilon}L^{\beta/\nu}$. Figure 3.5 shows collapses for both 2D and 3D data. Plots for different

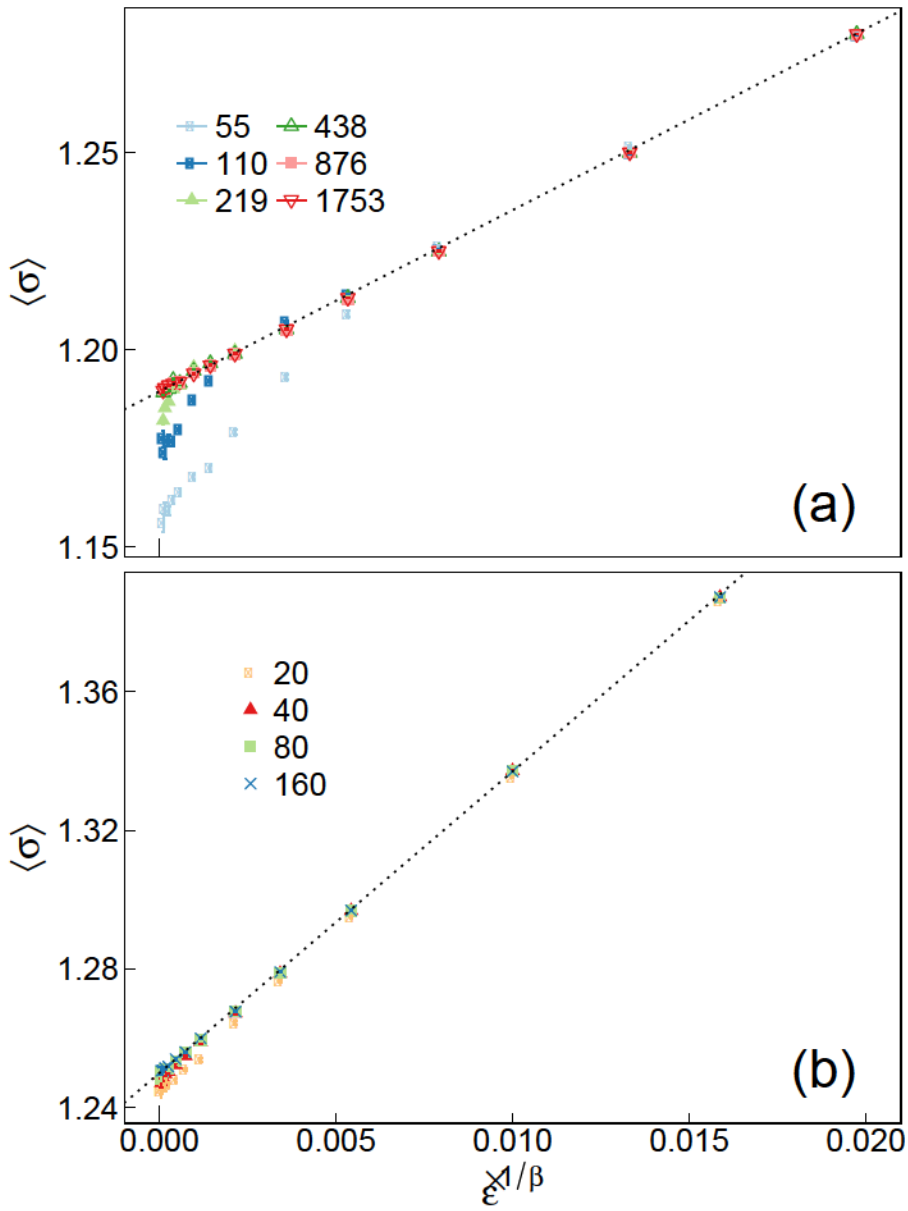

Figure 3.4: Stress plotted against strain rate to a power of $1/\beta$ chosen to give the linear scaling expected from Eq. 3.1. (a) 2D data for the indicated L with a straight line fit to data for $\dot{\epsilon}$ where $\xi < L$ that gives $\beta = 1.76$ and $\sigma_c = 1.1895$. (b) 3D data with a straight line fit giving $\beta = 1.50$ and $\sigma_c = 1.2500$.

exponents are consistent with $\sigma_c = 1.1895 \pm 0.0003 u/a^2$ and $\beta/\nu = 2.31 \pm 0.05$ in 2D and $\sigma_c = 1.2500 \pm 0.0003 u/a^3$ and $\beta/\nu = 3.0 \pm 0.1$ in 3D. Combined with the values of β given above, one has $\nu = 0.76 \pm 0.03$ and $\nu = 0.5 \pm 0.02$ for 2D and 3D, respectively.

3.5 Standard Deviation of the Shear Stress

Further information about the critical exponents can be obtained by considering fluctuations in the system. As noted above, the standard deviation of the stress, $\Delta\sigma \equiv \sqrt{\langle\sigma^2\rangle - \langle\sigma\rangle^2}$, decreases with system size in the QS limit.[39] One finds[39]

$$\Delta\sigma_{\rm QS} \sim L^{-\phi} \quad , \tag{3.5}$$

where ϕ is another critical exponent and the subscript QS indicates the relation holds in the quasistatic limit where $\xi > L$. The value of ϕ reflects the strength of correlations in the system and one can define two upper bounds for a d dimensional system.[39] If correlations have a finite range, stress-drops in different regions add incoherently and $\Delta\sigma \sim L^{-d/2}$. Correlations can only slow the decrease in fluctuations with L, implying $\phi \leq d/2$. The scale of fluctuations must also be at least as large as the magnitude of the stress drop during the largest avalanche. The energy released in the largest avalanche scales as $S_{\rm max} \sim L^{\alpha}$ implying a change in the intensive stress of $\Delta\sigma \sim L^{(\alpha-d)}$. Since this is a lower bound on fluctuations, $\phi \leq d - \alpha$.

At finite strain rates, regions of size ξ^d are uncorrelated and their contributions to σ will add incoherently. Near the critical point the fluctuations in stress within each subregion

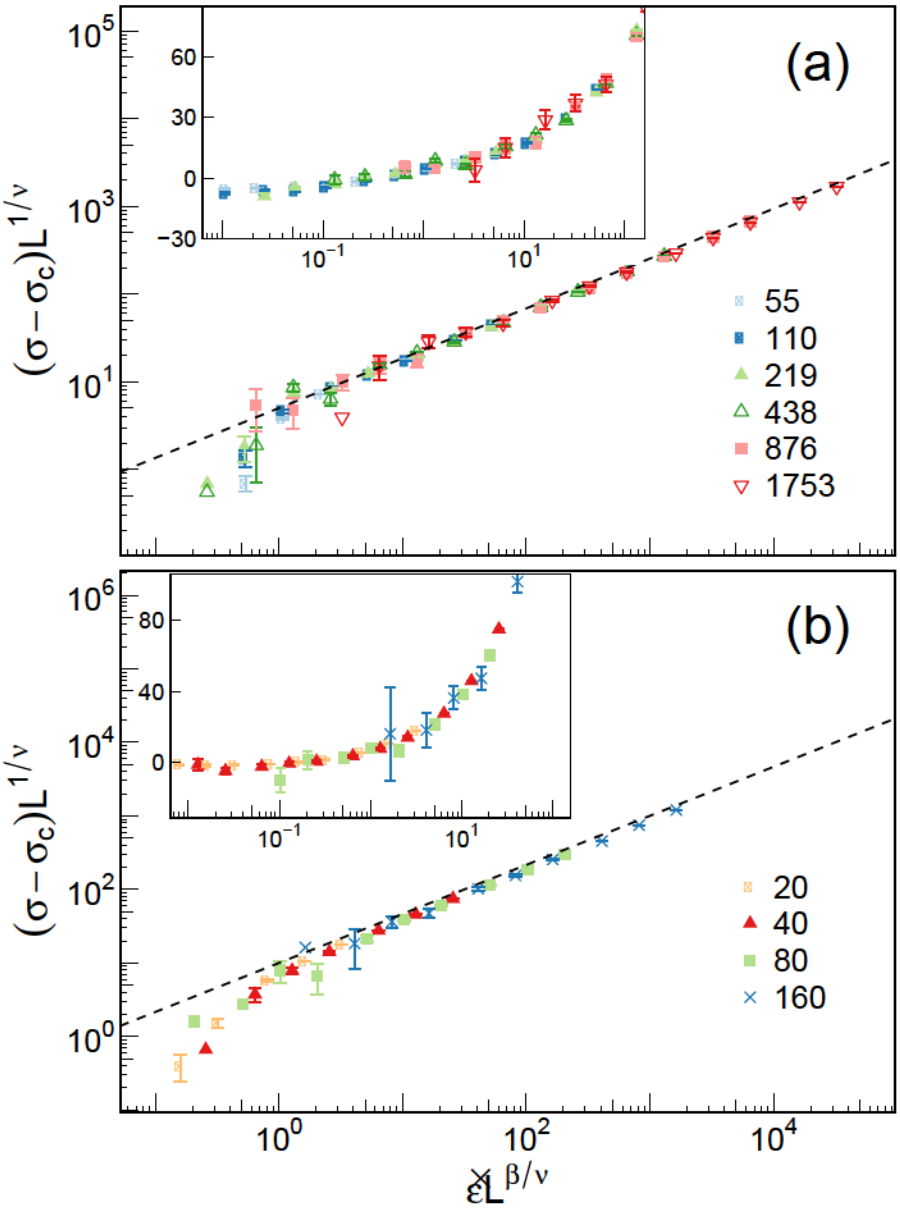

Figure 3.5: (a) The 2D data in Fig. 3.3(a) is rescaled using the finite-size scaling relation in Eq. (3.4) with values of $\beta = 1.76$, $\nu = 0.76$, and $\sigma_c = 1.1895$. The dashed line represents a power-law with an exponent $1/\beta = 0.57$. The inset includes a zoomed in view of the same scaled data on a linear-log scale to show values of $\langle\sigma\rangle < \sigma_c$ also collapse. (b) 3D data from Fig. 3.3(b) rescaled with $\beta = 1.5$, $\nu = 0.5$, and $\sigma_c = 1.25$. The dashed line is a power-law with exponent $1/\beta = 0.67$. The inset includes a zoomed in view of the same scaled data on a linear-log scale.

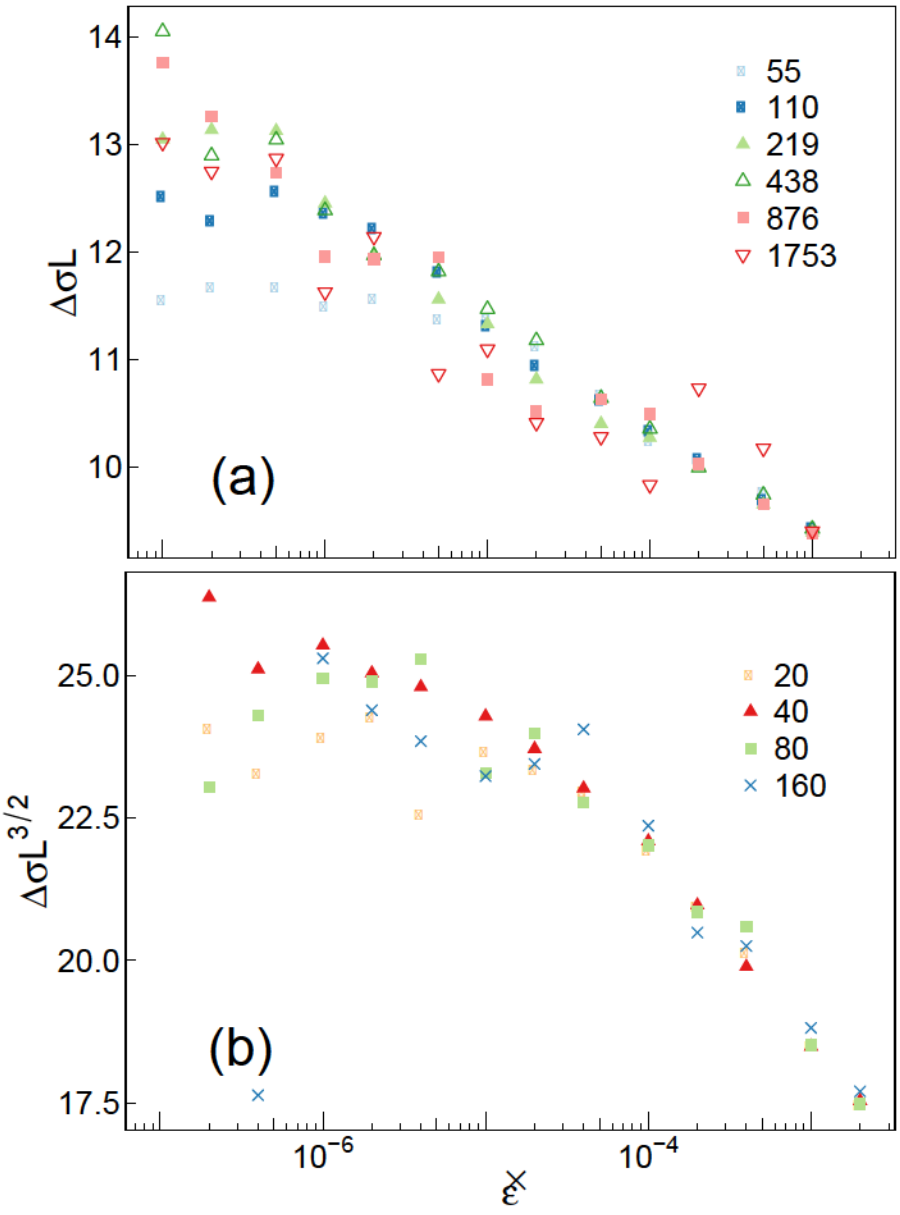

Figure 3.6: Standard deviation of stress multiplied by $L^{d/2}$ as a function of rate for the indicated L in (a) 2D and (b) 3D.

should scale as $\Delta\sigma_\xi \sim \xi^{-\phi}$. The number of these uncorrelated subregions will scale as $N_\xi \sim (L/\xi)^d$. Therefore, fluctuations in the total stress scale as $\Delta\sigma \sim \Delta\sigma_\xi N_\xi^{-1/2} \sim L^{-d/2}\xi^{d/2-\phi}$. This expression can be reexpressed in terms of strain rate using Eq. (3.3):

$$\Delta\sigma_{\rm FSR} \sim L^{-d/2}\dot{\epsilon}^{(\phi-d/2)\nu/\beta} \quad , \tag{3.6}$$

where the FSR subscript is used to emphasize that this scaling holds in the finite strain rate limit. Note that in the special case of $\phi = d/2$ the QS and FSR limits both scale as $L^{-d/2}$ and fluctuations are independent of rate.

In $d = 3$, Salerno and Robbins measured $\alpha = 1.1 \pm 0.1$ in the overdamped limit implying ϕ is more strictly bounded by $d/2$.[39] This upper limit was found to be consistent with their actual measurement of $\phi = 1.5 \pm 0.2$. From the above equations, this implies that $\Delta\sigma L^{3/2}$ should be nearly independent of system size and rate. Fig. 3.6(b) confirms this prediction. In the QS limit, $\Delta\sigma L^{3/2}$ is near 25 for all L. Results for $L = 20$ are below other curves by slightly more than statistical errors, but the deviation is only a few percent and previous QS results showed deviations from critical scaling for this small system size.[39] In this QS regime our results are consistent with $\phi = 1.47 \pm 0.07$ in agreement with Ref.[39] In the FSR limit, all of the results collapse within statistical errors. While there is a small decrease in $\Delta\sigma L^{3/2}$ with increasing rate that might suggest $\phi < d/2$, the change is only 30% over more than two decades in rate. This also implies that ϕ is no smaller than 1.4 and consistent with $\phi = d/2$.

For $d = 2$, past results gave $\alpha = 0.9 \pm 0.05$ in the overdamped limit.[39] This gives a

slightly larger upper bound than $d/2$, so we may expect that $\phi = d/2 = 1$. Fig. 3.6(a) shows a plot of $\Delta\sigma L$ against rate for multiple system sizes. In the QS limit the results for large L collapse, implying $\phi = d/2$. As L decreases the QS values drop slightly, which is consistent with deviations from critical scaling in small systems. All of the results collapse in the FSR limit. As in 3D, there is a small decrease with increasing rate, but the results are consistent with $\phi = d/2 = 1$ with an uncertainty of less than 0.1.

In Fig. 3.7, the variance of the kinetic energy ΔK per particle scaled by $L^{d/2}$ is plotted as a function of strain rate for the indicated values of L. As rate decreases, ΔK is seen to approximately decrease as $\dot{\epsilon}^{1/2}$. Deviations from this power-law are highlighted in the figure insets where $\Delta K \dot{\epsilon}^{-1/2}$ is plotted as a function of rate.

As demonstrated in Sec. 3.7, there is an approximate correspondence between K and $d\sigma/dt$. It is therefore reasonable to predict ΔK will scale with the same power of L as $\Delta\sigma$ in Eqs. (3.5) and (3.6). This is consistent with the high rate data seen in the insets of Fig. 3.7 where $\Delta K \sim L^{-d/2}$. At quasistatic rates, a minor deviation (< 10 %) in scaling from $L^{-d/2}$ is identifiable in 3D. This could either be a correction in scaling or indicate a deviation in ϕ from 1.5 consistent with $\phi = 1.42 \pm 0.03$.

In the QS limit, the dependence on strain rate can also be easily explained. As the rate continues to decrease, the same sequence of avalanches evolves. Therefore the integral of $K(t)$ or $K^2(t)$ will not depend on $\dot{\epsilon}$. However, any moment of $K(t)$ will be weighted by the total time and therefore will scale in proportion to $\dot{\epsilon}$. This implies $\langle K^2 \rangle$ will dominate $\langle K \rangle^2$

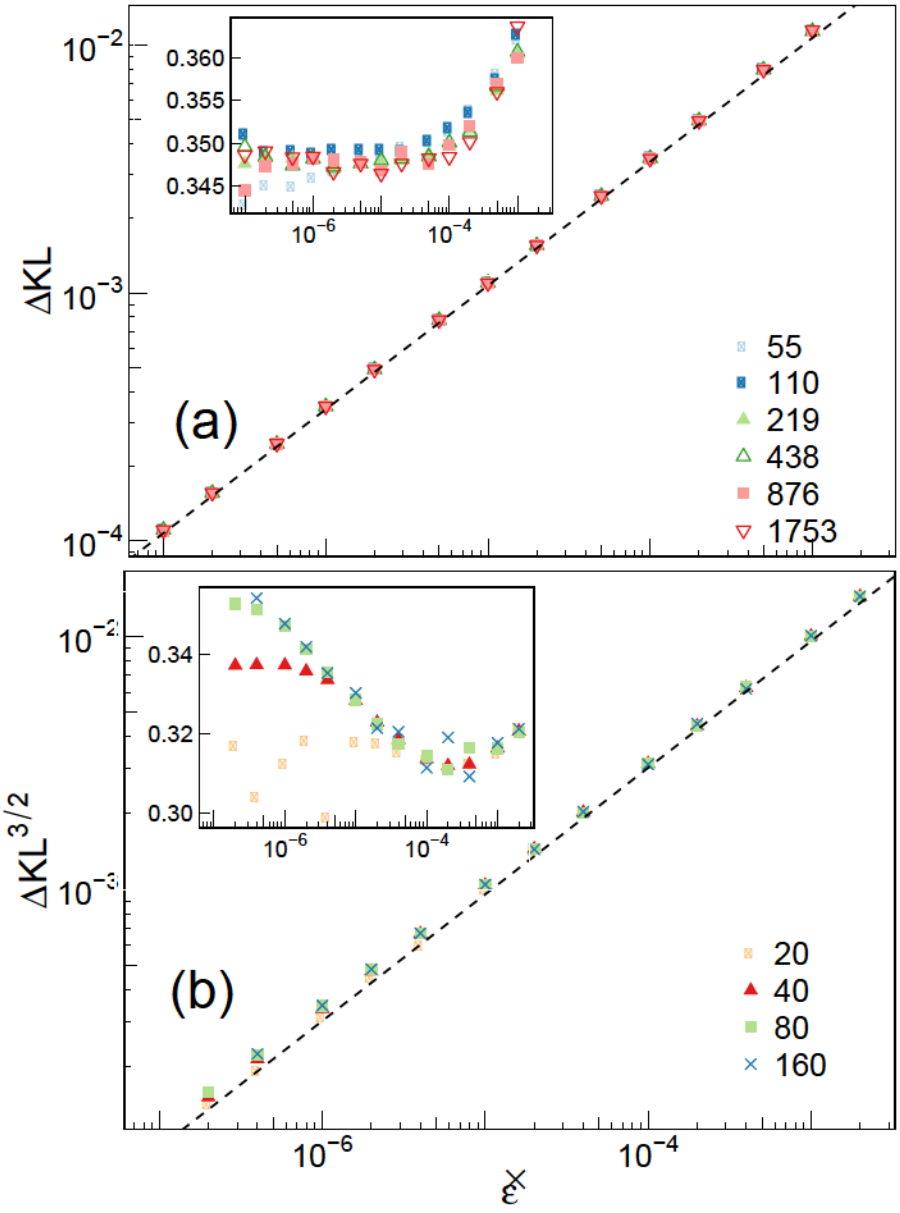

Figure 3.7: Standard deviation of kinetic energy multiplied by $L^{d/2}$ as a function of rate for the indicated L in (a) 2D and (b) 3D. Dashed lines in both panels show power laws with exponents of 1/2. Insets show $\Delta K \dot{\epsilon}^{-1/2}$ to highlight deviations in scaling.

such that the variance will scale as $\dot{\epsilon}$. Therefore we suggest:

$$\Delta K_{\mathrm{QS}} \sim L^{-\phi}\dot{\epsilon}^{1/2} \tag{3.7}$$

where the QS subscript emphasizes that this relation only holds in the quasistatic limit. In the FSR limit, one could imagine that similarly $\Delta K_{\mathrm{FSR}} \sim \Delta\sigma_{\mathrm{FSR}}\dot{\epsilon}^{1/2}$. This relation is appealing but no simple proof is known to the authors. In the next section, we will use this observation to place a limit on the value of β/ν.

3.6 Condition for Overlapping Avalanches

In the QS limit, the same sequence of avalanches occurs in a system independent of rate. Increasing $\dot{\epsilon}$ just decreases the quiescent periods between avalanches (Fig. 3.2). Growth will transition to the FSR limit above a rate $\dot{\epsilon}_L \sim L^{-\beta/\nu}$ where the largest avalanches do not have time to grow and are limited by ξ instead of L. A necessary, but not sufficient, condition for avalanches to grow to their maximum size is that there are quiescent periods between avalanches. In this section we identify the largest rate where there are quiescent periods $\dot{\epsilon}_{QL}$, which sets an upper bound on $\dot{\epsilon}_L$ and thus gives a lower bound for β/ν.

The strain rate $\dot{\epsilon}_{QL}$ will decrease with increasing system size as more avalanches are nucleated. We define a critical exponent x such that $\dot{\epsilon}_{QL} \sim L^{-x}$. To determine whether the system has quiescent periods we evaluate the minimum and maximum kinetic energy, K_{min} and K_{max}, during steady state shear. At rates $\dot{\epsilon} < \dot{\epsilon}_{QL}$, the ratio $R_K \equiv (K_{\mathrm{max}} - K_{\mathrm{min}})/K_{\mathrm{max}}$ is approximately unity as $K \approx 0$ during phases of inactivity. At rates $\dot{\epsilon} > \dot{\epsilon}_{QL}$, the system

undergoes constant activity and R_K will decrease with rate. This transition is demonstrated in Fig. 3.2b. Results for different L should collapse when R_K is plotted as a function of $\dot{\epsilon}/\dot{\epsilon}_Q \sim L^x\dot{\epsilon}$. Fig. 3.8 shows scaling plots for 2D and 3D systems. Results for all system sizes collapse with $x = 2 \pm 0.05$ and 3 ± 0.1 in 2D and 3D, respectively. The value of x sets a lower bound on β/ν. This bound appears to be an equality in 3D but not in 2D.

Other measures of the onset of quiescence give the same scaling. For example, the root mean squared kinetic energy $\sqrt{\langle K^2 \rangle}$ scales as $\dot{\epsilon}$ in the FSR as K is nearly constant and the average kinetic energy $\langle K \rangle$ grows linearly with rate due to conservation of energy. In the QS limit, the magnitude of fluctuations in the kinetic energy are much larger than the average and $\sqrt{\langle K^2 \rangle} \sim \Delta K_{\rm QS} \sim \sqrt{\dot{\epsilon}} L^{-\phi}$ from Eq. (3.7). When the fluctuations in kinetic energy are much larger than the average, one would anticipate reaching a quiescent state with effectively zero kinetic energy. As shown in Fig. 3.9, results for different L can be collapsed using the same values of $x = 2$ in 2D and $x = 3$ in 3D that collapsed data in Fig. 3.8. Note that this scaling suggests that $x = 2\phi$ if the assumptions used to derive Eq. (3.7) are valid.

To estimate the rate $\dot{\epsilon}_{QL}$ where there is no quiescent period, we calculate the total time T_L for all the avalanches in a unit strain under QS conditions. This would be the maximum time for non-overlapping avalanches and thus give a lower bound for $\dot{\epsilon}_{QL} > 1/T_L$. If the rate was decreased any further it would necessitate a gap between avalanches.

In the QS limit,[39] the number of avalanches per unit strain in a range dS scales as $R(S, L)dS$. The avalanche rate $R(S, L) \propto L^\gamma S^{-\tau}$ up to a maximum avalanche size $S_{\rm max}\ L^\alpha$.

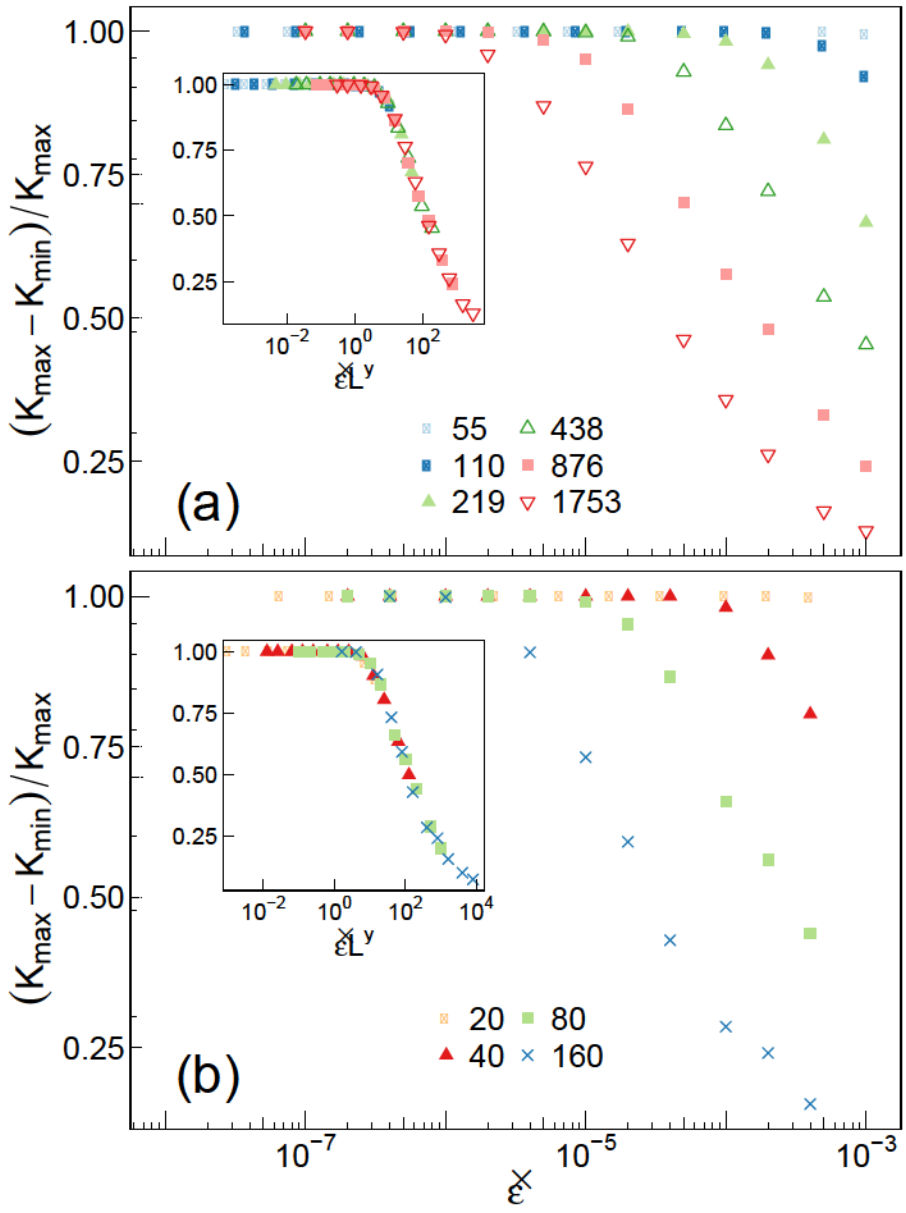

Figure 3.8: Ratio $R_K \equiv (K_{\max} - K_{\min})/K_{\max}$ plotted against $\dot{\epsilon}$ for (a) 2D and (b) 3D systems with the indicated L. The insets show that scaling rate by L^y collapses data for different sizes with $y = 2.0 \pm 0.05$ and 3.0 ± 0.1 in 2D and 3D, respectively.

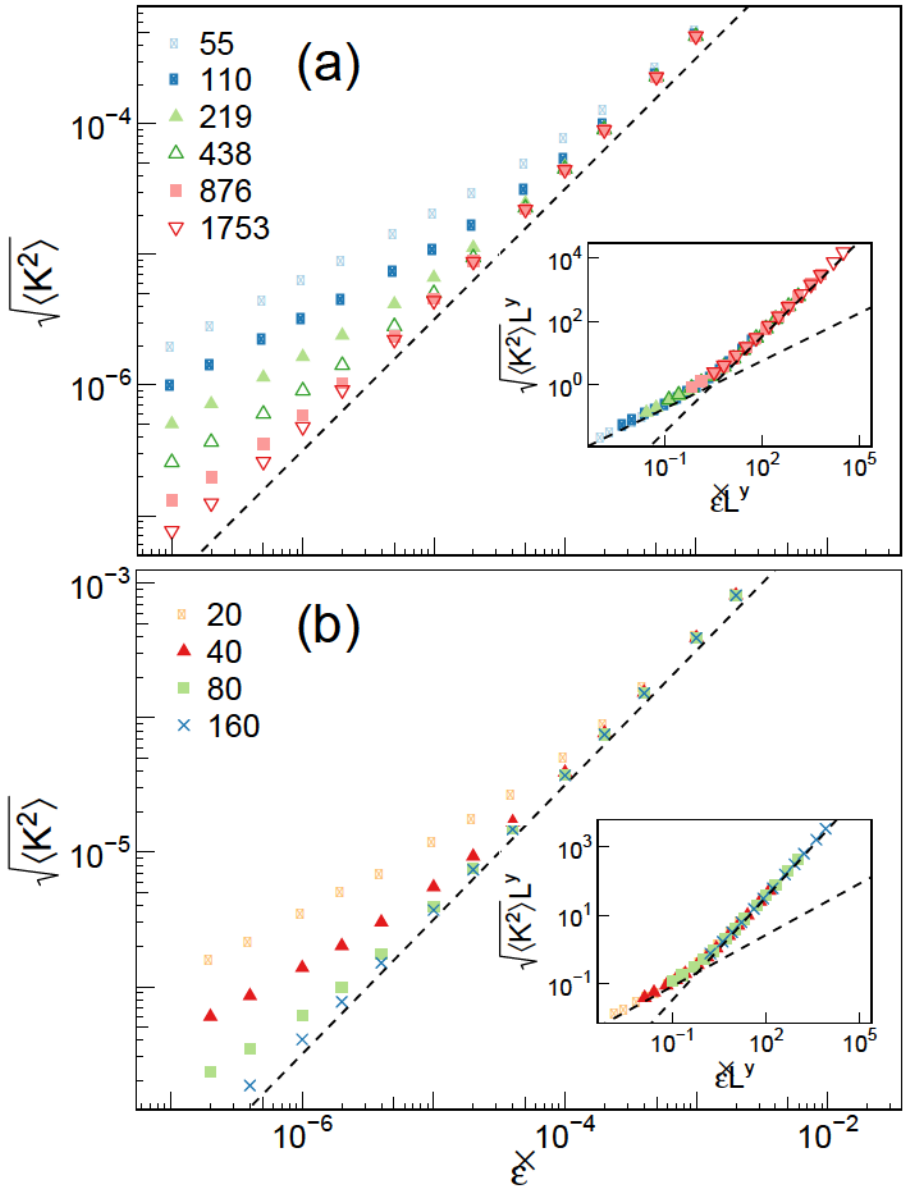

Figure 3.9: Root mean squared kinetic energy as a function of rate in (a) 2D and (b) 3D for the systems sizes indicated in the legends. Dashed lines show power laws with exponents of unity. Insets show that the data collapses when rate and rms kinetic energy are scaled by L^y for $y = 2.0$ and 3.0 in 2D and 3D respectively. Dashed lines indicate power laws with exponents of 1.0 and 0.5.

The duration T of an avalanche is usually expressed in terms of a dynamical exponent z relating T to the linear dimension ℓ of an avalanche: $T \sim \ell^z \propto S^{z/\alpha}$. Combining these relations we find:

$$T_L \propto L^\gamma \int^{S_{\max}} dS S^{-\tau} S^{z/\alpha} \tag{3.8}$$

$$\propto L^\gamma \int^{L^\alpha} dS S^{-\tau+z/\alpha} \propto L^y \tag{3.9}$$

with $y \equiv \gamma + z + \alpha(1-\tau)$. Inserting the values of these exponents determined elsewhere we find $y \sim 3$ in 3D and 2.4 in 2D. Thus $y \geq x$ and $y \approx \beta/\nu$ in both dimensions. The inequality between y and x in 2D implies that there is significant temporal overlap of avalanches that allows periods of quiescence at higher rates than expected from y or β/ν.

3.7 Temporal Power Spectra of K and σ in FSR Limit

The stress-strain and kinetic-strain curves in Fig. 3.2 contain additional information. In particular, the signals encode the dynamical structure of individual avalanches that can be revealed by calculating the temporal power spectrum $S(\omega)$. To calculate $S_\sigma(\omega)$ or $S_K(\omega)$ the time series of σ or K was divided into consecutive intervals of 10% strain in 2D and 5% strain in 3D with values at fixed time intervals of t_0. A fast Fourier transform (FFT) with Hamming windowing function was used to calculate the power spectrum for each interval and the results were then averaged over all intervals. Each spectrum was multiplied by the strain rate such that spectra would not depend on the duration of time over which they were calculated. To minimize noise, the ensemble averaged spectrum was further averaged

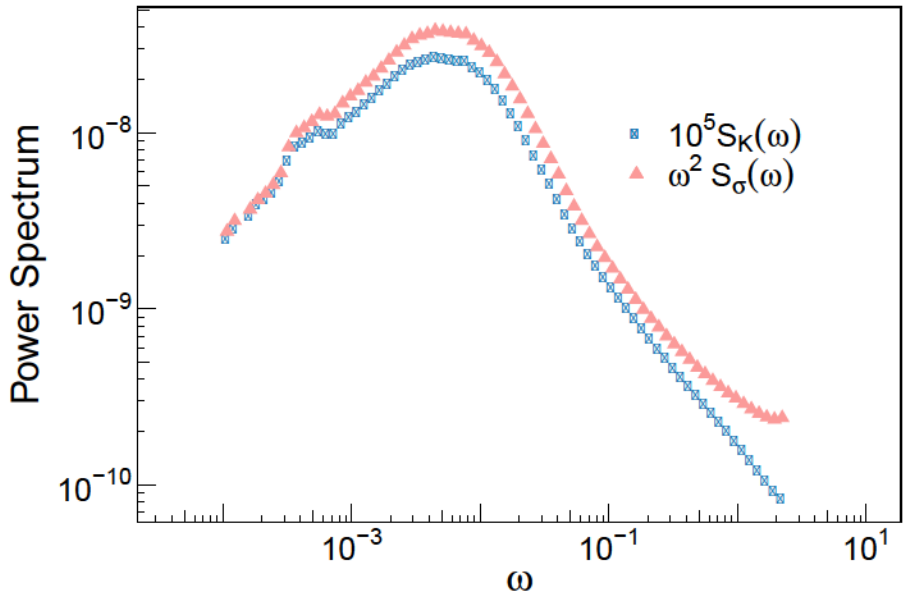

Figure 3.10: The power spectrum of the kinetic energy (blue) and $\omega^2 S_\sigma(\omega)$ (red) as a function of ω for a system of size $L = 80$ at a rate of 4×10^{-7}. The power spectrum of the kinetic energy is shifted vertically by a factor of 10^5.

over intervals of angular frequency ω that have a logarithmic spacing. The curves were then further smoothed by applying a rolling mean. Two data points at lower and higher frequencies were included in the average.

From Fig. 3.2 we see that σ has a saw tooth form, with drops that correspond to peaks in avalanche activity. Since the derivative, $d\sigma/dt$, corresponds to the rate of plasticity, $w^2 S_\sigma(\omega)$ reveals the temporal structure of avalanches. In contrast the power spectrum of plasticity is directly related to $S_K(\omega)$. Fig. 3.10 compares S_K and $\omega^2 S_\omega$ for a 3D system of size $L = 80$ at a rate of 4×10^{-7}. This rate is high enough that no finite-size effects are expected (see Fig. 3.4). The two quantities show very similar behavior. The main difference is that artifacts related to aliasing at the highest ω lead to a slightly slower drop in $\omega^2 S(\omega)$ than $S_K(\omega)$. We present data for $S_K(\omega)$ below, but found similar scaling collapses for $\omega^2 S_\sigma$.

Figures 3.11a-b show the power spectra of large 2D and 3D systems at the indicated rates, which are chosen to be in the FSR regime. For each rate there is an initial power law rise as ω^{ρ}, followed by a peak and a power law decay with $\omega^{-\delta}$. The initial rise as ω^{ρ} implies the existence of anticorrelation at long times. There appears to be a characteristic recurrence time in the time signal of the kinetic energy. The decay seen at large frequencies with an exponent δ is an example of pink noise and represents timescales on which there are temporal correlations due to intra-avalanche dynamics.[107] The peak frequency for each rate in Fig. 3.11a-b corresponds to the duration of the largest avalanche $T_{\max}$. As noted above, $T_{\max} \sim S_{\max}^{z/\alpha}$ where z is the dynamic exponent. In the FSR limit $T_{\max} \sim \xi^z \sim \dot{\epsilon}^{-z\nu/\beta}$.

At high frequencies, $S(\omega)$ increases with increasing rate. As derived later in this section, $S(\omega)$ scales as $\dot{\epsilon}^{\eta}$ where η is a critical exponent. In Fig. 3.11c-d, the high frequency data is collapsed with an exponent of $\eta = 1.00 \pm 0.02$ in 2D and 1.00 ± 0.01 in 3D. Direct measurement of the power laws associated with changes in ω are consistent with exponents of $\delta = 0.92 \pm 0.04$ and $\rho = 0.7 \pm 0.08$ in 3D and $\delta = 0.62 \pm 0.05$ and $\rho = 0.8 \pm 0.08$ in 2D.

To understand the form of $S(\omega)$ we follow past calculations[10] and assume the kinetic energy represents a sum over contributions from independent avalanches of energy S_i. Each is assumed to have a similar shape, but with a time duration $T_i \sim S_i^{z/\alpha}$. Since the dissipated energy is proportional to S_i and is given by the integral of $L^d K$ over an avalanche, the time profile of K during an avalanche at time t_i scales as $K(t - t_i) \sim L^{-d}(S_i/T_i)h((t - t_i)/T_i)$, where $h(x)$ is the characteristic avalanche shape. Summing over avalanches i during a unit

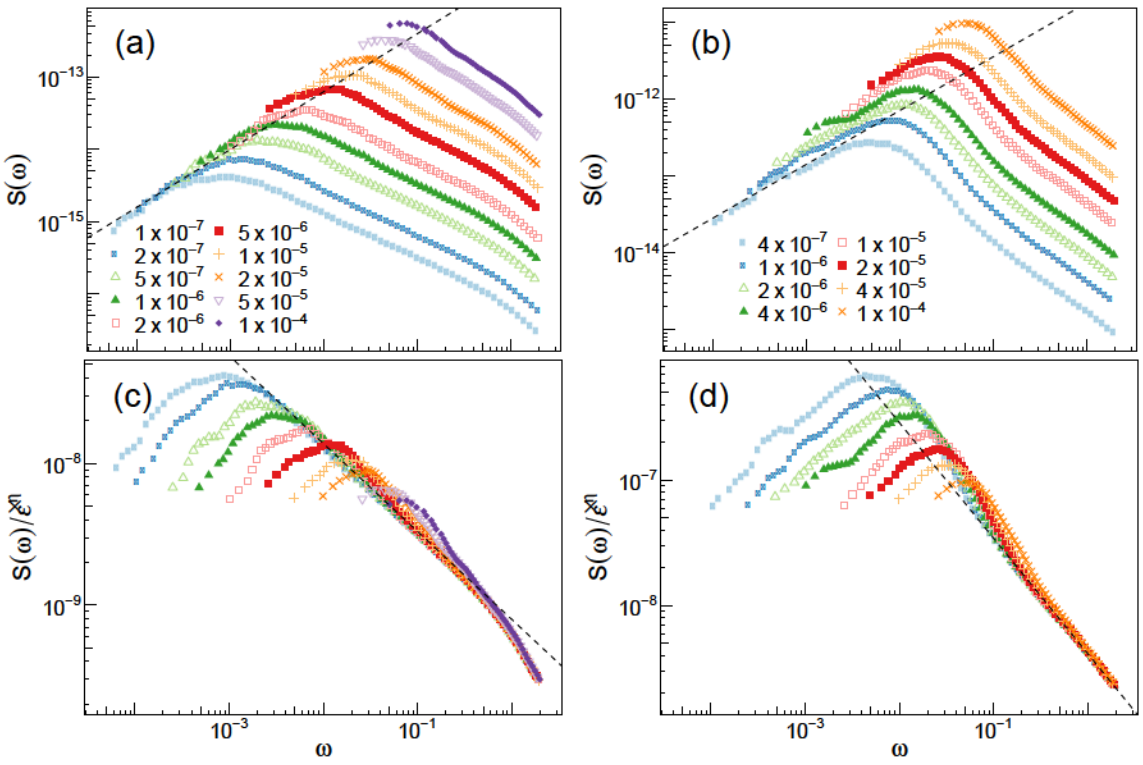

Figure 3.11: The power spectrum as a function of ω for a system of size (a) $L = 1753a$ in 2D and (b) 80 in 3D at the indicated strain rates. The data in (a) and (b) is replotted in (c) and (d), respectively, scaling $S(\omega)$ by $\dot{\epsilon}^{\eta}$ for $\eta = 1$ in 2D and 3D. Dashed lines in (a) and (b) represent power laws with exponents $\rho = 0.8$ in 2D and $\rho = 0.7$ in 3D. Dashed lines in (c) and (d) have exponents $\delta = 0.62$ in 2D and 0.92 in 3D.

strain yields:

$$K(t) = \sum_i L^{-d}(S_i/T_i)h((t-t_i)/T_i) \quad . \tag{3.10}$$

If the avalanches are uncorrelated, they contribute independently to the power spectrum:

$$S_K(\omega) = \sum_i L^{-2d} S_i^2 |f(\omega T_i)|^2 \tag{3.11}$$

where $f(\omega T_i)$ is the Fourier transform of an individual avalanche. Eq. 3.11 can converted into an integral over the rate of avalanches per unit strain:

$$S_K(\omega) = L^{-2d} \int dS R(S,L) S^2 |f(\omega T_i)|^2 \tag{3.12}$$

In the FSR limit $R(S,L) \sim S^{-\tau}(L/\xi)^d \xi^\gamma$ up to $S_{\max} \sim \xi^\alpha$. The number of events of size S over a fixed interval of strain $\Delta\epsilon = \dot{\epsilon}\Delta T$ is therefore equal to $\dot{\epsilon}\Delta T L^d \xi^{\gamma-d} R(S,L)$. One can then write

$$S_K(\omega) \sim L^{-d}\xi^{\gamma-d}\Delta T\dot{\epsilon} \int^{S_{\max}} dS S^{2-\tau} |f(\omega T_i)|^2, \tag{3.13}$$

where $T = S^{z/\alpha}$. As $T \sim S^{\alpha/z}$, we can write $f(\omega T_i) = g(\omega^{\alpha/z} S)$ then substitute $v = w^{\alpha/z} S$ leaving:

$$S_K(\omega) \sim L^{-d}\Delta T \dot{\epsilon}^{1+\nu/\beta(d-\gamma)} \omega^{-\alpha(3-\tau)/z} \int^{v_{\max}} dv v^{2-\tau} |g(v)|^2 \tag{3.14}$$

where $v_{\max} = \omega^{\alpha/z} S_{\max}$ and ξ was replaced using Eq. (3.3).

If one assumes the indefinite integral in (3.14) converges,[49] one finds $\delta = -\alpha(3-\tau)/z$

and $\eta = 1+\nu/\beta(d-\gamma)$. However, as $\tau < 2$, this integral will not converge unless $|g(v)|^2 \sim v^{-q}$ where $q > 3 - \tau$ in the limit of large v. Assuming that the integral does not converge for $v \to \infty$, the scaling depends on q. Carrying out the definite integral gives:

$$S_K(\omega) \sim L^{-d}\Delta T \dot{\epsilon}^{\eta}\omega^{-q\alpha/z} \tag{3.15}$$

where $\eta = 1 + \nu/\beta(d - \gamma + \alpha(\tau + q - 3))$ and $\delta = q\alpha/z$. Kuntz and Sethna argued that for depinning transitions $q = 1$.[10] Assuming this applies to yield, this would predict values of $\delta = 0.96 \pm 0.09$ and $\eta = 1.04 \pm 0.09$ in 3D and $\delta = 0.64 \pm 0.04$ and $\eta = 1.03 \pm 0.08$ in 2D.[38,39] These values are in strong agreement with the values of η and δ measured directly in Fig. 3.11.

Finite-size scaling implies that $T_{\max}$ is the only time scale in the critical regime. The power spectrum should obey a scaling relation:

$$S(\omega) \sim \dot{\epsilon}^{a} g_{\omega}(\omega\dot{\epsilon}^{z\nu/\beta}) \tag{3.16}$$

where a is a critical exponent and $g_\omega(x)$ is a new universal scaling function that scales as $x^{-\delta}$ for $x \gg 1$ and x^{ρ} for $x \ll 1$. As $S(\omega)$ scales as $\dot{\epsilon}^{\eta}$ in the high rate limit $a = \eta - z\delta\nu/\beta$. Figure 3.12 shows collapses of the data using Eq. 3.16. Given the values of β/ν, δ, and η determined above, the fits give $z = 1.15 \pm 0.04$ in 3D and $z = 1.40 \pm 0.05$ in 2D. In 2D, there appears to be a finite-size effect at high rates as the shape of the scaling function $g_\omega(x)$ varies with $\dot{\epsilon}$.

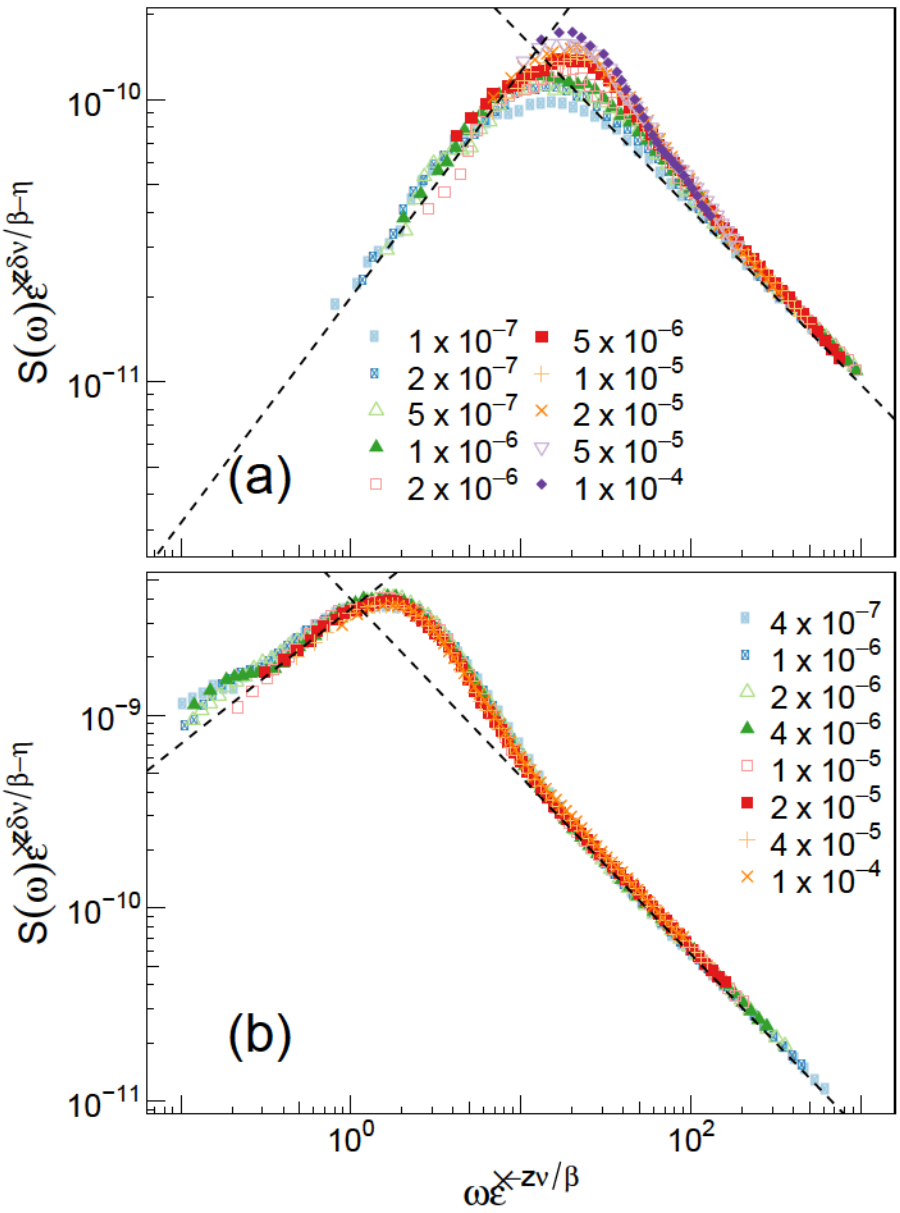

Figure 3.12: (a) The data in Fig. 3.11a is collapsed for frequencies $\omega < 0.5$ according to Eq. (3.16) with exponents $\eta = 1$, $\delta = 0.62$, $z = 1.4$, and $\beta/\nu = 2.3$. (b) A similar scaling for the 3D data with values of $\eta = 1$, $\delta = 0.92$, $z = 1.15$, and $\beta/\nu = 3.0$. Dashed lines represent power laws with exponents (a) $\delta = 0.62$ and $\rho = 0.8$ and (b) $\delta = 0.92$ and $\rho = 0.7$.

3.8 Finite-Size Effects in the Temporal Power Spectra

As the system begins to transition to the QS limit, $T_{\max}$ saturates at L^z. In Fig. 3.13, $S(\omega)$ is plotted for the indicated system sizes that have begun to show finite-size effects at a rate of (a) 10^{-7} in 2D and (b) 2×10^{-7} in 3D. At frequencies below $T_{\max}^{-1}$, the power spectrum plateaus over a range of ω before dropping with decreasing ω. This low frequency cutoff of the plateau is found to decrease with decreasing strain rate. This suggests that on timescales above $T_{\max}$, the time signal $K(t)$ resembles white noise before anticorrelations emerge at some value of the strain at which recurrence is seen. We note that in the largest systems, the plateau cannot be well resolved.

As the system size increases, we see $S(\omega)$ decreases at high frequencies. In the insets of Fig. 3.13, the power spectrum is scaled by a power of system size, L^λ. We find the spectra collapse at high frequencies for values of $\lambda = 2.00 \pm 0.02$ in 2D and 3.00 ± 0.02 in 3D. This can be understood using arguments similar to those in the previous section. In the QS limit, the number of avalanches of size S that nucleate over an interval of time ΔT will scale as $\dot{\epsilon}\Delta T L^\gamma R(S, L)$. One can then derive an analogy to Eq. (3.14):

$$S_K(\omega) \sim L^{-2d+\gamma}\dot{\epsilon}\Delta T\omega^{-\alpha(3-\tau)/z}\int^{v_{\max}} dv v^{2-\tau}|g(v)|^2 \tag{3.17}$$

where again $v = \omega^{\alpha/z}S$ and we assume $|g(v)|^2 \sim v^{-q}$. Using $T_{\max} \sim L^z$ and $S_{\max} \sim L^\alpha$, the integral can be evaluated yielding:

$$S_K(\omega)\dot{\epsilon}\Delta T \sim L^\lambda \omega^{-q\alpha/z} \tag{3.18}$$

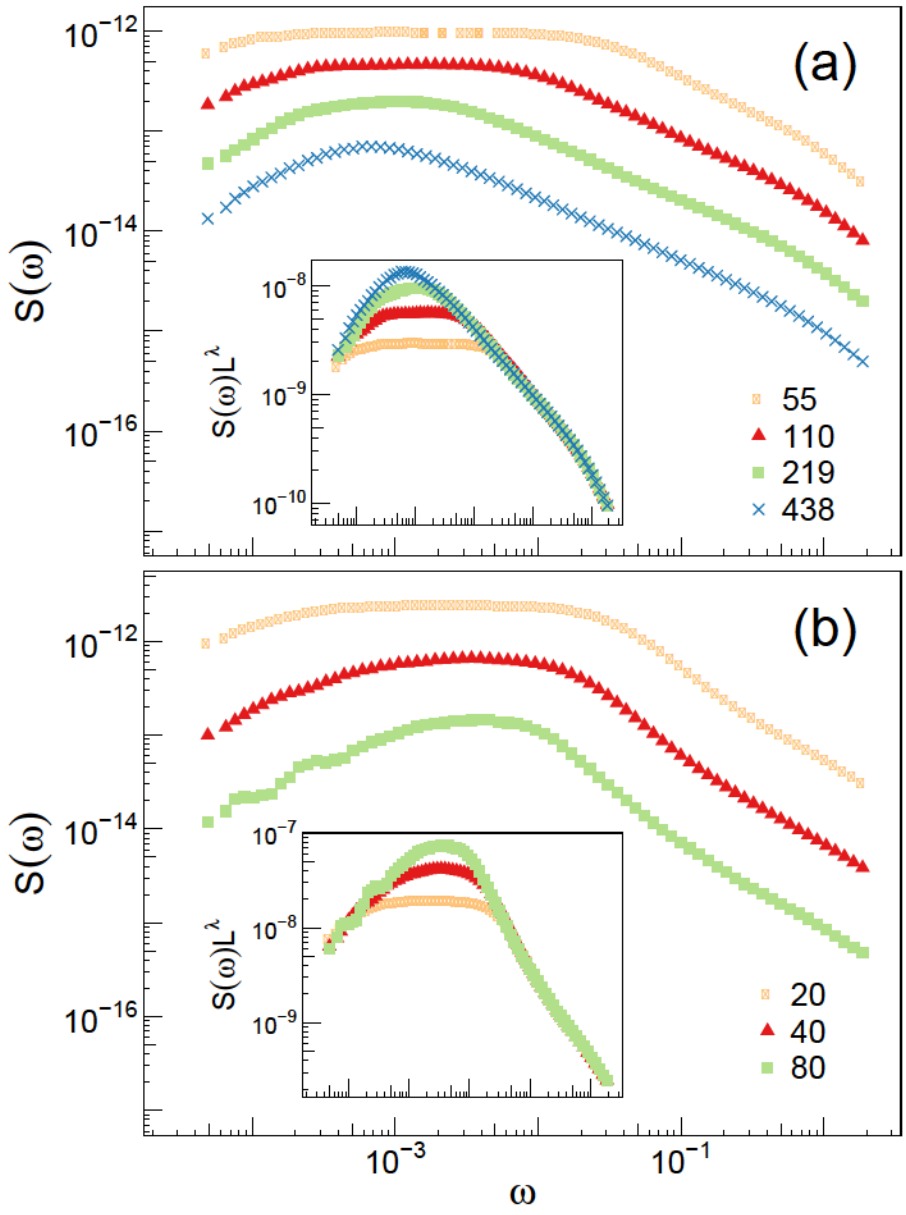

Figure 3.13: The temporal power spectra for systems strained at a rate of (a) 10^{-7} in 2D and (b) 2×10^{-7} in 3D. System sizes are indicated in the legend. Insets show the same data scaled by L^{λ} for $\lambda = 2.0$ in 2D and 3.0 in 3D.

where $\lambda = \gamma + \alpha(3 - \tau - q)$. If we assume $q = 1$ and use previous measurements of γ, α, and τ in Refs.,[38,39] this predicts $\lambda = 1.93 \pm 0.14$ in 2D and 2.78 ± 0.16 in 3D. This is consistent with the directly measured values of λ above.

As a final test of our theory, we narrow our focus to the peak value of the power spectrum $S_{\max}(\omega)$ as a function of both L and $\dot{\epsilon}$. From Eq. (3.16), we expect $S_{\max}(\omega)$ to scale as $\dot{\epsilon}^a L^{-d}$ in the FSR regime where $a = \dot{\epsilon}^{\eta - z\delta\nu/\beta}$. In Fig. 3.14a-b we plot $S_{\max}(\omega)$ normalized by $\dot{\epsilon}^a L^{-d}$ as a function of $\dot{\epsilon}$ for the indicated values of the system size. We find minimal dependence on ϵ for a value of $a = 0.70$ in 2D and 0.62 in 3D. This is consistent with the prediction of $a = 0.65 \pm 0.03$ in 3D but in 2D a is predicted to equal 0.63 ± 0.04. We note that in 2D there is significant error introduced due to the evolution of the universal scaling function at high rates which likely explains this inconsistency.

The data in Fig. 3.14a-b can be collapsed using finite-size scaling techniques. We assume the only relevant length scales are ϵ and L, implying the crossover will occur at a rate of $\dot{\epsilon} \sim L^{-\beta/\nu}$. In Fig. 3.14c-d, the above data is collapsed using the previous measurements of β/ν in both 2D and 3D.

3.9 Particle Diffusion

As a system is strained, particles will plastically rearrange and exchange neighbors during avalanches. The accumulated distance particles have travelled due to plasticity can be measured using the mean-squared non-affine displacement, $\langle |\Delta\vec{r}|^2 \rangle$. This specifically does not include the distance a particle has moved due to the affine motion from the box

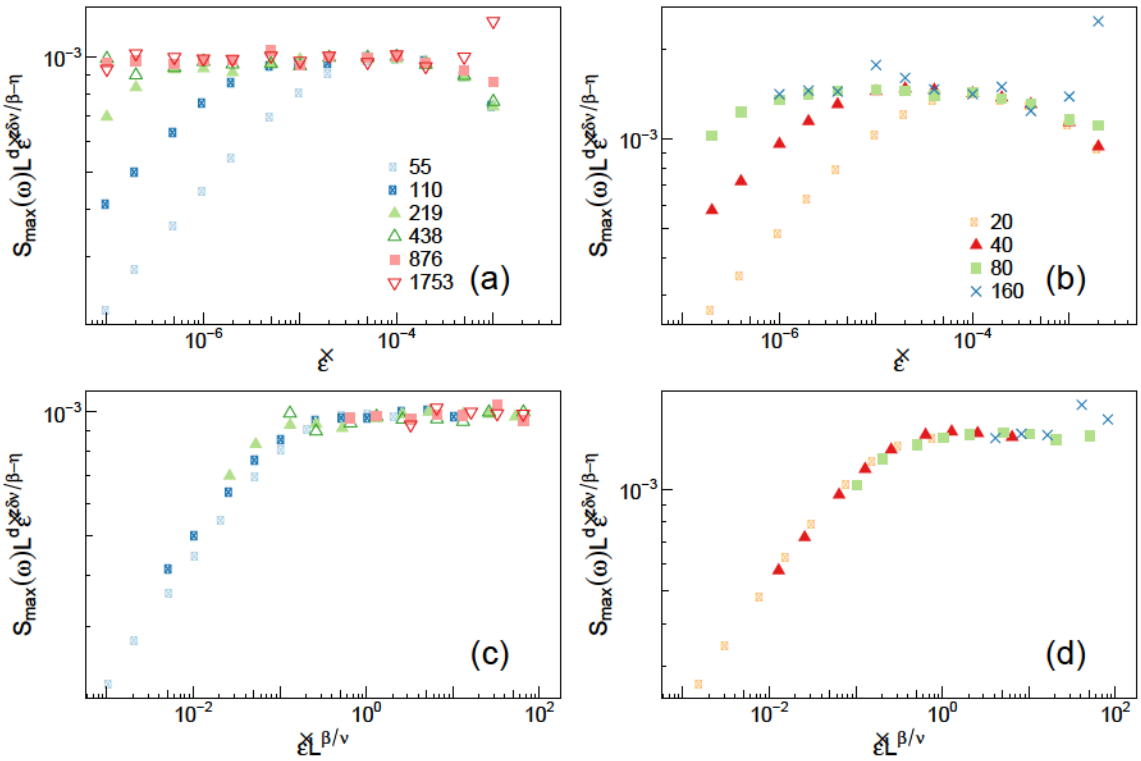

Figure 3.14: The maximum value of the power spectrum scaled by $\dot{\epsilon}^a L^{-d}$ as a function of strain rate for the indicated values of L in (a) 2D and (b) 3D for values of $a = 0.7$ in 2D and 0.62 in 3D. The peak in the spectrum is collapsed by scaling the strain rate with a factor of $L^{\beta/\nu}$ using a value of (c) $\beta/\nu = 2.3$ in 2D and (d) $\beta/\nu = 3.0$ in 3D.

shear. Previous studies have identified that the mean-squared non-affine displacement grows linearly with strain in 2D[94,108] and 3D.[109] One can therefore define an effective diffusion coefficient D quantifying the magnitude of particle transport. In this section we will first focus on diffusion in 2D then discuss changes in behavior in 3D.

In the QS limit, it has been observed that D grows linearly with L in 2D.[94,108] Two explanations have been proposed for this observation. The first is that the maximum span of a slip line L sets the diffusion of particles which assumes $\alpha = 1$.[108] The second is based on the observation that plastic deformation is correlated over an interval of strain that scales as L^{-1}.[94] In the FSR limit, D has been found to increase with decreasing rate before plateauing at a rate that decreases with increasing L.[110] Data for different system sizes was collapsed using a theory that assumes $\beta/\nu = 2$. This collapse included systems up to a maximum of order 10^5 particles ($L \sim 300$).

To calculate the diffusion coefficients, simulation runs were broken up into intervals of 5% strain. For each interval, the cumulative non-affine displacement was calculated and output every increment of 0.1% strain. We tested outputting the instantaneous as well as the average non-affine displacement over the increment but found no significant difference between the two methods. A least mean squares linear regression was then used to fit the data for each interval, providing an estimate of the diffusion coefficient at that particular value of the strain.

We first consider the effect of the global system geometry on the diffusion. In KR boundary conditions, the simulation box is regularly remapped with a period of strain

approximately equal to $\epsilon_{KR} \approx 0.96$. This remapping is what allows deformation to reach arbitrarily large elongational strains. We therefore define $\epsilon_M = \epsilon \bmod \epsilon_{KR}$ as the current location of the system in strain space. Different values of ϵ_M will correspond to different lattice vectors. We divided ϵ_M into equal sized bins and calculated an average diffusion coefficient for each interval at a given rate and system size. In Fig. 3.15a, the average diffusion coefficient is plotted as a function of ϵ_M for a system of size $L = 400$ for the indicated strain rates. At high rates of $\dot{\epsilon} = 10^{-3}$ or 10^{-4}, no dependence on ϵ_M can be identified. At these rates, the system is expected to be in the FSR regime based on Fig. 3.5. As the strain rate is decreased and QS effects emerge, one can identify peaks in the diffusion coefficient at values of $\epsilon_M = 1/4\epsilon_{KR}$ and $3/4\epsilon_{KR}$. The evolving diffusion coefficient implies the linear relation between the non-affine displacement and strain is not valid over large intervals of strain. However, this evolution is minor over the strains of 5% used here. In Fig. 3.15b the diffusion coefficient is plotted as a function of ϵ_M for systems of different sizes strained at a rate of 10^{-5}. At this rate, we see small systems, $L \leq 438$, all exhibit peaks at the vertical dashed lines while larger systems, which are still in the FSR limit, do not. This suggests the emergence of these peaks is a finite-size effect. It can also be observed that after a system has fully reached the QS limit, such as $L = 55$, the peaks stop growing and the diffusion coefficient reaches a limiting value at all values of ϵ_M.

At strains corresponding to $\epsilon_M = 1/4\epsilon_{KR}$ and $3/4\epsilon_{KR}$, the system is in a state where the direction of maximal shear stress remaps periodically onto itself as demonstrated in Fig. 3.16. Therefore we propose that this enhanced diffusion occurs when system-spanning avalanches are able to self reinforce across the period boundary. It is important to note that

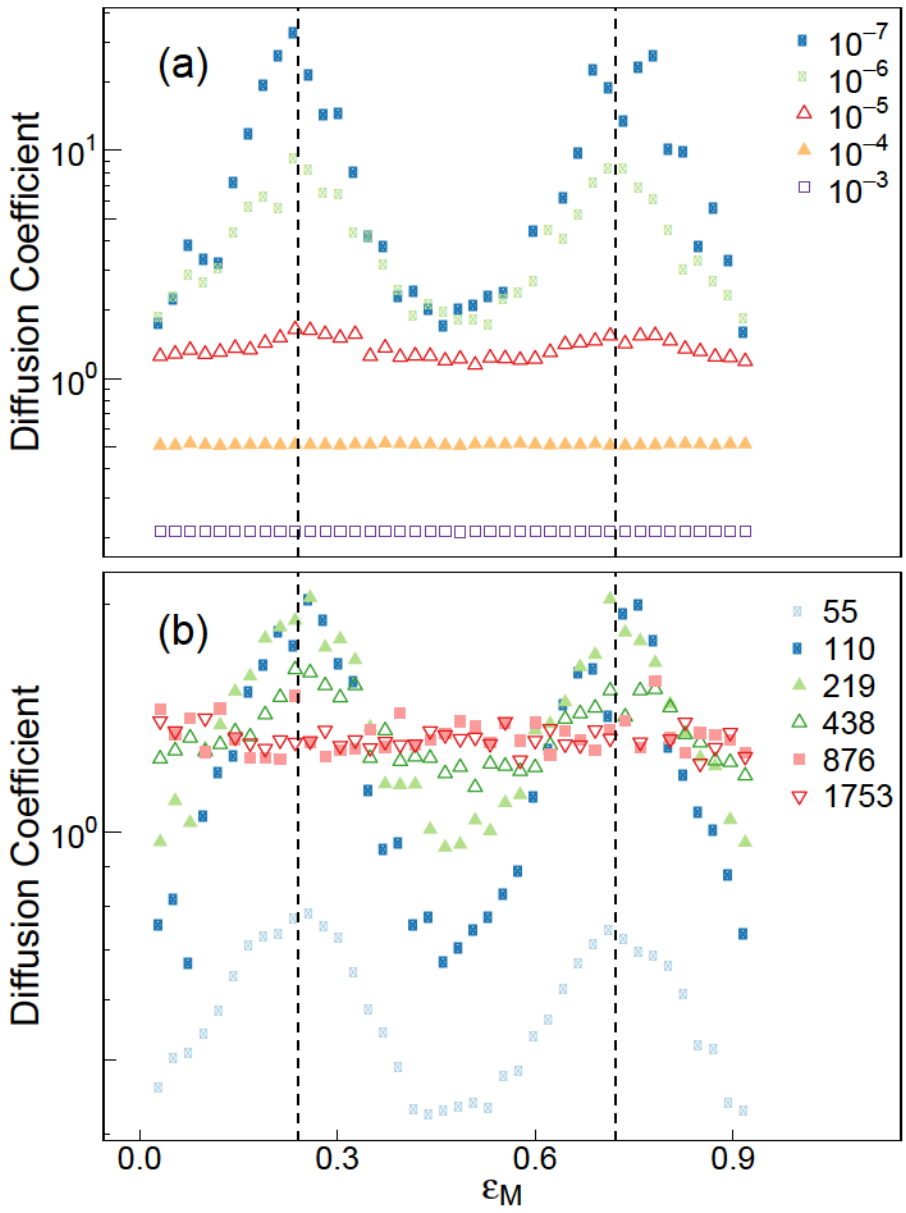

Figure 3.15: (a) The average diffusion coefficient plotted as a function of ϵ_M for 2D systems of $L = 438$ strained at the indicated rates. (b) Similar data is plotted at a fixed rate $\dot{\epsilon} = 10^{-5}$ for system sizes indicated in the legend. Vertical dashed lines represent values of $\epsilon_M = 1/4\epsilon_{KR}$ and $3/4\epsilon_{KR}$.

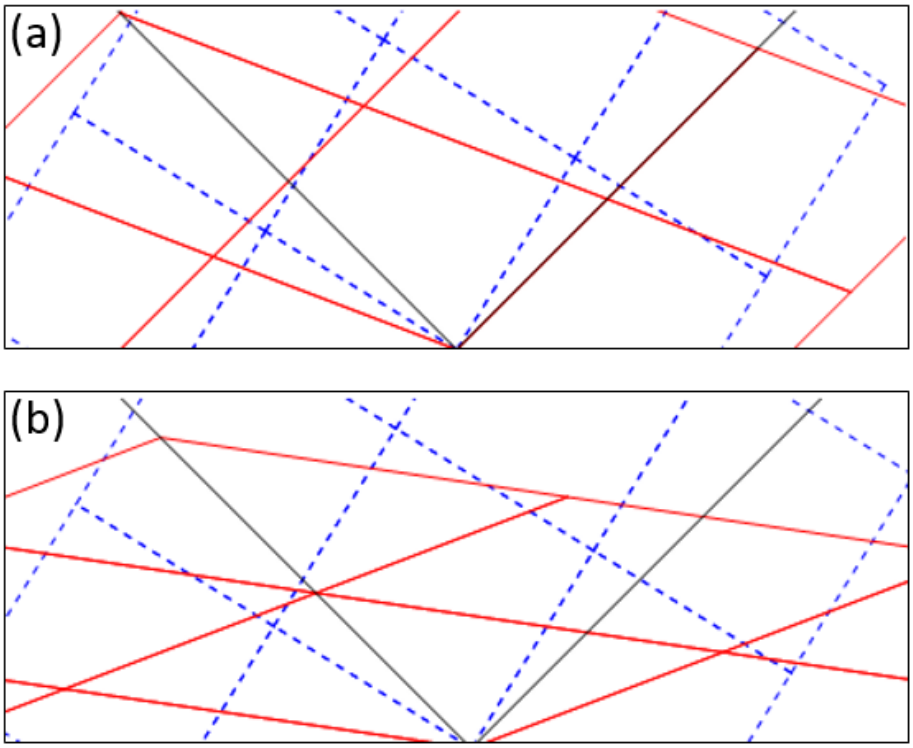

Figure 3.16: Periodic unit cells (red) using the KR boundary conditions at a value of (a) $\epsilon_M = 1/4\epsilon_{KR}$ and (b) $3/4\epsilon_{KR}$. Blue dashed lines indicate the unit cell at $\epsilon_M = 0$ for reference. The lattice has been rotated into the lab frame such that the principal stress vectors are aligned vertically and horizontally. Solid black diagonal lines at 45° therefore indicate the direction of maximal shear stress and are positioned to remap periodically back onto themselves at these values of ϵ_M. Pronounced plastic activity is observed along these lines for strains near these special values.

no other system properties discussed in this chapter demonstrated a dependence on ϵ_M.

Interestingly, it also appears that once finite-size effects emerge the value of the diffusion coefficient at $\epsilon_M = 0$ and $1/2\epsilon_{KR}$ becomes suppressed relative to the FSR value as seen in Fig. 3.15b. It is possible that at these values of ϵ_M an avalanche would misalign such that particles on one side of the slip plane would emerge on the other when crossing the periodic boundary conditions. Therefore, one could imagine the logarithmic average of the diffusion coefficient across ϵ_M for systems that have just reached the onset of finite-size effects would

still be comparable to that of systems fully in the FSR limit. This logarithmic average would only differ once the system fully reaches the QS regime and the peaks stop growing.

Based on this observation, we calculate a logarithmic average of the diffusion constant across all values of ϵ_M, D_{Ave}. This is a measure of the overall diffusion of the system for all strains. In Fig. 3.17a D_{Ave} is plotted as a function of $\dot{\epsilon}$ for the system sizes indicated in the legend. At large rates, D_{Ave} becomes independent of L and decreases with increasing $\dot{\epsilon}$. If the diffusion coefficient scales as the lateral span of the largest avalanche it would imply $D_{\mathrm{Ave}} \sim \xi \sim \dot{\epsilon}^{\nu/\beta}$ in the FSR limit. Direct measurement of this exponent yields a value consistent with $\nu/\beta = 0.42 \pm 0.03$ implying a value of $\beta/\nu = 2.38 \pm 0.07$ consistent with above measurements. Note that the behavior in the FSR limit is insensitive to ϵ_M. This implies that the scaling with $\dot{\epsilon}$ is not influenced by the choice of box geometry.

The power law divergence of D_{Ave} with decreasing rate in Fig. 3.17 is cut off at a strain rate that decreases with increasing L due to finite-size effects. We therefore propose the finite-size scaling ansatz

$$D_{\mathrm{Ave}} \sim L f_D(\dot{\epsilon} L^{-\beta/\nu}) \tag{3.19}$$

where $f_D(x)$ is a universal scaling function containing the expected scaling in the FSR and QS limits. In the limit $x \gg 1$, $f_D(x) \sim x^{\nu/\beta}$, and in the limit $x \ll 1$, $f_D(x)$ approaches a constant. In Fig. 3.17b the data in Fig. 3.17a can be collapsed using a value of β/ν consistent with 2.3 ± 0.1. This is in agreement with measurements of β/ν in previous sections and with the observed scaling of the diffusion coefficient in the QS limit.[94,108] We also tested calculating a linear mean D_{Ave} over different intervals of ϵ_D. While this does not

affect the power-law scaling observed in the FSR limit, the data was generally incapable of being scaled and the QS value of D_{Ave} generally did not scale as L.

The strong variation in diffusion with the alignment of periodic boundary conditions is a novel finding and is not unique to the KR boundary conditions. A similar effect was identified using simple shear and conventional pure shear geometries. In simple shear, a diffusion coefficient could be defined for the non-affine displacement in the gradient direction.[110] When the lattice vectors return to an orthogonal configuration such that avalanches aligned in the gradient direction would overlap with their periodic images, a similar increase in diffusion was noticed in the QS limit. Lastly, using conventional pure shear geometries, excess diffusion was noticed when the ratio of the box lengths reached an integer value such that a 45° line could wrap back onto itself. We note that previous studies of diffusion using conventional pure shear geometries started with an initial square box. Therefore, at strains shortly after yielding it is unlikely that one could identify a strong effect as no such alignment would be reached.[94] Furthermore, the magnitude of the effect increases with system size such that studies of small systems in simple shear may not identify it.[108,110]

In three dimensions, the diffusion displays relatively simple behavior. Previous QS studies failed to dientify a strong dependence on system size.[109] In Fig. 3.18, the diffusion coefficient is plotted as a function of strain rate for systems of size L indicated in the legend. As the strain rate decreases, a small rise in diffusion can be identified before the diffusion saturates for all systems sizes below rates of $\sim 2 \times 10^{-4}$. The plateau has a minor dependence on system size although it appears to reach an asymptotic maximum with increasing L. This suggests there is no divergence in diffusion at the critical point and

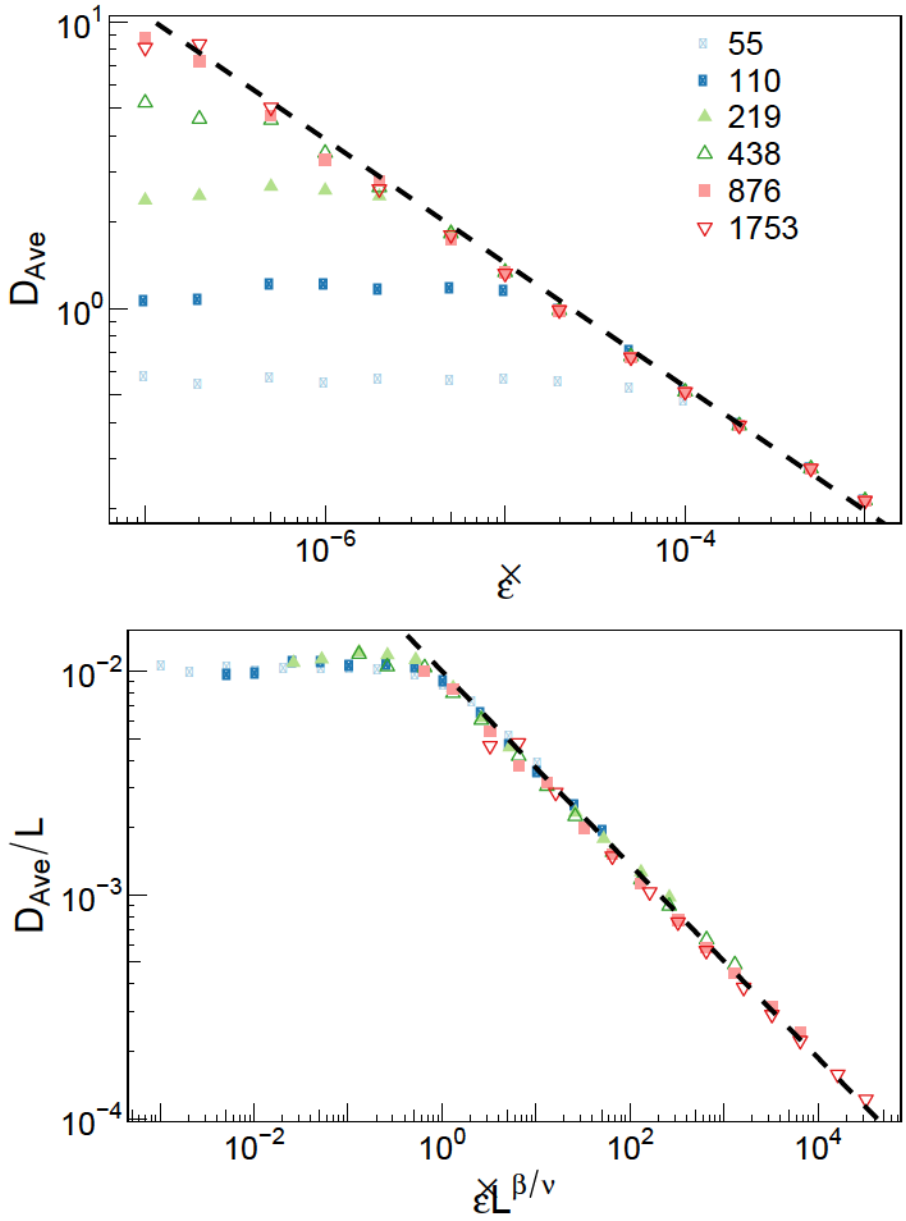

Figure 3.17: (a) The average diffusion coefficient D_{Ave} plotted as a function of rate for the indicated system sizes in 2D. (b) The above data is scaled according to the finite-size scaling procedure in Eq. (3.19) using a value of $\beta/\nu = 2.32$. Dashed lines in both panels represent power-law scaling with $\nu/\beta = 0.43$.

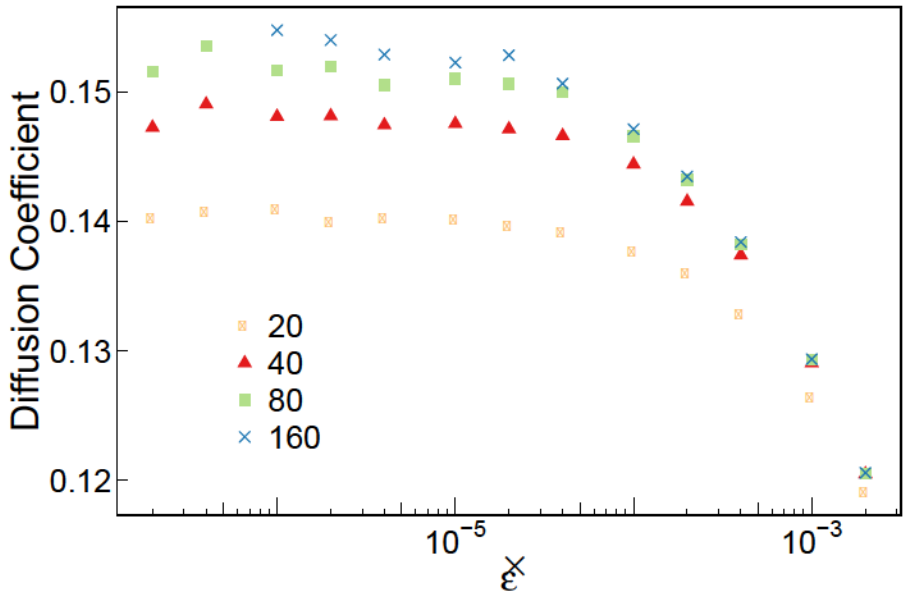

Figure 3.18: Diffusion coefficient as a function of strain rate for the system sizes indicated in the legend in 3D.

no critical exponents associated with its rate dependence. In 3D, avalanches can form slip planes oriented with any azimuthal angle to the compressive direction. It is possible this scrambles any correlations in particles transport.

3.10 Simple Shear Geometry

Simple shear deformation is fundamentally distinct from that of pure shear deformation due to the nature of the periodic boundary conditions. In particular, the direction of maximal shear stress (the flow direction) is always aligned with the periodic boundary conditions. As seen in the previous section, alignment of periodic boundaries can introduce effects on particle transport in the QS limit. Here we look at how such behavior may affect other properties such as the flow stress.

In Fig. 3.19a, the average shear stress from simulations with a simple shear geometry is plotted as a function of rate for 2D systems of size L indicated in the legend. This data was collected using the mixing model at equally large strains as the simulations run with KR boundary conditions. The trends in the data resemble those seen in 3.3a except the onset of finite-size effects is marked by a shoulder in the shear stress. In Fig. 3.19b, this data is scaled according to the procedure in Eq. (3.4) using the above measurements of β and ν as well as a value of $\sigma_c = 1.1645$. Notably, in the FSR limit, measurements of β are found to be consistent with KR results. The bump in shear stress however prevents the data from collapsing onto a single curve during the transition to the QS limit. However, the strain at which the bump in shear stress emerges still plausibly scales as $L^{\beta/\nu}$. This suggests the critical exponents ν and β may not depend on the deformation geometry. However, the origin of this transient deviation in in the shear stress is not known and it is surprising that σ_c is different. No noticeable difference was observed in the scaling of other system properties such as the temporal power spectrum. Future work studying the origin of this deviation and the spike in diffusion would be useful.

3.11 Summary of Yielding

Simulations of 2D and 3D sheared disordered packings of LJ particles were used to identify critical exponents in the yielding transition. This work focused on the effect of finite strain rates in order to identify scaling on the approach to the critical point. Exponents were accurately measured for the first time using finite-size scaling techniques. The measured exponents are summarized in Table 3.1.

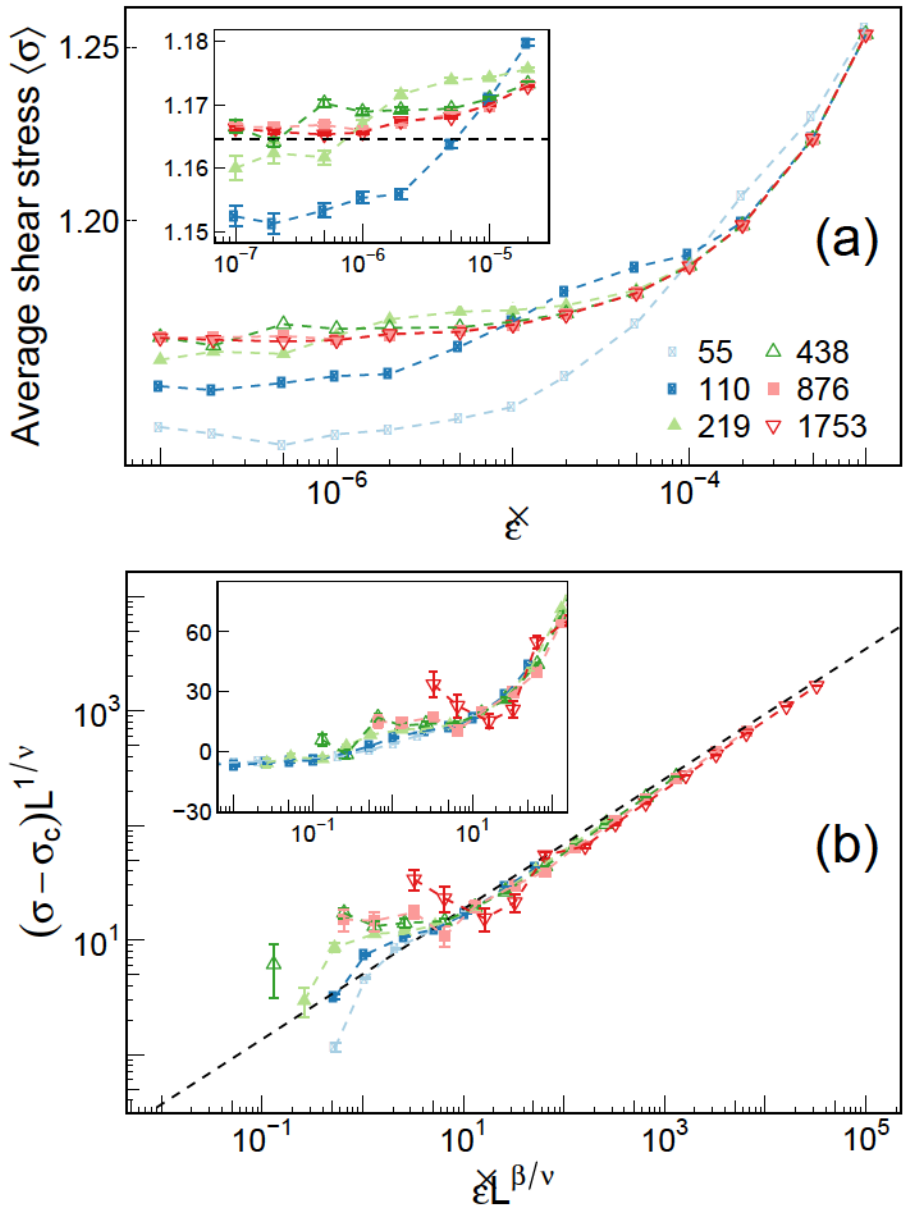

Figure 3.19: (a) The average shear stress as a function of the strain rate for 2D systems of size L indicated in the legend strained using a simple shear geometry. The inset contains an expanded view of low rate data. A dashed horizontal line highlights $\sigma_c = 1.1645$. (b) The above data is approximately scaled according to the finite-size scaling relation in Eq. (3.4) using values of $\beta = 1.76$, $\nu = 0.76$, and $\sigma_c = 1.1645$. The inset in (b) includes an expanded view of the same data using linear-log axes to highlight values of $\langle\sigma\rangle < \sigma_c$.

Values	2D Estimates	3D Estimates	Definition
ν	0.76 ± 0.03	0.50 ± 0.02	$\dot{\epsilon} \sim (\sigma - \sigma_c)^{\beta}$
β	1.76 ± 0.05	1.50 ± 0.05	$\xi \sim (\sigma - \sigma_c)^{-\nu}$
z	1.40 ± 0.05	1.15 ± 0.04	$T_{\text{Avalanche}} \sim \ell^{z}_{\text{Avalanche}}$
ϕ	1.0 ± 0.1	1.5 ± 0.1	$\Delta\sigma \sim L^{\phi}$
δ	0.62 ± 0.05	0.92 ± 0.04	$S(\omega) \sim \omega^{-\delta}$
η	0.7 ± 0.02	0.64 ± 0.02	$S(\omega) \sim \dot{\epsilon}^{\eta}$
x	2.0 ± 0.05	3.0 ± 0.1	$\dot{\epsilon}_{QL} \sim L^{-x}$

Table 3.1: Summary of critical exponents found here for 2D and 3D.

Using the finite-size scaling ansatz in Eq. (3.4), we were able to calculate accurate values of β and ν. This scaling ansatz only depends upon the value of the critical yield stress σ_c in the thermodynamic limit. In this chapter we also proposed the existence of a critical exponent x that determines the emergence of quiescence in the system. This exponent is argued to equal 2ϕ and provides a lower bound for β/ν. In 3D, x may be equal to β/ν.

The measured value of $\beta/\nu = 2.31 \pm 0.05$ in 2D is distinct from a previous report of 2 based on MD simulations.[110] The estimate of 2 was based on finite-size scaling of the diffusion coefficient in systems smaller than our $L = 200$ system. For these small system sizes, one would not be able to detect a deviation of β/ν from 2. Other measurements have been made of β using MD including $\beta = 2$[111] and $\beta = 2.33$[112] in 2D and $\beta = 3$[112] in 3D. These measurements were based on stress data from system sizes up to $\sim 10^4$ particles equivalent to our smallest or second smallest system. These measurements, particularly in 3D, are not consistent with the values measured in this work, however one would expect a very narrow range of critical scaling for these small system sizes. In contrast to the finite-

size scaling ansatz in Eq. (3.4), past work with discrete elasto-plastic models on a lattice used a size dependent $\sigma_c(L)$ in their proposed finite-size scaling ansatz.[40] The values found here for β and ν are also distinct from those measured in the elasto-plastic models.[40]

The scaling of fluctuations in stress is consistent with previous results[39] that demonstrated that $\phi = d/2$. This is further evidence that fluctuations in stress are set by the incoherent addition of $N \sim L^d$ incoherent signals. If the size of fluctuations were determined by the size of the largest avalanche, it would suggest that $\nu = 1/(d-\alpha)$.[39,40] Based on measurements of α from Salerno and Robbins,[38,39] this relation would predict a value of $\nu = 0.91 \pm 0.04$ and 0.53 ± 0.03 in 2D and 3D, respectively. Although it does not appear that $\nu = 1/\phi$, we do note that this scaling relation accurately predicts ν in 3D but not in 2D. It has been argued that when $\phi = d/2$, as seen here, one does not expect to have an equality between ν and $1/\phi$.[113]

In studies of lattice-based models with instantaneous information propagation, it was found that $z < 1$.[40] As physical restrictions of information transport require $z \geq 1$, it was therefore suggested that $z = 1$.[114] Measurements of the dynamical exponent here in fact show $z > 1$ in both 2D and 3D. Lin and Wyart have also proposed the dynamical exponent can been related to the Herchel-Bulkley exponent using a scaling relation $\beta = \nu(1 - \alpha + z)$.[40,114] Our estimates of z combined with previous estimates of α[38,39] predict values of $\beta = 1.9$ in 2D and 1.5 in 3D using this relation. While the 3D prediction agrees with our measured β, the 2D results disagree.

Finally, we also propose a scaling theory for the temporal power spectrum as a func-

tion of strain rate in the FSR limit. A scaling relation describing the QS limit in cases where the avalanche distribution exponent $\tau < 2$ has previously been proposed by Kuntz and Sethna.[10] This theory assumes that the typical avalanche profile contains many high frequency flutuations which they argue implies $q = 1$. As seen in Sec. 3.7, this suggests $\delta = 0.64 \pm 0.04$ in 2D and 0.96 ± 0.09 in 3D consistent with the directly measured values of δ in Table 3.1. One important difference with the work in this paper is that they considered a model related to interface growth where the rate of avalanches is extensive in system size. In yielding the rate of avalanches scales as L^γ with $\gamma < d$.

This work has provided accurate measurement of many exponents of the yielding transition in the overdamped limit for the first time. Earlier work in the quasistatic limit showed that the addition of inertia changes the nature of the critical point.[38,39] It would be valuable for future work to measure dynamic exponents in the underdamped and critically damped limits to determine how inertia affects the FSR regime. In addition, the work here has focused exclusively on the steady state. Recent work in MD has identified the presence of a second order critical point in the transition between ductile to brittle yielding in glasses as the quench rate of the glass is decreased.[115] Further studies of the transition to steady state as a function of strain rate and system preparation could prove valuable.

Chapter 4

Brittle Fracture

4.1 Introduction to Brittle Fracture

Brittle materials such as cement, rock, glass, and ceramics, fail rapidly with minimal prior plasticity. This abrupt failure therefore gives little to no forewarning. Due to the ubiquity of brittle materials in construction, it is no surprise that characterizing brittle crack growth has been a major focus of research for many decades. Improved theories of brittle fracture are also important to design better ballistic armor[116,117] and understand the mechanics of tectonic motion.[118]

Many brittle materials are isotropic at the scale of crack propagation. Glass is atomistically disordered and many ceramics or rocks are polycrystalline. On long enough length scales, the random orientation of polycrystalline domains averages to produce an isotropic response. The direction of crack growth in such isotropic materials is determined by the

spatial location of defects, flaws, and other cracks as well as the local stress field. Therefore in order to accurately simulate the microscopic details of brittle fracture, one needs a model that includes elastic interactions between regions of damage and is able to model strong nonlinearities at crack tips.[119] The fracture of brittle materials also involves many dynamic processes such as crack nucleation, growth, and coalescence that may need to be modeled for a large population of cracks.[120]

Particle-based models are an ideal simulation technique for brittle fracture as they naturally allow for material discontinuities.[121] In this chapter, we design a particle-based model and use it to study a wide range of phenomena in brittle fracture. These simulations allow us to fully resolve microscopic dynamics in failure and track the evolution of individual cracks as they merge to form fragments that are further broken during granular flow. The results in this chapter are focused on bridging length scales and providing the information needed for the construction of macroscopic continuum models.

In Sec. 4.2 we will describe the model, including the preparation of initial conditions, the functional form of interactions, and the numerical algorithms used. Following this, Sec. 4.3 describes the calibration of the parameters of the model to match the elastic response and fracture toughness of the target ceramic materials. Having laid out the model, we first focus on the initial fracture of brittle solids in Sec. 4.4. The dependence of failure on defect density and strain rate is found to agree with theories of wing crack growth in defected systems.[122] We will also discuss other findings, including a reduction in the elastic modulus due to damage. In Sec. 4.5 we look at the subsequent granular flow regime where confinement causes particle breakup, or comminution. In the quasistatic limit, we identify

a power-law distribution of grain sizes. The evolution of this distribution with strain is non-trivial and counters assumptions made in continuum models of breakage.[123,124] At finite strain rates, we find the size of the largest grain is limited, suggesting critical behavior emerges only in the quasistatic limit. We also measure the internal friction coefficient as a function of rate and material properties and show that changing Poisson's ratio affects the anisotropy of grains. Finally in Sec. 4.6 we will pull together results and discuss future directions of research.

4.2 Model

Discrete element models (DEMs) are a very popular technique for modelling brittle fracture. DEMs discretize a solid into a collection of particles each representing a fundamental region of matter with size much larger than atoms. These particles exert forces on each other using a variety of interactions including attractive bonds between regions of unbroken material. These bonds can break under specified conditions allowing for the nucleation and propagation of cracks.[121,125]

There also exist many continuum models that are able to resolve dynamic crack growth. These may require regular remeshing or may use meshless techniques,[126,127] but are generally not well suited to problems that involve the nucleation, growth, and coalescence of many cracks.[126] These models also require physically accurate constitutive equations to produce realistic dynamics. Despite these difficulties, sophisticated and accurate continuum methods have been used to study brittle fracture processes.[128]

In order to model brittle materials we use a combination of ideas from molecular dyanmics (MD) and DEMs. Our model is expanded from initial tests by Maloney and Robbins that used breakable bonds in MD simulations to study brittle shear bands.[129] The model is implemented using a powerful software package, the Large Scale Atomic/Molecular Massively Parallel Simulator (LAMMPS).[98] LAMMPS was chosen as it is open-sourced, easily modifiable, has a large userbase, supports MPI parallelization using spatial domain decomposition, and contains a large suite of numerical methods.

In order to simulate granular flows consisting of many decades of grain sizes, we require a computationally cheap model that can be scaled to large system sizes. The model was therefore designed to use a simplified representation of particles and minimalistic interactions. Removing nonessential degrees of freedom from a particle simplifies the numerical integration of the equations of motion. Minimizing the number of free parameters streamlines the process of calibrating material properties and reduces the computational cost of calculating forces. The model was also designed to include realistic defect distributions from experimental data. To ensure that these extrinsic defects dominate nucleation of cracks, it was important to minimize other sources of heterogeneity. In particular, the model ensures a homogeneous elastic response with little non-affine motion at low strains. Tests were made to ensure the model accurately produces results from experiments. For instance, a goal is to recreate emergent behavior such as wing crack growth.[130]

In the following subsections we describe the preparation, implementation, and parameterization of the model. In Subsec. 4.2.1 we describe the fundamental particles of the model and the preparation of the initial system. This includes preparing the initial population

of particles as well as building the topological network of interactions. In Subsec. 4.2.2 we then describe the specifics of the interactions used in the model. This includes details on how the interactions support fracture and how damping is incorporated in the system. Finally in Subsec. 4.2.3 we describe the numerical protocols used in simulations.

4.2.1 System Preparation

Systems are constructed out of collections of point particles. Each point particle represents some locally coarse-grained region of space. Some simulations use a 2D geometry that could be calibrated to model plane-strain deformations, while others are fully 3D. Each particle has d translational degrees of freedom where d is the dimension of the system. The rotational degrees of freedom of each particle are not resolved. This choice greatly reduces the complexity of the model. Note that a cluster of these point particles will still have rotational degrees of freedom that emerge from the translation of each particle. This is in contrast to most DEMs that use rotational spheres,[125,131–134] clusters of rotational spheres,[133] or polygons as the fundamental discrete element.[135,136] To date we have not identified any shortcomings due to removing rotational degrees of freedom.

In two dimensions, a bidisperse mixture of particles of type A and B was used to introduce geometric frustration and prevent crystallization.[96] Particles of type A have a radius of a and particles of type B have a radius of $3/5a$ where a is the fundamental unit of length.[93] A constant ratio of the number of particles of each species was used: $N_A/N_B = (1+\sqrt{5})/4$. This is the same choice made in Chapter 3. In three dimensions, monodisperse particles were used with a radius defined as a. As long as the system box

measured at least $10a$ in each dimension, no evidence of crystallization was identified. All particles were assigned a mass of m.

Our primary interest is studying isotropic, brittle fracture. This could represent glasses or polycrystalline materials on length scales larger than that of crystalline grains. We therefore initialize the system by preparing random packings of particles. Although a regular lattice of discrete elements can produce an isotropic elastic response on large length scales,[137,138] the lattice directions are expected to bias the direction of crack growth. Indeed, molecular dynamics studies of 2D hexagonal lattices of particles with breakable bonds found that the trajectory of cracks was highly anisotropic since bond breakage followed the lattice vectors.[139–141] In contrast, crack growth in a random packing of spheres does not have this anisotropy.[132]

The initial random packings of particles were prepared using a method similar to that used in prior papers[93,94] and described in Chap. 3. Particles were randomly placed in a box with periodic boundary conditions using a number density of $1.35a^{-2}$ in 2D and $0.86a^{-3}$ in 3D. A cosine potential and viscous damping term were used to rapidly push particles off of their neighbors. The potential was then swapped for an attractive Lennard-Jones (LJ) interaction and the system was melted and then rapidly quenched. An attractive interaction was chosen as it helped to space particles evenly around their neighbors. Examples of particle packings are shown in Fig. 4.1.

After producing the initial packing of particles, a Delaunay triangulation[142] was used to construct a network of neighboring particles. Each vertex coincides with a particle and

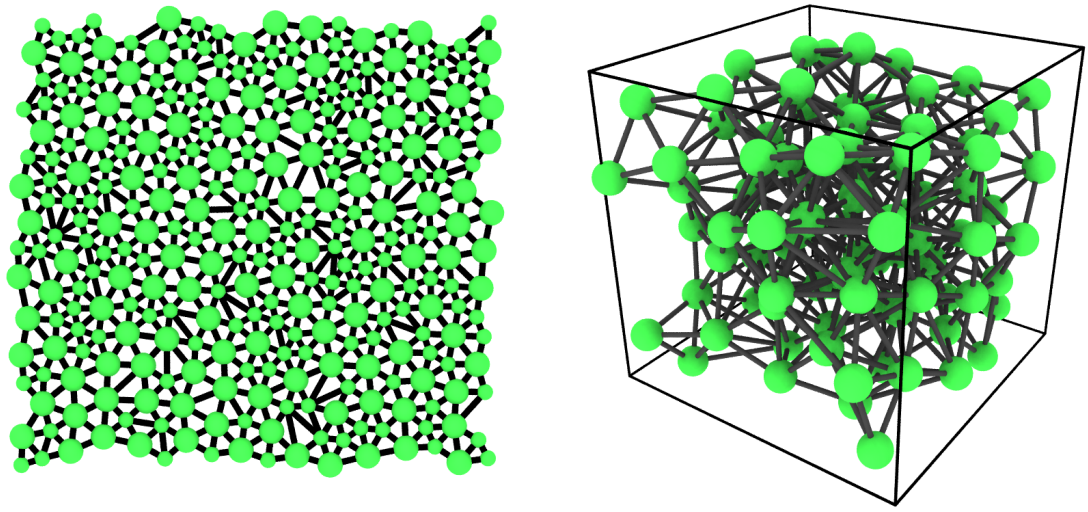

Figure 4.1: Small subsets of initial random packings of particles and their bond topology in 2D (left) and 3D (right). Note the presence of two distinct particle sizes in two dimensions.

each edge in the graph corresponds to a bond between two particles. In 2D, one bond angle was defined for every vertex in a given triangle. In 3D, three angles were defined for every vertex of a tetrahedron, one for each triangular face intersecting at the vertex. A Delaunay triangulation was chosen as it is easily reproducible and guarantees every particle is the vertex of at least one triangle or tetrahedron and has at least two bonds in 2D or three bonds in 3D. This ensures that there are no rattlers in the system - particles with unconstrained degrees of freedom.[143] Other methods of producing this network were tested and no significant changes were identified in the results. However, each method requires an independent parameterization of material properties as described in the next section.

The Delaunay triangulation resulted in an average of 6 or ∼14.2 bonds and 6 or ∼36.9 angles per particle in 2D or 3D, respectively. In order to reduce the amount of information communicated between subdomains of the spatial decomposition, a maximum bond length

of $5/4 \times 2^{1/6}a$ was defined in 3D. Any bond longer than this threshold was then pruned. Correspondingly, any angle defined using this bond was also removed. We found that this length restriction produced no new rattlers and had a minimal effect on results. However, removing these bonds reduced the interprocessor communication load by a factor of two. The number of bonds per atom decreased to ∼11.0 and the number of angles per atom to ∼24.4. Therefore, this restriction had the additional benefit of speeding up simulations by approximately 33%. Presumably stricter thresholds could be set to further accelerate simulations.

4.2.2 Interactions

Particles interact with three distinct types of interactions. The first is a repulsive central-body force between non-bonded particles. These interactions represent forces between separate solid grains. Within a connected grain, bonded particles interact with an attractive central-body force as well as a three-body angular interaction. In this section, we describe these three interactions: U_{NB}, U_B, and U_A where NB, B, and A stand for non-bonded, bonded, and angular. At the end we will discuss damping between particles.

The non-bonded potential is a function of the pairwise distance between two particles as well as, in 2D, the particle types. We model this interaction using a purely repulsive LJ potential:

$$U_{NB}(r) = \begin{cases} 4u\left(\left(\frac{a_{NB}}{r}\right)^{12} - \left(\frac{a_{NB}}{r}\right)^{6}\right) + u_B, & r < r_c = 2^{1/6}a_{NB} \\ 0, & r \geq r_c = 2^{1/6}a_{NB} \end{cases} \tag{4.1}$$

where u and a_{NB} are the energy and length scales of the interaction. The constant u is defined as the fundamental energy scale. If there are multiple types of materials in the system, there is a distinct value of u for each material, and the largest is chosen as the fundamental energy unit. We set a_{NB} as the arithmetic mean of the radii of the two types of interacting particles. In 3D, this implies $a_{NB} = a$, the fundamental unit of length in the system. One could imagine scaling a_{NB} by a constant factor to reduce the volume of a broken system. This could originate from fracturing a porous solid. Currently, if the entire initial bond network was removed such that all particles only interact with the repulsive U_{NB}, the system would be at a positive pressure due to the preparation of the initial system. This hypothetical pressure depends on the initial particle density and quench rate. We have not investigated how changing a_{NB} would affect results.

The second interaction is the pairwise force between bonded particles. This interaction is a function of both the current and initial distances between the two particles. Therefore, this potential depends on the reference state of the material. This construction contrasts with commonly used potentials in MD simulations which only depend on the current distance. We construct U_B piecewise out of a repulsive and attractive component:

$$U_B(r, r_0) = \begin{cases} U_{B,R}(r, r_0), & r < r_0 \\ U_{B,A}(r, r_0), & r \geq r_0 \end{cases} \tag{4.2}$$

where r_0 is the initial separation in the undeformed solid. We want the original reference state to be free of residual forces or stresses and therefore require $U_{B,R}(r_0, r_0) = U_{B,A}(r_0, r_0) = 0$.

For the repulsive force, we again use a cut and shifted LJ interaction as in Eq. (4.1). Here we set the length scale a_B equal to $2^{-1/6}r_0$ such that the potential is at its minimum at r_0. The energy scale u_B is set equal to ua_B^2. We choose to scale the energy by a_B^2 such that all bonds have an equal stiffness $k_{LJ} = 36 \times 2^{2/3}u/a^2$. Early tests indicated that homogenizing the stiffness helped minimize non-affine deviations from the elastic response of a solid under loading. We also shift the repulsive LJ potential by a constant $u_B + U_{A,R}(r_0, r_0)$ such that the energy is continuous at r_0.

For the attractive force, we choose to use a polynomial function:

$$U_{B,A}(r, r_0) = \begin{cases} C_0 + C_2(r - r_0)^2 + C_4(r - r_0)^4, & r < \lambda_c r_0 \\ 0, & r \geq \lambda_c r_0 \end{cases} \tag{4.3}$$

where λ_c is a new free parameter and C_0, C_2, and C_4 are four coefficients. Here λ_c represents a critical stretch for each bond. Once a bond stretches past this threshold it is irreparably broken and any further interactions between the two particles revert to U_{NB}. This allows for the model to support fracture.

The coefficients C_i are chosen to meet several conditions and depend on both r_0 and λ_c. The second coefficient, C_2, is chosen to be equal to $k_{LJ}/2$ where k_{LJ} is the stiffness of the LJ potential. This ensures the elastic response of the bonded potential is equivalent in compression and in stretch. The other two coefficients, C_0 and C_4 are chosen such that $U_{B,A}$ smoothly interpolates to zero with no discontinuities in the derivative at $r = \lambda_c r_0$.

Based on these conditions the values of these coefficients are:

$$C_0 = -9 \times 2^{2/3}(\lambda_c - 1)^2 u r_0^2 \tag{4.4}$$

$$C_2 = 18 \times 2^{2/3} u \tag{4.5}$$

$$C_4 = -9 \times 2^{2/3}(\lambda_c - 1)^{-2} u r_0^{-2} \tag{4.6}$$

One could consider adding a third order term to Eq. (4.3) which would allow one to control the energy of each bond or the critical force at which a bond breaks. This could be useful for fitting additional fracture properties of the material but we did not find it necessary.

Finally, we define the angular interaction U_A. The angular interaction will be a function of the initial angle θ_0, the current angle θ, and the current stretch of the two bonds that form the angle, λ_1 and λ_2. The potential is decomposed into the product of two functions:

$$U_A(\theta, \theta_0, \lambda_1, \lambda_2) = U_{A,\theta}(\theta, \theta_0) F_{A,\lambda}(\lambda_1, \lambda_2) \tag{4.7}$$

First we will discuss the angular component and then focus on the stretch component.

The angular interaction is also constructed piecewise:

$$U_{A,\theta}(\theta, \theta_0) = \begin{cases} D_0 + \frac{k_A}{2}(\theta - \theta_0)^2 + D_4(\theta - \theta_0)^4, & \theta < \theta_c \\ 0, & \theta \geq \theta_c \end{cases} \tag{4.8}$$

where k_A and θ_c are two new free parameters and D_0 and D_4 are constants. Here k_A is the stiffness of the angular interaction and θ_c represents a critical angle. If the deviation in the

angle from the initial angle exceeds θ_c the angular interaction will permanently break. The coefficients are chosen such that $U_{A,\theta}$ smoothly approaches zero at $\theta = \theta_c$ implying:

$$D_0 = -\frac{1}{4} k_A \theta_c^2 \tag{4.9}$$

$$D_4 = -\frac{1}{4} k_A \theta_c^{-2} \tag{4.10}$$

The other component of the angular interaction depends on the stretch of each bond. If one of the bonds associated with the angle breaks the angle will break as well. To avoid discontinuities in angular forces when bonds break, the angular interaction is multiplied by a smoothing function. This function is a function of the maximum stretch of the two bonds: $\lambda_{\max} = \max(\lambda_1, \lambda_2)$:

$$F_{A,\lambda}(\lambda_{\max}) = \begin{cases} 1, & \lambda_{\max} \leq 1 \\ 1 + S_2 \lambda_{\max}^2 + S_4 \lambda_{\max}^4, & 1 < \lambda_{\max} < \lambda_c \\ 0, & \lambda_{\max} \geq \lambda_c \end{cases} \tag{4.11}$$

where S_2 and S_4 are two new coefficients. The coefficients are chosen such that $F_{A,\lambda}$ and its derivative are zero at $\lambda_{\max} = \lambda_c$:

$$S_2 = -2(\lambda_c - 1)^{-2} \tag{4.12}$$

$$S_4 = (\lambda_c - 1)^{-4} \tag{4.13}$$

In the limit of large θ_c, the interaction can be approximated as a torque spring which only

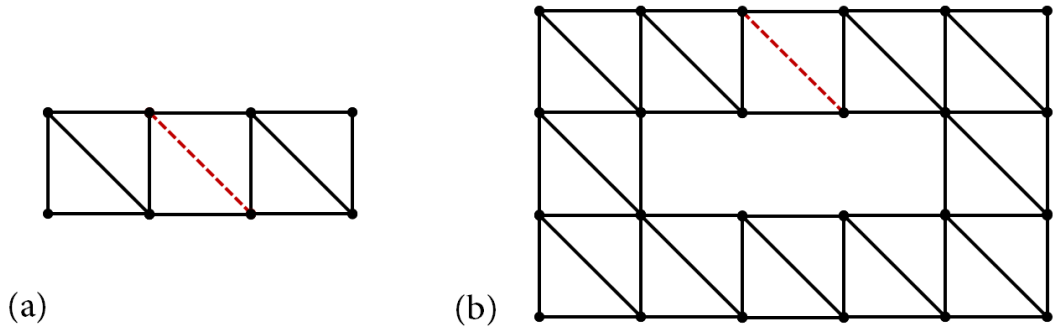

Figure 4.2: Two hypothetical bonded networks are shown in (a) and (b). The network in (a) will produce a floppy mode if the red dashed bond is deleted. The network in (b) would remain rigid if the same bond were to be deleted. This distinction cannot be made without traversing the entire ntework.

breaks when bonds break.

In d dimensions, a cluster of N particles will be rigid as long as $dN - d(d+1)/2 = N_c - N_{ss}$ where $d(d+1)/2$ is the number of rigid rotations and translations, N_c is the number of constraints (interactions), and N_{ss} is the number of states of self stress.[144,145] If this equation is not met, the cluster will contain at least one zero mode, an internal degree of freedom that costs no energy to move. Rigid, brittle materials of course do not have any zero modes. If one wanted to prevent the introduction of any free floppy modes in the system, one could possibly use two rules. First one could prevent a bond or angle from breaking if it introduced a floppy mode. This could be difficult to implement as one cannot generally determine whether a floppy mode is introduced without using expensive algorithms that scale as $\mathcal{O}(N)$ where N is the number of particles.[146] For instance, in Fig. 4.2 the removal of the dashed red line may or may not produce a floppy mode and one cannot tell without traversing the entire network.

Alternatively, one could imagine a second rule that may be unnecessarily strict but would ensure no floppy modes were introduced. For instance, one could require every bond have at least one angle in 2D and two angles in 3D. This ensures all bond connections are rigid. A model including this feature was tested but proved to be too computationally complex. Each bond needs to know the current number of associated atoms. This is an expensive procedure due to the data structures used in LAMMPS. In addition, one would also need to interpolate the bond potential to zero as angular interactions break, further increasing the computational cost. We find floppy modes are generally only prominent on small length scales, typically representing one or two dangling bonds. Therefore they are expected to have a minimal effect on macroscopic behavior and they were not eliminated from the system.

In a real solid, energy released in fracture will flow to degrees of freedom on smaller length scales. Therefore, there are usually no thermal effects in fracture or granular flow of brittle material. However, in our DEM there is a minimum length scale, and a constant influx of energy will cause a steady rise in temperature which can lead to melting. To prevent heating, we apply a damping force on all neighboring particles. Neighboring particles are defined as particles which interact either through bonds or non-bonded forces. We use a form of damping commonly used in dissipative particle dynamics (DPD):[147]

$$\vec{F}_D(\vec{r}, \delta\vec{v}) = -\gamma \left(1 - \frac{r}{r_{\max}}\right)^2 (\hat{r} \cdot \delta\vec{v}) \tag{4.14}$$

Here $\vec{r}$ is the vector between the two particles, $\delta\vec{v}$ is the difference in velocities, $r_{\max}$ is

the maximum distance of the interaction (r_c for nonbonded particles and $r_0\lambda_c$ for bonded particles), and γ is a free parameter. This force damps relative differences in velocity and is also known as Kelvin damping. It is Galilean invariant and is therefore the lowest order term that one would expect to emerge in an isotropic solid.[148] We find the specific value of γ has no apparent affect on material properties and only controls the rate at which energy is dissipated. In simulations that model single crack growth and do not release significant amounts of energy we set $\gamma = 0$. In simulations that are run to large strains we find $\gamma = 50$ dissipates energy sufficiently rapidly to prevent the emergence of thermal effects over the range of strain rates considered.

4.2.3 Simulation Protocol

One can define the fundamental time scale τ of the system using the fundamental length a, mass m, and energy u: $\tau = \sqrt{ma^2/u}$. As mentioned above, in instances where multiple materials are simulated, u represents the largest interaction energy and thus sets the smallest timescale. Particle dynamics are numerically integrated using a velocity-Verlet solver using a timestep of either 0.01 or 0.005τ.

Deformation is applied to a solid by expanding or compressing the periodic boundary conditions and moving particles affinely at constant strain rates unless otherwise mentioned. In periodic systems, a variety of lattice vectors were chosen including orthonormal lattice vectors as well as the KR and generalized KR boundary conditions discussed in Chap. 3.

4.3 Parameterization

The formulation of interactions in the last section contains three free parameters: k_A, λ_c, and θ_c for simulations of a single type of material. These three parameters all have measurable effects on simulation results. In this section we discuss how the model is calibrated to match real material properties.

4.3.1 Elastic Response

In order to calculate the bulk modulus of a system, we generate a square or cubic sample with a side length of $800a$ in 2D or $100a$ in 3D. Hydrostatic compression is applied up to a volumetric strain of 0.5% at a constant rate. A least mean-squared error (LMSE) linear regression was used to fit the pressure as a function of strain and estimate the bulk modulus. In Fig. 4.3 the bulk modulus is plotted as a function of the angular stiffness k_A in (a) 2D and (b) 3D. As the angular stiffness increases, we see the bulk modulus slightly increases. Adding in stronger interactions would be expected to increase the stiffness of the system. However, the effect is less than ten percent. We therefore roughly approximated B as a constant, $52u/a^2$ in 2D and $39u/a^3$ in 3D. This approximation implies that the energy scale essentially sets the bulk modulus of the system. The elastic response of the material does not depend on fracture properties of the model and therefore λ_c and θ_c have no impact on the bulk modulus.

In order to fully parameterize the elastic response, we need to be able to independently adjust the shear modulus relative to the bulk modulus. As seen above, the angular stiffness has a negligible affect on the bulk modulus of the system. However, one would anticipate

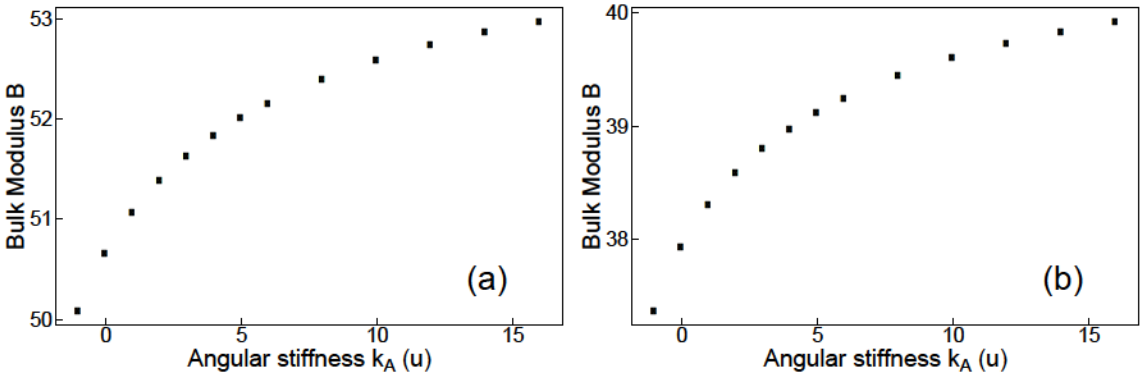

Figure 4.3: The bulk modulus versus angular stiffness k_A in (a) 2D and (b) 3D.

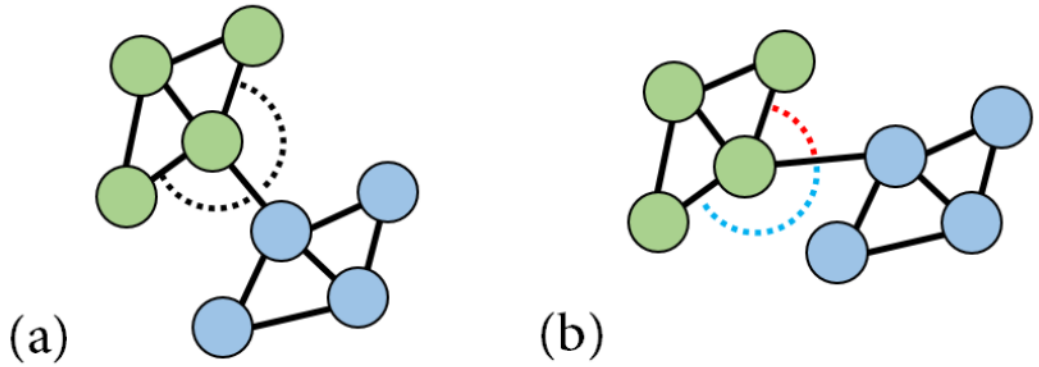

Figure 4.4: (a) A hypothetical set of bonded particles containing two angular interactions (dashed lines). (b) The same configuration after applying a theoretical diagonal shear leading to compression of the red angular interaction and extension of the blue angular interaction.

it would have a substantial impact on the shear modulus. This is motivated by the hypothetical configuration of bonded particles in Fig. 4.4a. One can apply a diagonal shear without elongating the central bond that connects the green and blue sets of particles. Thus the strength of the bonded interaction u would have no impact on the resistance to shear. However, the two angular interactions indicated by the dashed arcs would resist such a shear mode as seen in Fig. 4.4b.

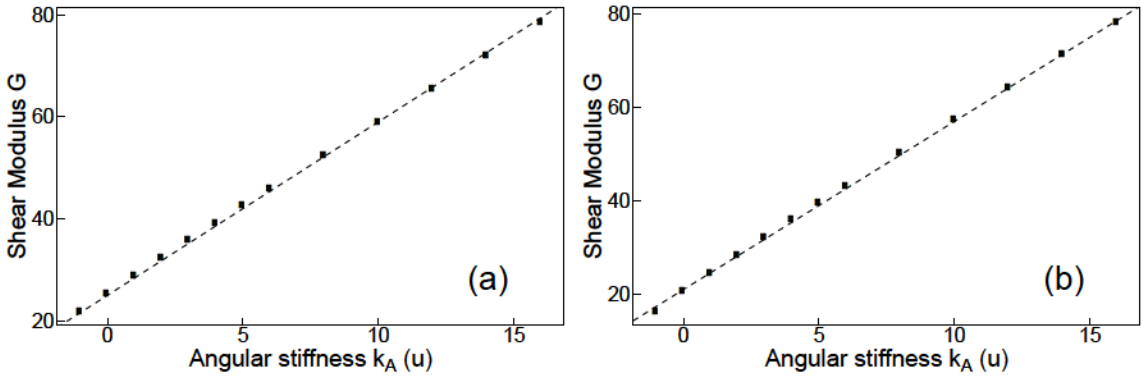

Figure 4.5: The shear modulus versus angular stiffness k_A in 2D (a) and 3D (b). Dashed lines have slopes of 3.4 and 3.6 and intercepts of 25 and 21 in (a) and (b) respectively.

In order to calibrate the shear modulus in the model, systems were prepared with dimensions of $800 \times 800a$ in 2D and $200 \times 200 \times 12$ in 3D. Systems were then strained under simple shear to a strain of 0.5% at a constant rate. As before, the shear modulus was calculated using a LMSE fit to the resulting shear stress. In Fig. 4.5 the fitted shear modulus is plotted as a function of angular stiffness. In contrast to the results for the bulk modulus, the shear modulus increases roughly linearly with increasing angular stiffness.

In Fig. 4.6, we calculate Poisson's ratio, $\nu = (B-G)/(B+G)$ in 2D and $(3B-2G)/(6B+2G)$ in 3D, as a function of angular stiffness. Poisson's ratio decreases with increasing angular stiffness due to the increase in the shear modulus. This data demonstrates the ability to model the elastic response of a wide range of materials. Increasing k_A can even model auxetic materials ($\nu < 0$). Note that the measured Poisson's ratio at $k_A = 0$, 0.268 in 2D and 0.329 in 3D, is very close the theoretical result for a random packing of smooth spheres with central body forces, 1/4 in 2D and 1/3 in 3D.[149]

Several other DEMs have been calibrated to model a large range of elastic responses.

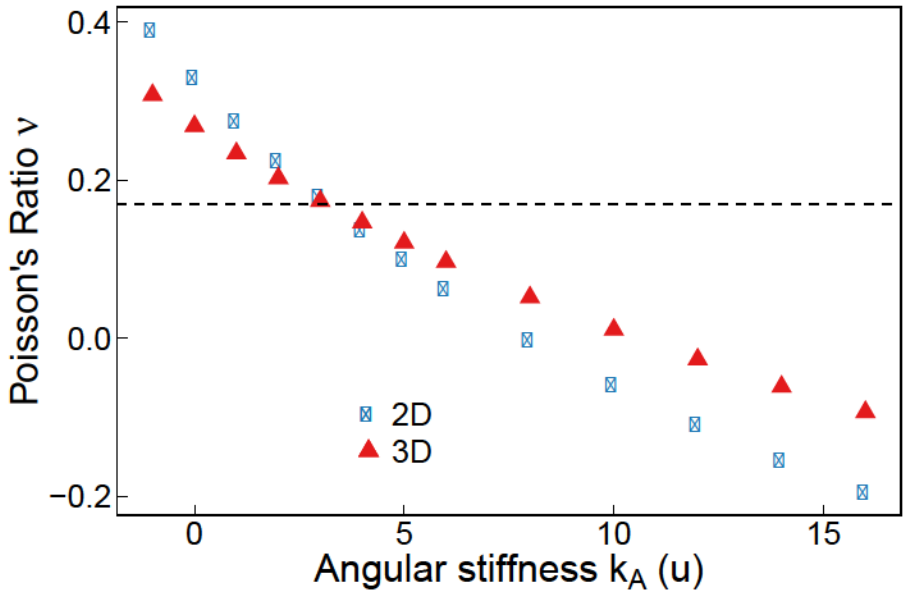

Figure 4.6: Poisson's ratio versus angular stiffness k_A in 2D (blue circles) and 3D (red triangles). A horizonal dashed line highlights a Poisson's ratio of 0.17, the approximate value of boron carbide.[150]

Some of these models use regular lattices of discrete elements[137,138] and others use random packings of spheres.[134,136] These models all control the elastic reponse by using bonds that transmit both radial and transverse forces. This requires either resolving the rotational degrees of freedom or modelling irregular polygons. Other DEMs that do not model such transverse forces have been restricted to fixed Poisson's ratios.[131] The use of point particles with three body interactions in this work is a novel method of controlling the elastic response.

4.3.2 Fracture Toughness

Having fit the elastic response of the model, we next turn our attention to measuring fracture properties of the model. Often DEMs calibrate the compressive or tensile strength

of a simulated solid[134,151] which is distinct from the toughness.[152] The strength of a material depends heavily on preexisting distributions of defects or cracks. Microscopic defects have been experimentally observed to dominate failure of brittle materials and greatly affect the measured strength.[116,153,154] Defects provide nucleation sites for crack growth, greatly reducing energy barriers for fracture. One goal is to model individual defects in a homogeneous matrix of material. Therefore, the ideal calibration of strength should be independent of defect distributions. In experimental tests of fracture toughness, an initial crack is typically provided to diminish the dependence on other preexisting cracks or defects. In this section, we calibrate the mode I and mode II fracture toughnesses, K_{IC} and K_{IIC}, respectively. Mode I crack growth is due to tensile opening and mode II crack growth is due to simple shear.

In order to measure the mode I fracture toughness, we prepare a sample with a preexisting crack. In 2D, an elliptical crack was created with the major axis aligned perpendicular to the direction of loading in a square sample with side length $800a$. The ellipse had a minor axis of $2a$ and a major axis of $20a$. The crack was created by removing all particles that lay within the region and their associated bonds and angles. Any other bonds that crossed the minor axis and their associated angles were also removed. All bonds that spanned periodic boundary conditions were broken to produce free boundary conditions. In 3D, a similar quasi-2D, plane-strain configuration was used. An elliptical crack with major and minor axes of $20a$ and $2a$ was placed in a square of side length $200a$ with free boundary conditions. The crack was extended through the third dimension of length $12a$ with periodic boundary conditions. The geometry of the 3D system is seen in Fig. 4.7. After preparing the sample,

all particles within a distance of $3a$ from the boundary perpendicular to the major axis of the crack were displaced at a constant speed to produce tension. Systems were strained until the initiation of crack growth and failure of the sample.

From the peak tensile stress σ_f, we calculated the approximate fracture toughness given the width of the square box L and length of the initial crack L_C:[155]

$$K_{IC} = \sigma_f \sqrt{\pi L_C/2} \left[1 - 0.025(L_C/L)^2 + 0.06(L_C/L)^4\right] \sqrt{\sec \frac{\pi L_C}{2L}} \tag{4.15}$$

This calculation assumes an infinitely thin crack. Tests varying crack width, box height, and system size found results varied only $\sim$10% which we take as the uncertainty due to finite size. Larger simulations can be run if there is a need for more precision. The resulting fracture toughness as a function of critical stretch λ_c is plotted in Fig. 4.8 in (a) 2D and (b) 3D for the values of the angular stiffness indicated in the legend. In both cases, the fracture toughness is seen to rise roughly linearly with λ_c. This is reasonable as λ_c is approximately proportional to the failure strain. In addition, the slope of the relation is seen to rise with increasing angular stiffness or decreasing Poisson's ratio. This is primarily due to changes in Young's modulus. Finally, there is a dependence on θ_c that is not shown. At large values of λ_c, there exists a measurable dependence on θ_c. If θ_c is small, angles begin to break before bonds break, reducing the fracture toughness. However, this dependence is small, at most 10%, and is therefore ignored.

In Fig. 4.9, the distance between a broken bond and the initial crack tip is plotted as a function of the time at which the bond broke in (a) 2D and (b) 3D for different values of

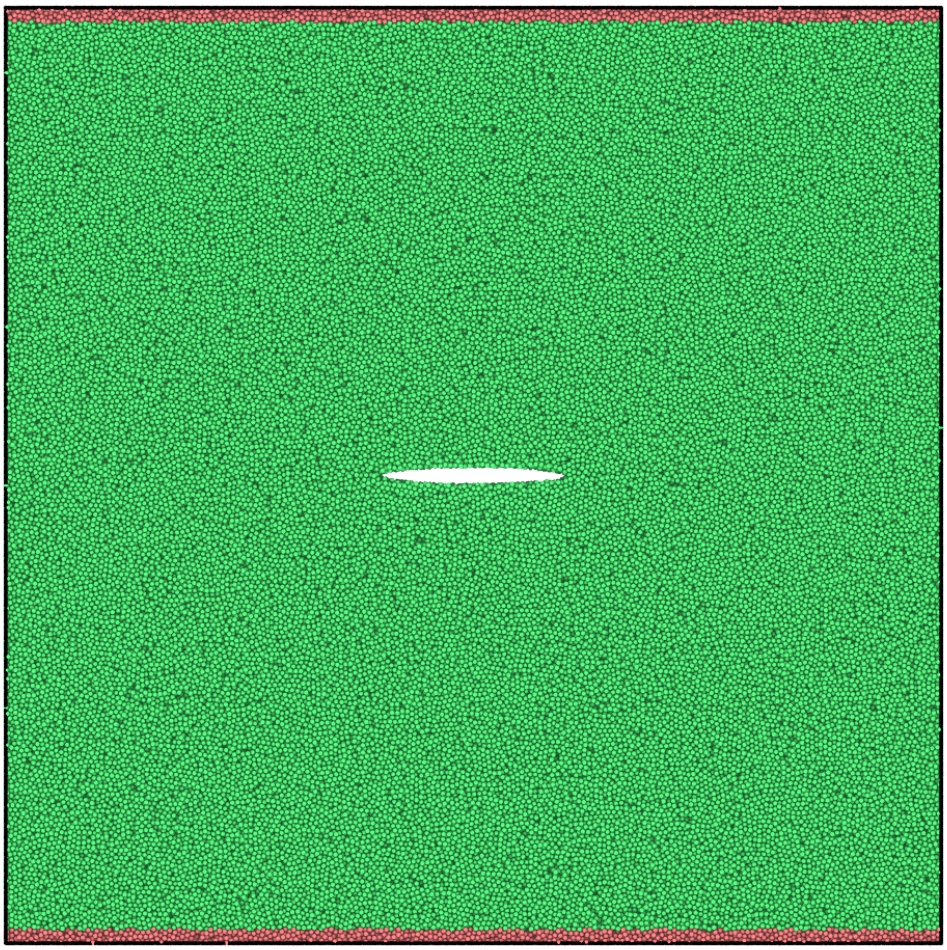

Figure 4.7: Rendered image of crack geometry used for mode I fracture calibration in 3D looking into the periodic dimension along the crack. The black border indicates the initial extent of the free boundary. The box has a side length of $800a$ and the elliptical crack has a major axis of $20a$ and a minor axis of $2a$. A tensile displacement was applied on the red particles located within a distance of $3a$ from the top and bottom of the box.

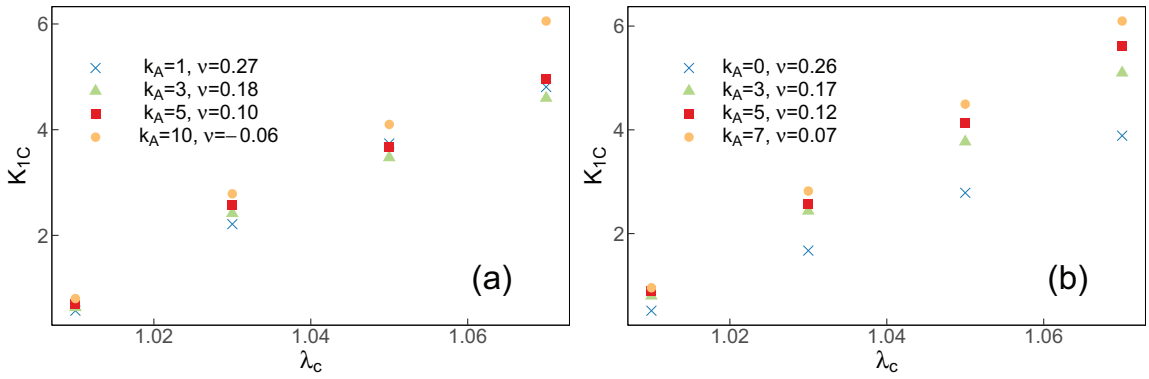

Figure 4.8: Mode one fracture toughness K_{IC} as a function of critical bond stretch λ_c for values of the angular stiffness indicated in the legend in (a) 2D and (b) 3D.

Poisson's ratio. The maximal distance of a broken bond ahead of the initial crack provides a measure of the distance the crack has travelled. Initially a few bonds break right at the tip of the crack. This breakage accelerates until eventually the crack begins to grow at a constant speed equal to the maximum crack velocity V_c. In isotropic, brittle materials, the maximum crack velocity is found to be less than the theoretical maximum set by the Rayleigh wave speed c_R.[156] Here we find the maximum crack velocity to be approximately $0.55c_R$ at all values of ν considered in 3D. The crack velocities are indicated by the dashed lines in Fig. 4.9b. No significant dependence of V_c on λ_c or θ_c was observed. We also tested the dependence of the crack velocity on the damping. No significant dependence of the crack speed on γ was found. However if one were to damp the absolute velocity as opposed to relative velocities, an increase in the damping strength would cause a decrease in the maximum crack velocity. These results do not change with a reduction in the loading rate.

Studies of crack growth in MD simulations have found that reflections of sound waves from the boundaries can affect measurements of the crack speed.[141,157] However, in 2D and 3D the speed of sound is approximately $10a/\tau$ implying propagation of phonons across the

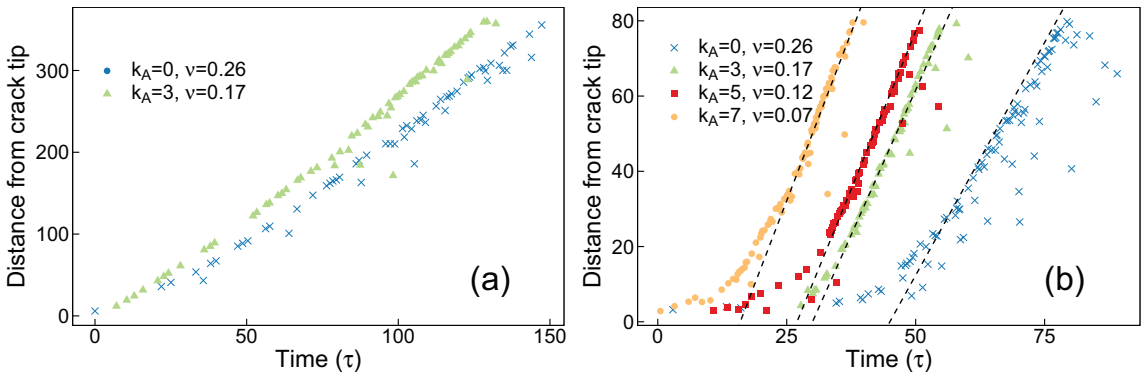

Figure 4.9: The distance between broken bonds and the initial crack tip as a function of the time at which the bond broke for the indicated values of the angular stiffness in (a) 2D and (b) 3D. Dashed lines in (b) have slopes of $0.55c_R$ where the Rayleigh speed c_R is 4.5, 5.6, 6.1, and 6.5 a/τ for systems of k_A equal to 0, 3, 5, and 7 u respectively.

system would take roughly 80τ in 2D or 20τ in 3D. Aside from a few bonds that break at very small strains, the crack is seen to reach its maximum speed on a shorter timescale. This suggests that reflections do not affect our measurements. If more accurate measurements of V_c were required, one could consider increasing the system size or constructing a surrounding region of viscious damping to remove the possibility of phonon reflection.[141,157]

Measuring mode II fracture toughness is experimentally challenging in brittle materials such as rock where $K_{\mathrm{IIC}} > K_{\mathrm{IC}}$. Measurements require complicated loading geometries in order to suppress mixed mode crack growth.[158,159] In simulations however, we can artificially suppress mode I crack growth and force shear cracks even with simple loading geometries. Systems were prepared with identical geometries described above except that the box is fully periodic and the crack is oriented diagonally to the box lattice vectors as seen in Fig. 4.10. Pure shear is applied, compressing vertically and expanding horizontally, at a constant strain rate. In order to suppress mode I growth, two classes of bonds are defined as seen in Fig. 4.10. Bonds that are associated with particles aligned along the

shear crack direction (red) will break at the given values of λ_c or θ_c. All other bonds (blue) are not allowed to break. Two classes of angles are also defined in a similar fashion. This forces cracks to grow diagonally, producing a pure mode II shear crack.

In Fig. 4.11a-b, the ratio of $K_{\mathrm{IIC}}/K_{\mathrm{IC}}$ is plotted as a function of θ_c for the values of λ_c indicated in the legend and $k_A = 3$. Increasing θ_c increases mode II fracture toughness relative to mode I fracture toughness. The effect is more pronounced at smaller values of λ_c. Alternatively, in Fig. 4.11c-d, k_A is varied for a fixed value of $\lambda_c = 1.05$. The increase in $K_{\mathrm{IIC}}/K_{\mathrm{IC}}$ with increasing θ_c is also enhanced for larger values of k_A which leads to larger angular forces. Although untangling the relation between these parameters is complicated, this data does demonstrate that it is possible to independently calibrate K_{IIC} relative to K_{IC}. As accurate values of K_{IIC} do not exist for many brittle materials, we do not further characterize this dependence.

4.3.3 Boron Carbide Calibration

Our focus is modeling the behavior of boron carbide (BC), a very hard ceramic used to make ballistic armor. Experimentally measured material properties of BC are summarized in Table 4.1. In this subsection, we describe the procedure of calibrating the above model to represent BC. First we describe a mapping of the fundamental constants to real units based on a coarse-graining length scale. Next a particular set of model parameters is chosen and the resulting elastic response and fracture toughness of the model are compared to those of BC. Finally, we validate that this choice of model parameters is capable of reproducing important features of compressive failure in brittle solids such as BC.

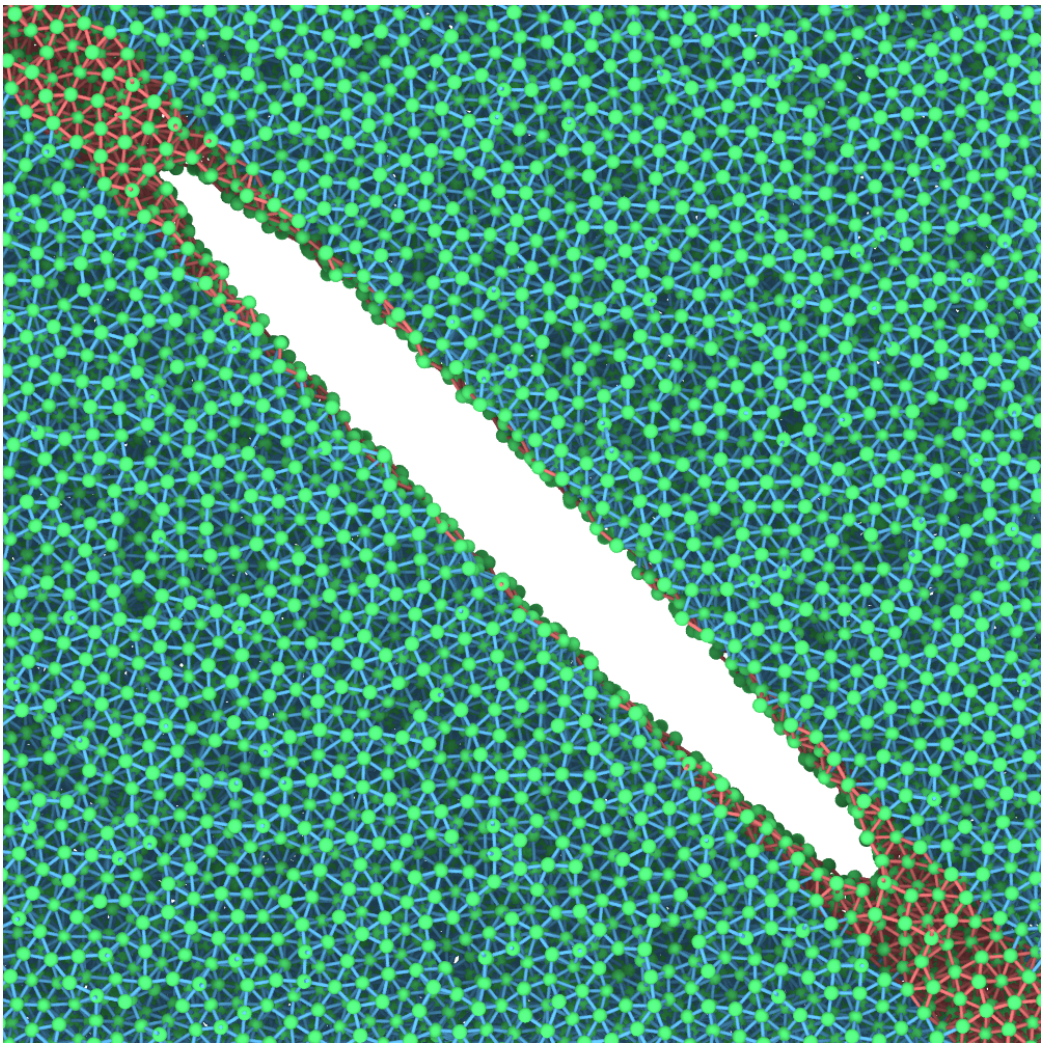

Figure 4.10: Zoomed in image of crack geometry used for mode II fracture calibration in 3D. The image shows a region of approximately $50a$ by $50a$. The elliptical crack has a major axis of $20a$ and a minor axis of $2a$. Particles are bonded by two types of bonds, unbreakable bonds (blue) and breakable bonds(red).

Material property	Measurements
Density	$\rho = 2520$ kg/m^3[160]
Bulk modulus	$B = 232$ GPa[161]
Poisson's ratio	$\nu = 0.17$[160]
Mode I fracture toughness	$K_{\mathrm{IC}} = 2.5$ MPa $\sqrt{\mathrm{m}}$[160]
Mode II fracture toughness	Unknown
Maximum crack velocity	480 m/s,[160] 2000 m/s[154]

Table 4.1: Summary of BC material properties.

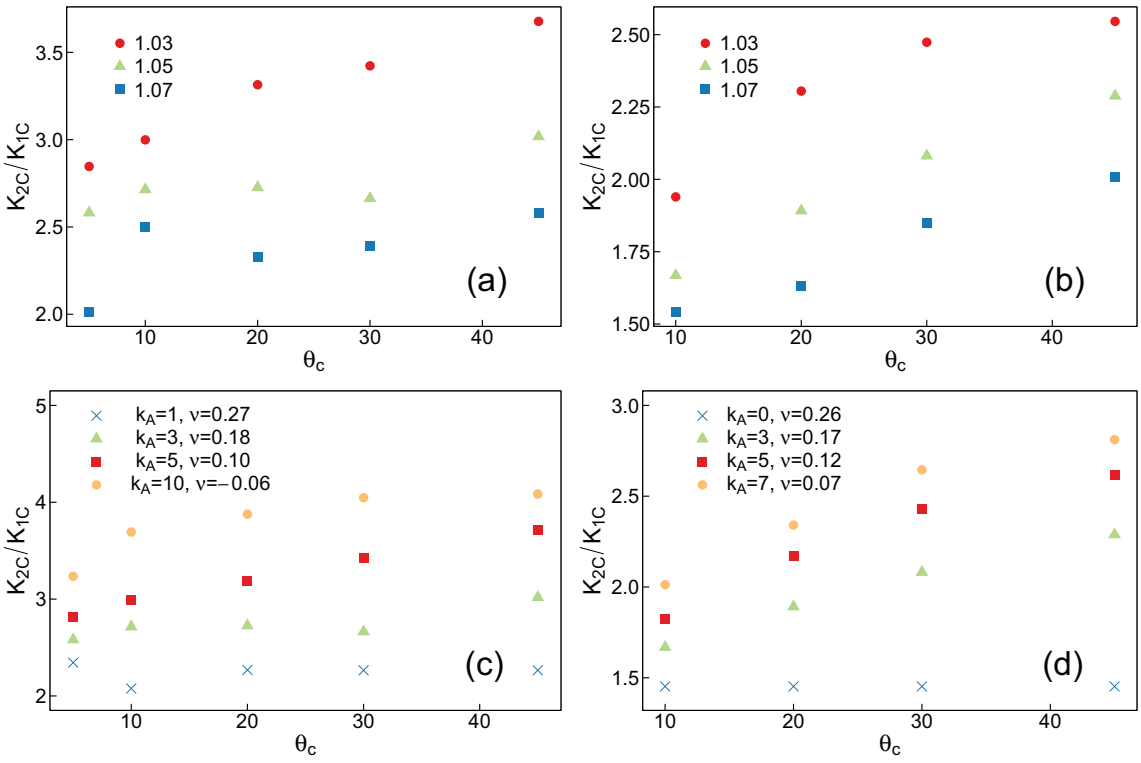

Figure 4.11: Ratio of mode II fracture toughness K_{2C} to mode I fracture toughness K_{1C} as a function of critical bond stretch θ_c. Ratio calculated for values of λ_c indicated in the legend and $k_A = 3$ in 2D (a) and 3D (b). Ratio calculated for values of k_A indicated in the legend and $\lambda_c = 1.05$ in 2D (c) and 3D (d).

Parameters	Value	Dependence on a
a	0.125μm	a
m	20 fg	a^3
u	10^{-11} J	a^3
τ	0.2 ns	$a^{1/2}$

Table 4.2: Summary of fundamental constants for the 3D model based on the chosen coarse graining of BC.

Given the length scale of a coarse grained particle, a, one can calculate the corresponding values of the other fundamental constants m, u, and τ in real units. Here we set the radius of each particle to 0.125μm and calculate the values of the other fundamental constants listed in Table 4.2. The choice of a is based on the spatial resolution of micro CT scans described in the next section. The value of m is determined by matching the mass of a single coarse-grained particle to an equivalent volume of BC. Similarly, the value of u is derived by equating the bulk modulus of the model to that of BC. Lastly, the value of τ is calculated as $\sqrt{a^2 m/u}$. If a different value of a is chosen, these fundamental constants will scale as a power of $a/0.125\mu$m indicated in Table 4.2.

The free parameters of the model, k_A, λ_c, and θ_c, are then determined by fitting the Poisson's ratio, mode I fracture toughness, and mode 2 fracture toughness to those of BC. For the 3D system, we choose values of $k_A = 3.0u$, $\lambda_c = 1.05$, and $\theta_c = 10^\circ$ corresponding to values of $\nu = 0.17$, $K_{IC} = 5.6$ MPa m$^{1/2}$, and $K_{IIC} = 12.9$ MPa m$^{1/2}$. The Poisson's ratio is equivalent to that listed in Table 4.1 for BC. The value of K_{IC} is within a factor of two of the predicted value for BC. However, one could calibrate λ_c to match K_{IC} exactly.

As we do not know of a published value of K_{IIC} for BC, the value of θ_c does not correspond to an experimental measurement and was simply chosen. If an accurate measurement of K_{IIC} was made for BC, one could determine the appropriate value of θ_c. It is interesting to note that the model has a crack velocity that corresponds to 1930 m/s, which is within the range of experimentally measured values for BC in Table 4.1.

In 2D we use a similar set of parameters except $k_A = 2.5$ corresponding to $\nu = 0.20$. These parameters are used in the rest of this work unless otherwise specified. As there is no measure of thickness in the 2D system, one cannot make the conversion to real units. However, we made the decision to define $\tau = 0.2$ ns and $u = 1.3 \times 10^{-11}$ J/a such that the bulk modulus of the 2D system corresponds to the bulk modulus of BC. Here the factor of $1.3/a$ is the ratio of the measured 3D bulk modulus to the 2D bulk modulus. This decision was made to ease comparisons between data for 2D and 3D systems.

In boron carbide, uniaxial compressive failure is expected to be dominated by the growth of wing cracks.[122] To test for wing crack growth in our model, we use simulation protocols and geometries similar to those described above to measure the mode I fracture toughness. As shown in Fig. 4.7, we use a diagonal crack instead of a horizontal crack and apply a compressive displacement. Using the parameterization for BC in Table 4.1, we found this geometry produced wing crack growth as seen in Fig. 4.12a. The growth of wing cracks is found to be quite robust to variations in the crack geometry. Wing cracks are often a challenge to reproduce in DEMs but have been seen before in both 2D[162,163] and 3D[164] models. Wing cracks were also identified in simulations of elliptical penny cracks.

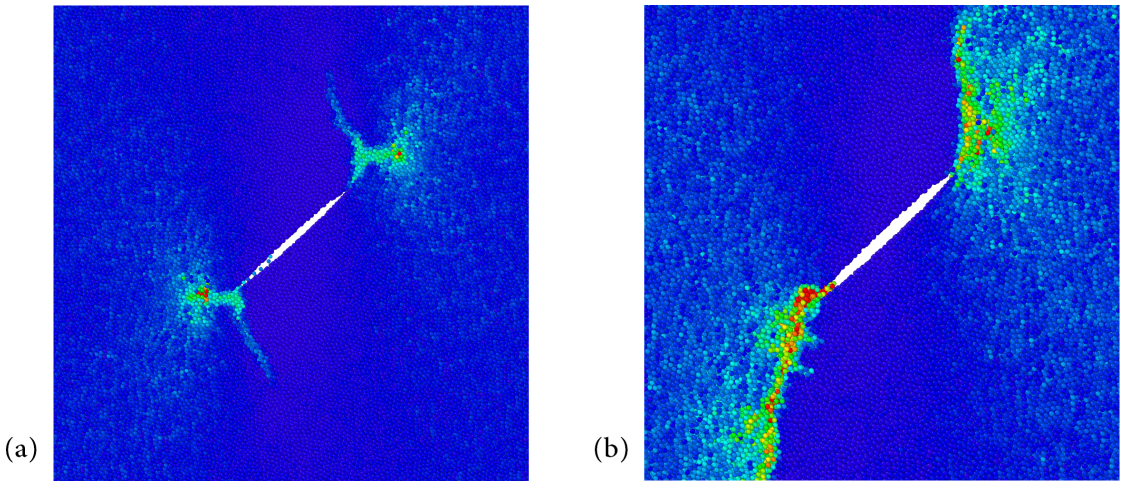

Figure 4.12: Spatial images of crack growth for uniaxially compressed samples with a Poisson's ratio of (a) 0.17 and (b) 0.25. Particles are colored by the change in bond energy qualitatively highlighting regions of bond breakage.

Interestingly, if we turn off angular interactions (set $k_A = 0$) we generally find a stronger mix of shear crack growth as seen in Fig. 4.12b. However the direction of secondary crack growth is quite sensitive to the crack width and system size.

4.4 Transition from Fracture to Granular Flow

Brittle solids fail very rapidly and the transition from an intact solid to a broken mass of fragments depends strongly on the initial defects in the sample.[116,153,154] These defects could include preexisting cracks or inclusions. Such flaws have been seen to nucleate wing cracks which can subsequently grow and rapidly coalesce leading to failure.[120] A perfectly homogeneous brittle solid would have no such extrinsic nucleation sites and one would expect a larger energy barrier to initiate crack growth. This would increase the yield stress. Not only does the distribution of defects impact when and where wing cracks grow, the

resulting wing cracks affect the elastic response of the material.[165,166]

The fracture of brittle materials also depends strongly on the rate of mechanical loading. Brittle materials often fail at larger yield stresses at higher rates.[167] At higher rates, a larger population of cracks participate in failure due to an interplay between the strain rate and crack velocity.[153,168] At low rates, only a small population of the weakest defects may be activated, making the extremes of the defect distribution important. At high rates a larger population of defects comes into play and more typical defects contribute to failure.[122,169] Rate also affects the nature of the fragmented state. More crack growth at higher rates will produce a finer distribution of fragments.[151,170] Several theories have been proposed to capture this behavior.[171,172]

Constitutive models have been designed that include these effects.[122,173,174] These models often dsecribe the evolution of a damage parameter which measures the local concentration of wing cracks in a single element.[175] To produce physically accurate results, the evolution of the damage and its effect on the stress in the system must be understood.

The evolution of damage has been studied using finite-element models[168] but mesh effects can limit the evolution of cracks. Measuring damage experimentally in situ is not an easy task. Experiments have been performed that use high-speed photography to track a projected view of crack growth[153] or fully track the 3D growth of fracture planes in quasistatic loading at incremental strains.[176,177] New techniques are being developed that may allow experimentalists to track the dynamical evolution of crack distributions.[178] However, full access to the dynamical evolution of the microstructure remains a challenge.

In this section, we used the model described in the preceding sections to study general trends in the effect of defect density and strain rate on the fracture and failure of brittle solids. We also calculate and track the evolution of damage in the model and relate it to the evolution of the stress. In the next subsection we discuss simulation details specific to this section. In Subsec. 4.4.2 we track the evolution of the stress, crack growth, and damage at a fixed density of defects. Finally in Subsec. 4.4.3 results are presented for simulations with varying initial defect densities.

4.4.1 Simulation Methods

In order to capture a realistic population of defects we use micro CT scans of BC provided by Moorehead et al.[179] As seen in Fig. 4.13a, these BC samples contain three populations of defects: voids (black), low density carbonaceous regions (dark gray), and high density aluminum nitride (white). Each image is roughly partitioned into the four categories using a simple thresholding of pixel intensity. We do not attempt to perform an accurate decomposition of the images into different phases, perform noise reduction, or limit the maximum defect sizes such as in the work by Moorehead et al. To further simplify the model, we only include carbonaceous defects. We assume aluminum nitride regions behave like BC and treat voids as carbonaceous. The carbonaceous regions are soft enough that they nucleate cracks almost as efficiently as voids. Fig. 4.13b shows an example of the resulting geometry of carbonaceous defects.

In order to model carbonaceous defects, we first require calibration of model parameters. Specific material properties of these defects are difficult to measure experiementally.

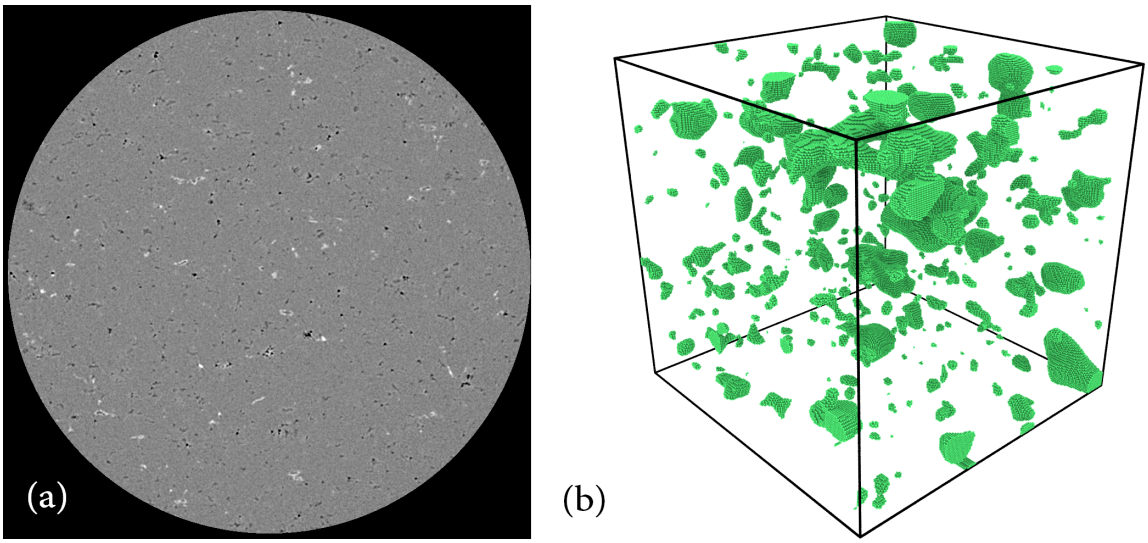

Figure 4.13: (a) Example micro CT scan provided by Moorehead et al.[179] The image is approximately 550 μm in diameter. (b) Rendered set of three dimensional defects extracted from a volume of $\sim (25\mu\text{m})^3$.

However nanoidentation tests of BC samples found that the elastic modulus of graphitic inclusions is approximately a quarter of that of BC.[180] We therefore define $u_{\text{defect}} = 0.25u$ and $k_{A,\text{defect}} = 0.75u$ assuming no change in Poisson's ratio. Since we have no information on the fracture toughness of defects we leave $\lambda_c = 1.05$ and $\theta_c = 10°$. The interactions at the interface between regions of BC and carbonaceous defects have values of u_{cross} and $k_{A,cross}$. These values are set to the harmonic mean of the corresponding coefficients for BC and the carbonaceous defects.

Initial systems were generated with periodic boundaries of size $L = 200\mu$m in 2D and $L = 25\mu$m in 3D. Spatial maps derived from the micro CT scans described above were overlaid on the periodic cell of the simulation to produce defects. The maps were coarse grained on a length scale of $a = 0.125\mu$m. This method produces planar boundaries of defects that end at the edges of the CT image. These truncated defects could potentially bias

the location of crack growth however no evidence of abnormal behavior at the boundaries was detected. Future studies could remove discontinuities by mapping defects across the boundaries, removing boundary defects, or using fixed boundary conditions.

The initial area or volume fraction of defected material is defined as ρ_i. Based on CT scans, this density was found to be $\sim 3\%$ in 2D and $\sim 17\%$ in 3D. Adjacent regions of defected material were spatially clustered to identify individual defects. To vary the defect density, individual defects were randomly deleted until a desired lower density of ρ was reached. We define $\rho_R = \rho/\rho_i$ as a measure of the number of defects in the sample.

Simulations in this section were run using constant volume, pure shear deformations. The box lattice vectors were chosen to align with the directions of principal stress. In 2D, the box period in the x direction L_x was compressed at a rate $\dot{\epsilon}$ while the box period in the y direction L_y was expanded. In 3D, L_x was compressed at a rate $\dot{\epsilon}$ while both L_y and L_z were expanded at a rate $\dot{\epsilon}/2$. The shear stress is defined as $\sigma_s \equiv (\sigma_{xx} - \sigma_{yy})/2$ in 2D and $\sigma_s \equiv (2\sigma_{xx} - \sigma_{yy} - \sigma_{zz})/4$ in 3D where σ_{ij} are the components of the stress tensor. Units of time and stress have been converted to seconds and GPa to ease the comparison to real materials.

4.4.2 Rate Effects in Brittle Fracture

In Fig. 4.14, stress-strain curves at the indicated strain rates are plotted for (a) 2D and (b) 3D systems with relative defect density $\rho_R = 1$. Note that these abnormally high rates reflect the particularly small length scale that is being resolved. High rate effects will not emerge on micron length scales unless there are extraordinarily large rates.

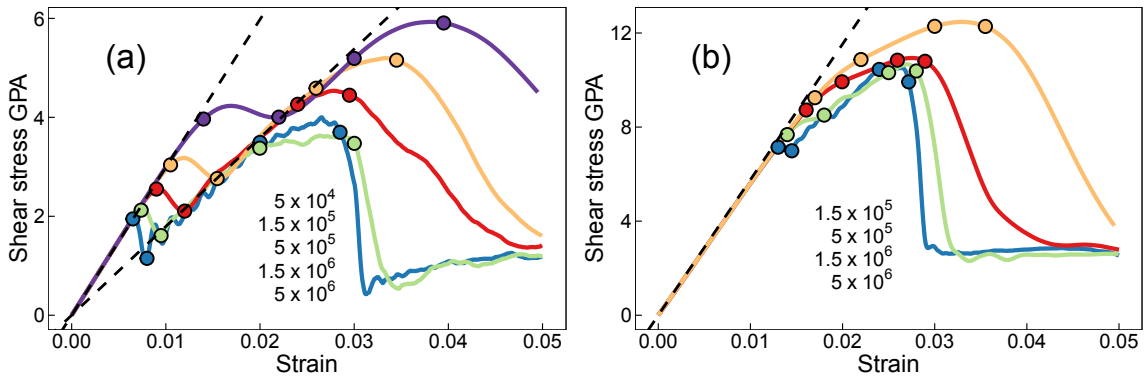

Figure 4.14: The shear stress as a function of strain for a sample strained at the rates indicated in the legend in (a) 2D and (b) 3D. Dashed lines in (a) have a slope of $2G$ and $1.2G$ and the dashed line in (b) has a slope of $3G$. Large filled points highlight approximate strains where the initial elastic response ends, the damaged elastic loading starts and stops, and the system fully fails for each rate.

First we focus on behavior seen in the 2D system. At low strains at all rates, the shear stress increases linearly with strain with a slope equal to $2G$. This is consistent with the definition of shear stress and strain in the previous subsection. Elastic loading extends up until an initial yield strain $\epsilon_{Y,i}$. As the strain rate increases, $\epsilon_{Y,i}$ increases. At low rates there is a rapid, almost discontinuous drop in stress at $\epsilon_{Y,i}$. As rate increases, this transition becomes smoothed out. At all rates the system returns to elastic loading after the initial yield. However, the damage has caused a 40% reduction in the elastic modulus of the system. The system finally fragments into discrete grains at a strain $\epsilon_{Y,f}$. Higher fragmentation stresses are identified at higher rates, consistent with what is observed in experiments.

Similar behavior is identified in the 3D system. The system elastically loads as the shear stress grows with a slope of $3G$ up to a strain of $\epsilon_{Y,i}$ that increases with increasing rate. After initially yielding, the system loads with a reduced modulus before ultimately

failing. However, in 3D the reduction in the modulus depends on the rate at which the system was strained. At the lowest rate a 35% reduction in the modulus is measured while there is a 65% reduction at the highest rate.

Decreasing $\dot{\epsilon}$ below the rates shown in Fig. 4.14 did not significantly affect the response, indicating that the lowest rates correspond to quasistatic (QS) loading. At higher rates than those shown, transitions associated with damage and failure are difficult to define. Future work should focus on larger systems in 3D in order to probe a wider range of strain rates.

The stress response in the system can be connected to the growth of cracks in the sample. In Fig. 4.15 the spatial positions of broken bonds are rendered in the material reference frame for a 2D sample strained at a rate of (a) $1.5 \times 10^6 s^{-1}$ and (b) $1.5 \times 10^5 s^{-1}$. The color of bonds corresponds to the designated values of strain in Fig. 4.14a. Prior to initial yielding, bonds colored in red have broken. These represent small wing cracks that nucleated from defects. At the higher rate, more wing cracks have been activated. After the initial yield, wing crack growth accelerates as indicated by green bonds. Cracks have grown to span the compressive axis in the low rate limit. In an unconfined simulation, this could potentially correspond to failure. At higher strains the system still behaves as an elastic solid with a reduced modulus. Crack growth slows during this new elastic regime and only the bonds highlighted in blue have been broken. At still higher strains, the system begins to deviate from elastic loading and the bonds in purple break leading to material failure. This late stage growth consists primarily of crack coalesce. The percolation of cracks in both periodic directions leads to the complete failure of the solid and the transition to granular flow.

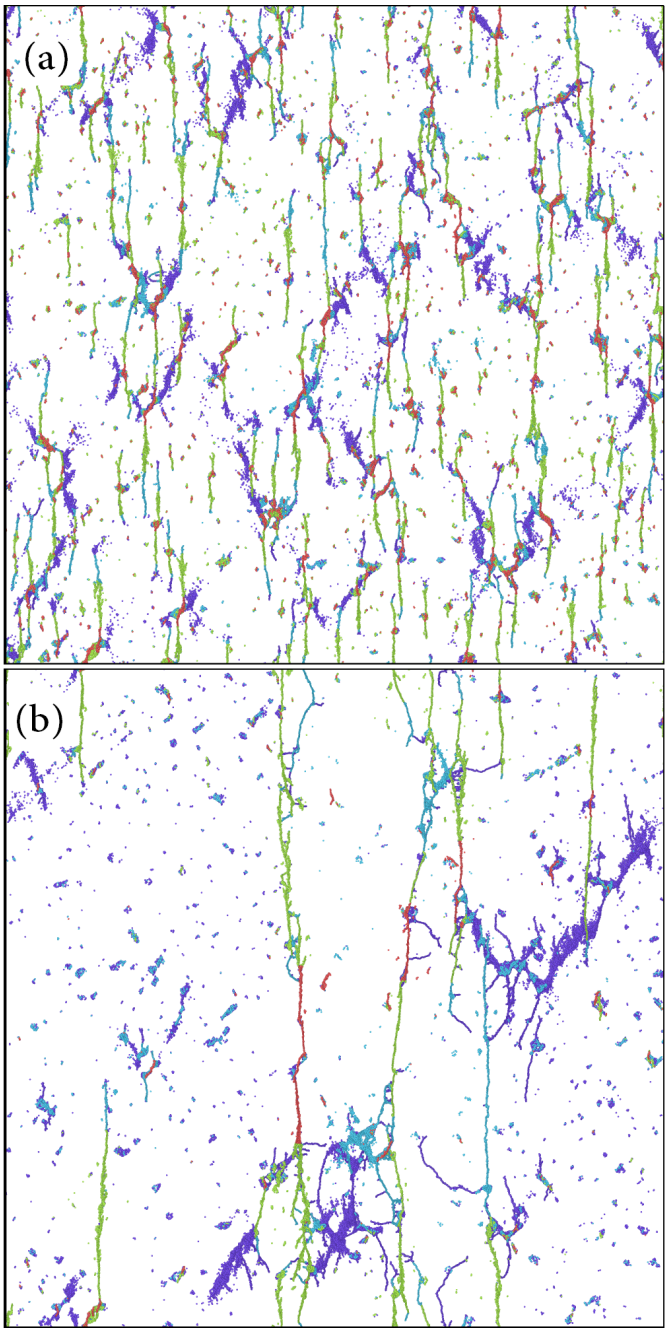

Figure 4.15: Locations of broken bonds in the material reference frame from a 2D sample strained to failure at a rate of $1.5 \times 10^6 s^{-1}$ (a) and $1.5 \times 10^5 s^{-1}$ (b). The vertical direction is the direction of compression. Colors of bonds correspond to the interval of strain in which they broke. These strain intervals are highlighted by large filled circles in Fig. 4.14a. Red bonds correspond to bonds that broke before the initial elastic response ends. Green bonds broke before the onset of elastic loading with the reduced modulus. Blue bonds broke before the end of this elastic loading. Lastly, purple bonds broke right before the system failed.

The general trends in wing crack growth seen here agree very well with observed experimental behavior. In uniaxial compression of ice, wing cracks are seen to nucleate off of parent cracks.[120] These cracks then grow until surface interactions lead to the growth of coalescent cracks and failure. The colaescence of cracks is often linked to the peak stress in loading.[153] A similar partitioning of crack growth was performed in 2D systems using finite-element models.[168]

We also performed a similar characterization of crack growth in 3D samples. The locations of broken bonds in a 3D sample strained at the lowest rate are rendered in Fig. 4.16. As before, the color represents the interval of strain over which the cracks broke as indicated in Fig. 4.14b. At low strains, several planar wing cracks nucleate in red before yield. Note that some of these wing cracks are occluded by other broken bonds. After the initial yielding, cracks in green span one of the periodic boundary conditions lead to a reduction in the modulus. Elastic loading continues until all of the blue bonds have broken and a crack has grown to span the other periodic boundary. Failure occurs rapidly as purple bonds break causing the coalescence of different wing cracks. At high rates, a much larger population of cracks participate in failure and visibility is greatly reduced.

In order to quantify the size and number of cracks in the system, we calculate a damage metric D:[122,174]

$$D = \frac{1}{V} \sum_{\text{Cracks}} \ell_i^3 \tag{4.16}$$

where V is the volume of the sample and ℓ_i is the length of the i^{th} crack. An analogous definition in 2D uses the sum of ℓ_i^2 normalized by the area of the sample. To calculate D,

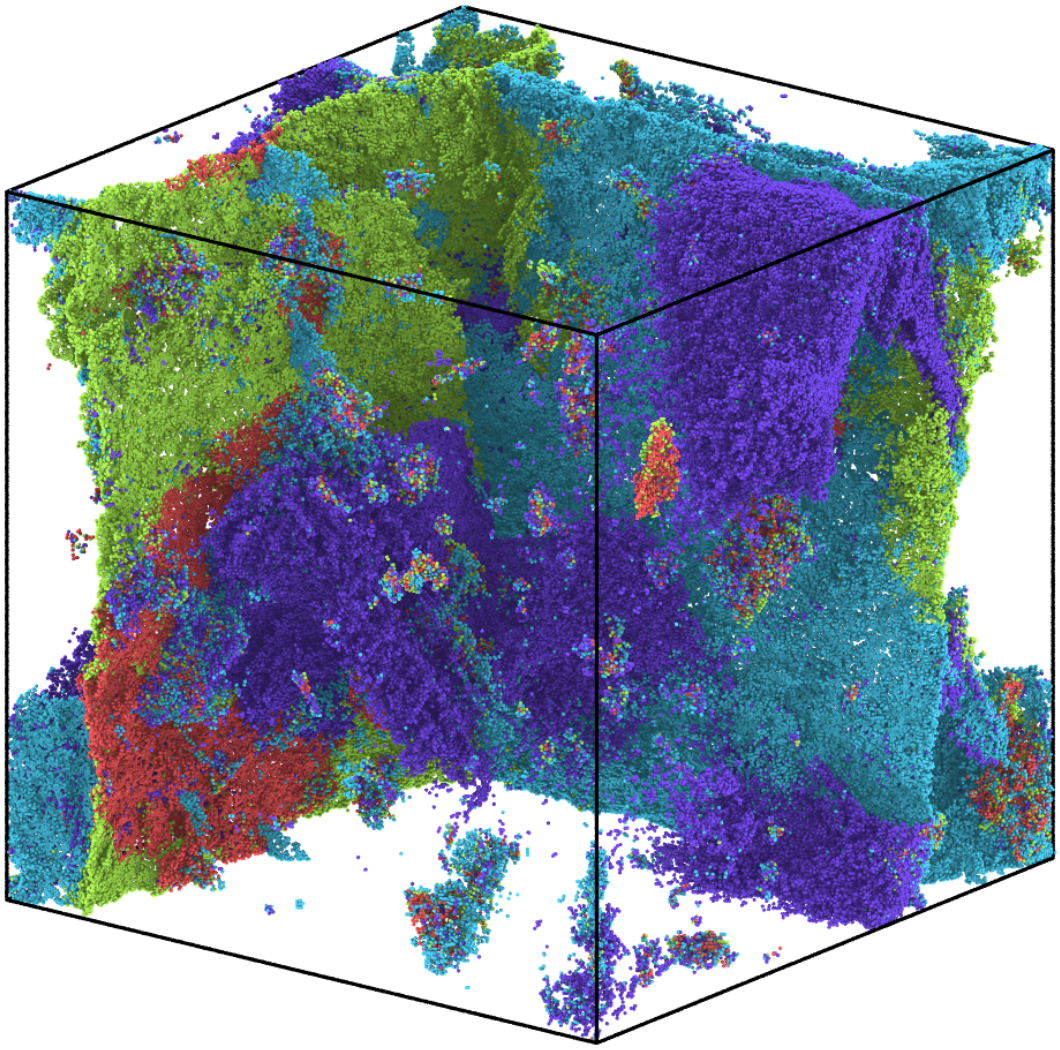

Figure 4.16: Locations of broken bonds in the material reference frame from a 3D sample strained to failure at a rate of $1.5 \times 10^5 s^{-1}$. The vertical direction is the direction of compression. As in Fig. 4.15, colors of bonds correspond to the interval of strain in which they broke as indicated by filled circles in Fig. 4.14b. Red bonds broke prior to the initial yield. Note that some smaller red wing cracks are occluded by later growth. Green bonds broke prior to the interval of damaged elastic loading. Blue bonds broke before the end of this interval and lastly purple bonds broke prior to complete failure. Stray, isolated broken bonds were filtered out to improve visibility.

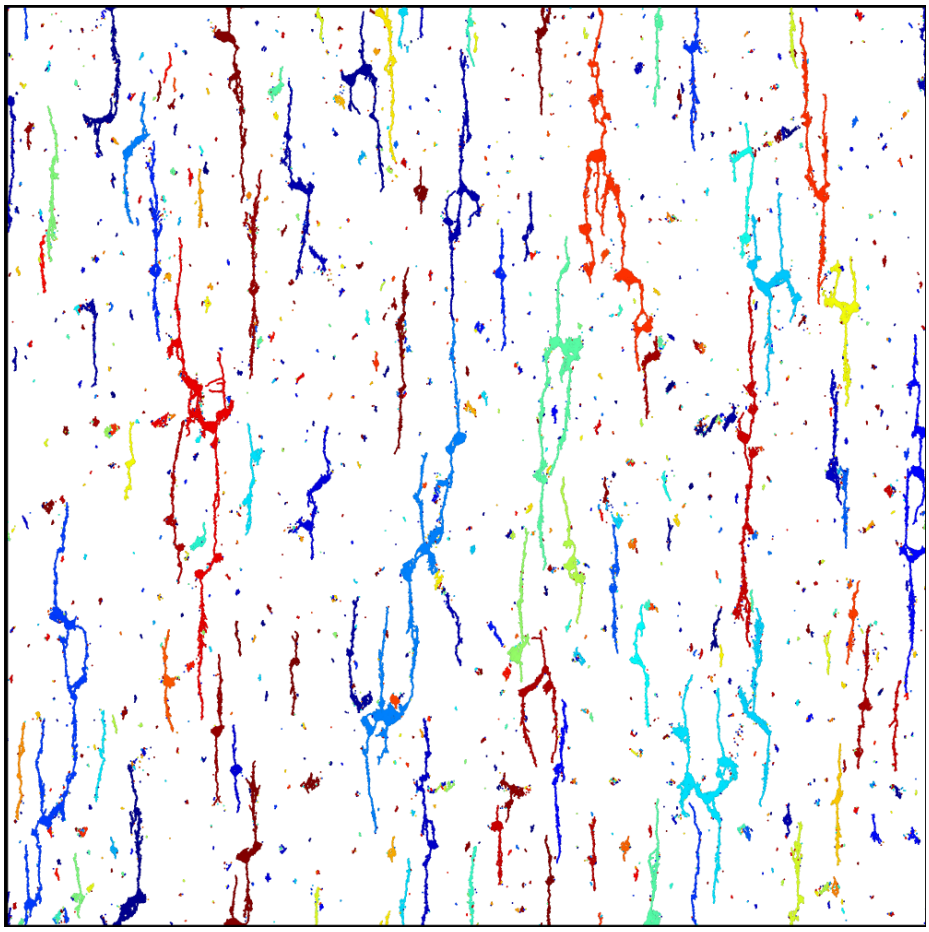

Figure 4.17: Sample configuration of clustered broken bonds in 2D. All bonds constituting a single crack are color coordinated.

we first need to cluster sets of broken bonds into cracks. Broken bonds were mapped to a discrete cubic or square lattice with a cell length of a. Cells containing broken bonds were grouped with any nearest or second nearest neighbor to form clusters. Sample clusters of broken bonds identified as cracks are shown in Fig. 4.17.

Each clustered set of broken bonds was used to calculate the length of a crack. Unless the crack percolated, any disjointed section of a crack that crossed a periodic boundary was remapped to the corresponding image. A bounding box was then placed over the crack and

its diagonal was used to calculate a length scale ℓ of the crack. This definition maximizes the length of a crack. A value of D was then calculated at regular strain increments. It is important to note that this measure of the damage is not guaranteed to grow monotonically with strain. If two system spanning cracks with length $\ell = L$ were to coalesce, the damage defined in Eq. (4.16) would decrease by a factor of at least $(2 - \sqrt{2})L^3/V$. We therefore define the damage at a strain ϵ as the maximum value of D in the interval $[0, \epsilon]$. This guarantees that the damage increases monotonically with strain.

The damage is plotted as a function of strain in Fig. 4.18 for (a) 2D and (b) 3D systems at the indicated values of the rate. Damage is accumulated more rapidly at low rates. The strains at which the system initially yields are approximately indicated by the first filled-in circle for each curve and failure corresponds to the final point. In 2D, the damage remains below 0.1 in the elastic regime. During the initial yield, D rises above unity. Damage continues to grow during the interval where the system responds with a lower elastic modulus, and failure occurs at D between 3 and 5. In 3D, D has reached 1.4 to 3.0 before yield and rises less precipitously during yield. Failure occurs at $D = 8$ to 12. The level of damage corresponding to the initial yield may increase with increasing rate but statistical fluctuations are comparable to the changes. As seen in Figs. 4.15 and 4.16, the initial yield demarcates the onset of system spanning crack growth. Therefore, at larger strains the damage becomes poorly defined due to the periodic boundary conditions.

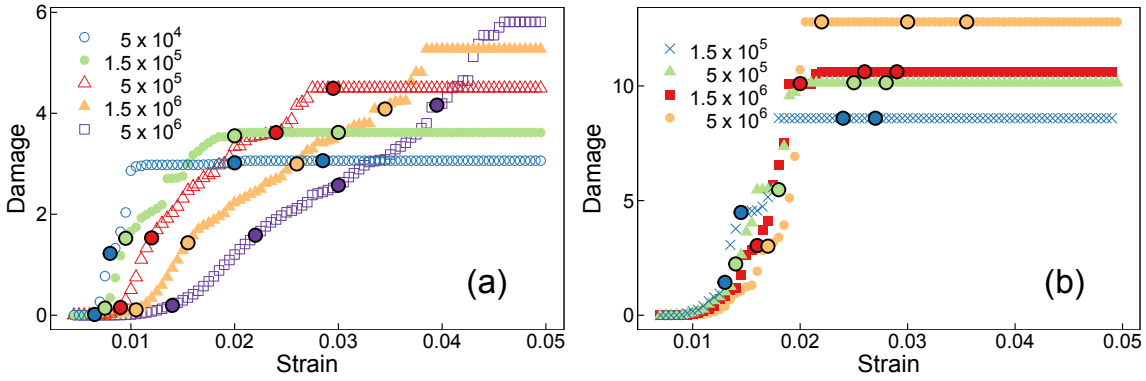

Figure 4.18: Damage as a function of strain for a sample strained at the rates indicated in the legend in (a) 2D and (b) 3D. Large, filled points correspond to the same values of strain indicated in Fig. 4.14.

4.4.3 Impact of Defect Density on Failure

In the above subsection, we studied the behavior of a sample prepared with a fixed defect density. We now explore how varying the density of defects ρ_R impacts the brittle failure of solids. Here we primarily focus on the initial yield at a strain $\epsilon_{Y,i}$. In Fig. 4.19a, traces of stress versus strain are plotted for 2D systems with the indicated values of ρ_R, that are strained at (a) $\dot{\epsilon} = 5 \times 10^4 s^{-1}$ and (b) $\dot{\epsilon} = 5 \times 10^6 s^{-1}$. As ρ_R decreases, $\epsilon_{Y,i}$ generally increases. However, the magnitude of this effect depends on the rate. At low rates, $\epsilon_{Y,i}$ is insensitive to ρ_R until ρ_R decreases below about 0.1. In contrast, at high rates $\epsilon_{Y,i}$ varies rapidly as ρ_R drops from unity and changes less at low ρ_R. At both rates, the ultimate fragmentation stress does not appear to depend on defect density in a systematic way.

These observations are consistent with theoretical expectations.[122,168,169] Failure at low rates is expected to depend on the extremes of the distribution of defects: only the least stable defects participate in failure. At $\rho_R = 1$, the 2D sample contains approximately 1100 discrete defects. If ρ_R is reduced by a half, one still has approximately 500 defects.

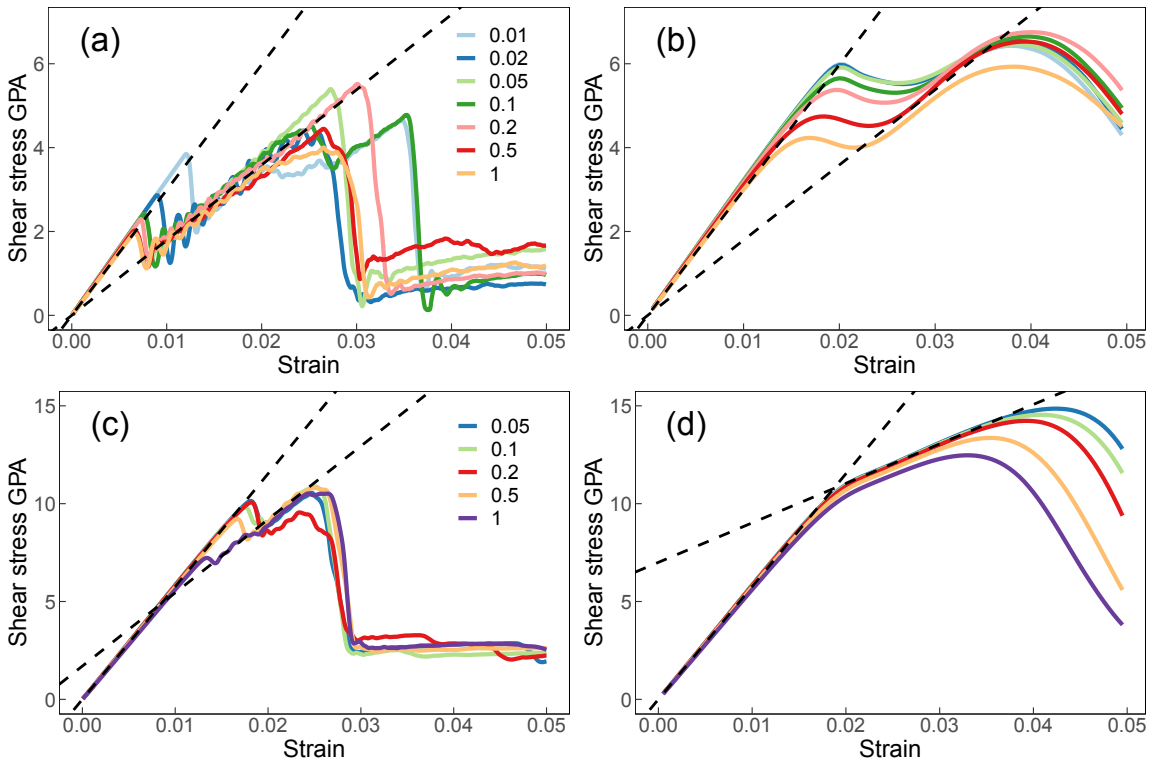

Figure 4.19: (a-b) Stress versus strain for 2D systems strained at a rate of (a) $5 \times 10^4 s^{-1}$ and (b) $5 \times 10^6 s^{-1}$ for the indicated relative density ρ_R of defects. (c-b) Similar data is plotted for 3D systems strained at a rate of (c) $1.5 \times 10^5 s^{-1}$ and (d) $5 \times 10^6 s^{-1}$. Dashed lines in (a) and (b) have slopes of $2G$ and $1.2G$. Dashed lines in (c) have slopes of $3G$ and $1.95G$. Dashed lines in (d) have slopes of $3G$ and $1.05G$.

The distribution of defects is still well sampled and it is likely the least stable defects are still represented. Therefore little change in $\epsilon_{Y,i}$ is expected. In contrast, once the defect density drops by a factor of 20, only 50 or so defects remain. Further reductions in ρ_R have a high probability of pruning the relevant defects and significantly increasing $\epsilon_{Y,i}$.

At high rates, the average number of defects is important. Many cracks need to grow simultaneously in order to keep up with the high rate of deformation. Many or all defects participate in failure so a reduction in the number of defects from 1000 to 500 has a large probability of reducing the number of defects that are activated and thus increasing $\epsilon_{Y,i}$. In contrast, when one has only a handful of defects, say 20, some cracks will need to nucleate in the homogeneous bulk regardless of which defects remain. This requires a much larger local stress and effectively sets $\epsilon_{Y,i}$ at the bulk strength. Therefore, the removal of additional defects is unlikely to significantly affect $\epsilon_{Y,i}$.

In order to solidify these observations and begin making quantitative predictions, it is important that future work simulate a large ensemble of random initial conditions. Measuring the variation in $\epsilon_{Y,i}$ at a given ρ_R and rate is much more informative than studying results from a single ensemble. Furthermore, it is also important to characterize the distribution of defects being used and activated.

In Fig. 4.19c-d, similar stress versus strain curves are plotted for 3D systems strained at rates of (c) $1.5 \times 10^5 s^{-1}$ and (d) $5 \times 10^6 s^{-1}$. These samples contain a smaller number of initial defects, approximately 300 at $\rho_R = 1$, so it is even harder to make claims without more statistics. As in the 2D case, decreasing the density of defects is generally associated

with larger values of $\epsilon_{Y,i}$ at both rates. For this particular sample, $\epsilon_{Y,i}$ does not depend much on ρ_R for values of $\rho_R \leq 0.5$. In the QS limit, this observation could result if the relevant defect was never removed. As in the 2D case, the ultimate failure stress does not exhibit a strong dependence on initial defect density at low rates but does in the high rate limit where there is an increase in the ultimate failure stress with decreasing ρ_R.

In Fig. 4.20 the damage is plotted as a function of strain for the same samples as in Fig. 4.19. In 2D, low rate results for all ρ_R show a rapid rise in damage from $D < 0.1$ in the elastic regime ($\epsilon < \epsilon_{Y,i}$) to $D > 1$ after yielding. At higher strains, D is fairly constant. At high rates (Fig. 4.19b), damage accumulates more slowly with strain and does not saturate before fragmentation. The rate of damage accumulation rises as the relative defect density decreases.

The dependence on ρ_R at high rates can be understood in terms of the evolution of cracks in the system. At high values of ρ_R, defects nucleate wing cracks at small strains and the cracks grow gradually with strain. At a low value of ρ_R, the few remaining defects all nucleate wing cracks that slowly grow until suddenly cracks begin nucleating in the defect-free bulk leading to a rapid acceleration in damage accumulation.

In 3D systems sheared at the low strain rate (Fig. 4.20c), damage gradually rises to $\sim$1 in the elastic regime before yield. During yielding, D rapidly grows to values of $D > 5$. At higher strains, $\epsilon > \epsilon_{Y,i}$, damage continues to rise before plateauing around $8 - 10$ for all ρ_R. At the faster strain rate, D does not rise as rapidly during the initial yield. However, D increases much more dramatically at higher strains plateauing at a larger value of $13 - 14$.

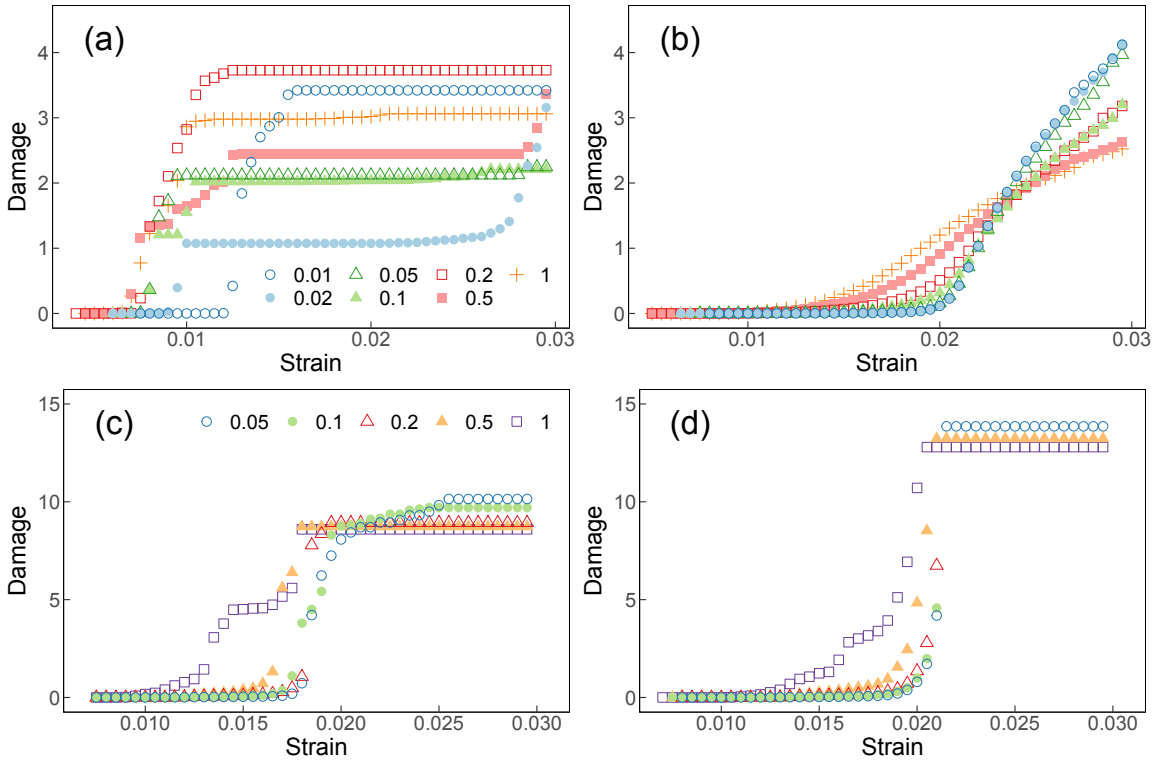

Figure 4.20: (a-b) Damage versus strain for 2D systems strained at a rate of (a) $5 \times 10^4 s^{-1}$ and (b) $5 \times 10^6 s^{-1}$ for the indicated density ρ_R of defects. (c-d) Similar data is plotted for 3D systems strained at a rate of (c) $1.5 \times 10^5 s^{-1}$ and (d) $5 \times 10^6 s^{-1}$.

4.5 Granular Flow

After fracture, the material has fragmented into separate grains and shear produces granular flow. If there is little to no confining pressure, the system will dilate to facilitate relative motion of grains.[181] In a confined system, grains may need to fracture in order to maintain flow in a process known as comminution. The behavior of granular flow without fracture already reveals a wealth of interesting phenomena[182] and the addition of grain breakage only further expands this realm. In this section we will study shear at larger strains to observe comminution in the granular flow regime.

A particularly intriguing phenomenon is the emergence of a scale invariant distribution of grains in fracture and comminution. In many granular samples, the distribution of grain sizes V is found to decay as a power of size: $P(V) \sim V^{-\tau}$. Such distributions have been identified in media collected from the lunar surface,[183] fault gorges,[184] residue from crushed ores,[185] fractured gypsum spheres,[45] as well as many other sources.[13] In addition, the size of ice floes in the ocean also is power-law distributed due to fracture from collisions.[16,186] Due to the scale-invariance of power-law distributions, breakage has been proposed to be an example of self-organized criticality.[14,45,46] In some sense, this phenomena is the opposite of the problem of bubble coarsening where bubbles in foams coalesce to form larger bubbles and can produce a scale invariant state[187]

If this behavior originates from an underlying critical point, the nature of the critical point is poorly understood in comparison to the nonequilbrium critical points of depinning and yielding discussed in Chapters 2 and 3. For instance, the critical point in depinning

and yielding corresponds to the steady-state evolution of a quasistatically driven system. In fracture, grains are created over a very short time span and there is no steady-state. In comminution, it is not clear whether a steady state could exist as one can imagine grains will continue to break. In compression of grains, there is some indication that an ultimate state is reached as the void ratio goes to zero.[188–190] However experiments using shear have identified breakage at large strains[191] and have suggested the distribution may not reach a steady state until strains in excess of 150%.[192] One also might wonder whether the exponent τ produced in fracture is the same as the exponent produced in comminution or if there even exists a universal τ. A range of values of τ have been measured in granular media ranging from 1.48 to 2.18.[13] Finally, there is no knowledge of what non-equilibrium dynamical equation describing comminution could be studied using renormalization group theory.

Analytic latticed-based models of fragmentation have been devised based on the probability of failure in a cubic section of a solid.[13,193,194] Renormalization procedures using coarse graining of these lattice models have been proposed and their results suggest there may be a fixed point in fragmentation. However, these models do not describe dynamic behavior nor has their connection to experiment been robustly tested.[194] Furthermore, the predicted exponent τ depends on the specifics of the model used and estimates can vary from 1.66 to 1.95.[13] One would expect a unique exponent for a critical point.

Scale invariance has also been studied using discrete element models. Such particle-based models are ideal as they naturally allow the presence of discontinuities, and grains can fracture without any need for remeshing. Many DEM simulations are based on arti-

ficial fracture rules where discrete particles are replaced with a predetermined collection of particles upon reaching a critical stress state.[195–197] Such work has found power-law distributions of grain sizes in compression. These models depend upon a separation of time scales between the strain rate and the time scale on which grains fracture, restricting results to the quasistatic limit. In addition, the results depend on the implementation of fracture, and different values of τ have been measured depending on how fracture occurs.[197] This suggests poorly devised, unphysical rules of fracture could lead to artificial behavior.

Other discrete element models, such as the one described earlier in this chapter, represent grains as collections of smaller discrete particles which can break apart.[151,198,199] Such models have been applied to study the fragmentation of an impacted sphere[151,198] or the crushing of a confined granular media.[199] These studies have generally been restricted to small system sizes and have only been able to measure less than one or two decades of power-law scaling in the grain size distribution. Measurements of τ for the impact of spheres include 1.9,[151,198] 1.25,[198] and 1.0[198] depending on the details of interactions. In granular compression, a range of exponents from 1.27 to 1.82 was measured with increasing compressive force.[199]

In this section, we focus on the evolution of the grain size distribution with strain and methodically test the impact of finite strain rate and variations in material properties. In Subsec. 4.5.1, we lay out the simulation details and shear geometry. Following this, we study the evolution of an initially intact sample sheared to large strains. We then look at the impact of rate in Subsec. 4.5.1 and find the maximum grain size and internal friction coefficient both decrease with increasing rate. Lastly, in Subsec. 4.5.4 we briefly look at

how decreasing Poisson's ratio leads to an increase in granular anisotropy and an increase in the friction coefficient.

4.5.1 Simulation Methods

In this section, we again use pure shear as described in Subsec. 4.4.1. However, in order to reach large strains, we use Kraynick-Reinelt (KR) boundary conditions in 2D[100] and generalized KR boundary conditions in 3D,[101] as described in Chapter 3.

We again use values of $k_A = 2.5$ and 3.0 in 2D and 3D, respectively. As before, we also set $\lambda_c = 1.05$ and $\theta_c = 10^\circ$ in both 2D and 3D. This choice in 3D corresponds to the elastic response of boron carbide. All units of stress are therefore scaled to units of GPa based on the bulk modulus of boron carbide.

For simplicity, all samples are initially homogeneous and contain no defects. Therefore, there is no underlying length scale which represents a. In this section, all measurements of length or time are in units of a or τ.

4.5.2 Quasistatic Granular Flow

We first discuss granular flow results in the quasistatic limit. Rates of 10^{-5} and 3×10^{-5} were identified to be sufficiently slow in 2D and 3D, respectively, such that no significant changes in behavior were identified at lower rates. Therefore, all results in this subsection use these rates. In Fig. 4.21 typical stress strain curves are plotted for 2D and 3D systems. The initial solids are fully intact with no defects. Failure coincides with the nucleation of

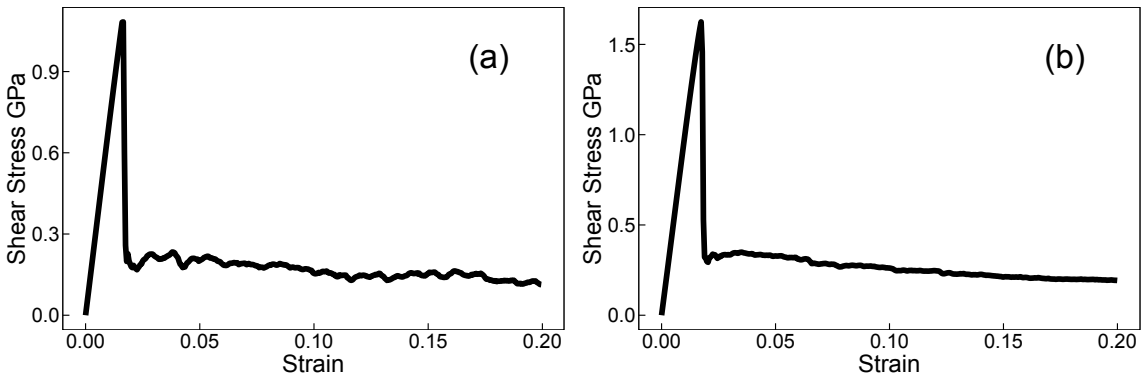

Figure 4.21: Stress strain curves for a systems strained at a rate of (a) 10^{-5} in 2D and (b) 3×10^{-5} in 3D.

cracks in the homogeneous bulk that then rapidly grow, leading to failure. Upon yielding, the system flows at a relatively low flow stress that gradually decreases with increasing strain.

An example 2D granular state at a strain of 100% is rendered in Fig. 4.22. Grains consist of a set of connected particles. Every independent grain is colored differently to highlight the large disparity in grain sizes. A large fraction of the mass of the system is contained in a single large grain that is colored blue. As can be seen, this grain is unstable and is about to fracture in several locations.

To characterize such granular states, we study the evolution of the grain size distribution. In this section we define $N(M)$ as the number of grains of a particular mass M. The distribution is not normalized so that changes in the number of particles with increasing strain can be seen. At predetermined values of the strain, the set of grains is calculated using a list of broken bonds in the system. Grain sizes are then binned in logarithmically spaced intervals of mass M. The total number of grains in each bin is then divided by

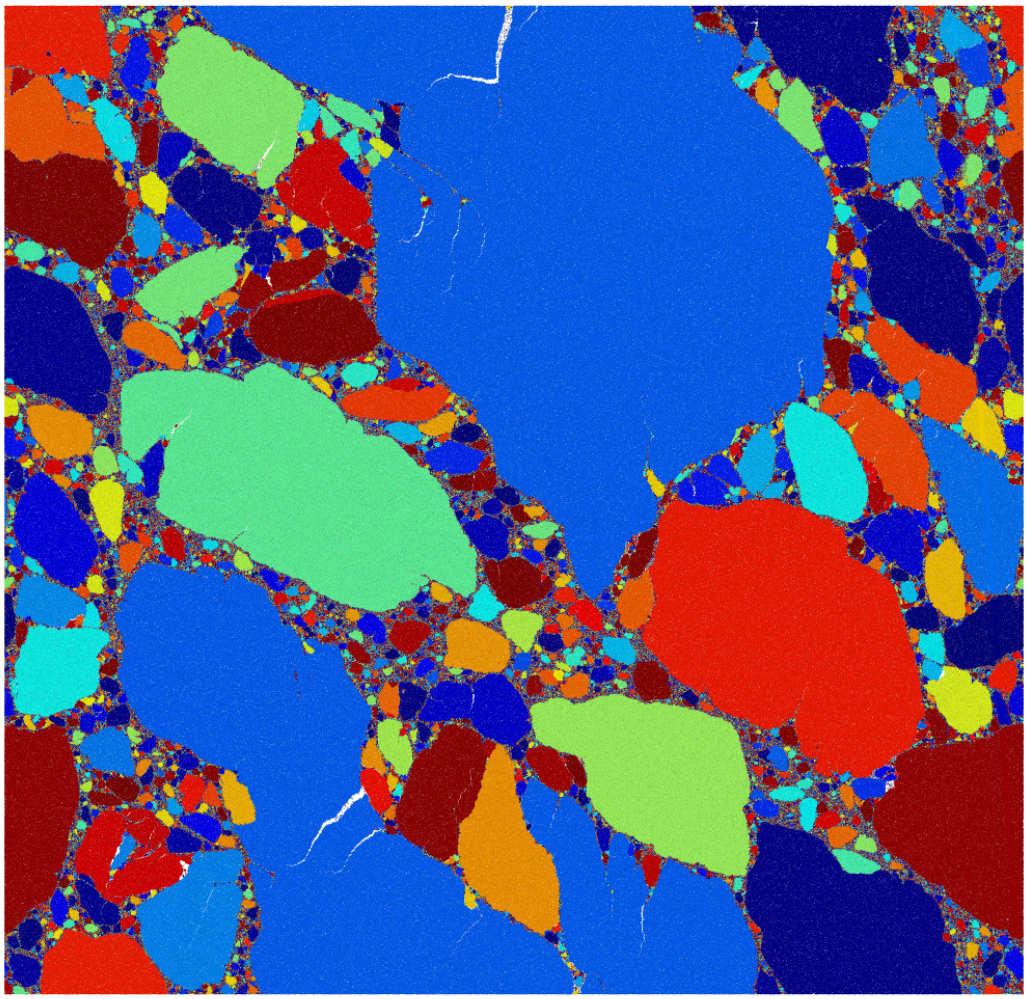

Figure 4.22: Grains in a 2D system sheared to 100% strain. Particles comprising a single grain are indicated by color. The large blue grain spans the periodic boundary conditions at the top and bottom of the simulation box. Many cracks in this grain are visible.

the bin's width to account for increasing bin width with increasing M. The resulting distributions were then averaged across different random ensembles to improve statistics. To further reduce noise, a rolling mean was applied to the distribution, averaging all sets of three adjacent data points.

In Fig. 4.23a-b, size distributions are plotted for (a) 2D and (b) 3D systems at the values of strain indicated in the legends. Small grains are not expected to represent critical behavior and statistics are likely affected by the finite size of a single particle. We estimate the lower limit of critical behavior is set by $M_{\min} \sim 10$ particles in 2D and 80 particles in 3D. Focusing on values of $M > M_{\min}$, $N(M)$ is consistent with a power law decay up to an upper cutoff $M_{\max}$. For $M > M_{\max}$, the distribution rapidly drops to zero. At even higher values of M, the distribution spikes back up. This spike represents mass in very large fragments of size M_{bulk}. Such grains, as the large blue grain seen in Fig. 4.22, represent some bulk portion of the fragmented mass that is non-critical and is degrading with time.

As the strain increases, $M_{\max}$ increases, extending the power-law regime. There is growth in $N(M)$ for $M < M_{\max}$ as M_{bulk} decreases. This represents the flow of mass from large remnants of the initially fractured solid to smaller lengths that are part of the critical distribution. As mass flows downwards, the number of particles on all scales $M < M_{\text{bulk}}$ appears to grow at the same rate, preserving the power law. Direct measurements of the exponent at high strains are consistent with a value of $\tau = 1.67 \pm 0.04$ and 1.55 ± 0.05 in 2D and 3D, respectively.

In Fig. 4.23c-d, $N(M)$ is scaled by M^{τ} to emphasize deviations from scaling and the

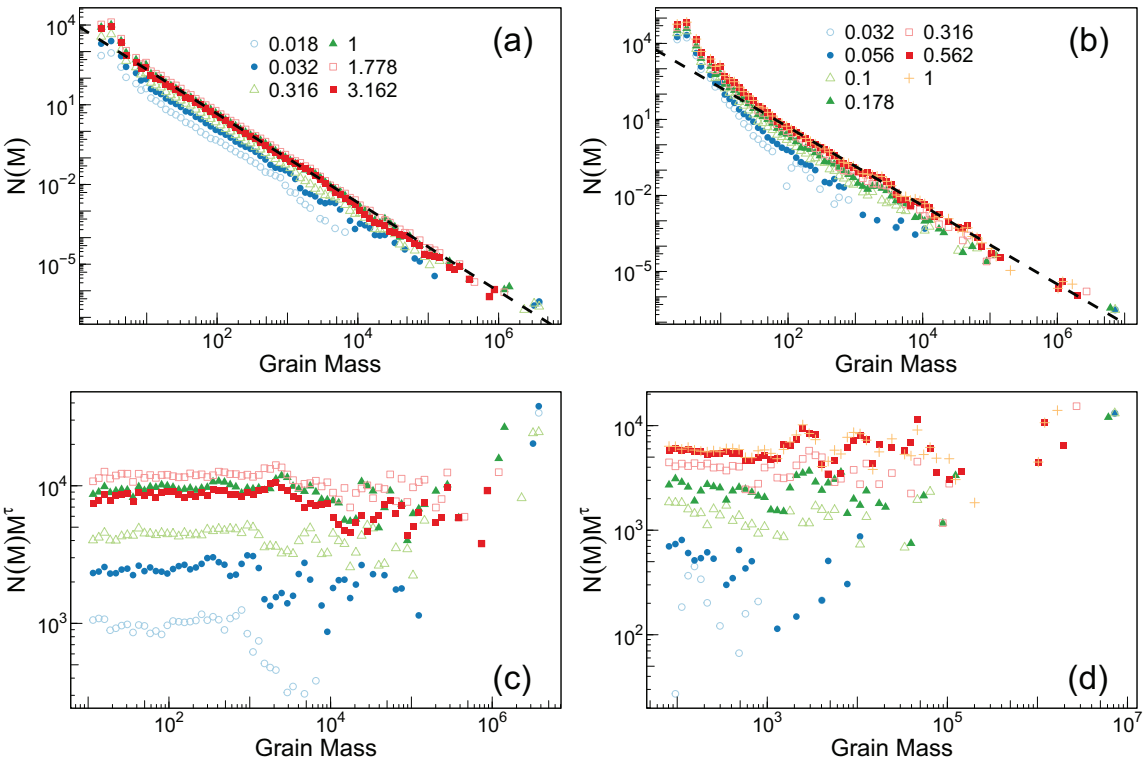

Figure 4.23: (a-b) The number of grains as a function of volume at the indicated values of strain for a system in (a) 2D and (b) 3D. Dashed lines represent power-law scaling with an exponent $\tau = 1.67$ in (a) 2D or 1.55 in (b) 3D. (c-d) The above data is scaled by M^τ to emphasize deviations from scaling for (c) $M > M_{\min} = 10$ in 2D and (d) $M > M_{\min} = 80$ in 3D.

decay in M_{bulk}. All curves are nearly horizontal between M_{min} and M_{max} indicating that τ is independent of strain. The height of the curves rises at first. In this regime, M_{bulk} provides a source of mass, fueling the growth of the critical regime and an increase in M_{max}. In the 2D system, M_{max} reaches M_{bulk} at $\epsilon \approx 1.778$. At larger strains, there is no bulk source of mass and $N(M)$ decreases as continued granular breakup transfers mass from the power-law regime to length scales $M \leq M_{\text{min}}$. In 3D simulations M_{max} has not reached M_{bulk} at the largest strains, indicating systems should be further strained to maximize M_{max}.

These results provide novel insight into the evolution of the grain size distribution and the possible nature of a critical point. Upon fracture, a power-law distribution is already identifiable. This is consistent with previous findings that impacted spheres produce a scale invariant distribution of fragments without undergoing significant granular flow.[45,151,198] The power-law is cut off at some upper length scale defined by M_{max}. As the system subsequently flows, M_{max} appears to grow with increasing strain. This continues until finite-size effects emerge when M_{max} approaches M_{bulk}. This suggests the critical point may exist at the limit of infinite system size and strain. This may correspond to a steady state in the flow of mass to smaller length scales. It would be useful to have data for different system sizes to test this possibility with finite-size scaling techniques.

4.5.3 Rate Effects

Having studied the quasistatic limit, we now look at the effect of finite strain rates on comminution. In Fig. 4.24, results from the same initial sample are rendered after shearing

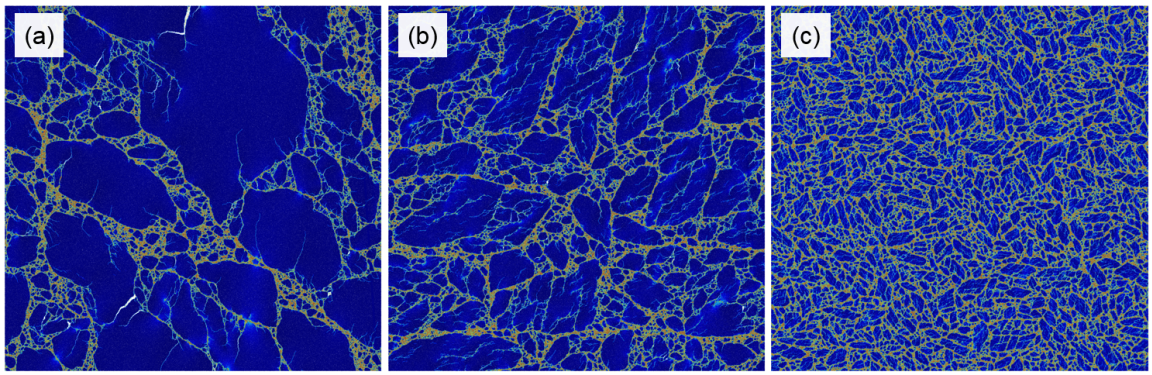

Figure 4.24: Sample comminuted samples strained to 100% at a rate of (a) 10^{-5}, (b) 10^{-4}, and (c) 10^{-3}. Color corresponds to the change in energy in bonds. Blue roughly represents particles that have no broken bonds while red represents particles that have broken the majority of their bonds.

to strains of 100% at a rate of (a) 10^{-5}, (b) 10^{-4}, and (c) 10^{-3}. Color emphasizes the locations of broken bonds. Note that the configuration in Fig. 4.24a is the same as Fig. 4.22. As the strain rate increases, a smaller maximum grain size is identified. To quantify this effect, we study the dependence of $N(M)$ on rate.

Figure 4.25a includes plots of $N(M)M^{\tau}$ for 2D systems strained at a rate of 10^{-4} up to the value of strain indicated in the legend. Distributions are truncated at a value of $M_{\text{min}} = 10$. After the initial fracture at low strains, one can already identify a power-law decay in $N(M)$. However, in contrast to the QS limit, this decay has a different exponent. As the strain increases, there is an increase in both the upper cutoff of the power law, M_{max}, as well as the apparent exponent. M_{bulk} decreases faster such that $M_{\text{max}} \sim M_{\text{bulk}}$ at lower strains of around 0.3. This explains the limitation of M_{max} observed in Fig. 4.24. As M_{max} grows, the measured exponent also increases until saturating at a value consistent with 1.73 ± 0.05 that is distinct from the value measured in the QS limit. Upon saturation, M_{max} begins to decrease and the distribution again starts to fall as mass flows to length

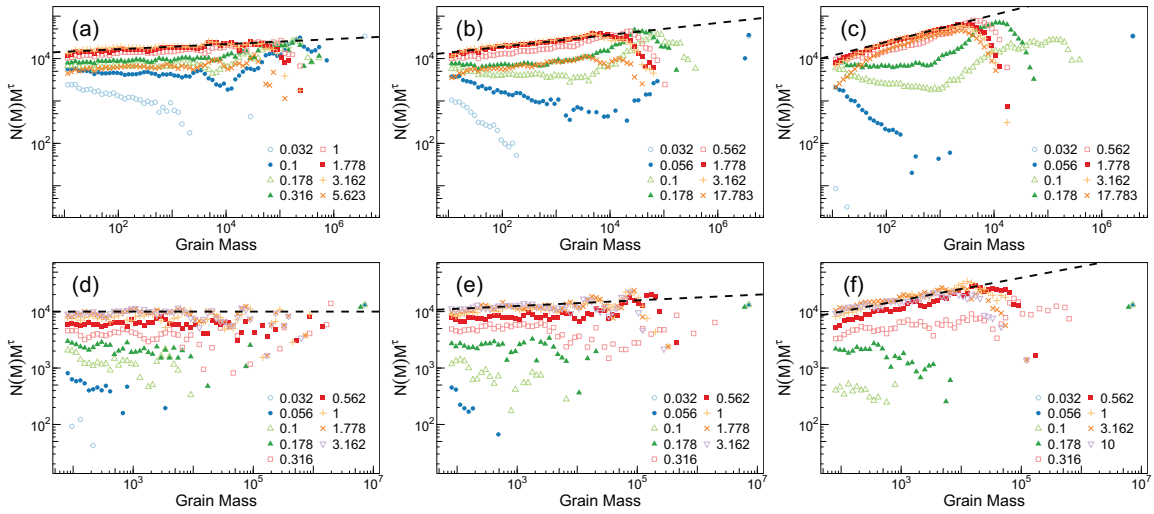

Figure 4.25: Number of grains of a particular volume M scaled by M^τ for systems sheared to strains indicated in the legend in (a-c) 2D and (d-f) 3D. Systems were strained at rates of (a) 10^{-4}, (b) 3×10^{-4}, and (c) 10^{-3} in 2D and (d) 10^{-4}, (e) 3×10^{-4}, and (f) 10^{-3} in 3D. Data only plotted for grains of volume $M > 10$ in 2D and $M > 80$ in 3D. Dashed lines in (a-c) represent power-law scaling with an exponent (a) $\tau + 0.06$, (b) $\tau + 0.14$, and (c) $\tau + 0.32$ in 2D systems for $\tau = 1.67$. Dashed lines in (d-f) represent power-law scaling with an exponent (d) τ, (e) $\tau + 0.05$, and (f) $\tau + 0.2$ in 3D systems for $\tau = 1.55$.

scales represented by $M < M_{\text{min}}$.

At higher rates of 3×10^{-4} and 10^{-3} in Fig. 4.25b-c, respectively, similar trends emerge. The measured decay exponent of $N(M)$ increases with strain before saturating at even higher values of 1.81 ± 0.08 and 2.0 ± 0.15 at rates of 3×10^{-4} and 10^{-3}, respectively. In 3D systems, qualitatively similar behavior is seen with increasing rate. At a rate of 10^{-4} no deviation in τ is detected but at rates of 3×10^{-4} and 10^{-3} direct measurements of the exponent are consistent with values of 1.6 ± 0.04 and 1.85 ± 0.15, respectively.

These observations suggest the presence of highly unusual behavior at finite rates. The decrease in the maximum grain size suggests the critical point only exists in the quasistatic limit. However, the origin of the variation in exponent is unknown. More detailed analysis

of these distributions with improved statistics is required. As seen in Chapter 3, a finite correlation length is expected at a finite rate. This finite correlation length sets the extent of the power-law distribution but does not affect the exponent τ in the yielding transition.

These simulations can also be used to extract useful information about the rate dependence of the flow stress and internal friction coefficient, roughly approximated as the ratio of the pressure to the shear stress. In order to reduce the magnitude of fluctuations, the stress and pressure versus strain curves were averaged across different random ensembles and smoothed using a rolling mean. In Fig. 4.26a-b, the shear stress is plotted as a function of strain for (a) 2D and (b) 3D systems strained at rates indicated in the legend. The shear stress increases with rate. In Fig. 4.26c-d, the ratio of the shear stress to the pressure is plotted as a function of strain. This is a measure of the internal friction in the system and shows a decreasing friction coefficient with increasing rate. This is driven by a larger increase in the pressure relative to the shear stress with increasing rate. This may explain why shock experiments measure lower friction coefficients in granular packings than quasistatic experiments.

4.5.4 Material Properties

Finally, we briefly look at how changes in the elastic properties of the solid affect granular flow. Two dimensional simulations were run for sheared samples with different values of the angular stiffness k_A. As discussed in Subsec. 4.3.1, increasing k_A decreases Poisson's ratio. In Fig. 4.27a, $N(M)M^\tau$ is plotted from simulations sheared to strains of 56% at a rate of 10^{-5} using different values of k_A. For all values of k_A except for $k_A = 12$,

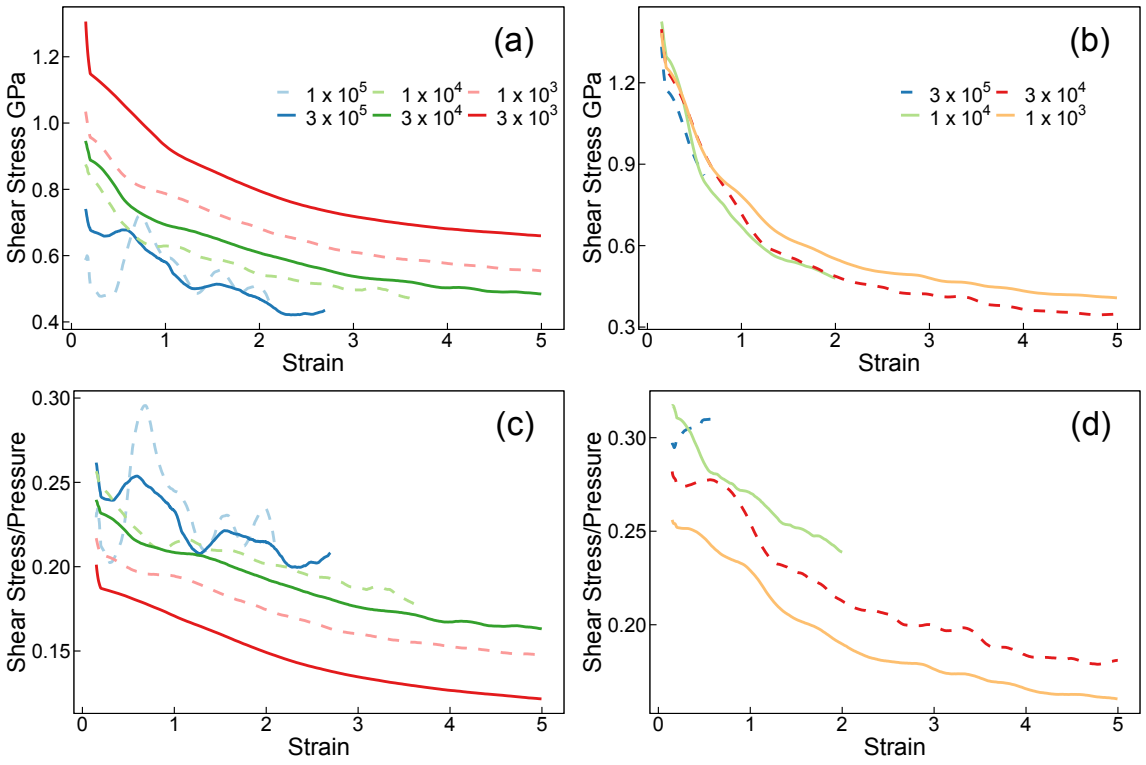

Figure 4.26: Stress strain curves for (a) 2D and (b) 3D systems strained at the rates indicated in the legends. The ratio of shear stress to pressure is plotted as a function of strain for (c) 2D and (d) 3D systems strained at the rates indicated in the legends of (a) and (b), respectively.

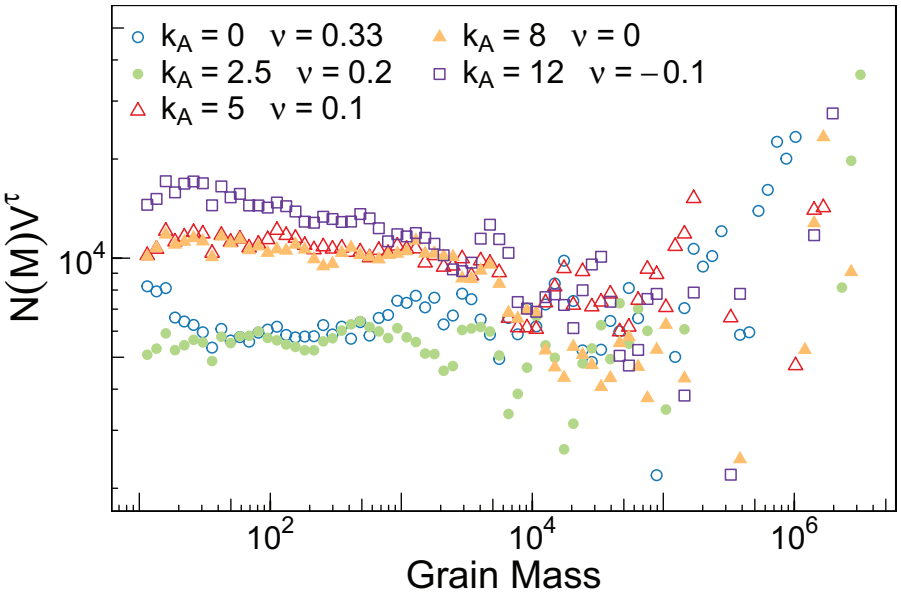

Figure 4.27: Number of grains of a particular volume M scaled by M^τ for systems sheared to a strain of 56% at a rate of 10^{-5} (a) and 10^{-4} (b) for the values of k_A indicated in the legend.

no deviation in τ can be identified. For $k_A = 12$ there may be a minor increase in τ. This data suggests τ does not depend significantly, if at all, on the elastic response of the system in the QS limit. To confirm this result would require better statistics. In addition, the evolution of $N(M)$ should be studied as a function of strain for each value of k_A and the rate dependence should be checked to confirm the data is in the QS limit for all k_A. For instance, it is possible that a lower rate is required to reach the QS limit for large k_A (small ν). If so, this could explain why a deviation is only seen for the largest value of k_A.

Next we look at how the structure of grains may depend on k_A. In Fig. 4.28 a granulated state generated from strains of 100% at a rate of 10^{-4} is rendered using a value of (a) $k_A = 0$ and (b) $k_A = 12$. These values correspond to values of $\nu = 0.25$ and -0.1, respectively. The sample with a larger Poisson's ratio appears to have to more angular and less anisotropic

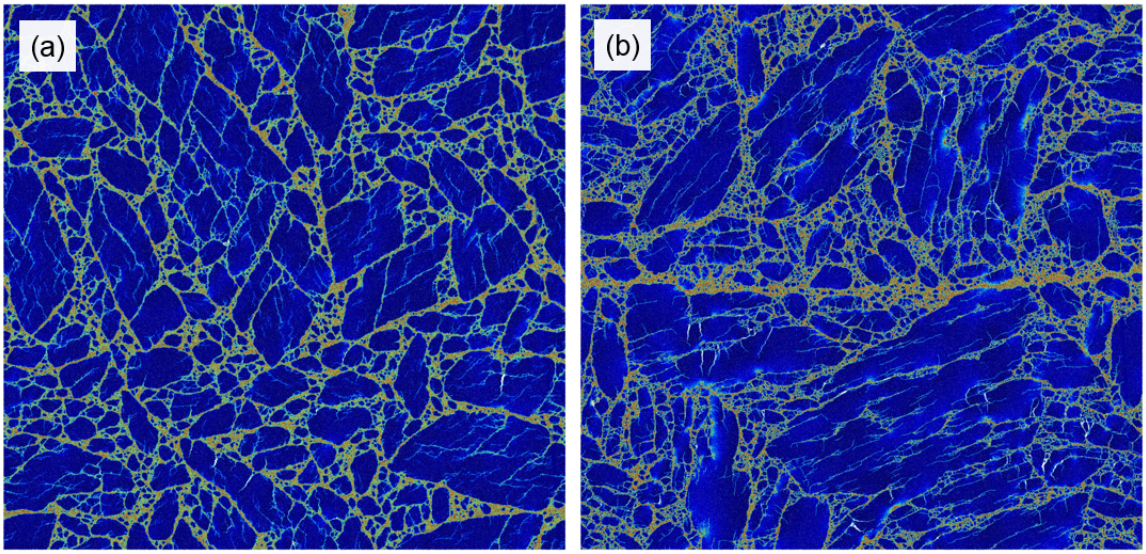

Figure 4.28: Example comminuted samples strained to 100% at a rate of 10^{-4} for a value of $k_A = 0$ or $\nu = 0.25$ (a) and $k_A = 12$ or $\nu = -0.1$ (b). Color corresponds to the change in energy in bonds. Blue roughly represents particles that have no broken bonds while red represents particles that have broken the majority of their bonds.

grains.

To quantify the anisotropy of grains, we use the technique used in Chapter 2 to quantify the anisotropy of avalanches. The second moment tensor of each grain is calculated and diagonalized. The ratio r^2 of the maximum and minimum eigenvalues then characterizes the aspect ratio of each grain. Data was collected for systems sheared to 100% strain at a rate of 10^{-4} for different values of k_A. Grains were divided into logarithmically spaced bins of volume and an average aspect ratio r was calculated for each bin. The average aspect ratio is plotted as a function of angular stiffness in Fig. 4.29 for grain sizes indicated in the legend. Small grains have no detectable anisotropy, but larger grains generally become more anisotropic at larger values of k_A or smaller Poisson's ratios. This is an interesting effect and suggests that the elastic response of a material may have a significant impact on

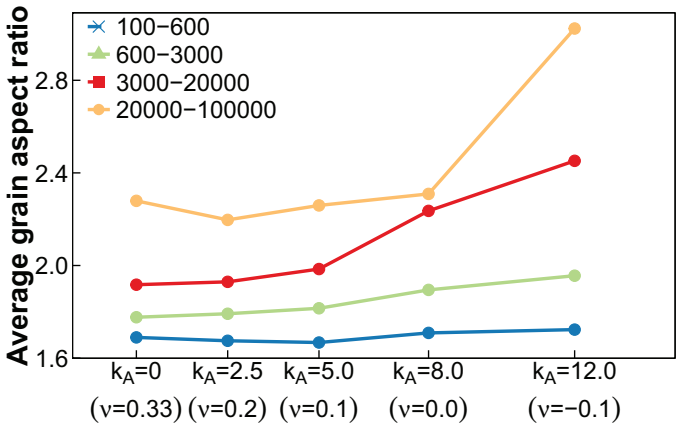

Figure 4.29: The average aspect ratio of grains with a volume in the range indicated in the legend as a function of angular stiffness for a system sheared to a strain of 100% at a rate of 10^{-4}. Corresponding values of ν are indicated.

granular structure without changing critical exponents.

Lastly, we look at the effect of the elastic response on the flow curves. In Fig. 4.30a, stress-strain curves are plotted for the indicated values of k_A. Increasing k_A or decreasing ν leads to a larger flow stress. In Fig. 4.30b, the ratio of shear stress to pressure is plotted, revealing a general increase in the friction coefficient with larger k_A or smaller ν. Other work has shown that grain shape affects friction in flow[200] suggesting that this effect may originate from the change in grain structure.

4.6 Summary

Simulations of sheared 2D and 3D brittle solids were used to probe the dependence of fracture and comminution on rate, defect density, and material properties. These simulations demonstrate the flexibility of the proposed discrete element model and highlight

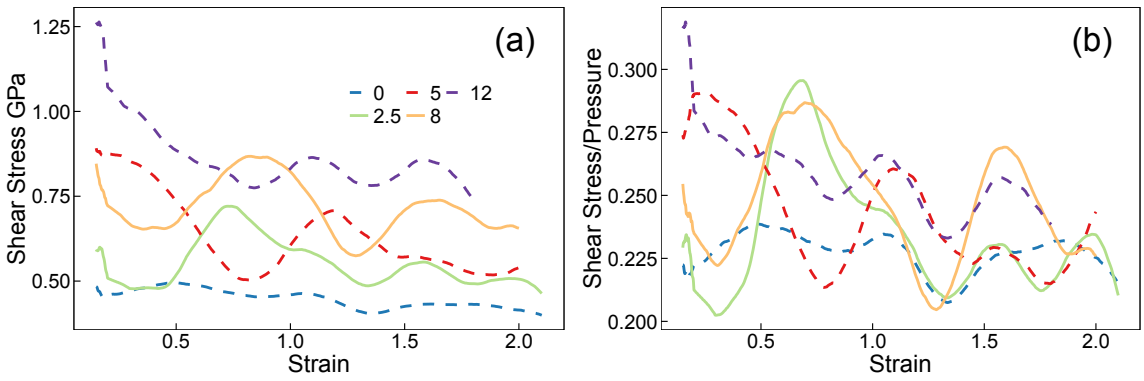

Figure 4.30: (a) Stress strain curves for systems strained at a rate of 10^{-4} for the values of k_A indicated in the legends. (b) The ratio of shear stress to pressure is plotted as a function of strain for the values of k_A indicated in the legend of (a).

a broad range of applications. Many results in this chapter were drawn from initial exploratory simulations indicating there is a great deal of potential future work.

Focusing on fracture and failure, direct measurement of damage was compared to changes in the stress-strain curves and mapped to different regimes of crack growth. Damage was found to accumulate over a broader interval of strain at high rate and failure involved the participation of many more defects, as expected from prior work.[122,169] If macroscopic changes in the stress or other system properties can be related to well defined thresholds of damage as a function of rate, it would be very useful for damage-based constituitive models.[122,174]

In pure shear deformation, we found that the initial yield occured when cracks spanned the system. This did not lead to failure of the sample, as the solid continued to elastically load with a reduced modulus. This reduction in modulus depended on rate in 3D samples. No reduction in the elastic modulus was detected in the lead up to the initial yield. Failure of brittle materials depends heavily on loading geometry[201] so it would be useful to apply

these methods to other loading geometries such as uniaxial compression. It would also be useful to evaluate how elastic properties of materials change with damage. The effect of damage on Poisson's ratio is unknown and any information on the dependence could improve constituitive models.[122,174]

Studying failure in samples with different defect densities, we found an interaction between the number of active defects and rate that is consistent with theoretical predictions.[122,169] This observation was based on a single sample, and more quantitative statements could be made if a full ensemble of systems was studied. The interaction of rate and defect activation has been studied before using continuum based 2D simulations[168,169] and it would be helpful to compare to results from DEM simulations. Furthermore, information on the impact of defect density and rate on the distribution of fragment sizes could help test theories of fracture[157,171,172] or provide a framework for the development of continuum scale models that capture the transition from fracture to granular flow.

In comminution we find evidence that a critical point may exist at quasistatic rates in the limit of infinite strains. The exponent characterizing the decay of the distribution of grain sizes likely does not depend on the elastic response of the material. We find a power-law can be identified immediately after fracture and it extends up to a maximum grain size that increases with strain. The evolution of grain size distributions plays an essential role in continuum models of comminution[123,124,202] and the evolution seen here conflicts with common assumptions that distributions linearly evolve to reach an ultimate state.[123,124] While an ultimate distribution may exist in compression where the void ratio goes to zero, in pure shear we see continued breakup of mass as mass always flows to smaller length

scales.

At high rates, we see the introduction of a maximum grain size. Interestingly, we identify a complicated evolution of the distribution. At small strains, the exponent describing power-law decay is smaller than the QS value. As the strain increases, the exponent increases before saturating at some maximum value that increases with increasing rate. The origin of such an effect is unknown but it could suggest a mechanism for the variety of power-law exponents measured in natural systems and simulations. Other mechanisms may also exist, such as changes with loading geometry.

Future work should focus on the evolution of the grain size distribution in systems of varying sizes. Presumably smaller systems would exhibit QS behavior at higher rates. It is unknown whether a different value of τ would be measured in the QS limit. Varying system size would also allow for the use of finite-size scaling techniques.

Lastly, we briefly looked at the dependence of flow stress and measures of internal friction as a function of rate and material properties. The flow of comminuted systems is very complicated and very little data is available on the rate dependence.[203,204] Additional information could therefore be useful in calibrating continuum models.

Chapter 5

Conclusion

In this thesis the dynamics of three types of systems have been explored using simulations. In each system, scale invariant behavior was observed and characterized. This work has identified new phenomena in each of the three systems, and has also accurately measured many critical exponents for the first time.

We first studied the driven dynamics of magnetic domain walls in the random field Ising model. Here we simulated a fully d dimensional interface and identified a new anisotropy in avalanches. The anisotropy exponent is distinct from previous measurements of the roughness exponent and suggests that the random field Ising model may be in a distinct universality class from the quenched Edwards-Wilkinson model.[57,59,60,65] This work also explores novel evolution in surface morphology, particularly in the growth of overhangs. Whether the anisotropy exponent for avalanche growth χ is equal to the roughness exponent ζ or if the surface is even self-affine is still an open question.

Next we studied the yielding transition using molecular dynamics simulations of sheared disordered solids. Using finite-size scaling techniques, we performed the first accurate measurements of many dynamic exponents in a continuum system. Exponents are found to be distinct from those measured in discrete lattice models,[40] suggesting that discrete models describe a separate universality class. In particular, this work found that the dynamical exponent z is greater than one in both 2D and 3D. The observation of $z < 1$ in lattice models suggest an unphysically rapid transfer of information.[40] Results were also used to test many scaling relations proposed here as well as in previous work. Interesting geometrical effects are identified in the transport of particles in 2D, suggesting an avenue for future research.

Finally we studied brittle fracture and granular flow using a particle-based model related to discrete element models (DEMs). This model used a novel combination of ideas from MD simulations and typical DEMs. The model contained a minimal number of free parameters which were used to calibrate both the elastic response and the fracture toughness of a solid. Simulations were then used to study the transition from fracture to granular flow. Tracking the evolution of cracks allowed for the calculation of damage as a function of strain. Growth in damage was then related to changes in stress-strain curves and regimes of crack growth. Complicated interactions were identified between defect density and rate and compared to existing theories.[122,168,169] Finally, we studied simulations of comminution. Results suggest a critical point may exist for quasistatically sheared systems at infinite strains. The introduction of finite rate led to a variation in the measured exponent which could partially explain the wide variety of experimentally measured exponents. Results from a range of system sizes would help resolve this question. Results also explored the effect of strain rate

and material properties on flow stress and internal friction.

Grant Acknowledgements

This material is based upon work supported by the National Science Foundation under Grant No. DMR-1411144 and DMR-1006805 as well as the Army Research Lab under the MEDE Collaborative Research Alliance, through Grant W911NF-12-2-0022. Support and training was also provided by the NSF under the IGERT training grant 0801471

Bibliography

[1] B. Mandelbrot, W. Freeman, and Company, *The Fractal Geometry of Nature*, ser. Einaudi paperbacks. Henry Holt and Company, 1983.

[2] A. L. Barabási and H. E. Stanley, *Fractal concepts in surface growth*. Cambridge University Press, 1995.

[3] T. Vicsek, *Fractal Growth Phenomena*. World Scientific, 1992.

[4] B. Gutenberg and C. F. Richter, *Seismicity of the Earth and Associated Phenomena*, 2nd ed. Princeton University Press Princeton, N. J, 1954.

[5] C. Godano, E. Lippiello, and L. de Arcangelis, "Variability of the b value in the Gutenberg–Richter distribution," *Geophysical Journal International*, vol. 199, no. 3, pp. 1765–1771, 2014.

[6] A. Clauset, C. R. Shalizi, and M. E. Newman, "Power-law distributions in empirical data," *SIAM Review*, vol. 51, no. 4, pp. 661–703, 2009.

[7] P. J. Cote and L. V. Meisel, "Self-organized criticality and the Barkhausen effect,"

Physical Review Letters, vol. 67, no. 10, pp. 1334–1337, 1991.

[8] O. Perković, K. A. Dahmen, and J. P. Sethna, "Disorder-induced critical phenomena in hysteresis: Numerical scaling in three and higher dimensions," *Physical Review B*, vol. 59, no. 9, pp. 6106–6119, 1999.

[9] P. Dutta and P. M. Horn, "Low-frequency fluctuations in solids: 1f noise," *Reviews of Modern Physics*, vol. 53, no. 3, pp. 497–516, 1981.

[10] M. C. Kuntz and J. P. Sethna, "Noise in disordered systems: The power spectrum and dynamic exponents in avalanche models," *Physical Review B - Condensed Matter and Materials Physics*, vol. 62, no. 17, pp. 11 699–11 708, 2000.

[11] K. J. Måløy, S. Santucci, J. Schmittbuhl, and R. Toussaint, "Local waiting time fluctuations along a randomly pinned crack front," *Physical Review Letters*, vol. 96, no. February, pp. 1–4, 2006.

[12] D. Bonamy and E. Bouchaud, "Failure of heterogeneous materials: A dynamic phase transition?" *Physics Reports*, vol. 498, no. 1, pp. 1–44, 2011.

[13] D. L. Turcotte, "Fractals and fragmentation," *Journal of Geophysical Research*, vol. 91, no. B2, p. 1921, 1986.

[14] I. Einav, "Fracture propagation in brittle granular matter," *Proceedings of the Royal Society A: Mathematical, Physical and Engineering Sciences*, vol. 463, no. 2087, pp. 3021–3035, 2007.

[15] A. C. Palmer and T. J. O. Sanderson, "Fractal Crushing of Ice and Brittle Solids,"

Proceedings of the Royal Society A: Mathematical, Physical and Engineering Sciences, vol. 433, no. 1889, pp. 469–477, 2006.

[16] M. Gherardi and M. C. Lagomarsino, "Characterizing the size and shape of sea ice floes," *Scientific Reports*, vol. 5, pp. 1–11, 2015.

[17] M. Kardar, *Statistical Physics of Fields*. Cambridge University Press, 2007.

[18] H. Stanley, "Scaling, universality, and renormalization: Three pillars of modern critical phenomena," *Reviews of Modern Physics*, vol. 71, no. 2, pp. S358–S366, 1999.

[19] D. S. Fisher, "Threshold behavior of charge-density waves pinned by impurities," *Physical Review Letters*, vol. 50, no. 19, pp. 1486–1489, 1983.

[20] O. Narayan and D. S. Fisher, "Threshold critical dynamics of driven interfaces in random media," *Phys. Rev. B*, vol. 48, no. 10, p. 7030, 1993.

[21] T. Nattermann, S. Stepanow, L.-H. Tang, and H. Leschhorn, "Dynamics of Interface Depinning in a Disordered Medium," *Journal De Physique Ii*, vol. 2, no. 8, pp. 155–158, 1992.

[22] D. S. Fisher, "Collective transport in random media: from superconductors to earthquakes," *Physics Reports*, vol. 301, no. 1-3, pp. 113–150, 1998.

[23] M. Kardar, "Nonequilibrium Dynamics of Interfaces and Lines," *Physics Reports*, vol. 301, p. 36, 1997.

[24] H. Gao and J. R. Rice, "A First-Order Perturbation Analysis of Crack Trapping by

Arrays of Obstacles," *Journal of Applied Mechanics*, vol. 56, no. 4, p. 828, 1989.

[25] J. F. Joanny and M. O. Robbins, "Motion of a contact line on a heterogeneous surface," *The Journal of Chemical Physics*, vol. 92, no. 5, pp. 3206–3212, 1990.

[26] D. Ertaş and M. Kardar, "Critical dynamics of contact line depinning," *Physical Review E*, vol. 49, no. 4, pp. R2532–R2535, 1994.

[27] K. Schenk, B. Drossel, S. Clar, and F. Schwabl, "Finite-size effects in the self-organized critical forest-fire model," *European Physical Journal B*, vol. 15, no. 1, pp. 177–185, 2000.

[28] N. Martys, M. Cieplak, and M. O. Robbins, "Critical phenomena in fluid invasion of porous media," *Physical Review Letters*, vol. 66, no. 8, pp. 1058–1061, 1991.

[29] J. S. Urbach, R. C. Madison, and J. T. Markert, "Interface depinning, self-organized criticality, and the Barkhausen effect," *Physical Review Letters*, vol. 75, no. 2, pp. 276–279, 1995.

[30] H. Ji and M. O. Robbins, "Percolative, self-affine, and faceted domain growth in random three-dimensional magnets," *Physical Review B*, vol. 46, no. 22, pp. 14 519–14 527, 1992.

[31] O. Chepizhko, C. Giampietro, E. Mastrapasqua, M. Nourazar, M. Ascagni, M. Sugni, U. Fascio, L. Leggio, C. Malinverno, G. Scita, S. Santucci, M. J. Alavaa, S. Zapperi, and C. A. La Porta, "Bursts of activity in collective cell migration," *Proceedings of*

the National Academy of Sciences of the United States of America, vol. 113, no. 41, pp. 11 408–11 413, 2016.

[32] B. Miller, C. O'Hern, and R. P. Behringer, "Stress Fluctuations for Continuously Sheared Granular Materials," *Physical Review Letters*, vol. 77, no. 15, pp. 3110–3113, 1996.

[33] N. W. Hayman, L. Ducloué, K. L. Foco, and K. E. Daniels, "Granular Controls on Periodicity of Stick-Slip Events: Kinematics and Force-Chains in an Experimental Fault," *Pure and Applied Geophysics*, vol. 168, no. 12, pp. 2239–2257, 2011.

[34] P. Coussot, Q. D. Nguyen, H. T. Huynh, and D. Bonn, "Avalanche Behavior in Yield Stress Fluids," *Physical Review Letters*, vol. 88, no. 17, p. 175501, 2002.

[35] M. Dennin, "Statistics of bubble rearrangements in a slowly sheared two-dimensional foam," *Physical Review E*, vol. 70, no. 4, p. 041406, 2004.

[36] S. S. Park and D. J. Durian, "Viscous and elastic fingering instabilities in foam," *Physical Review Letters*, vol. 72, no. 21, pp. 3347–3350, 1994.

[37] J. T. Uhl, S. Pathak, D. Schorlemmer, X. Liu, R. Swindeman, B. A. Brinkman, M. LeBlanc, G. Tsekenis, N. Friedman, R. Behringer, D. Denisov, P. Schall, X. Gu, W. J. Wright, T. Hufnagel, A. Jennings, J. R. Greer, P. K. Liaw, T. Becker, G. Dresen, and K. A. Dahmen, "Universal Quake Statistics: From Compressed Nanocrystals to Earthquakes," *Scientific Reports*, vol. 5, pp. 1–10, 2015.

[38] K. M. Salerno, C. E. Maloney, and M. O. Robbins, "Avalanches in Strained Amor-

phous Solids: Does Inertia Destroy Critical Behavior?" *Physical Review Letters*, vol. 109, no. 10, p. 105703, 2012.

[39] K. M. Salerno and M. O. Robbins, "Effect of inertia on sheared disordered solids: Critical scaling of avalanches in two and three dimensions," *Physical Review E - Statistical, Nonlinear, and Soft Matter Physics*, vol. 88, pp. 1–15, 2013.

[40] J. Lin, E. Lerner, A. Rosso, and M. Wyart, "Scaling description of the yielding transition in soft amorphous solids at zero temperature," *Proceedings of the National Academy of Sciences*, vol. 111, no. 40, pp. 14 382–14 387, 2014.

[41] P. Bak, C. Tang, and K. Wiesenfeld, "Self-organized criticality," *Physical Review A*, vol. 38, no. 1, pp. 364–374, 1988.

[42] S. R. Nagel, "Instabilities in a sandpile," *Reviews of Modern Physics*, vol. 64, no. 1, pp. 321–325, 1992.

[43] H. M. Jaeger, C.-h. Liu, and S. R. Nagel, "Relaxation at the Angle of Repose," *Physical Review Letters*, vol. 62, no. 1, pp. 40–43, 1989.

[44] J. P. Sethna, K. A. Dahmen, and C. R. Myers, "Crackling noise," *Nature*, vol. 410, no. 6825, pp. 242–250, 2001.

[45] L. Oddershede, P. Dimon, and J. Bohr, "Self-organized criticality in fragmenting," *Physical Review Letters*, vol. 71, no. 19, pp. 3107–3110, 1993.

[46] J. A. Åström, B. L. Holian, and J. Timonen, "Universality in fragmentation," *Physical Review Letters*, vol. 84, no. 14, pp. 3061–3064, 2000.

[47] M. Cieplak and M. O. Robbins, "Dynamical transition in quasistatic fluid invasion in porous media," *Physical Review Letters*, vol. 60, no. 20, pp. 2042–2045, 1988.

[48] H. Ji and M. O. Robbins, "Transition from compact to self-similar growth in disordered systems: Fluid invasion and magnetic-domain growth," *Physical Review A*, vol. 44, no. 4, pp. 2538–2542, 1991.

[49] O. Perković, K. Dahmen, and J. Sethna, "Avalanches, Barkhausen Noise, and Plain Old Criticality," *Physical Review Letters*, vol. 75, no. 24, pp. 4528–4531, 1995.

[50] S. Ramanathan, D. Ertaş, and D. S. Fisher, "Quasistatic crack propagation in heterogeneous media," *Physical Review Letters*, vol. 79, no. 5, pp. 873–876, 1997.

[51] O. Duemmer and W. Krauth, "Depinning exponents of the driven long-range elastic string," *Journal of Statistical Mechanics: Theory and Experiment*, no. 1, pp. –, 2007.

[52] J. Adler, Y. Meir, A. Aharony, and A. B. Harris, "Series study of percolation moments in general dimension," *Physical Review B*, vol. 41, no. 13, pp. 9183–9206, 1990.

[53] N. Martys, M. O. Robbins, and M. Cieplak, "Scaling relations for interface motion through disordered media: Application to two-dimensional fluid invasion," *Physical Review B*, vol. 44, no. 22, pp. 12 294–12 306, 1991.

[54] B. Koiller and M. O. Robbins, "Morphology transitions in three-dimensional domain growth with Gaussian random fields," *Physical Review B - Condensed Matter and Materials Physics*, vol. 62, no. 9, pp. 5771–5778, 2000.

[55] L. A. N. Amaral, A. L. Barabási, and H. E. Stanley, "Universality classes for interface

growth with quenched disorder," *Physical Review Letters*, vol. 73, no. 1, pp. 62–65, 1994.

[56] M. Kardar, G. Parisi, and Y.-C. Zhang, "Dynamic scaling of growing interface," *Physical Review Letters*, vol. 56, no. 1, pp. 1–4, 1986.

[57] P. Chauve, P. Le Doussal, and K. J. Wiese, "Renormalization of pinned elastic systems: How does it work beyond one loop?" *Physical Review Letters*, vol. 86, no. 9, pp. 1785–1788, 2001.

[58] A. Rosso, A. Hartmann, and W. Krauth, "Depinning of elastic manifolds," *Physical Review E*, vol. 67, no. 2, p. 021602, 2003.

[59] A. Rosso, P. Le Doussal, and K. J. Wiese, "Avalanche-size distribution at the depinning transition: A numerical test of the theory," *Physical Review B - Condensed Matter and Materials Physics*, vol. 80, no. 14, pp. 1–10, 2009.

[60] P. Le Doussal, A. A. Middleton, and K. J. Wiese, "Statistics of static avalanches in a random pinning landscape," *Physical Review E - Statistical, Nonlinear, and Soft Matter Physics*, vol. 79, no. 5, pp. 3–6, 2009.

[61] X. Cao, V. Démery, and A. Rosso, "Pinning by rare defects and effective mobility for elastic interfaces in high dimensions," *Journal of Physics A: Mathematical and Theoretical*, vol. 51, no. 23, pp. –, 2018.

[62] S. N. Coppersmith, "Phase slips and the instability of the Fukuyama-Lee-Rice model of charge-density waves," *Physical Review Letters*, vol. 65, no. 8, pp. 1044–1047, 1990.

[63] A. T. Krummel, S. S. Datta, S. Münster, and D. A. Weitz, "Visualizing multiphase flow and trapped fluid configurations in a model three-dimensional porous medium," *AIChE Journal*, vol. 59, no. 3, pp. 1022–1029, 2013.

[64] C. S. Nolle, "The effects of quenched disorder on moving interfaces," Ph.D. dissertation, Johns Hopkins University, 1996.

[65] S. F. Edwards and D. R. Wilkinson, "The Surface Statistics of a Granular Aggregate," *Proceedings of the Royal Society A: Mathematical, Physical and Engineering Sciences*, vol. 381, no. 1780, pp. 17–31, 1982.

[66] D. Wilkinson and J. F. Willemsen, "Invasion percolation: A new form of percolation theory," *Journal of Physics A: Mathematical and General*, vol. 16, no. 14, pp. 3365–3376, 1983.

[67] J. P. Sethna, K. Dahmen, S. Kartha, J. A. Krumhansl, B. W. Roberts, and J. D. Shore, "Hysteresis and hierarchies: Dynamics of disorder-driven first-order phase transformations," *Physical Review Letters*, vol. 70, no. 21, pp. 3347–3350, 1993.

[68] L. A. N. Amaral, A.-L. Barabási, H. A. Makse, and H. E. Stanley, "Scaling properties of driven interfaces in disordered media," *Physical Review E*, vol. 52, no. 4, pp. 4087–4104, 1995.

[69] B. Koiller and M. O. Robbins, "Growth and morphology transitions in anisotropic disordered media," *Physical Review B - Condensed Matter and Materials Physics*, vol. 82, no. 6, pp. 1–8, 2010.

[70] L. Roters, A. Hucht, S. Lübeck, U. Nowak, and K. D. Usadel, "Depinning transition and thermal fluctuations in the random-field Ising model," *Physical Review E - Statistical Physics, Plasmas, Fluids, and Related Interdisciplinary Topics*, vol. 60, no. 5, pp. 5202–5207, 1999.

[71] A. A. Middleton, "Asymptotic uniqueness of the sliding state for charge-density waves," *Physical Review Letters*, vol. 68, no. 5, pp. 670–673, 1992.

[72] A. A. Middleton and D. S. Fisher, "Critical behavior of charge-density waves below threshold: Numerical and scaling analysis," *Physical Review B*, vol. 47, no. 7, pp. 3530–3552, 1993.

[73] A. Stukowski, "Visualization and analysis of atomistic simulation data with OVITO-the Open Visualization Tool," *Modelling and Simulation in Materials Science and Engineering*, vol. 18, no. 1, pp. –, 2010.

[74] J. Lin, T. Gueudré, A. Rosso, and M. Wyart, "Criticality in the Approach to Failure in Amorphous Solids," *Physical Review Letters*, vol. 115, no. 16, p. 168001, 2015.

[75] J. Lin, A. Saade, E. Lerner, A. Rosso, and M. Wyart, "On the density of shear transformations in amorphous solids," *EPL (Europhysics Letters)*, vol. 105, no. 2, p. 26003, 2014.

[76] P. Meakin, *Fractals, scaling and growth far from equilibrium.* Cambridge University Press, 1998.

[77] G. Grinstein and S. K. Ma, "Surface tension, roughening, and lower critical dimension

in the random-field Ising model," *Physical Review B*, vol. 28, no. 5, pp. 2588–2601, 1983.

[78] C. S. Nolle, B. Koiller, N. Martys, and M. O. Robbins, "Morphology and dynamics of interfaces in random two-dimensional media," *Physical Review Letters*, vol. 71, no. 13, pp. 2074–2077, 1993.

[79] ——, "Effect of quenched disorder on moving interfaces in two dimensions," *Physica A: Statistical Mechanics and its Applications*, vol. 205, no. 1-3, pp. 342–354, 1994.

[80] F. Family and T. Vicsek, "Scaling of the active zone in the Eden process on percolation networks and the ballistic deposition model," *Journal of Physics A: Mathematical and General*, vol. 18, no. 2, pp. L75–L81, 1985.

[81] H. Leschhorn, "Interface depinning in a disordered medium - numerical results," *Physica A: Statistical Mechanics and its Applications*, vol. 195, no. 3-4, pp. 324–335, 1993.

[82] L. A. N. Amaral, A. L. Barabási, S. V. Buldyrev, S. T. Harrington, S. Havlin, R. Sadr-Lahijany, and H. E. Stanley, "Avalanches and the directed percolation depinning model: Experiments, simulations, and theory," *Physical Review E*, vol. 51, no. 5, pp. 4655–4673, 1995.

[83] D. Bonn, M. M. Denn, L. Berthier, T. Divoux, and S. Manneville, "Yield stress materials in soft condensed matter," *Reviews of Modern Physics*, vol. 89, no. 3, pp. 1–40, 2017.

[84] A. J. Liu and S. R. Nagel, "The Jamming Transition and the Marginally Jammed

Solid," *Annual Review of Condensed Matter Physics*, vol. 1, no. 1, pp. 347–369, 2010.

[85] W. H. Herschel and R. Bulkley, "Consistency measurements of rubber-benzol solutions," *Kolloid-Zeitschrift*, vol. 39, no. 4, pp. 291–300, 1926.

[86] B. a. Sun, H. B. Yu, W. Jiao, H. Y. Bai, D. Q. Zhao, and W. H. Wang, "Plasticity of Ductile Metallic Glasses: A Self-Organized Critical State," *Physical Review Letters*, vol. 105, no. 3, p. 035501, 2010.

[87] J. Antonaglia, W. J. Wright, X. Gu, R. R. Byer, T. C. Hufnagel, M. LeBlanc, J. T. Uhl, and K. a. Dahmen, "Bulk Metallic Glasses Deform via Slip Avalanches," *Physical Review Letters*, vol. 112, no. 15, p. 155501, 2014.

[88] M. Talamali, V. Petäjä, D. Vandembroucq, and S. Roux, "Avalanches, precursors, and finite-size fluctuations in a mesoscopic model of amorphous plasticity," *Physical Review E - Statistical, Nonlinear, and Soft Matter Physics*, vol. 84, no. 1, pp. 1–9, 2011.

[89] Z. Budrikis, D. F. Castellanos, S. Sandfeld, M. Zaiser, and S. Zapperi, "Universal features of amorphous plasticity," *Nature Communications*, vol. 8, no. 1, p. 15928, 2017.

[90] B. Tyukodi, D. Vandembroucq, and C. E. Maloney, "Avalanches, thresholds, and diffusion in meso-scale amorphous plasticity," *arXiv e-prints*, p. arXiv:1905.07388, May 2019.

[91] M. L. Falk and J. S. Langer, "Dynamics of Viscoplastic Deformation in Amorphous

Solids," *Physical Review E*, vol. 57, no. 6, p. 16, 1997.

[92] J. S. Langer, "Microstructural shear localization in plastic deformation of amorphous solids," *Physical Review E - Statistical Physics, Plasmas, Fluids, and Related Interdisciplinary Topics*, vol. 64, no. 1, p. 12, 2001.

[93] C. E. Maloney and A. Lemaître, "Amorphous systems in athermal, quasistatic shear," *Physical Review E - Statistical, Nonlinear, and Soft Matter Physics*, vol. 74, pp. 1–22, 2006.

[94] C. E. Maloney and M. O. Robbins, "Evolution of displacements and strains in sheared amorphous solids," *Journal of Physics: Condensed Matter*, vol. 20, no. 24, p. 244128, 2008.

[95] C. Maloney and M. Robbins, "Anisotropic Power Law Strain Correlations in Sheared Amorphous 2D Solids," *Physical Review Letters*, vol. 102, no. 22, p. 225502, 2009.

[96] F. Lançon and L. Billard, "Two-dimensional system with a quasi-crystalline ground state," *Journal de Physique*, vol. 49, no. 2, pp. 249–256, 1988.

[97] J. A. Van Meel, B. Charbonneau, A. Fortini, and P. Charbonneau, "Hard-sphere crystallization gets rarer with increasing dimension," *Physical Review E - Statistical, Nonlinear, and Soft Matter Physics*, vol. 80, no. 6, pp. 1–14, 2009.

[98] S. Plimpton, "Fast Parallel Algorithms for Short-Range Molecular Dynamics," *Journal of Computational Physics*, vol. 117, no. 1, pp. 1–19, 1995.

[99] M. Allen, M. Allen, D. Tildesley, T. ALLEN, and D. Tildesley, *Computer Simulation of Liquids*, ser. Oxford Science Publ. Clarendon Press, 1989.

[100] A. Kraynik and D. Reinelt, "Extensional motions of spatially periodic lattices," *International Journal of Multiphase Flow*, vol. 18, no. 6, pp. 1045–1059, 1992.

[101] T. A. Hunt, "Periodic boundary conditions for the simulation of uniaxial extensional flow of arbitrary duration," *Molecular Simulation*, vol. 42, no. 5, pp. 347–352, 2016.

[102] D. A. Nicholson and G. C. Rutledge, "Molecular simulation of flow-enhanced nucleation in n-eicosane melts under steady shear and uniaxial extension," *Journal of Chemical Physics*, vol. 145, no. 24, 2016.

[103] D. J. Evans and G. P. Morriss, "Nonlinear-response theory for steady planar Couette flow," *Physical Review A*, vol. 30, no. 3, pp. 1528–1530, 1984.

[104] F. Varnik, L. Bocquet, and J. L. Barrat, "A study of the static yield stress in a binary Lennard-Jones glass," *Journal of Chemical Physics*, vol. 120, no. 6, pp. 2788–2801, 2004.

[105] Y. Shi and M. L. Falk, "Strain localization and percolation of stable structure in amorphous solids," *Physical Review Letters*, vol. 95, no. August, pp. 1–4, 2005.

[106] J. Rottler and M. O. Robbins, "Unified Description of Aging and Rate Effects in Yield of Glassy Solids," *Physical Review Letters*, vol. 95, no. 22, p. 225504, 2005.

[107] K. Christensen, Z. Olami, and P. Bak, "Deterministic 1/ f noise in nonconserative

models of self-organized criticality," *Physical Review Letters*, vol. 68, no. 16, pp. 2417–2420, 1992.

[108] A. Lemaître and C. Caroli, "Plastic response of a two-dimensional amorphous solid to quasistatic shear: Transverse particle diffusion and phenomenology of dissipative events," *Physical Review E*, vol. 76, no. 3, p. 036104, 2007.

[109] K. M. Salerno, "Inertia and the critical scaling of avalanches in sheared disordered solids," Ph.D. dissertation, Johns Hopkins University, 2013.

[110] A. Lemaître and C. Caroli, "Rate-Dependent Avalanche Size in Athermally Sheared Amorphous Solids," *Physical Review Letters*, vol. 103, no. 6, p. 065501, 2009.

[111] P. Chaudhuri, L. Berthier, and L. Bocquet, "Inhomogeneous shear flows in soft jammed materials with tunable attractive forces," *Physical Review E - Statistical, Nonlinear, and Soft Matter Physics*, vol. 85, pp. 1–11, 2012.

[112] S. Karmakar, E. Lerner, I. Procaccia, and J. Zylberg, "Statistical physics of elastoplastic steady states in amorphous solids: Finite temperatures and strain rates," *Physical Review E - Statistical, Nonlinear, and Soft Matter Physics*, vol. 82, no. 3, pp. 1–11, 2010.

[113] F. Pázmándi, R. T. Scalettar, and G. T. Zimányi, "Revisiting the theory of finite size scaling in disordered systems: ν can be less than $2/d$," *Physical Review Letters*, vol. 79, no. 25, pp. 5130–5133, 1997.

[114] J. Lin and M. Wyart, "Microscopic processes controlling the Herschel-Bulkley expo-

nent," *Physical Review E*, vol. 97, no. 1, pp. 1–8, 2018.

[115] M. Ozawa, L. Berthier, G. Biroli, A. Rosso, and G. Tarjus, "Random critical point separates brittle and ductile yielding transitions in amorphous materials," *Proceedings of the National Academy of Sciences*, vol. 115, no. 26, pp. 6656–6661, 2018.

[116] W. W. Chen, A. M. Rajendran, B. Song, and X. Nie, "Dynamic fracture of ceramics in armor applications," *Journal of the American Ceramic Society*, vol. 90, no. 4, pp. 1005–1018, 2007.

[117] J. D. Hogan, L. Farbaniec, D. Mallick, V. Domnich, K. Kuwelkar, T. Sano, J. W. McCauley, and K. T. Ramesh, "Fragmentation of an advanced ceramic under ballistic impact: Mechanisms and microstructure," *International Journal of Impact Engineering*, vol. 102, pp. 47–54, 2017.

[118] H. Kanamori and E. E. Brodsky, "The physics of earthquakes," *Reports on Progress in Physics*, vol. 67, no. 8, pp. 1429–1496, 2004.

[119] A. Bobet, "The initiation of secondary cracks in compression," *Engineering Fracture Mechanics*, vol. 66, no. 2, pp. 187–219, 2000.

[120] E. M. Schulson, G. A. Kuehn, D. A. Jones, and D. A. Fifolt, "The growth of wing cracks and the brittle compressive failure of ice," *Acta Metallurgica Et Materialia*, vol. 39, no. 11, pp. 2651–2655, 1991.

[121] A. Lisjak and G. Grasselli, "A review of discrete modeling techniques for fracturing

processes in discontinuous rock masses," *Journal of Rock Mechanics and Geotechnical Engineering*, vol. 6, no. 4, pp. 301–314, 2014.

[122] B. Paliwal and K. T. Ramesh, "An interacting micro-crack damage model for failure of brittle materials under compression," *Journal of the Mechanics and Physics of Solids*, vol. 56, no. 3, pp. 896–923, 2008.

[123] I. Einav, "Breakage mechanics-Part I: Theory," *Journal of the Mechanics and Physics of Solids*, vol. 55, no. 6, pp. 1274–1297, 2007.

[124] ——, "Breakage mechanics-Part II: Modelling granular materials," *Journal of the Mechanics and Physics of Solids*, vol. 55, no. 6, pp. 1298–1320, 2007.

[125] P. A. Cundall and O. D. L. Strack, "A discrete numerical model for granular assemblies," *Géotechnique*, vol. 29, no. 1, pp. 47–65, 1979.

[126] T. Rabczuk, "Computational Methods for Fracture in Brittle and Quasi-Brittle Solids: State-of-the-Art Review and Future Perspectives," *ISRN Applied Mathematics*, vol. 2013, pp. 1–38, 2013.

[127] K. Rege and H. G. Lemu, "A review of fatigue crack propagation modelling techniques using FEM and XFEM," *IOP Conference Series: Materials Science and Engineering*, vol. 276, no. 1, p. 012027, 2017.

[128] M. A. Homel and E. B. Herbold, "Field-gradient partitioning for fracture and frictional contact in the material point method," *International Journal for Numerical Methods in Engineering*, vol. 109, no. 7, pp. 1013–1044, 2017.

[129] C. E. Maloney and M. O. Robbins, "Shear faults in a model brittle solid," *Chaos: An Interdisciplinary Journal of Nonlinear Science*, vol. 17, no. 4, p. 041105, 2007.

[130] P. S. Steif, "Crack extension under compressive loading," *Engineering Fracture Mechanics*, vol. 20, no. 3, pp. 463–473, 1984.

[131] P. Mora and D. Place, "Simulation of the frictional stick-slip instability," *Pure and Applied Geophysics PAGEOPH*, vol. 143, no. 1-3, pp. 61–87, 1994.

[132] M. Jirásek and Z. P. Bažant, "Particle Model for Quasibrittle Fracture and Application to Sea Ice," *Journal of Engineering Mechanics*, vol. 121, no. 9, pp. 1016–1025, 1995.

[133] D. O. Potyondy and P. A. Cundall, "A bonded-particle model for rock," *International Journal of Rock Mechanics and Mining Sciences*, vol. 41, no. 8 SPEC.ISS., pp. 1329–1364, 2004.

[134] Y. Wang and F. Tonon, "Calibration of a discrete element model for intact rock up to its peak strength," *International Journal for Numerical and Analytical Methods in Geomechanics*, vol. 34, no. 5, pp. 447–469, 2010.

[135] H. J. Tillemans and H. J. Herrmann, "Simulating deformations of granular solids under shear," *Physica A: Statistical Mechanics and its Applications*, vol. 217, no. 3-4, pp. 261–288, 1995.

[136] G. Cusatis, D. Pelessone, and A. Mencarelli, "Lattice Discrete Particle Model (LDPM)

for failure behavior of concrete. I: Theory," *Cement and Concrete Composites*, vol. 33, no. 9, pp. 881–890, 2011.

[137] Y. Wang and P. Mora, "Macroscopic elastic properties of regular lattices," *Journal of the Mechanics and Physics of Solids*, vol. 56, no. 12, pp. 3459–3474, 2008.

[138] A. P. Jivkov and J. R. Yates, "Elastic behaviour of a regular lattice for meso-scale modelling of solids," *International Journal of Solids and Structures*, vol. 49, no. 22, pp. 3089–3099, 2012.

[139] F. F. Abraham, D. Brodbeck, W. E. Rudge, and X. Xu, "A molecular dynamics investigation of rapid fracture mechanics," *Journal of the Mechanics and Physics of Solids*, vol. 45, no. 9, pp. 1595–1619, 1997.

[140] P. Gumbsch, S. J. Zhou, and B. L. Holian, "Molecular dynamics investigation of dynamic crack stability," *Physical Review B*, vol. 55, no. 6, pp. 3445–3455, 1997.

[141] B. L. Holian and R. Ravelo, "Fracture simulations using large-scale molecular dynamics," *Physical Review B*, vol. 51, no. 17, pp. 11 275–11 288, 1995.

[142] C. B. Barber, D. P. Dobkin, and H. Huhdanpaa, "The quickhull algorithm for convex hulls," *ACM Transactions on Mathematical Software*, vol. 22, no. 4, pp. 469–483, 1996.

[143] B. D. Lubachevsky and F. H. Stillinger, "Geometric properties of random disk packings," *Journal of Statistical Physics*, vol. 60, no. 5-6, pp. 561–583, 1990.

[144] C. R. Calladine, "Buckminster Fuller's "Tensegrity" structures and Clerk Maxwell's

rules for the construction of stiff frames," *International Journal of Solids and Structures*, vol. 14, no. 2, pp. 161–172, 1978.

[145] C. L. Kane and T. C. Lubensky, "Topological boundary modes in isostatic lattices," *Nature Physics*, vol. 10, no. 1, pp. 39–45, 2014.

[146] D. J. Jacobs and B. Hendrickson, "An Algorithm for Two-Dimensional Rigidity Percolation: The Pebble Game," *Journal of Computational Physics*, vol. 137, no. 2, pp. 346–365, 1997.

[147] R. D. Groot and P. B. Warren, "Dissipative particle dynamics: Bridging the gap between atomistic and mesoscopic simulation," *The Journal of Chemical Physics*, vol. 107, no. 11, pp. 4423–4435, 1997.

[148] J. Sethna, *Statistical Mechanics: Entropy, Order Parameters and Complexity*, ser. Oxford Master Series in Physics. OUP Oxford, 2006.

[149] K. Walton, "The effective elastic moduli of a random packing of spheres," *Journal of the Mechanics and Physics of Solids*, vol. 35, no. 2, pp. 213–226, 1987.

[150] N. S. Brar, Z. Rosenberg, and S. J. Bless, "Applying Steinberg's model to the Hugoniot elastic limit of porous boron carbide specimens," *Journal of Applied Physics*, vol. 69, no. 11, pp. 7890–7891, 1991.

[151] H. A. Carmona, F. K. Wittel, F. Kun, and H. J. Herrmann, "Fragmentation processes in impact of spheres," *Physical Review E*, vol. 77, no. 5, p. 051302, 2008.

[152] R. O. Ritchie, "The conflicts between strength and toughness," *Nature Materials*, vol. 10, no. 11, pp. 817–822, 2011.

[153] B. Paliwal, K. T. Ramesh, and J. W. McCauley, "Direct observation of the dynamic compressive failure of a transparent polycrystalline ceramic (AION)," *Journal of the American Ceramic Society*, vol. 89, no. 7, pp. 2128–2133, 2006.

[154] J. D. Hogan, L. Farbaniec, M. Shaeffer, and K. T. Ramesh, "The effects of microstructure and confinement on the compressive fragmentation of an advanced ceramic," *Journal of the American Ceramic Society*, vol. 98, no. 3, pp. 902–912, 2015.

[155] H. Tada, P. Paris, and G. Irwin, *The Stress Analysis of Cracks Handbook*. ASME Press, 2000.

[156] P. D. Washabaugh and W. G. Knauss, "A reconciliation of dynamic crack velocity and Rayleigh wave speed in isotropic brittle solids," *International Journal of Fracture*, vol. 65, no. 2, pp. 97–114, 1994.

[157] S. J. Zhou, P. S. Lomdahl, R. Thomson, and B. L. Holian, "Dynamic crack processes via molecular dynamics," *Physical Review Letters*, vol. 76, no. 13, pp. 2318–2321, 1996.

[158] T. Backers, O. Stephansson, and E. Rybacki, "Rock fracture toughness testing in Mode II—punch-through shear test," *International Journal of Rock Mechanics and Mining Sciences*, vol. 39, no. 6, pp. 755–769, 2002.

[159] Q. Rao, Z. Sun, O. Stephansson, C. Li, and B. Stillborg, "Shear fracture (Mode II) of

brittle rock," *International Journal of Rock Mechanics and Mining Sciences*, vol. 40, no. 3, pp. 355–375, 2003.

[160] B. Paliwal and K. T. Ramesh, "Effect of crack growth dynamics on the rate-sensitive behavior of hot-pressed boron carbide," *Scripta Materialia*, vol. 57, no. 6, pp. 481–484, 2007.

[161] D. P. Dandekar, "Shock response of boron carbide," Army Research Laboratory, Aberdeen Proving Ground, MD, Tech. Rep. ALR-TR-2456, April 2001.

[162] A. Manouchehrian and M. F. Marji, "Numerical analysis of confinement effect on crack propagation mechanism from a flaw in a pre-cracked rock under compression," *Acta Mechanica Sinica/Lixue Xuebao*, vol. 28, no. 5, pp. 1389–1397, 2012.

[163] Y. Wang and P. Mora, "Modeling wing crack extension: Implications for the ingredients of discrete element model," *Pure and Applied Geophysics*, vol. 165, no. 3-4, pp. 609–620, 2008.

[164] L. Scholtès and F. V. Donzé, "Modelling progressive failure in fractured rock masses using a 3D discrete element method," *International Journal of Rock Mechanics and Mining Sciences*, vol. 52, pp. 18–30, 2012.

[165] B. Budiansky and R. J. O'Connell, "Elastic moduli of a cracked solid," *International Journal of Solids and Structures*, vol. 12, no. 2, pp. 81–97, 1976.

[166] G. Vekinis, M. Ashby, and P. Beaumont, "The compressive failure of alumina contain-

ing controlled distributions of flaws," *Acta Metallurgica et Materialia*, vol. 39, no. 11, pp. 2583–2588, 1991.

[167] J. Lankford, "High strain rate compression and plastic flow of ceramics," *Journal of Materials Science Letters*, vol. 15, no. 9, pp. 745–750, 1996.

[168] N. P. Daphalapurkar, K. T. Ramesh, L. Graham-Brady, and J. F. Molinari, "Predicting variability in the dynamic failure strength of brittle materials considering pre-existing flaws," *Journal of the Mechanics and Physics of Solids*, vol. 59, no. 2, pp. 297–319, 2011.

[169] L. Graham-Brady, "Statistical characterization of meso-scale uniaxial compressive strength in brittle materials with randomly occurring flaws," *International Journal of Solids and Structures*, vol. 47, no. 18-19, pp. 2398–2413, 2010.

[170] J. Lankford and C. R. Blanchard, "Fragmentation of brittle materials at high rates of loading," *Journal of Materials Science*, vol. 26, no. 11, pp. 3067–3072, 1991.

[171] D. E. Grady and M. E. Kipp, "Geometric statistics and dynamic fragmentation," *Journal of Applied Physics*, vol. 58, no. 3, pp. 1210–1222, 1985.

[172] S. Levy and J. F. Molinari, "Dynamic fragmentation of ceramics, signature of defects and scaling of fragment sizes," *Journal of the Mechanics and Physics of Solids*, vol. 58, no. 1, pp. 12–26, 2010.

[173] C. Huang, G. Subhash, and S. J. Vitton, "A dynamic damage growth model for

uniaxial compressive response of rock aggregates," *Mechanics of Materials*, vol. 34, no. 5, pp. 267–277, 2002.

[174] A. L. Tonge and K. Ramesh, "Multi-scale defect interactions in high-rate brittle material failure. Part I: Model formulation and application to ALON," *Journal of the Mechanics and Physics of Solids*, vol. 86, pp. 117–149, 2016.

[175] R. de Borst, "Fracture in quasi-brittle materials: A review of continuum damage-based approaches," *Engineering Fracture Mechanics*, vol. 69, pp. 95–112, 2001.

[176] R. C. Hurley, J. Lind, D. C. Pagan, M. C. Akin, and E. B. Herbold, "In situ grain fracture mechanics during uniaxial compaction of granular solids," *Journal of the Mechanics and Physics of Solids*, vol. 112, pp. 273–290, 2018.

[177] R. C. Hurley and D. C. Pagan, "An in-situ study of stress evolution and fracture growth during compression of concrete," *International Journal of Solids and Structures*, vol. 168, pp. 26–40, 2019.

[178] A. F. T. Leong, E. Asare, R. Rex, X. H. Xiao, K. T. Ramesh, and T. C. Hufnagel, "Determination of size distributions of non-spherical pores or particles from single x-ray phase contrast images," *Optics Express*, vol. 27, no. 12, p. 17322, 2019.

[179] C. A. Moorehead, J. M. Sietins, and J. J. Swab, "Meso-scale microstructural agglomerate quantification in boron carbide using X-ray microcomputed tomography," *Materials Characterization*, vol. 141, no. April, pp. 177–185, 2018.

[180] L. Farbaniec, J. Hogan, J. McCauley, and K. Ramesh, "Anisotropy of Mechanical

Properties in a Hot-Pressed Boron Carbide," *International Journal of Applied Ceramic Technology*, vol. 13, no. 6, pp. 1008–1016, 2016.

[181] O. Reynolds, "LVII. On the dilatancy of media composed of rigid particles in contact. With experimental illustrations," *The London, Edinburgh, and Dublin Philosophical Magazine and Journal of Science*, vol. 20, no. 127, pp. 469–481, 1885.

[182] P. A. Thompson and G. S. Grest, "Granular flow: Friction and the dilatancy transition," *Physical Review Letters*, vol. 67, no. 13, pp. 1751–1754, 1991.

[183] W. K. Hartmann, "Terrestrial, lunar, and interplanetary rock fragmentation," *Icarus*, vol. 10, no. 2, pp. 201–213, 1969.

[184] C. Sammis, G. King, and R. Biegel, "The kinematics of gouge deformation," *Pure and Applied Geophysics PAGEOPH*, vol. 125, no. 5, pp. 777–812, 1987.

[185] A. Taşdemir, "Fractal evaluation of particle size distributions of chromites in different comminution environments," *Minerals Engineering*, vol. 22, no. 2, pp. 156–167, 2009.

[186] J. Weiss, "Fracture and fragmentation of ice: A fractal analysis of scale invariance," *Engineering Fracture Mechanics*, vol. 68, no. 17-18, pp. 1975–2012, 2001.

[187] A. Saint-Jalmes, "Physical chemistry in foam drainage and coarsening," *Soft Matter*, vol. 2, no. 10, p. 836, 2006.

[188] G. R. McDowell, "On the Yielding and Plastic Compression of Sand." *Soils and Foundations*, vol. 42, no. 1, pp. 139–145, 2002.

[189] F. Altuhafi and M. Coop, "Changes to particle characteristics associated with the compression of sands," *Géotechnique*, vol. 61, no. 6, pp. 459–471, 2011.

[190] Y. Xiao, H. Liu, Q. Chen, L. Long, and J. Xiang, "Evolution of particle breakage and volumetric deformation of binary granular soils under impact load," *Granular Matter*, vol. 19, no. 4, 2017.

[191] M. R. Coop, K. K. Sorensen, T. B. Freitas, and G. Georgoutsos, "Particle breakage during shearing of a carbonate sand," *Géotechnique*, vol. 54, no. 3, pp. 157–163, 2004.

[192] C. Marone and C. H. Scholz, "Particle-size distribution and microstructures within simulated fault gouge," *Journal of Structural Geology*, vol. 11, no. 7, pp. 799–814, 1989.

[193] C. J. Allègre, J. L. Le Mouel, and A. Provost, "Scaling rules in rock fracture and possible implications for earthquake prediction," *Nature*, vol. 297, no. 5861, pp. 47–49, 1982.

[194] E. Perfect, "Fractal models for the fragmentation of rocks and soils: a review," *Engineering Geology*, vol. 48, no. 3-4, pp. 185–198, 2002.

[195] J. A. Åström and H. J. Herrmann, "Fragmentation of grains in a two-dimensional packing," *European Physical Journal B*, vol. 5, no. 3, pp. 551–554, 1998.

[196] O. Tsoungui, D. Vallet, and J. C. Charmet, "Numerical model of crushing of grains inside two-dimensional granular materials," *Powder Technology*, vol. 105, no. 1-3, pp. 190–198, 1999.

[197] O. Ben-Nun and I. Einav, "The role of self-organization during confined comminution of granular materials," *Philosophical Transactions of the Royal Society A: Mathematical, Physical and Engineering Sciences*, vol. 368, no. 1910, pp. 231–247, 2010.

[198] G. Timár, J. Blömer, F. Kun, and H. J. Herrmann, "New universality class for the fragmentation of plastic materials," *Physical Review Letters*, vol. 104, no. 9, pp. 1–4, 2010.

[199] P. S. Iliev, F. K. Wittel, and H. J. Herrmann, "Evolution of fragment size distributions from the crushing of granular materials," *Physical Review E*, vol. 99, no. 1, pp. 1–10, 2019.

[200] J. L. Anthony and C. Marone, "Influence of particle characteristics on granular friction," *Journal of Geophysical Research: Solid Earth*, vol. 110, no. 8, pp. 1–14, 2005.

[201] J. D. Hogan, L. Farbaniec, N. Daphalapurkar, and K. T. Ramesh, "On Compressive Brittle Fragmentation," *Journal of the American Ceramic Society*, vol. 99, no. 6, pp. 2159–2169, 2016.

[202] C. K. Lieou, A. E. Elbanna, and J. M. Carlson, "Grain fragmentation in sheared granular flow: Weakening effects, energy dissipation, and strain localization," *Physical Review E - Statistical, Nonlinear, and Soft Matter Physics*, vol. 89, no. 2, pp. 1–14, 2014.

[203] L. W. Meyer and I. Faber, "Investigations on Granular Ceramics and Ceramic Powder," *Le Journal de Physique IV*, vol. 07, no. C3, pp. C3–565–C3–570, 1997.

[204] M. B. Cil, R. C. Hurley, and L. Graham-Brady, "A rate-dependent constitutive model for brittle granular materials based on breakage mechanics," *Journal of the American Ceramic Society*, vol. 102, no. 9, pp. 5524–5534, 2019.

Vita

Joel T. Clemmer began his studies in physics at Williams College in 2008. During his undergraduate years, Clemmer worked on research with Professor Protik Majumder and completed a senior thesis with Professor Daniel Aalberts. After receiving his B.A. degree in physics in 2012, Clemmer worked at Massachusetts General Hospital where he performed research with Dr. Alejandro Rauh-Hain. Clemmer joined Johns Hopkins University in 2013 as a graduate student under the supervision of Professor Mark Robbins. In August 2019, Clemmer received his PhD in physics for his dissertation on the scale invariant dynamics of interfaces and sheared solids. Starting in September 2019, Clemmer will be a postdoctoral researcher at Sandia National Labs.